Transmission Electron Microscopy Study of Nanostructured Nd-Fe-B Hard Magnetic Materials

A thesis presented for the degree of Doctor of Philosophy

Seyed Pirooz Hoveida Marashi

The University of Sheffield

Faculty of Engineering

Department of Engineering Materials

2001

To my parents

my wife

and my son

Acknowledgements

I wish to express my gratitude to Prof. H. A. Davies and Prof. W. M. Rainforth for their inspiring guidance and continuous encouragement during the completion of this work. I am also thankful for their invaluable advice and suggestions regarding this thesis.

I am grateful to the Ministry of Science, Research & Technology of Iran for providing the scholarship for this study.

I wish to express my appreciation to the Chairman and staff of the Engineering Materials Department for providing facilities and assistance in the course of this research project.

Thanks are due to the staff of the Sorby Electron Microscope Centre, particularly Miss D. Bussy and Dr. M. A. Al-Khafaji for their valuable help and advice on electron microscopy.

I am also indebted to the members of "Rapidly Solidification and Magnetic Materials" group (including several former members) for their patience, tolerance and helpfulness.

I also thank the members of the "Iranian Society" for their valuable help outside the normal study circle.

Summary

In the present study the effect of melt spinning roll speed on mean grain size and magnetic properties of near stoichiometric Nd-Fe-B alloy ribbons is investigated. A decrease in the ribbon thickness and mean $Nd_2Fe_{14}B$ grain size and improvement in magnetic properties, including remanence enhancement, were observed on increasing the roll speed, prior to vitrification and consequent collapse of properties at higher speeds.

The effect of roll speed and also annealing temperature on the microstructure and the magnetic properties and hysteresis loops of the stoichiometric alloy were studied and it was found that optimum nanostructure and magnetic properties could be achieved for a range of roll speeds and annealing temperatures which makes it an attractive route for commercial production of this alloy.

The effect of 0-3 at.% Ga substitution for Fe in the *stoichiometric* alloy of composition $Fe_{82.3}Nd_{11.8}B_{5.9}$, produced by both optimally quenching and over-quenching and annealing were studied and compared. Broadly, comparable results for both sets with some improvement in coercivity were observed for up to 2 at.% Ga addition.

The effect of 0-3 at.% Ga substitution for Fe were also investigated in overquenched and optimally annealed *substoichiometric* alloy of composition $Fe_{85.1}Nd_9B_{5.9}$ and were compared with those achieved for ribbons prepared by optimally quenched route. Inferior magnetic properties especially for ${}_jH_c$ and $(BH)_{max}$, were observed for over-quenched and annealed alloys compared with those prepared by directly quenching. The Ga addition did however result in some improvement in ${}_jH_c$ and $(BH)_{max}$, especially for the directly quenched alloy containing 1.5 at.% Ga.

The microstructure of ribbon samples were studied extensively by TEM and, in addition to normal polygonal $Nd_2Fe_{14}B$ grains, other more unusual morphologies such as spherical and plate like grains, were found in a number of samples. Various grain size distributions were also observed.

Texture and the orientation relationship between α-Fe precipitates and $Nd_2Fe_{14}B$ matrix were studied in the near stoichiometric sample containing 3 at.% Ga, melt spun at low roll speeds, and an attempt was made to identify additional phases observed in this sample.

Some dislocation-type features found in some samples were also studied.

Table of Contents

1. Introduction

Permanent magnets can be characterised by their intrinsic properties. The important factors to consider in designing magnets are the size, cost and their ability to do useful work which can be expressed for instance by the maximum energy product, $(BH)_{max}$. The selection of an appropriate magnetic material depends mainly on a) the value of flux density in the gap or in a specific volume in the absence of an applied external field (B_r), b) resistance to an external demagnetising field ($_jH_c$), c) good stability with respect to temperature (T_c) and d) high energy product $(BH)_{max}$.

Probably the first important application of permanent magnets was in marine compasses, a very important invention at the time that enabled travellers to navigate, regardless of the weather conditions, on long voyages [1]. Up to the end of the nineteenth century lodestone and carbon steels were the only available permanent magnets. The quest for better magnets has led to the discovery of new materials, and to increasingly important technological roles for the magnets. The milestones in this route to better properties have been cobalt magnet steels in 1917, Alnico alloys in 1931, hard ferrites in the late 1940's, CoPt around 1960 and SmCo in the early 1970's. Later, two approaches were adopted to develop more powerful and more economical magnets: (i) a search for new phases with better intrinsic properties, especially based on Fe rather than Co and (ii) the utilisation of new or improved manufacturing methods. Systematic studies following these two approaches led to the discovery of Nd-Fe-B magnetic materials in 1983 by Croat et al. [2] at General Motors, USA, employing the melt spinning process, and at Sumitomo, Japan by Sagawa et al. [3] using the powder metallurgy, a process already employed for SmCo magnets. The Nd-Fe-B alloys, based on the $Nd_2Fe_{14}B$ phase with a complex tetragonal crystal structure and having an easy magnetisation direction parallel to its c-axis, had generally better magnetic properties than the SmCo magnets (except for a lower T_c of ~590 K) and also had the advantage that Nd and Fe are cheaper than Sm and Co, respectively. Values of $(BH)_{max}$ up to 430 kJm^{-3} [4] have been achieved for this type of magnets.

The excellent coercivities and good energy products promoted wide interest in the development of further new alloy compositions and variants based on the tetragonal $RE_2Fe_{14}B$ compounds, partly because of the technological and economic advantages offered by polymer bonded magnets, based on melt spun ribbons, and partly because of the further benefits to be gained from property improvements. Thus a considerable amount of research has been conducted in recent years with the aim of gaining a better understanding of the behaviour of melt spun RE-Fe-B alloys with the aim of achieving improved exploitation and control of the magnetic properties of this type of compounds [5].

In the principal applications for magnets today, the different categories of permanent magnet material generally do not compete with one another. For cost efficiency alone, ceramic ferrites are used; for volumetric efficiency alone, the choice is neodymium-iron-boron; while for a combination of good properties and wide temperature range, i.e. good thermal stability, it is usually samarium-cobalt. While it appears that ceramic ferrites will retain the major portion (currently around 60% by value) of the world-wide market for permanent magnets on the basis of low cost, neodymium-iron-boron will continue to attract new applications that will draw upon its far superior magnetic properties. The growth rate of all permanent magnet production world-wide is around 10% per year but for neodymium-iron-boron this growth is 20% per year. About 80% of the latter are currently fully dense sintered or die-upset magnets, while about 20% are bonded, of which at least 60% goes to the computer industry, for use in brushless d.c. spindle motors and in stepper motors [6]. Further improvements in properties such as J_r, $_jH_c$, $(BH)_{max}$, Curie temperature and corrosion resistance, would lead to new applications for Nd-Fe-B magnets or reduce the size and/or increase the power of the devices made using these magnets.

The melt-spinning processing route produces ribbon material which is normally cast to yield a microcrystalline, single domain $RE_2Fe_{14}B$ structure (designated MQ) with a mean grain size 50-100 nm and a random crystallographic orientation which leads to modest values (0.8 T) for remanent polarisation, J_r. For melt spun Nd-Fe-B material, reducing the grain size to below ~40 nm by Al and Si addition [7-9] or by careful control of processing parameters [10-13], provides the condition for

considerable exchange coupling between $Nd_2Fe_{14}B$ grains. Therefore, remanence is enhanced so that J_r/J_s is greater than the value of 0.5, predicted by the Stoner-Wohlfarth theory [14] for randomly oriented, noninteracting, single domain particles. Further remanence enhancement is achieved by lowering the Nd content to the substoichiometric region and developing a nanocomposite structure of $Nd_2Fe_{14}B$ and α-Fe (or Fe_3B) [15]. This nanocomposite material with lower cost, higher formability, better corrosion resistance and especially higher remanence is an attractive choice for polymer bonded magnets.

Optimum magnetic properties, represented by a fully developed second quadrant demagnetisation curve, can in principle be obtained either by quenching directly from the melt or by annealing an overquenched precursor. However, because of the narrowness of the process window over which optimum direct quench results can be obtained, the usual commercial manufacturing process is the annealing route [16]. In the present study, the effects of processing parameter and also the effects of Ga additions on magnetic properties and microstructures were systematically investigated for stoichiometric single phase and substoichiometric two phase Nd-Fe-B alloy ribbons produced by both routes. Detailed microstructural studies were performed by SEM, HREM and TEM, in particular.

2. Literature Review

2.1 Introduction

Very early in recorded history, one finds references to man's attempt to use and understand magnets. The only magnetic material available in ancient times was a form of magnetite (Fe_3O_4) called lodestone (literally guiding stone, from its use in navigation by mariners). Magnet steels were available in China from about 500 A.D. The earliest systematic reporting of magnets was a classical paper by William Gilbert in 1600 [1].

2.1.1 Origin of Magnetism and Magnetic State of Matter

The origin of the concept of the magnetic moments was first suggested by Ampere who, with great insight, suggested that they were due to "electrical currents continually circulating within the atom", some seventy five years before the discovery of the electron by Thomson [17].

Electrons constantly spin on their own axis giving rise to a magnetic moment which has a constant magnitude and, in a magnetic field, it can only orient itself either parallel or anti-parallel to the field. In order to have a net magnetic moment, the atom must have an unfilled electron shell, as in the case of transition metals and rare earth elements. The movement of each electron in an orbit around the nucleus also produces a magnetic moment, which is more important in vapours, solutions or molten materials and rare earths. Materials in which none of the atoms, or molecules, have a permanent magnetic dipole moment are diamagnetic, whereas materials that contain some atoms or molecules with a permanent magnetic moment are paramagnetic, ferromagnetic, antiferromagnetic or ferrimagnetic. The distinction between paramagnetic materials and materials in the last three classes is that, in the former, the magnetic moments point in random directions at all temperatures in zero magnetic field whereas, in the latter, the magnetic moments of the atoms tend to align themselves with those of their neighbours. In a ferromagnetic material, the

moments try to become parallel to one another. In an antiferromagnetic material, the tendency is for neighbouring moments to be aligned antiparallel to each other. In a ferrimagnetic material, the tendency is also for antiparallel alignment, but either the number or the size of the moments in one direction is greater than in the other direction, Figure 2- 1 [18].

2.1.2 Definitions of Magnetic parameters

When a field is generated in a volume of space it means that there is an energy gradient in that volume so that a force is produced which can be detected by the acceleration of an electric charge moving in the field, or the force on a current-carrying conductor or by the torque on a compass needle, which is an example of a magnetic dipole. The magnetic field strength H can be defined as follows [17]: a current of 1 ampere passing through a straight 1 meter length of conductor generates a tangential field strength of $1/4\pi$ amperes per meter (A/m) at a radial distance of 1 meter.

The presence of a magnetic field in a medium generates magnetic flux Φ which is measured in units of webers. Small magnetic particles such as iron filings align themselves along the direction of this magnetic flux. The weber is the amount of magnetic flux which, when reduced uniformly to zero in one second, produces an e.m.f. of one volt in a one-turn coil of a conductor through which the flux passes.

When a magnetic field H has been generated in a medium by a current, the response of the medium is its magnetic induction B. In the other words, the amount of flux generated by a given field strength depends on the properties of the medium and varies from one medium to another and the magnetic induction B is the flux density in webers/meter^2 (w/m^2). A flux density of 1 w/m^2 is identical to a magnetic induction of one Tesla (T). A magnetic induction B of 1 Tesla generates a force of 1 N/m on a conductor carrying a current of 1 A perpendicular to the direction of the induction.

In many medium B is a linear function of H. In free space we can write:

$$(2\text{-}1) \qquad B = \mu_o H$$

where μ_o is the permeability of free space and is a universal constant having a value of $4\pi\times10^{-7}$ henries per meter (H/m). In other media, particularly ferromagnets and ferrimagnets, B is no longer a linear function of H but is related by the permeability of the medium μ through the equation:

$$(2\text{-}2) \qquad B = \mu H$$

where μ is now not necessarily a constant.

Much of the primary literature on magnetism is still written using CGS units or a confusing mixture where large fields are quoted in tesla and small ones in oersted [19]. Fundamental CGS units are cm, g and s. However, there is a movement towards the international system (MKS) which is based on five fundamental units, kg, m, s, K and A. Table 2- 1 and Table 2- 2 show physical quantities and conversion factors for CGS and SI systems.

2.1.3 The Hysteresis Loop

The magnetic properties of ferromagnetic materials are best represented using a hysteresis loop, Figure 2- 2. Point O shows the unmagnetised specimen's state. When the magnetic field is applied, the magnetic induction B is composed of two components: the lines of force due to the magnetic field H and the lines of magnetism due to presence of the magnetic material which is termed the intensity of magnetisation (magnetisation polarisation) J.

$$(2\text{-}3) \qquad B = \mu_o H + J \qquad \text{where}$$

$$(2\text{-}4) \qquad J = \mu_o M$$

M is the magnetisation or the magnetic moment per unit volume of a solid. At saturation, J becomes constant and B then increases as $\mu_0 H$. If the field is reduced to zero, B will not fall to zero but retain a value B_r (remanence, which is equal to J_r). It is necessary to apply a negative field to reduce B to zero. This value of H is defined

as the coercive force, H_c or the normal coercivity ${}_nH_c$, and the value of H which reduces the J to zero is called the intrinsic coercivity, ${}_jH_c$.

The second quarter of the hysteresis loop is characterised by the remanence, J_r, the intrinsic coercive field, ${}_jH_c$, and its rectangularity. These characteristic properties are determined by the intrinsic properties such as the saturation magnetisation, J_s, the anisotropy constants, K_i, as well as by the microstructure, the domain configuration and the magnetisation processes [20].

2.1.4 Curie Temperature

There is a critical temperature above which the magnet material is no longer behaving as a ferromagnet but shows paramagnetic response to an applied field. This temperature is called the Curie temperature (T_c). At temperatures near or above T_c, the material no longer has useful permanent magnet properties. For $Nd_2Fe_{14}B$ for instance, T_c is about 315°C [21-23].

2.1.5 Maximum Energy Product

$(BH)_{max}$ represents the useful magnetic flux B that can be produced by the magnet in a given volume or air gap. Moreover, since the required volume of magnetic material is inversely proportional to the value of $(BH)_{max}$, then an increase of $(BH)_{max}$ would reduce the required volume for the magnet [1].

A certain theoretical upper limit exists for the performance of permanent magnet materials [24]. In an ideal case, the hysteresis loop will take a perfect square shape and the second quadrant is a horizontal line parallel to the μ_oH axis with a value of $J=J_s$, Figure 2- 3. At remanence, where $\mu_oH=0$, using equation (2-3) gives $B_r=J_r$. For the linear horizontal part of the intrinsic curve $J= B_r$ and substituting this for J in equation (2-3):

$$B = B_r + \mu_o H \qquad (2\text{-}5)$$

This is the equation for the demagnetisation curve and is a straight line. The value of the coercivity H_c, when B=0 is given by:

$$\mu_o H_C = -B_r \qquad (2\text{-}6)$$

The demagnetisation curve, the straight line between $B=B_r$ and $-\mu_0 H=B_r$, is the limiting curve, B cannot have values above this straight line for a specific value of B_r. Using equation (2-5) and multiplying by H gives:

$$BH = B_r H + \mu_o H^2 \qquad (2\text{-}7)$$

and, by differentiation:

$$\frac{d(BH)}{dH} = B_r + 2\mu_o H \qquad (2\text{-}8)$$

Equating this to zero gives $H=-B_r/2\mu_0$. Substituting this value of H back into (2-7) gives the maximum value of $(BH)_{max}$:

$$(BH)_{\max}(\lim) = \frac{-B_r^2}{4\mu_o} \qquad (2\text{-}9)$$

It is only necessary for the values of J to equal J_s or B_r up to $-\mu_0 H=B_r/2$ to obtain this limiting value. The world record for the largest saturation magnetisation at room temperature is held by an alloy of about 35% Co, 65% Fe, J_s=2.45 T ($M_s=1.91\times10^6$) [18]. To get an idea of the highest possible value of $(BH)_{max}$; if we assume that the value of J_r equals the value of J_s then the maximum possible value of $(BH)_{max}$ is $(2.45)^2/4\mu_0 = 1194\ kJm^{-3}$.

2.1.6 Demagnetisation

In a magnetic field H the presence of a magnetic material affects the magnetic induction B due to its permeability μ. The flux lines are continuous throughout the material and have a similar form to the flux lines in and around a current loop dipole such as a single turn of current-carrying conductor or short solenoid. The field lines around a bar magnet are the same as the flux lines outside the material. However, inside the magnet, the generation of poles near the ends of specimen gives rise to a magnetic field opposing the applied field, Figure 2- 4. This opposing field is called

the demagnetisation field H_d and its strength depends on the geometry and magnetisation polarisation $J=\mu_o M$ of the material. Thus:

$$H_d = N_d J \qquad (2\text{-}10)$$

where N_d is a demagnetising factor which is calculated solely from the sample geometry. Tables and charts of approximate calculated demagnetising factors are available for solids of various shapes other than spheres for which $N_d = 0.333$.

If a body is magnetised by an applied field to some level A, Figure 2- 5, and the applied field is then removed, the magnetisation will decrease to C under the action of the demagnetising field H_d. The specimen then contains stored energy E_{ms} equal to the area of the shaded triangle OCD. This energy is called the magnetostatic energy, the self-energy, or the energy of a magnet in its own field. When dealing with samples of finite dimensions in an applied magnetic field H_{app} it is necessary to make some demagnetising field correction to determine the exact internal field in the solid H_{in} [17]:

$$H_{in} = H_{app} - N_d J \qquad (2\text{-}11)$$

2.2 Domains

Historically, the concept of domains was introduced to explain why two pieces of iron do not attract each other (can exist in demagnetised state) [19]. In 1907, Weiss argued that soft iron is ferromagnetic on a local scale but loses its net magnetisation by domain formation. Based on Weiss' idea Bloch (1932) suggested the domain wall.

A uniformly magnetised specimen generates a large amount of stray magnetic field, H, Figure 2- 6a [18]. The energy of this field will be much smaller for a specimen subdivided into two domains, and will get progressively smaller with increasing number of domains because H is confined to a smaller region near the specimen surface, Figure 2- 6b, c. Although, since the creation of domain walls costs energy, there are no walls if the gain in magnetostatic energy is smaller than the wall

energy cost. Another way to understand why the uniformly magnetised state is unstable is to consider the demagnetizing field. Free poles are formed on any surface along which there is a discontinuous change in the component of magnetization normal to the surface. These poles can be thought of as the sources of H, which always points towards south poles and away from north poles. A field is therefore also present inside the specimen, where it points in the opposite direction to the magnetization, which makes the situation unstable. In multidomains, the demagnetization field does not extend from the top to the bottom, but between the south and north poles of adjacent domains in the region near the two ends of the specimen and most of the volume of the specimen, is not affected by the demagnetizing field.

Magnetostriction is another parameter that affects the shape and size of domains in cubic materials and is defined as expansion or contraction of a specimen by changing its magnetization state for positive and negative magnetostriction, respectively. To prevent the specimen with domain structure, such as that in Figure 2- 7a, from splitting along the domain walls under such tension, Figure 2- 8, domains can be formed such as Figure 2- 7b in which the distortion produced by magnetization in opposite directions is the same and much less elastic distortion is associated with the small triangular domains (closure domains) compared to large domains of Figure 2- 7a.

The domain structure of uniaxial materials will consist of long, narrow domains magnetised in opposite direction, rather like Figure 2- 6c. Near surfaces or grain boundaries "reverse spike" domains often form. Their role is to decrease the demagnetising energy by introducing small areas of poles of opposite sign to these on the ends of the "main" domain, without adding too much extra domain wall energy.

The normal wall in magnets with strong uniaxial anisotropy is the 180° Bloch wall, Figure 2- 9. The thickness of a domain wall is determined by a balance between the increase in anisotropy energy due to the number of spins not pointing in an easy direction and the increase in exchange energy between adjacent spins which are not parallel. Minimisation of the former would lead to a very thin wall containing few

spins, whereas minimisation of the latter would lead to a thick wall with only a small angle between adjacent spins [25]. Typical domain walls are much thicker than interatomic distances but much smaller than the domain size. The domain wall width is given by:

$$\delta_B = \pi\sqrt{\frac{A}{K_1}} \qquad (2\text{-}12)$$

where A is exchange parameter and K_1 is the first anisotropy constant. Typical δ_B values are 50 nm and 4 nm for iron and $Nd_2Fe_{14}B$, respectively [19].

2.3 Magnetic Anisotropy

In anisotropic magnetic materials, it is energetically favourable for the magnetisation to lie along a particular direction, or set of directions (easy direction). This property of anisotropy is essential for permanent magnets, and it brings with it the associated property of coercivity. If the anisotropy energy, whether due to crystalline anisotropy or shape, can be presented as a single constant expression, then 17:

$$E_{an} = -K\sin^2\theta \qquad (2\text{-}13)$$

When the magnetisation is oriented at an angle θ to the easy direction, as shown in Figure 2- 10, this will give rise to a torque of:

$$\tau_{an} = \frac{-d\,E_{an}}{d\theta} = 2k\sin\theta\cos\theta \qquad (2\text{-}14)$$

The torque produced by a field H will be dependent on the angle ϕ between the magnetisation and the field direction as shown in Figure 2- 10.

$$\tau_H = \mu_o H \times M_S = \mu_o H M_S \sin\phi \qquad (2\text{-}15)$$

and when the torque produced by the field H equals the torque due to the anisotropy we will have equilibrium.

$$\tau_H = \tau_{an} \qquad \mu_o H M_s \sin\phi = 2K \sin\theta\cos\theta \tag{2-16}$$

The field strength H_s needed to saturate the magnetisation in a polycrystalline specimen is therefore the field needed to overcome the anisotropy and rotate the magnetic moments from the easy axes at 90° to the field direction into the field direction. Then in the above equation $\sin\phi=\sin(90-\theta)=\cos\theta$ and at saturation $\theta=90$, thus the maximum field strength is:

$$H_S = \frac{2K}{\mu_o M_S} \tag{2-17}$$

This is also the theoretical maximum value for the coercivity H_c (Stoner and Wohlfarth [14]). The coercivity for random orientation of the easy axes would be considerably smaller.

There are several possible causes of magnetic anisotropy in a magnetic material. In real materials, there may be several contributions to the anisotropy, arising from different sources. Some form of anisotropy is a requirement for permanent magnets, as it is this property which prevents the direction of magnetisation varying from its preferred direction, thus increasing the ability of the magnet to retain its magnetisation.

2.3.1 Shape Anisotropy

Any magnetic body with an elongated shape possesses anisotropy in the sense that a larger magnetic field is required to magnetise it to saturation parallel to a short than to a long dimension [24]. The reason for this is that the demagnetizing field along a short axis is stronger than along a long axis [26]. In other word, the long axis of the specimen plays the same role as the easy axis of the crystal. For a prolate ellipsoid of revolution, it can be shown that:

$$K_s = \frac{1}{2}(N_y - N_x) M^2 \qquad (2\text{-}18)$$

where the N_x and N_y are the demagnetisation factors along the major and minor axes, respectively. If the particles are small enough to be single domain, they can have large coercivity:

$$_jH_c = H_a = (N_y - N_x) M \qquad (2\text{-}19)$$

The magnitude of the shape anisotropy depends both on the extent of the magnetisation and on the axial ratio of the specimen y/x, which determines (N_y-N_x). A symmetrically shaped body, such as a sphere, shows no shape anisotropy unless it consists of fine, asymmetrically shaped particles. Magnetic materials which derive their hardness from shape anisotropy (e.g. Alnico) consist of a fine dispersion of elongated magnetic particles in a matrix of non-magnetic (or weakly magnetic) phase.

2.3.2 Stress Anisotropy

This type of anisotropy is closely related to the phenomenon of magnetostriction, which is the change in length in the direction of an applied field which some materials undergo. The application of a stress along a particular crystallographic direction of a magnetic material may result in a change in the magnetisation for a given applied field in that direction. Cooling the melt of a magnetic material of this type in an applied field can lead to the "freezing in" of stresses, which then leads to magnetic anisotropy in the finished material. The most common example of this type of anisotropy is in steel magnets produced by quenching.

2.3.3 Surface Anisotropy

At the surface of a crystal, the atoms are in an environment of different symmetry from that of the interior. This may give rise to a magnetic anisotropy experienced only by these superficial atoms, causing the spins to be oriented in particular directions relative to the surface.

2.3.4 Exchange Anisotropy

This effect is also interfacial in nature, and determines the anisotropy of materials comprising two phases which are coherently joined to each other, but each having different magnetic coupling i.e. one phase is ferromagnetic, and the other antiferromagnetic. In this case, the magnetisation in the ferromagnetic phase is bound to the direction in which it is coupled to the antiferromagnetic phase, and its anisotropy and coercivity are thus improved over those of the ferromagnetic phase alone.

2.3.5 Magnetocrystalline Anisotropy

All ferromagnetic crystals exhibiting magnetocrystalline anisotropy, have a preferred magnetisation direction, called the "easy" direction in which the total magnetic energy is a minimum. To magnetise in the "hard" direction the applied field must do work against the anisotropy force to turn the magnetisation vector away from an easy direction. The energy required to rotate the spins away from the direction of minimum energy is called the magnetocrystalline anisotropy energy and is given by the energy required to overcome the spin orbit coupling. In materials such as $Nd_2Fe_{14}B$, which has uniaxial symmetry (due to its tetragonal unit cell), the anisotropy energy is as follows:

$$E_a(\theta) = K_o + K_1 \sin^2\theta + K_2 \sin^4\theta + \ldots \qquad (2\text{-}20)$$

where θ is the angle between the local magnetisation and the c-axis and K_o, K_1, K_2, ... are the anisotropy constants. The direction of minimum energy is known as the "easy direction" and will depend upon the relative magnitudes and signs of K_1 and K_2 [26].

When the first anisotropy constant K_1 is dominant, the anisotropy field can be defined in items of the saturation magnetisation M_s as:

$$H_a = \frac{2\ K_1}{\mu_o M_s} \qquad (2\text{-}21)$$

which is the field necessary to saturate the magnetisation along a direction perpendicular to the easy direction. This anisotropy field is the upper limit to the coercivity which could be attained if there were no domain process in effect. In practice, domain processes lower the coercivity; however, the anisotropy constants are still very important in determining H_c via domain wall pinning and the nucleation energies of the walls themselves [26].

2.4 Anisotropy and Coercivity

When a specimen of a particular hard magnetic material has been magnetised to saturation, and the external field is removed, the specimen remains magnetised. The reverse field necessary to return the magnet to its unmagnetised state is called the coercivity $_jH_c$. If there were no anisotropy in a single phase material, there could be no coercivity, as there would be nothing stopping the magnetisation vector rotating in order to align with the applied field. The maximum theoretical coercivity of a material is defined by its anisotropy field. However, real materials always fall short of the theoretical maximum of coercivity, due to demagnetisation to states of lower energy by mechanisms such as fanning, twisting, curling or buckling, as well as microstructural effects, including grain boundaries, inter-phase boundaries and in particular, the interaction of the domain walls with these. Rare earth-transition metal alloys generally have very large magnetocrystalline anisotropies, and this inhibits incoherent demagnetisation mechanisms such as curling and buckling in a way that shape anisotropy cannot.

The effect of the microstructure for nearly all types of permanent magnets has been found to be described by the following relation [27],

$$\mu_o H_c = 2\frac{K_1}{M_s}\alpha - N_{eff}\mu_o M_s \qquad (2\text{-}22)$$

The microstructural parameters α and N_{eff} describe the complex influence of the microstructure, e.g., reduced anisotropy constants at the grain surface, misaligned grains, dipolar stray fields due to edges and corners of the polyhedral grains [28]. Since, in general, all these effects occur simultaneously, the microstructural parameters are complex and, in general, require the use of computational physics.

2.5 Magnetic Reversal Mechanisms

The application of an external field can either cause the spins within a domain to rotate against the anisotropy forces toward the field direction or it can cause the domain configuration to change to reduce the volume of material magnetised in a high energy direction with respect to the field direction. This latter process can occur by motion of the domain walls or by nucleation and growth of new domains having a local magnetisation oriented in a favourable (low energy) direction with respect to that field. For the $Nd_2Fe_{14}B$ phase, the anisotropy field is very large (~6.13 MA/m [29]); therefore, domain wall motion and/or nucleation should occur before spin rotation [25].

2.5.1 Nucleation

In the nucleation model, coercivity is determined by the level of field required to form nuclei for domain reversal or perhaps to release walls anchored in surface regions. The nucleation of domain walls (and hence formation of new domains) can similarly take place near structural or chemical inhomogenieties, misalignment, porosity, etc., where the local values of exchange and anisotropy fields vary so as to make a local reversal of magnetisation energetically possible. Therefore, magnetic reversals can occur in much smaller fields than the anisotropy field of the material. This nucleation of new walls can occur either spontaneously to lower the magnetostatic free energy, or under the influence of a sufficiently large applied magnetic field known as the nucleation field H_n. If the domain walls were completely free to move throughout the material (i.e. no domain wall pinning), an abrupt reversal

of magnetisation would then occur whenever the demagnetising field becomes equal to H_n. The magnitude of H_n, like H_p (pinning field), again depends upon the detailed size, shape, and magnetic properties of the defect. In practice, reversible domain wall bowing processes and a distribution of H_p and H_n values contribute to a reduction in B in demagnetising fields and a considerable rounding of the B-H loop. This leads to a blurring of the distinction between the two limiting behaviours [25].

2.5.2 Domain Wall Pinning

The total magnetic free energy will be lowered if the domain walls pass through regions of nonuniform magnetisation such as at fluctuations in composition or in stress, non-(or less) magnetic inclusions, or internal and external surfaces. Work then has to be expended to move the walls away from these "pinning" centres. The strength of the pinning depends upon the local magnitudes of the anisotropy, saturation magnetisation, and the size and shape of the pinning centre. Irreversible wall displacement from one pinning centre to another (as opposed to reversible domain wall bowing between centres) can only take place when the pressure exerted upon the wall by the applied field exceeds a critical pinning field H_p, which then determines the observed coercivity [25].

2.5.3 Magnetisation Rotation

The thickness of a domain wall is determined by a balance between the increase in anisotropy energy due to the number of spins not pointing in an easy direction and the increase in exchange energy between adjacent spins which are not parallel. Minimisation of the former would lead to a very thin wall containing few spins, whereas minimisation of the latter would lead to a thick wall with only a small angle between adjacent spins [26]. In $Nd_2Fe_{14}B$, the minimum energy occurs at a domain wall thickness δ of about 4 to 5 nm. However, if the size of the body becomes small enough (critical size, D_c), it is no longer energetically favourable to divide the body into multiple domains since a smaller proportion of the spins would then lie along an easy direction or be parallel to each other. Instead, the particle becomes uniformly magnetised as a single domain. For $Nd_2Fe_{14}B$, D_c is generally found to be in the

range of 150 to 440 nm [30]. A change in magnetisation can then only occur by nucleation of an instability leading to a reversal in spin direction which passes instantaneously through the body or by some co-operative twisting of the spins away from the easy direction. All of these processes produce a considerable initial increase in magnetic free energy and so require the application of relatively large fields to cause magnetisation reversal. Useful permanent magnetic properties can thus be obtained by preparing the material as fine (single domain) particles in a non- or weakly magnetic matrix. Even if ideal single domain behaviour is not obtained, due to particle interactions, the large surface area of the particles should lead to a high degree of domain wall pinning and hence useful properties.

In nucleation-controlled systems, pinning of domain walls is required to impede the propagation of magnetisation reversal from grain to grain since, otherwise, reversal in a single grain would precipitously reverse the entire magnet and, in the pinning controlled case, unpinning of a domain wall from a localised defect is virtually indistinguishable from nucleation of a reverse domain [31].

2.6 Permanent Magnets

Modern permanent magnets have a major influence on the size, efficiency, stability, and cost of magnetoelectric devices and systems. Today the permanent magnet is a vital component in a wide range of industrial, consumer, and defence products.

2.6.1 Historical Developments

Permanent magnets have many applications, the most important being in motors and generators, and also in telecommunication, measuring control devices and acoustic devices. As they have become more powerful, they have taken over areas of application previously occupied by electromagnets.

Figure 2- 11 shows how the $(BH)_{max}$ obtainable from permanent magnet materials has improved during the last 100 years. When a new class of materials has been discovered, there has been for a few years a very rapid improvement in $(BH)_{max}$,

followed by an asymptotic approach to a maximum, until a breakthrough has been made with a new class of material. Schematic of Figure 2- 12 shows that with the development of new improved magnetic materials, the volume of the magnet to store the same amount of magnetic energy is considerably reduced.

2.6.2 Magnet Steels

Until about the end of the nineteenth century the only materials available for permanent magnets, apart from natural lodestone, were the hardenable carbon steels. A 1% carbon steel was probably the best of these. The first steels made specially for permanent magnets contained up to 6% W or Cr. About 1917 cobalt magnet steels were discovered in Japan. Any quantity of Co up to about 40% may be used [24].The origins of the coercive force in these quench hardened steels is due to the difficulty of domain boundary movement resulting from the combined effects of nonmagnetic inclusions, a very large concentration of lattice dislocations, internal strains and submicroscopic inhomogeneities in the material [1]. Typically, these alloys had a remanence, J_r, of about 0.88 T. Coercivities, ${}_jH_c$, ranged from about 4 to 20 kAm^{-1} and $(BH)_{max}$ from about 1.6 to over 7 kJm^{-3} from carbon steel to the best cobalt steels [18].

2.6.3 Alnico Alloys

The excellent magnetic properties of an Al-Ni-Fe alloy were discovered by Mishima in 1931 [24]. The beneficial effects of cobalt and of small amounts of copper were recognised and were also added. In general the Al-Ni-Co alloys are all, more or less, brittle. The purity of the raw materials and especially of the aluminium content are critical. They are made either by casting or sintering of particulate, followed by heat treatment, which is performed in three steps, a high temperature solution treatment followed by a controlled cooling and finally a low temperature ageing.

In all Alnico alloys, optimum magnetic properties are produced after the alloy has undergone spinodal decomposition. This results in a two-phase structure, strongly magnetic Fe-Co rich α_1 (elongated in the ⟨100⟩ direction) and weakly magnetic or non-magnetic Ni-Al rich α_2, which are very finely intermixed [18]. The single domain

behaviour of these alloys is a result of the size and shape of the magnetic phase [1]. These isotropic magnets have a $(BH)_{max}$ of 15 kJm^{-3} [18].

In addition to such isotropic magnets, by applying a magnetic field during cooling, especially in the range 850 to 750°C, over which the spinodal decomposition takes place, anisotropic magnetic properties in high cobalt content alloys can be produced. These have $(BH)_{max}$ of about 43 kJm^{-3}. For these materials J_r can vary between 1.25 and 1.3 Tesla while $_jH_c$ varies in the opposite sense to J_r between 46 and 54 kAm^{-1} [24].

Higher coercivity can be obtained by adding 5% Ti (with 30-35% Co) or 8% Ti (with 40% Co). Directional solidification leads to columnar Al-Ni-Co alloys with further improved properties.

The best laboratory properties for any Al-Ni-Co alloy are quoted by de Vos [24] as J_r=1.15 T, $_jH_c$= 121.5 kAm^{-1}, and $(BH)_{max}$=106.5 kJm^{-3}.

2.6.4 Hard Ferrites

The next important step in the evolution of permanent magnet materials was the development of fine-particle theory, which predicts that an aggregate of very small magnetic particles has a coercive force much greater than that of the same material in the bulk. The theory of the magnetic behaviour of an assembly of single domains was developed in great detail by Stoner and Wohlfarth [14], and their predictions of high coercivities from coherent rotation processes had a strong impact on the further development of permanent magnet materials as well as magnetic recording media. The aim was to produce an assembly of particles of a material that are small enough to be single domain. Anisotropy impedes the rotation of magnetisation within the particles, and the single domain nature of the particles ensures that demagnetisation occurs only by the rotation of the direction of spontaneous magnetisation and not by domain wall movement processes. High coercivities should therefore be achieved if the particles are highly anisotropic. The search led first to the development of hexagonal ferrites, which have high magnetocrystalline anisotropy, and are commercially produced as sintered magnets with grain sizes of roughly 1 μm, and

then to the development of the rare-earth transition metal magnets described below. However, although the development of new magnet materials with high coercivities was inspired by the theory, the coercivities achieved were never as high as those predicted by the theory. In practice, it is difficult to ensure that changes in magnetisation occur only by coherent rotation, and the coercivity is determined by energy barriers to nucleation and pinning processes, which had previously been thought to be important only in soft magnetic materials.

In the 1940's and 1950's, much work was done on the development of the ferrites, which may be considered to include any material containing the ferrite group Fe_2O_3, (natural lodestone Fe_3O_4 may be regarded as $FeOFe_2O_3$). Ferrites are also referred to as ceramic or oxide magnets. Hard ferrites are based on barium, strontium or lead and have the nominal formula $MFe_{12}O_{19}$ or $MO(Fe_2O_3)_6$. They have $(BH)_{max}$ typically 45 kJm^{-3}, although somewhat better results can be obtained with rather less ferric oxide, e.g. $MO(Fe_2O_3)_{5.5}$. They are cheap, effective and reliable. Ferrites today account for 90% of the mass and a little over half the value of all magnets produced worldwide.

2.6.5 CoPt alloys

It is worth noting that as early as 1936, it was found that the coercive force in CoPt is fairly high owing to the presence of a high magnetocrystalline anisotropy associated with an ordered phase with tetragonal structure. Powders made from this material can have very good magnetic properties, up to J_r ~0.63 T, $_jH_c$~400 kAm^{-1}, and $(BH)_{max}$ ~76 kJm^{-3}. CoPt alloys were developed for commercial use around 1960. However, their price is extremely high, since they contain about 75% Pt by weight, and are now commercially uninteresting except for specialised applications such as surgical implantation.

2.6.6 Sm-Co Alloys

The advent of modern rare-earth magnets, combining high saturation magnetisation with a large magnetocrystalline anisotropy, occurred in the late 1960's and early 1970's with the discovery of the magnetic properties of $SmCo_5$. They were based on the hexagonal phase $SmCo_5$ which has an outstandingly large anisotropy field of ~23 T. The first $SmCo_5$ magnets were made by Philips in Eindhoven, by

simply pressing the milled alloy powder with a binder. High energy products of ~160 kJm^{-3} and high intrinsic coercivity of ~1400 kAm^{-1} were obtained by liquid phase sintering of magnetically aligned single domain particles with its low melting point rare earth rich phase being paramagnetic and acting to damp the nucleation of reverse domains.

Sm_2Co_{17} has a higher saturation magnetisation of 1.04-1.2 T, compared with 0.92-0.97 T for $SmCo_5$, and a higher Curie temperature of 750-850°C, compared with 700-750°C for $SmCo_5$. Although, the magnetocrystalline anisotropy and coercivity are inferior to $SmCo_5$, they can be improved by small additions of Cr and Mn. The first satisfactory magnet in this system was $Sm(Co, Cu, Fe)_z$ where z is between 7 and 8. Further improvements were made by addition of small amounts of Ti or Hf, and especially Zr with typical $(BH)_{max}$ of 200-240 kJm^{-3}. Very complex structures can be obtained by heat treatment of $Sm(Co, Cu, Fe, X)_z$ where X is Ti, Zr or Hf. The microstructure consists of twinned rhombohedral $Sm_2(CoFe)_{17}$ separated by a coherent boundary of $Sm(CuCo)_5$. Thin hexagonal $Sm_2(Co, Fe, Cu, X)_{17}$ platelets cross both the $Sm_2(CoFe)_{17}$ and $Sm(CuCo)_5$ areas. Both sintered and bonded magnets are produced commercially. Low and high iron and zirconium contents lead to low (~480 kAm^{-1}) and high (~960 kAm^{-1}) coercivity magnets, respectively. Low and high copper contents, however, lead to high and low coercivity magnets.

As with $Sm(CuCo)_5$, the coercivity mechanism for the Sm_2Co_{17} type phase is basically "nucleation-type". Its virgin magnetisation curve initially shows a steep increase in magnetisation at low fields and a roughly linear increase in the coercivity H_c with applied field, reaching saturation at an internal field which is much smaller than H_c, Figure 2- 13. However, in precipitation-hardened $Sm(Co, Fe, Cu, Zr)_7$, heat treatment at ~800°C causes the formation of a fine cellular microstructure that is ideal for uniform domain wall pinning (pins are randomly distributed throughout the sample). The virgin magnetisation curve of this "pinning-type" magnets show little change in magnetisation for fields less than H_c but there is a drastic increase of magnetisation for fields greater than H_c. Also, the coercivity of these magnets is almost negligible up to the critical field (H_c), above which it suddenly increases to saturation, Figure 2- 13.

Permanent magnet materials based on 4f rare earths and 3d transition elements offer the best prospects for high-performance magnets and owe their favourable magnetic properties both to the 4f and 3d sublattices. The former is the main contributor to the magnetocrystalline anisotropy whereas the latter is mainly responsible for most of the magnetization and the sufficiently high magnetic ordering temperatures (an adequate Curie temperature) [32]. Elements in the first half of the 4f series, the light rare-earths, are preferred because their exchange coupling with the ferromagnetic 3d elements leads to parallel alignment of 3d and 4f moments.

There was a drive to develop magnets containing little or no Co, since it is a very expensive element and because it is largely sourced from politically volatile regions of the world, subject to large price fluctuations. Also the light rare earth metals are interesting because they are more plentiful and cheaper than the heavier RE's. Hence, light rare-earth-iron compounds were investigated comprehensively. However, the binary compounds have the disadvantage of low Curie temperatures, and there are very few stable intermetallic phases. The breakthrough came with the addition of boron to the Nd-Fe system to form the compound $Nd_2Fe_{14}B$ which has J_s=1.6 T and an anisotropy field H_a of 6.13 MA/m ($\mu_o H_a$=7.7 T) [29].

2.7 Nd-Fe-B Based Permanent Magnets

Following systematic study to develop new materials and processes in order to obtain better magnets, in 1983, the discovery and development of Nd-Fe-B magnets were announced simultaneously by Sagawa et al. [3] at Sumitomo Special Metals (Japan), and Croat and co-workers [2] at General Motors (USA), using pressing and liquid phase sintering of aligned single crystal particles and chill block melt spinning, to thin ribbon, followed by pulverisation and polymer bonding, respectively.

The main advantages of this new magnetic material compared with Sm-Co are the cheaper constituents and the significantly larger J_s and $(BH)_{max}$. The weak point of Nd-Fe-B magnets is the low Curie temperature of 312°C, compared with 720°C for samarium-cobalt.

2.7.1 Crystal Structure

The intrinsic magnetic properties of Nd-Fe-B based hard magnets can be attributed to the tetragonal hard magnetic $Nd_2Fe_{14}B$ phase, which has a very high magnetocrystalline anisotropy constant, $K_1 = 4.5$ MJ m^{-3} [33]. This crystal structure is shown in Figure 2- 14. The original structural determination was carried out by Herbst, et al. [34, 35] through neutron diffraction studies. This crystal structure identification was confirmed by Shoemaker, et al. [36], Givord, et al. [37], Sagawa, et al. [30] and Boller and Oesterreicher [38]. The lattice symmetry is tetragonal and the structure belongs to the $P4_2/mnm$ space group with a complex unit cell comprised of 68 atoms [25]. Iron atoms belonging to five crystallographically distinct sites form puckered, connected triangular nets above and below the $z = 0.5$ plane. Iron atoms of the sixth crystallographically independent site are positioned in the $z = 0$ and $z = 0.5$ planes. Neodymium and boron atoms are located in two and one crystallographically inequivalent sites, respectively. Isomorphous rare-earth compounds with the $Nd_2Fe_{14}B$ structure are formed for all the lanthanide elements, excluding europium and ytterbium [33].

2.7.2 Phase Diagram

The first information on the ternary Nd-Fe-B phase diagram was provided by Chaban et al. in 1979, some four years before it was realised that the $Nd_2Fe_{14}B$ phase could be used to produce permanent magnets. The liquidus projection shown in Figure 2- 15 is based on the work of Matsuura et al. [39]. Table 2- 3 lists the reactions, as indicated in the phase diagram, with the corresponding temperatures, and Table 2- 4 lists the chemical compositions of the symbols used in Figure 2- 15 and Figure 2- 16.

Figure 2- 16 shows the isothermal section at 1050°C [40], the approximate temperature used for liquid phase sintering of Nd-Fe-B magnets. There is a two-phase region where $Nd_2Fe_{14}B$ (ϕ) is in equilibrium with liquid, and a three-phase region where ϕ is in equilibrium with liquid, and $Nd_{1.1}Fe_4B_4$ (η). The commonly used sintered magnet composition $Nd_{15}Fe_{77}B_{6.5}$ falls in the three-phase region. The

presence of the η phase is associated with sharp edges on the ϕ grains which contribute to the dipolar stray field, thereby tending to reduce the coercivity. η does not form on sintering the composition $Nd_{18.5}Fe_{73}B_{6.5}$ which falls in a two-phase region. In the other two-phase regions ϕ coexists with at least one ferromagnetically soft phase, Nd_2Fe_{17}, Fe or Fe_2B which tend to destroy the coercivity. Although the phase diagram represents the equilibrium conditions, it helps to understand the phase formation during processing.

In practice, several phases are observed [41-43] in sintered magnets of the commonly used composition $Nd_{15}Fe_{77}B_8$. The majority phase is the $Fe_{14}Nd_2B$ phase, which is always observed to be free of any defects such as dislocations or stacking faults. This forms peritectically by reaction between the primary α-Fe phase and the liquid phase. The first minority phase is the Nd-rich phase, having an fcc structure with a=0.52 nm. Several Nd-rich regions with different Nd/Fe ratios have been observed [44] including hexagonal NdO and $Nd_5Fe_2B_6O$. Other phases observed in smaller amounts are the oxide Nd_2O_3, $R_{1+\epsilon}Fe_4B_4$ and α-Fe. The $R_{1+\epsilon}Fe_4B_4$ phase has a one-dimensional incommensurate tetragonal structure with a=0.71 nm and c=1.446 nm. Grains of this phase are characterized by a very high density of planar faults with a high density of dislocations associated with the faults.

α-Fe is found in the form of small precipitates typically of diameter ~6 nm and/or as larger grains. The latter can derive from incomplete peritectic transformation to $Nd_2Fe_{14}B$ when the cooling rate in precursor ingot is insufficiently high to bypass the solidification of γ-Fe dendrites. Other Fe-rich regions have also been observed [43] with Fe:Nd ~4. This phase is close to the one observed in as-cast and melt spun Nd-rich alloys. The Nd-rich and $R_{1+\epsilon}Fe_4B_4$ phases have been observed at intersections of $R_2Fe_{14}B$ grains, but not all around the grain boundaries. Other studies [45] reported the presence of a bcc phase around the $Nd_2Fe_{14}B$ grains with an Fe:Nd ratio close to that of the $Nd_2Fe_{14}B$ phase but with a lattice parameter close to α-Fe. Magnets with low coercivity showed a microstructure with fine platelets of this phase extending from the grain boundaries into the grains. Annealing around 650°C led to the

disappearance of these platelets and enhanced coercivity. The effects of these platelets on coercivity has been challenged by other investigators [46, 47].

2.7.3 Processing Routes

2.7.3.1 Powder Metallurgy

The powder metallurgy method was first described by Sagawa et al. [3] working at the Japanese company Sumitomo. The sequence of processing steps in making Nd-Fe-B magnets by the sintering method is alloy preparation by vacuum melting in an induction furnace, crushing chill cast ingots using a hammer mill or a jaw crusher under an inert atmosphere or hydrogen decrepitation [48, 49] and ball-milling or jet-milling. The purpose is to obtain single crystal particles, so that each particle is a single crystal of $Nd_2Fe_{14}B$ with only one crystallographically easy direction. Particle alignment is carried out next by placing the batch of powder particles in a die in the presence of a magnetic field, which is usually pulsed, and slightly agitating so that each particle can settle into its equilibrium position. The next steps are pressing and liquid phase sintering involving the low-melting, Nd-rich phase at the grain boundaries, heat treatment to achieve high coercivity and, finally, machining and magnetising.

According to Bogatin [50] optimum magnetic properties are obtained at a powder particle size of 2 μm, when each particle is a single crystal with a continuous surface layer that is chemically heterogeneous and plastically deformed.

To produce magnets with high $(BH)_{max}$, a low oxygen content, the maximum volume fraction of the hard magnetic $Nd_2Fe_{14}B$ phase, a maximum alignment of easy axes of magnetisation, and small and homogeneous crystallite grain sizes in the finished magnets should be realised. High energy products exceeding 400 kJm^{-3} (50 MGOe) have been now realised routinely for anisotropic sintered Nd-Fe-B magnets and a value in excess of 430 kJm^{-3} was reported by Kaneko and Ishigaki [4]. Advantages of the sintering process are: 1) high degree of homogeneity of magnetic

properties can be achieved, 2) near-net shape production is possible, and 3) a high degree of magnetic texture and thus high $(BH)_{max}$ can be achieved [4].

2.7.3.2 Hydrogen Processing

A technique called Hydrogen Decrepitation (HD) was developed [48, 49] whereby the cast Nd-Fe-B (or Sm-Co) alloy is exposed to around 1 bar (~1 atmosphere [51]) of hydrogen at room temperature (above 150°C for stoichiometric, single phase $Nd_2Fe_{14}B$). The large volume change normally associated with the formation of metal hydrides usually results in the decrepitation of the bulk material. Hydrogen decrepitation appears to be a two-stage process whereby hydrogen is first absorbed into the Nd-rich phase (intergranular fracture) which then activates hydrogen absorption by the $Nd_2Fe_{14}B$ matrix phase (transgranular fracture). The vacuum desorption process also consists of two stages such that on continuous heating, hydrogen is lost from the matrix phase around 200°C and from the grain boundary phase over the range 350°C to 650°C. The powder formed by this method (50-100 μm in size), must still undergo final size reduction, usually by jet-milling. Hydrogen decrepitation overcomes the problems of breaking up ingots, which can be extremely tough if they contain significant amounts of the free iron. Also the extremely friable nature of the hydride enables it to be milled for a shorter time or at a higher feed rate, compared to conventionally premilled material [52].

The Hydrogen-Disproportionation-Desorption-Recombination (HDDR) process was developed later [53-55] in which heating cast Nd-Fe-B ingots at above 650°C in hydrogen results in the disproportionation of $Nd_2Fe_{14}B$ into α-Fe, Fe_2B and $NdH_{2.7}$, and, during subsequent vacuum annealing, recombination to $Nd_2Fe_{14}B$ takes place. The temperature of the disproportionation decreases with increasing hydrogen pressure and also as the amount of Nd-rich phase is increased. The latter suggests that the Nd-rich grain boundary acts as a hydrogen diffusion path during the disproportionation reaction. The HDDR process produces a powder in which the particles contain randomly oriented $Nd_2Fe_{14}B$ grains of mean diameter of ~0.3 μm, which thus possess a coercivity of up to 1000 kAm^{-1} without need for sintering and heat treatment to redistribute the Nd-rich phase. The powder is also sufficiently fine

to polymer bond to magnets without further treatment. By doping the alloy with small amounts of other elements such as Hf, Zr and Ga, anisotropic powder can also be produced by this HDDR route. The reason for this phenomenon is still a matter for some conjecture. Buschow [56] suggested that hydrogen is not absorbed in the small areas of grains where the concentration of the additive element is relatively high. These regions can therefore become centres for nucleation and growth of the HDDR grains, with the centres having have kept the orientations of the original cast grains.

2.7.3.3 Rapid Solidification

Croat and co-workers [2] adopted an alternative route for producing Nd-Fe-B magnets. This involves melt spinning a jet of the molten alloy onto a rapidly rotating copper roll, Figure 2- 17. In this process a turbulent, though dimensionally fairly stable pool of melt is formed at the point of impingement of a round jet on the roll, and a continuous stream of rectangular section, typically 10-100 μm thick and 0.5-5 mm wide, is extracted and solidified from its underside. Vincent and Davies [57] proposed that the thickness controlling mechanism is hydrodynamic and not the previously thought solidification mechanism. They observed that the extracted ribbon thickness corresponds remarkably well with the thickness of the displacement boundary layer at the end of the melt pool. Very thin (~30 μm) and brittle ribbons are normally produced from Nd-Fe-B materials. This process makes the alloy solidify rapidly (with cooling rates of $\sim 10^{6}$ Ks^{-1}). The $Nd_2Fe_{14}B$ crystallites nucleate probably homogeneously and grow extremely perfectly until they impinge at their boundaries, trapping any excess liquid in an off-stoichiometric melt to yield one or more secondary phases. The scale of the microstructure and magnetic properties are directly related to the roll speed.

The effects of different processing parameters on the dimensions of free jet melt spin ribbon has been subject of investigations [57, 58]. For constant orifice diameter and gas over pressure:

$$t \propto V^{-a} \qquad \text{and} \tag{2-23}$$

$$w \propto V^{-b} \tag{2-24}$$

where t is the ribbon thickness, w is its width and V is the circumferential roll speed. The values of a and b mainly depend on the composition of the alloy and on the roll material and have values in the range 0.65-0.85 and ~0.25, respectively. Thus the higher the roll velocity, the smaller the ribbon thickness. The range of t and w within which an alloy may be cast to uniform ribbon is controlled by many factors, particularly the melt surface tension and viscosity, and the degree of substrate wetting. Often, alloy ribbon produced at very high V tends to be porous, depending on the wetting characteristics of the roller, and have uneven edges, depending on the ribbon width and ambient gas pressure. Material cast at very low V suffers gross dimensional unevenness in width, thickness, and section shape, as the melt pool becomes unstable, and, in extreme cases, a stable melt pool is not established, resulting in the production of molten droplets.

The effect of quench rate on the demagnetisation curves for Nd-Fe-B [16] is shown in Figure 2- 18. A microcrystalline structure with a mean grain diameter of 50-100 nm was considered to be the optimum condition, which can be achieved in a narrow range of roll speeds of a few m/s. In this condition, the grains in the ribbon have random crystallographic orientations, the polycrystalline aggregate is magnetically isotropic and the remanent polarisation, J_r is equal to one half of J_s, that is 0.8 T. However, it has been shown that quenching at slightly higher rate (higher roll speed) results in finer grain size (below ~40 nm) and that this is progressively enhances the remanence [7, 59]. Higher roll speeds still result in the formation of amorphous phase, which reduces the coercivity and energy products substantially. Lower roll speeds produce progressively coarser grains, which reduces both J_r and ${}_jH_c$. Further decrease of roll speed results in some preferential orientation with the c-axis tending to be normal to the ribbon plane, especially adjacent to the free (non-contact) surface [60]. Anisotropic powders for anisotropic bonded magnets can be produced by grinding these ribbons [61]. In nanocrystalline hard magnetic materials, if the grain size is uniformly small throughout the ribbons, improved and more consistent magnetic properties would result (as both J_r and ${}_jH_c$ are partly dependent on grain size).

Melt spinning at ambient (1 atm) pressure yields ribbon that is characterised by localised depressions on the roll contact surface. It is believed that these depressions

are due to pockets of gas which are trapped between the roll and the molten metal during the solidification process, which cause areas of locally lower cooling rates and these regions have substantially coarser grains which causes the magnetic properties to become less uniform.

There have been several reports of the effects of ambient gas pressure on surface features [62, 63], which concluded that the use of a lower ambient argon gas pressure, or the use of a low atomic weight gas (such as helium) led to an improvement in the surface quality of the ribbons.

It is observed by Yapp et al. [64] that quenching at reduced pressure of argon (<0.5 atmosphere) leads to much improved quality of ribbon, with the absence of major gas pockets and to more consistent magnetic properties for a nanophase Nd-Fe-B alloy. It was also observed that the grain size is consistently smaller and more uniform with no localised regions of coarse grains in the ribbons optimally quenched at 380 torr ambient pressure (380 mm Hg=0.5 atmosphere [51]).

This supports the suggestion made by Matsuura et al. [65] and Luborsky et al. [66] for soft magnetic materials, that when the surface of the ribbon is of good quality (as a result of a low ambient gas pressure, or fabrication in helium) this leads to more uniform cooling. In ribbons fabricated at higher pressures (e.g. 760 torr argon), it is speculated that the large grains form near surface dents, as a result of the gas pockets, which have a lower localised cooling rate, compared with the rest of the ribbon. Investigations by Harland and Davies [67] also confirmed this effect in nanophase Pr-Fe-B alloys. They found the range 0.6 to 0.5 atm as the threshold pressure for the avoidance of the gas pockets when spinning a nanophase alloy in argon.

2.7.4 Continuous Cooling Transformation (CCT) Diagram

Regions on phase diagrams show the stability of phases at certain temperatures and compositions. Jha et al. [68] presented the first predicted time-temperature-transformation (T-T-T) curve for the crystallisation of ϕ-phase from the melt. Branagan and McCallum [69] developed a model continuous cooling transformation

(CCT) diagram for stoichiometric alloy which represents phase formation during the solidification process under continuous cooling conditions for a wide range of cooling rates from rapid solidification to equilibrium cooling, Figure 2- 19. They developed this diagram from the ternary isopleth at the tie line between Fe and $Nd_2Fe_{14}B$ representing equilibrium phase reactions, Figure 2- 20. Seven regions are indicated which are representative of different phase reactions, Table 2- 5.

At sufficiently high cooling rates, curve A, a glass is formed. At equilibrium cooling, curve F, Fe begins to precipitate. When the peritectic temperature is reached the properitectic Fe and the remaining liquid react to form the 2-14-1 phase. Curves D and E represent solidification rates during casting in the powder atomisation route. The peritectic reaction which follows Fe formation requires bulk solid state diffusion and is very sluggish. The ingot cooling rates are fast enough in this region to allow only limited diffusion which causes bulk segregation in both the liquid and solid phases. The solidification sequence after the peritectic reaction occurs through the hyperperitectic, proeutectic and ternary eutectic reaction regions, as seen by following the liquidus curve in the isopleth [30].

The cooling rate corresponding to of curve B is sufficient to undercool below the peritectic temperature and direct solidification of 2-14-1 occurs. Materials cooled with cooling rates intermediate between A and B are partially crystalline and represent overquenched condition. The optimum cooling rate, which is slightly faster than B, gives the ideal microstructure of an almost completely crystallised nanosized grain structure with a small amount of amorphous grain boundary phase, which can act to magnetically decouple adjacent grains [70]. In cooling curve C, a completely crystalline 2-14-1 structure is formed but the alloy is in the under-quenched condition [69].

In conventional 2-14-1 magnets, the formation of free iron would be suppressed because properitectic iron formation usually results in a diminished level of coercivity. In the newly developing high remanence isotropic magnets, the size and distribution of the iron that precipitates out at a particular cooling rate will directly determine the level of hard magnetic properties [11].

2.7.5 Consolidation Routes

2.7.5.1 Polymer Bonding

Coarsely ground optimally quenched ribbon is mixed with a bonding agent such as epoxy and compression moulded at relatively low pressures, 600 to 700 Mpa (1 atm≈10^5 Pa [51]), to give compacts with densities of up to 85% of the density of $Nd_2Fe_{14}B$. At this loading, the remanent induction (B_r) of the optimally quenched ribbon of about 0.8 T is reduced to about 0.65 T, which gives magnets with $(BH)_{max}$ of about 72 kJm^{-3}, since the grains in each ribbon fragment are randomly oriented. The magnets are isotropic and, of course, other polymers and other moulding techniques can be used, particularly injection moulding, with lower powder loadings to facilitate mould filling. An advantage of moulding is that high dimensional tolerances can be achieved and, for injection moulding, with intricate shapes, without costly finishing operations.

The polymer bonded Nd-Fe-B market has experienced the fastest growth of any permanent magnet market. These magnets are now used extensively in a wide and growing range of computer peripherals, office automation, and consumer electronic applications. The major drive for growth in the use of these materials has been the significant size, weight and performance advantage they can provide over sintered and particularly, bonded ferrite permanent magnets at reasonable cost [71].

Other rapid solidification techniques, such as gas atomisation, are being investigated for providing initial powders. Recently, new anisotropic powders, prepared by the HDDR process, having high and low intrinsic coercivities have been introduced. The higher energy products of these powders should extend the range of applications for bonded magnets [72].

2.7.5.2 Hot Pressing

Full densification of the melt-spun ribbons, can be achieved by uniaxial hot pressing in a suitable die cavity in vacuum or in an inert atmosphere at moderate pressures (about 100 MPa) and temperatures (about 1000K) and with pressing times

of about a minute [35]. At these temperatures, grain growth is not excessive, and good results can be obtained starting with optimally quenched ribbon, although better results can be obtained by starting with overquenched ribbons. The hot pressed magnets are characterised by high coercivity, and $(BH)_{max}$ up to about 115 kJm^{-3} can be obtained [73]. The microstructure of hot-pressed magnets consists of randomly oriented, polygonal $Nd_2Fe_{14}B$ grains, roughly 80-100 nm in diameter, with sharp boundaries. An intergranular phase, similar to that of directly quenched ribbons, is present at the grain boundaries of the slightly super-stoichiometric ribbons, i.e. Nd:Fe ratios>1:7 [34].

2.7.5.3 Die-Upset Forging

With uniaxial hot pressing, only slight (about 10%) magnetic alignment of the easy c-axis occurs, with the preferred direction parallel to the pressing direction. If the hot pressed block is then plastically deformed at about the same temperature by compressing it to below 50% of its thickness in a die cavity of larger diameter (die upsetting) or back extended to a tubular form, the degree of alignment is substantially increased (about 75%), parallel to the pressing direction (or radially for the back extrusion case) with a concomitant increase in $(BH)_{max}$. Electron microscopy shows that die upsetting modifies the roughly spherical $Nd_2Fe_{14}B$ grains in the melt spun ribbons to platelets 100 to 500 nm in diameter, with their easy c-axis parallel to the pressing direction and (001) planes normal to the stress axis. This requires that all slip takes place only in the (001) plane. The requirement of five independent slip systems to be active for general deformation (Von Mises' rule) of a body then cannot be satisfied in this case. Moreover, dislocations have rarely, if ever, been reported to be seen in the $Nd_2Fe_{14}B$ structure. It is suggested that dislocations exist and move at high temperature but disappear at room temperature [74]. Other mechanisms such as grain boundary sliding [75], diffusion slip [76], dissolving of misaligned grains and growth of the favourably oriented crystallites [77] are suggested for deformation, which are mainly based on the presence of Nd rich grain boundary phase, which is liquid at the forming temperature. However, Leonowicz and Davies [78] showed that, although alignment was only achieved when the Nd-content exceeded the

stoichiometric composition, plastic deformation occurred for low Nd samples, too, i.e. in the absence of liquid phase. Mendoza et al. [79] achieved the same results for Pr-Fe-B alloys. Independent of the preparation process for the initial powders (melt-spinning, mechanical alloying or HDDR process), a minimum grain size should be aimed for (this also applies for the following processing steps) in order to obtain optimum magnetic properties and minimum deformation stress [80].

Anisotropic Nd-Fe-B, produced by means of hot deformation and consisting of sub-micron $Nd_2Fe_{14}B$ grains, do not rely on liquid phase sintering and the process is free from handling of fine powder, resulting in much less oxygen contamination. Hence, bulk magnets may be processed with lower excess amounts of Nd than those processed by powder metallurgical techniques [4].

Recently, Saito et al. reported that, by die-upsetting amorphous bulk materials prepared by shock compaction of amorphous powder, an energy product over 430 kJm^{-3} had been obtained [4].

2.7.6 Other Processing Routes

2.7.6.1 Mechanical Alloying

In this process, the elemental powder particles are mixed and milled for several hours in a high energy ball mill during which they are progressively compressed and welded together, fractured, folded and recompressed until the particles consist of alternate elemental layers on an extremely fine scale are produced. The heat of the process leads to intermixing diffusion, i.e. solid state alloying. Mechanical alloying for producing $Nd_2Fe_{14}B$ powders was first employed by Schultz et al. [81, 82]. The Nd, Fe and B powders are mixed together and first produce powder with a layered microstructure of Fe and Nd. After reaction for 1 hour at 600°C, the boron particles dissolve in Nd-Fe powder and form $Nd_2Fe_{14}B$ phase. The best magnetic properties of J_r=0.8 T, ${}_jH_c$=1020 kAm^{-1} and $(BH)_{max}$=103 kJm^{-3} were achieved for $Nd_{15}Fe_{77}B_8$ alloy after reaction for 30 minutes at 700°C.

2.7.6.2 Hot Extrusion

This process involves direct extrusion of a cast ingot, or powders, produced by crushing or atomisation of ingot or melt spun ribbons contained in a circular evacuable container and heated within the range 800 to 1000°C. A [100] fibre texture is thought to be developed as a result of an anisotropic deformation process. As a result, one of the a-crystallographic axes is aligned parallel to one of the major axes of the magnet, and the magnetically easy c-axis are randomly distributed in the plane normal to the major axis, therefore, any direction in the plane containing the c-axis exhibits very good hard magnetic behaviour, although the properties are diluted by radial as opposed to uniaxial alignment [83]. The best magnetic properties are achieved for magnets extruded from spherical atomised particles.

2.7.6.3 Hot Pressing and Rolling

The hot deformation is performed at temperatures of about 800-1000°C with strains reaching 60 to 80%. Low and high strain rates are normally used for pressing [84] and rolling [85], respectively. Magnetic alignment induced by hot-working is found to be closely related to the macrostructure of the cast ingots and the direction of principal stress. The appropriate initial grain structure is a columnar structure. The c-axes lie in the plane perpendicular to the growth direction of the dendrites. The principal stress during working should be applied perpendicular to the growth direction. It has been found that Pr-based alloys are more suitable than Nd alloys for pressing and rolling cast alloys and that a Cu addition is beneficial with respect to achieving a suitable texture. Typical $(BH)_{max}$ obtained by these two routes were 285 kJm^{-3} [84] and 240 kJm^{-3} [86], respectively.

2.7.7 Coercivity Mechanisms in RE-Fe-B

The highest coercive fields reported for iron-based magnets have been obtained in Nd-Fe-B alloys [3, 87, 88], with record values exceeding 3.3 MA/m [89].The fundamental origin of the coercivity in these magnets is the large magnetocrystalline anisotropy of $Nd_2Fe_{14}B$. If magnetisation reversal involved only coherent rotation, the intrinsic coercivity ${}_jH_c$ would equal the anisotropy field H_a of ~7.7 T (~ 6.13

MA/m) at room temperature [29]. However, the experimentally measured coercive fields are much smaller than the anisotropy fields because of metallurgical factors such as the distribution, chemical composition and crystal structures of phases, and also processing parameters [90]. Since the microstructure and metallurgy of Nd-Fe-B magnets is quite complex, it is to be expected that the coercivity mechanism is also complicated. The coercivity is connected with the total anisotropy field via the relation [91],

$$ {}_jH_c = CH_a - N_{eff}\frac{M_s}{\mu_o} \qquad (2\text{-}25)$$

where C and N_{eff} are parameters related to the grain structure and grain boundaries. The microstructural parameter C is, in fact, dependent on the alignment of the magnetic particles, and on the nature and the size of the defect regions in which nucleation and/or pinning of domain walls take place. The microstructural parameter N_{eff} is the effective demagnetization factor. μ_o is the permeability of free space.

For an ideal magnet, C=1. However, actual magnets have lower values because of imperfect grain orientation and grain boundary defects. Therefore, controlling the grain structure and grain boundary chemistry is as important as increasing the anisotropy field in enhancing ${}_jH_c$.

2.7.8 Magnetisation Reversal Mechanisms

Most of the numerous efforts to understand the coercivity of RE-Fe-B magnets rely on interpretations based on either the nucleation of reverse domains or the pinning of domain walls by inhomogeneities [92]. Distinctions between these two possibilities have been drawn according to guidelines such as the initial susceptibility behaviour, domain structure, microstructure and the dependence of ${}_jH_c$ on magnetising field, temperature and the angle between the applied field and the alignment direction.

2.7.8.1 Sintered Nd-Fe-B

The grain diameters in sintered magnets are larger than that required for single domain behaviour. Electron microscopy indicates that the interiors of the $Nd_2Fe_{14}B$ grains are largely free from defects [93], apparently eliminating pinning in the bulk of the grains as the dominant coercivity mechanism. It thus appears that the coercivity is controlled by nucleation of reverse domains [3, 31, 42, 90, 94-96]. However, some authors reported evidence for a domain wall pinning mechanisms in sintered Nd-Fe-B magnets [97, 98]. On the other hand it has been proposed [31, 95] that the coercivity mechanism in sintered magnets is nucleation-type at room temperature, and pinning type at higher temperatures.

Many microstructural investigations have been carried out with a view to obtaining a better understanding of the coercivity mechanism [42, 45, 93, 97, 99, 100].The ideal microstructure for sintered magnets is believed to be two phases, with the spherical $Nd_2Fe_{14}B$ grains being perfectly isolated by the paramagnetic Nd rich phase [101] to serve as a barrier and prevent wall propagation over the entire magnet volume and thus impede the formation of reverse domains. It has been proposed that the degree of continuity between the $Nd_2Fe_{14}B$ phase and the intergranular phase determines the coercivity [93]. The overall grain morphology should not show sharp edges since a high density of magnetic surface poles creates large demagnetising fields. In addition, the overall grain size should be reduced in order to minimise the strength and the interaction range of the demagnetising fields [33]. Non-ferromagnetic inclusions reduce the remanence as well as the coercive field in a permanent magnet. They cause large stray fields, inducing nucleation of reverse domains in the neighbourhood of these non-magnetic inclusions [101].

In sintered Nd-Fe-B magnets the heat treatment at around 600°C does not alter the overall morphology of the ϕ grains but it probably produces subtle changes around the grain boundaries [102, 103] which impede the nucleation and propagation of reverse domains [41].

2.7.8.2 Melt Spun Nd-Fe-B

Magnets prepared by the melt spinning route have much smaller grain sizes than their sintered counterparts. In fact, optimally prepared materials have a grain size smaller than D_c. Magnetic force microscopy and Lorentz studies generally indicates a domain structure, with each domain encompassing a number of grains and strong pinning of domain walls at the grain boundaries. In the ribbon form, it also appears that the optimum condition is each grain of $Nd_2Fe_{14}B$ surrounded by a thin layer of grain boundary phase, which is rich in Nd. However, because of the small grain size, typically ~60 nm in commercial alloys, the motion of domain walls involves jumps between the grains, because the nucleation of reverse domains is relatively easy in small grains, but the pinning is strong, due to the presence of the distributed grain boundary phase. Virgin magnetisation curves for melt-spun Nd-Fe-B ribbons also exhibit much lower initial susceptibility compared to aligned sintered magnets. Moreover, the coercivity develops more slowly with increasing applied field, attaining its maximum value only for $H>_jH_c$. These characteristics are in favour of a pinning-dominated mechanism [31, 104, 105]. However, the actual mechanism of the magnetisation reversal in melt-spun material is still not entirely clear [33].

2.7.9 Stoner-Wohlfarth Theory

Stoner and Wohlfarth [14] predicted that for an assembly of independent, randomly oriented and non-interacting, single domain magnetic particles, each of which is uniformly magnetised along its easy axis of magnetisation; the remanence, J_r, should have a value half that of the saturation, J_s, i.e. $J_r/J_s=0.5$.

To explain this, let us start with the coherent magnetisation rotation for a small particle with a positive uniaxial anisotropy either as a result of particle shape or from the magnetocrystalline anisotropy in which the magnetisation rotates coherently. Consider a particle in the shape of a prolate spheroid, Figure 2- 21a. Such a shape leads to a uniaxial anisotropy with easy directions parallel to the major axis.

When there is no magnetic field applied, the magnetisation points in the direction OA, one of the easy directions. If a gradually increasing field is applied along OX,

the magnetisation will gradually rotate towards OB. In Figure 2- 21b, the magnetisation is plotted as a function of field, or rather the component of the magnetisation along OX, which is given by $M_s\cos(\theta+\phi)$, where θ is the angle between the easy axis and OX (applied field) and ϕ is the angle between the magnetisation and some fixed direction in the particle. Corresponding points are denoted by the same letter in Figure 2- 21a and b. The point B corresponds to saturation in the direction of the field. If the field is reduced, the magnetisation returns to A. Suppose we now apply a field in the -OX direction. The magnetisation rotates to C, say. At C, the magnetisation suddenly jumps to a new direction, D, because at this point, the field has become large enough to pull the magnetisation from near one easy direction (A) to near the other (F). If the field is increased further, then eventually saturation is reached, at E. If the field is now reduced, the magnetisation rotates from E to D, and reaches F when the field reaches zero. If an increasing field is now applied in the +OX direction, the magnetisation gradually rotates to G, from where it suddenly jumps to J. On further increase of the field, the magnetisation rotates to B, and the cycle is then repeated as the field is changed from a large value in the +OX direction to a large value in the -OX direction and back again. Thus, this process leads to hysteresis, as shown in Figure 2- 21b. The shape of the hysteresis curve depends on the angle θ, and curves for various values of θ are shown in Figure 2- 22. For $\theta=0$, the curve is rectangular and the coercivity is largest. As θ increases, the coercivity decreases, and for $\theta=90°$, it is zero. At $\theta=0°$, the largest coercivity, $H=2K/\mu_0 M_s$. In the case when the anisotropy is due to the crystal structure, this maximum coercivity is referred to as the anisotropy field, because it is the field needed to rotate the magnetisation from an easy to a hard direction.

Those curves for the specimens with more or less randomly oriented easy axes lie between the extremes of square loops and almost linear loops [26]. For the uniaxial material each grain has a single easy axis and the grains are randomly oriented. Figure 2- 23a illustrates several states of magnetisation. The arrangements of J_s vectors in space is represented by a set of vectors drawn from a common origin, each vector representing a group of domains. The ideal demagnetised state is shown at point O. When a positive field is applied, domains magnetised in the minus direction are eliminated first, by 180° wall motion, leading to the distribution shown at point

B. Further increase in field rotates vectors into the state of saturation shown at C. When the field is now removed, the domain vectors fall back to the easy direction in each grain nearest to the +H direction. Because the easy axes are assumed to be randomly distributed (and that no interaction exists), the domain vectors are then uniformly spread over one half of a sphere, as indicated at D. If J_s in any one domain makes an angle θ with the +H direction, the magnetisation of that domain in this direction is equal to $J_s\cos\theta$, and the retentivity J_r of the specimen as a whole is given by the average of $J_s\cos\theta$ over all domains. In Figure 2- 23b, the population of particles with orientation between θ and θ+dθ is given by $\delta n=\sin\theta\delta\theta$, the magnetisation of particles resolved in the field direction with orientation in the range θ to θ+dθ is then $J_s\cos\theta\delta n$. Therefore, for an isotropic material, the theory predicts that the remanence J_r of the specimen as a whole is given by the average of $J_s\cos\theta$ over all domains, which should have a value of:

$$(2\text{-}26)\qquad J_r = \int J_S \cos\theta dn = \int_0^{\pi/2} J_S \cos\theta \sin\theta d\theta = \frac{1}{2} J_S \int_0^{\pi/2} \sin 2\theta d\theta = \frac{1}{2} J_S$$

2.7.10 Interaction Effects and Enhanced Remanence

There is evidence that intergranular interactions between $RE_2Fe_{14}B$ grains play a non-trivial role in melt-spun RE-Fe-B magnets. Conventionally, melt-spun alloys have what can be described as a microcrystalline structure with grains of the hard magnetic phase, $Nd_2Fe_{14}B$, ranging in size from ~60 to 100 nm [106]. $Nd_2Fe_{14}B$ has a value of J_s=1.6 T, and therefore, a remanence of ~0.8 T is predicted as they have random grain orientation and no significant exchange coupling since the coupled volume is too small a fraction of the mean total grain volume. However, even quite early research recorded values of remanence that were greater than predicted by the Stoner-Wohlfarth theory, i.e. $J_r/J_s>0.5$, for randomly oriented polycrystalline aggregates based on uniaxial anisotropy which could be interpreted as indicative of particle interaction effects [107].

In 1986, the Ovonics Company in the USA announced the discovery of enhanced remanence, isotropic Nd-Fe-B magnets, containing Si and/or Al additions [7-9],

resulting from a mean grain size less than 40 nm. Their results were confirmed by several researchers [108-110]. Similar results were found for Nd-Fe-B ribbons with small amounts of Nb additions [111], which is also thought to act as a grain refiner. Manaf et al. [59] subsequently demonstrated in a study of the effect of grain size on magnetic properties for single phase $Nd_{13.2}Fe_{74.6}B_6Si_{1.2}$ melt spun alloy that J_r began to increase above its Stoner-Wohlfarth value of $J_s/2$ for a mean grain size $d_g \leq 45$ nm with a corresponding decrease in ${}_jH_c$.

In a later publication [112] a model was put forward to explain the observation of enhanced remanence. In ferromagnetic materials, conduction electrons, which are responsible for the ferromagnetism, couple via the exchange interaction. The spins of these electrons also couple to the crystal lattice along specific directions of crystalline symmetry; for $Nd_2Fe_{14}B$ this is the c axis, which is known as the "easy axis". This interaction gives rise to an anisotropy energy. It was proposed that, where any two grains having different easy axis orientations contact, the spins at and near the common boundary in the two grains couple with one another via the exchange interaction. Thus, there is a tendency for the magnetic spins in the two grains to line up. However, because the c axes are not parallel in the two grains, the anisotropy energy fields of the two grains try to keep the electrons aligned along their respective c directions. A compromise results; the energy reduction due to the exchange interaction is offset by the energy increase due to misalignment of electrons with the c axis. The further the atom is from the boundary the smaller the exchange coupling effect, and it is effectively zero beyond a distance governed by A/K (where A is the exchange constant and K is the anisotropy constant) and is referred to as "exchange length" in some literature and is computed to be ~4 nm for the $Nd_2Fe_{14}B$ phase. This results in enhancement of the average remanent magnetisation over what would be predicted in the absence of the exchange interaction, i.e. the Stoner Wohlfarth value of 0.8 T. For larger grains (when the ratio of surface atoms to volume atoms is decreasing) the enhancement decreases until it becomes insignificant. Conversely, as the size of the particles decreases, the ratio increases and so J_r becomes progressively more enhanced below the observed threshold of about 45 nm. This effect was confirmed experimentally in systematic studies of the effect of grain size on J_r [59].

Figure 2- 24 produced by Schrefl et al. [113] based on numerical calculations, indicates the regions where J_s deviates from its local easy axes by more than 10° and 20°. It can be seen that the volume fraction of the inhomogeneous magnetic state along the grain boundaries becomes larger for smaller grain size. Only the magnetic moments within the boundary region where J_s deviates from the easy axes can increase the remanence. Therefore remanence enhancement is more significant for smaller grains.

However, it was shown that the decrease in grain size also causes a decrease in coercivity as the exchange alignment tends to reduce the resistance to reverse magnetisation [59]. The grain size dependence of the magnetic properties in isotropic nanocrystalline magnets is shown in Figure 2- 25 in which, the numerically calculated values for the remanence and the coercive field are compared with experimental results from Manaf et al. [59] obtained for $Nd_{13.2}Fe_{79.6}B_6Si_{1.2}$ melt spun ribbons. There is however, a limit, at which point decreasing the grain size further no longer causes an increased energy product, because, although the remanence continues to increase with decreasing grain size, the coercivity is decreased to such an extent that it leads to a non linear B-H second quadrant and a collapse in $(BH)_{max}$ [114].

For melt spun samples the relative difficulty in demagnetising a sample at low fields is attributed to magnetic interactions between neighbouring grains, as more crystallites reverse, these interactions facilitate easier reversal of the remaining grains. The interactions are likely to be responsible for the "interaction domains", extended structures comprised of many grains, observed in melt-spun ribbons by Lorentz microscopy [92] and by magnetic force microscopy [115].

Coehoorn et al. [15] also observed that two-phase permanent magnets containing metastable compound Fe_3B as the main phase and $Nd_2Fe_{14}B$ as an important secondary phase, prepared by the crystallisation of amorphous melt spun alloys with the appropriate composition $Nd_4Fe_{78}B_{18}$, show a very high J_r/J_s ratio of the order 0.7-0.8. μ_oM_r=1.2 T, μ_oH_c=0.4 T and $(BH)_{max}$= 95 kJm^{-3} were achieved by these workers for this alloy. It was subsequently shown that remanence enhancement, associated

with a nanocrystalline structure, is a general phenomenon in Nd-Fe-B alloys, occurring not only for small alloying additions [59, 116, 117], but also for ternary Nd-Fe-B alloys [10-13], with no additional fourth element. This was also observed for Iron-Misch Metal-Boron alloys by Dobson et al. [118] and for Sm_2Co_{17} by Crabbe et al. [119], who reported J_r enhancements of up to 0.75 T, a 40% increase above the theoretical limit for Sm_2Co_{17} of 0.525 T. Moreover, by reducing the Nd:Fe ratio, the presence of α-Fe phase in addition to the $Nd_2Fe_{14}B$ phase leads to further enhancement of J_r due to additional exchange interaction between the $Nd_2Fe_{14}B$ phase and the Fe grains which have a larger J_s than the former [12]. This was a similar effect to that seen in the $Nd_2Fe_{14}B/Fe_3B$ nanocomposite alloys by Coehoorn et al [15].

2.7.11 Nd Content

The effect of Nd content on the magnetic properties of nano phase melt-spun Nd-Fe-B is shown in Figure 2- 26. If Nd-Fe-B alloys have compositions other than $Nd_2Fe_{14}B$, the microstructure is usually composed of two or more phases.

2.7.11.1 High Nd Alloys

In Nd-Fe-B nanophase alloys which have Nd contents in excess of the stoichiometric concentration (> 11.76 at.%), the second phase is a neodymium-rich non-magnetic phase which tends to be located around the boundaries between the $Nd_2Fe_{14}B$ grains. Al-Khafaji et al. [120] report the composition of 73 at.% Nd and 27 at.% Fe obtained from quantitative EDS spectra taken from Nd-rich grain boundary phase for $Nd_{18}Fe_{76}B_6$ alloy. They also suggest an fcc structure with a lattice parameter of 0.56 ± 0.02 nm from the data provided by nanodiffraction patterns for this phase. These conclusions agree with those of Koestler et al. [121]. Although there is no stable fcc structure in the Fe-Nd phase diagram, it was suggested that, in the presence of oxygen, this structure can be stabilised.

Most commercial alloys, sintered or melt spun contain excess Nd [69]. As the neodymium concentration increases, the ferromagnetic $Nd_2Fe_{14}B$ crystallites are decoupled to an increasing degree. Thus, even when the structure is nanoscale, the

remanence enhancement disappears rapidly. Also, with increasing Nd concentration the ferromagnetic $Nd_2Fe_{14}B$ phase becomes increasingly diluted by the paramagnetic phase which also reduces J_r. However, the coercivity increases because the neodymium-rich phase damps the nucleation of reverse domains. Girt et al. [122] observed an increase of μ_oH_c from 1.2 T in over-quenched and annealed $Nd_{2.05}Fe_{13.1}B$ ribbons to 2.75 T in $Nd_{96.63}Fe_{3.32}B_{0.05}$ alloy which is the highest reported so far for a ternary alloy. They attributed it to the majority of $Nd_2Fe_{14}B$ grains being completely isolated in this alloy. The rare-earth-rich grain boundary phase acts as a liquid phase sintering aid. Wetting of grain surfaces of $Nd_2Fe_{14}B$ by Nd-rich metallic liquid phase during sintering removes oxidised layers on the grain surfaces to promote formation of a defect-free lattice in the $Nd_2Fe_{14}B$ grains and, hence, is necessary to develop $_jH_c$ to its full value for a given composition [4]. Excess Nd also moves the composition nearer to the ternary eutectic composition [123], and this limits the formation of pro-peritectic iron which is a detriment to the achievement of optimum properties and also the liquidus temperature is reduced. This allows for less undercooling to avoid the peritectic and eutectic reactions and, for melt spun alloys, enhances glass forming ability. For samples with high Nd content, coercivity only moderately depends on the roll speed and also sizeable coercivities are achieved even for large $Nd_2Fe_{14}B$ grains [69, 124].

2.7.11.2 Low Nd, Nanocomposite Alloys

Recent studies have centred on sub-stoichiometric Nd-Fe-B alloys with a mixture of two phases, hard and soft, with the aim of enhancing magnetic properties, whilst reducing the Nd content, which has economic benefits and improves corrosion resistance [15]. The microstructure of these alloys consists of $Nd_2Fe_{14}B$ with substantial volume fractions of either α-Fe (J_s=2.2 T) [125-127] or Fe_3B (J_s=1.6 T) [15, 128] which would, ordinarily, lead to collapse of $_jH_c$ but, providing it is present on a sufficiently fine scale (smaller than the exchange distance for α-Fe, ~40 nm), typically <15 nm, then this does not occur. In such composite magnets the soft magnetic grains are completely exchange coupled with the adjacent hard magnetic phase [129], i.e. exchange interactions align the magnetic moments of the soft phase

with those of the neighbouring $Nd_2Fe_{14}B$ grains, which thus acts to further enhance J_r in nanocrystalline alloys, though $_jH_c$ is reduced since the resistance to reverse magnetisation is diminished further by the exchange coupling of the hard phase to the soft phase [113, 127, 130]. This type of magnet with the soft phase embedded in the hard magnetic phase possesses a high J_r, whilst retaining good $_jH_c$, and therefore has excellent $(BH)_{max}$ values in excess of 160 kJm^{-3} [11-13, 131-133].

Manaf et al. [114] investigated the correlations between J_r, $_jH_c$ and $(BH)_{max}$ for a wide range of as-cast melt spun Nd-Fe-B ribbons of varying compositions, quench rates and mean grain sizes (Figure 2- 27). It shows that the highest degree of enhancement occurs for alloys with the lower Nd contents which is attributed to the combination of the enhancement arising from ferromagnetic exchange coupling due to nanoscale grains, combined with an increase in overall mean J_s due to the presence of the α-Fe phase. Data in Figure 2- 27 also indicate that the $(BH)_{max}$ derived from the second quadrant of the experimental demagnetising curves is also increased, initially with a similar trend, but when $_jH_c$ falls below ~900 kAm^{-1} the rate of increase of $(BH)_{max}$ decreases whilst the J_r continuous to increase beyond 0.9 T. Eventually $(BH)_{max}$ collapses after reaching a maximum corresponding $_jH_c$ at about 400 kAm^{-1}.

The demagnetisation curves presented in Figure 2- 28, show the numerically calculated magnetic properties of isotropic two-phase magnets for increasing volume fraction of the soft magnetic phase [113]. The insets show the corresponding microstructures, being composed of magnetically soft and hard grains. In addition, Figure 2- 28 compares the demagnetisation curves obtained for average grain sizes of 10 and 20 nm. The results clearly show that a small grain size improves both the remanence and the coercivity of isotropic two-phase magnets.

Inoue et al. [126] also report the properties of amorphous $Fe_{93-x}Nd_7B_x$ (x=3, 4 and 5) alloys that have been annealed to produce a three phase structure of α-Fe, Fe_3B (soft magnetic phases) and $Nd_2Fe_{14}B$ grains, with some remaining amorphous material. They report a very high remanence of 1.28 T owing to the high volume fraction of soft magnetic phase, but because of the very low coercivity (~250 kAm^{-1})

the energy product rather smaller, only 146 kJm^{-3}. They claim that the co-existence of the *three* nanoscale ferromagnetic phases is important in order to achieve good magnetic properties although they do not clarify why soft phases are required.

Theoretical investigations by Schrefl et al. [113] predicted that, unlike the B-H relationship in single phase $Nd_2Fe_{14}B$ in which higher remanences results in diminishing coercivity [114], both the coercivity and remanence increase with decreasing particle size for the isotropic two-phase magnets. This has been observed experimentally by Zhang and Davies (unpublished data) and by Liu and Davies [134]. Schrefl et al. [113] predicted that, for a grain size of about twice the domain wall width of the hard phase, the volume fraction of the magnetically soft phase can be increased up to 50% without a significant reduction of the coercive field.

The effect of low RE content on the magnetic properties has also been studied for substoichiometric Pr-Fe-B alloys. Mendoza and Davies [135] observed better thermal stability of the coercive field and of the remanence with increasing content of α-Fe for nanocrystalline melt-spun $Pr_xFe_{94-x}B_6$ alloys ($6 \leq x \leq 20$ at.%). High values of J_r observed for higher α-Fe concentrations near the Curie temperature T_c(PrFeB)=565 K are attributed to the ferromagnetism of α-Fe (T_c(α-Fe)=1043 K). Goll and Kronmuller [136] also observed the same effect for nanocomposite Pr-Fe-B alloys.

Resin-bonded exchange coupled magnets made from nanocomposite materials, although typically disadvantaged by decreased coercivities, have the following advantages:

- the possibility of remanence above 0.5 J_s without the need to induce anisotropy by magnetic or mechanical means,
- high thermal stability,
- decreased variation in magnetic properties with temperature,
- low-cost production route because of lower Nd content and near-net shape product [137].

2.7.12 The Effect of Alloying Addition

Since the development of Nd-Fe-B magnets, attempts have been made to improve their properties by the addition of other elements to the system. There have been significant improvements in the magnetic properties of Nd-Fe-B alloys modified by alloying elements, which can be useful in changing the microstructure and the magnetic properties. The maximum theoretical energy product for single phase Nd-Fe-B magnetic material is ~516 kJm^{-3} [132], which has not yet been achieved, although values of ~430 kJm^{-3} (i.e. 83% of this value) have been realised for sintered magnets [4].

Various additional elements are reported, which may be separated into two groups. Firstly, there are those elements which simply replace some of either the Nd or Fe in the $Nd_2Fe_{14}B$ main phase compound, such as dysprosium (Dy) or praseodymium (Pr) for Nd or Co for Fe. These substitutions alter the intrinsic properties of the main magnetic phase, improving the properties of the magnet material. For instance, the Curie temperature T_c is increased by Co additions or the anisotropy field H_a increases by Dy or Pr additions.

Secondly, there is the addition of those elements which do not simply replace the RE or TM in the hard phase, but which also modify the paramagnetic grain boundary phase and/or contribute to the formation of new phases which affect the magnetic properties of the finished magnet. Thus the modified microstructure of the finished magnet can influence the oxidation and wettability characteristics of the low melting grain boundary phase in addition to enhancing the coercive field H_c, and/or the remanence B_r.

2.7.12.1 Substitution for Neodymium

Substitution of Nd by other elements has been investigated by many researchers. Livingston [138] conducted a comprehensive literature survey for intermetallic phases of the type $Fe_{14}RE_2B$. Figure 2- 29 shows the reported magnetisation, anisotropy field and Curie temperature, for these compounds. It can be seen from these

investigations that $Nd_2Fe_{14}B$ has relatively high T_c, magnetisation and anisotropy field.

It has been found that substitution of Nd with Pr, Dy or Tb increase H_a and H_c while Ce, La and Sm have the opposite effect. Except for cerium, these substitutions have the reverse effect on remanence [2]. Dysprosium is now widely used to increase the coercivity of sintered magnets (by increasing the anisotropy field of the hard magnetic phase) and temperature stability [139-141], though it reduces J_r because the Dy atoms align ferrimagnetically in the $Nd_2Fe_{14}B$ phase.

Seeger et al. [142] investigated Fe(NdPr)B ribbons, finding that the magnetic properties in the series $Fe_{78}(Nd_xPr_{1-x})_{15}B_7$ remained more or less constant, as did the microstructure. They found that the Pr based magnets exhibited their best properties at the composition $Fe_{78}Pr_{15}B_7$.

The substitution of Nd by Pr in nanocrystalline alloys was also investigated by Yamamoto et al. [143] who obtained a remanence of 0.99 T and a $(BH)_{max}$ of 164 kJm^{-3} for an alloy with half the Neodymium substituted by praseodymium ($(Nd_{0.5}Pr_{0.5})_{11}Fe_{72}Co_8B_9$). Also, Sequeira et al. [144] investigated nanophase (NdPr)FeB alloys, finding a maximum enhanced remanence of 1.14 T and a $(BH)_{max}$ of 176 kJm^{-3} in nanophase melt spun $Fe_{84}Pr_{10.6}B_{5.4}$, and $(BH)_{max}$=164 kJm^{-3} for the composition $Fe_{84}(Nd_{0.72}Pr_{0.28})_{10.6}B_{5.4}$.

2.7.12.2 Replacement of Fe

Co substitution for Fe in RE-Fe-B magnets is known to increase the Curie temperature substantially, from 310°C in $Nd_2Fe_{14}B$ to 720°C in $Nd_2Co_{14}B$ (~100°C for each 10 at.% substitution of Fe by Co [145]) but with substantial reduction of the remanence and coercivity [146]. However, partial substitution of Fe by Co up to ~20 at.% can be beneficial in increasing T_c often without significant reduction in J_r and $_jH_c$ [21]. The Co also increases the corrosion resistance of the magnets.

2.7.12.3 Effects of Further Alloying Additions

It should be noted that the observed changes in magnetic properties of the magnets due to alloying must be carefully interpreted, and may be due mainly to microstructural effects rather than to any changes in intrinsic properties of the main phase. For example, aluminium is known to increase the coercivity ${}_jH_c$ of Nd-Fe-B sintered magnets [102]. However, it is observed that the anisotropy field H_a of single crystal $Nd_2(Fe_{1-x}Al_x)_{14}B$ at room temperature is approximately constant for small x [147]. Therefore, the increase in ${}_jH_c$ of Nd-Fe-B with Al addition is deduced to be due to microstructural changes rather than changes in the intrinsic properties. Similarly, the addition of Cr to the system leads to an increase in ${}_jH_c$ and, although modest increase in H_a occurs, this is not large enough to account for the observed increase in ${}_jH_c$. In fact it can be seen from Table 2- 6 that the presence of the added elements in the main phase is not generally desirable. Therefore, production of high performance sintered magnets using a mixture consisting of fine powder of nearly single phase $Nd_2Fe_{14}B$ and very small amounts of fine powder of another alloy regarded suitable as intergranular phase material has been investigated [56].

Two types of dopant elements can be distinguished, each with similar microstructural features[148]. Type 1 dopants, elements such as Cu, Al, Ga and Zn, having low melting point, and type 2 dopants, the refractory elements, such as Nb, Ti, Mo, V and W. This division is made independent of the processing technique.

According to Fidler [148], the effects of either type of dopant on the magnetic properties of the finished magnet is predominantly microstructural. The formation of additional intergranular phases due to the addition of dopants reduces the local demagnetising stray fields between neighbouring grains, and thus improves the coercivity. Intergranular phases are formed due either to the addition of refractory (type 2), or type 1 dopants. The type 1 dopants all show eutectic in their binary phase diagrams with Nd (and Pr), and therefore one of the effects of doping with this type of element is a reduction of the melting point of the intergranular phase. This leads to superior wetting behaviour and better separation of the main phase grains. On the other hand, the refractory type dopants form borides, which can act as a grain growth

inhibitor, thus also enhancing the coercivity. Further, the corrosion resistance of the magnets can be increased by decreasing the grain size and replacing some of the Nd-rich intergranular phase (which is most prone to oxidation) with phases containing the dopant element. Usually, in the production of sintered Nd-Fe-B based magnets, a combination of both types of dopant is used, to obtain optimum properties of the finished magnet. Thus, the effects of individual elements and of combinations of elements will be discussed. Particular attention is given to Ga in separate sub-section additions since they represent a significant part of the present study.

2.7.12.3.1 Sintered Alloys

Fidler et al. [44] attributed the increase of coercivity for sintered $Nd_{20}Fe_{71}B_{6.5}Al_{2.5}$ to the presence of $Nd(Fe,Al)_2$ and hcp Nd-rich phases in Al-containing magnets. These phases have better wettability compared to fcc Nd-rich phase; thus, the volume fraction of grain boundaries containing an intergranular phase is increased, which leads to a large magnetic decoupling factor; and the smoothness of the surfaces of the hard magnetic grains as a result of the liquid phase sintering process is also influenced.

Investigations by Chen et al. [149] showed that a small amount of oxygen leads to the formation of a stable Nd-Fe-O ferromagnetic phase in the intergranular regions of $Nd_xFe_{93-x}B_7$ (x=16-28) sintered magnets, which has a strong hindrance effect on the propagation of reverse domain walls between $Nd_2Fe_{14}B$ grains, and thus enhances the coercivity. The coercivity and thermal stability of Nd-Fe-B magnets can be further enhanced by adding MgO, Al_2O_3, Cr_2O_3, ZnO, CaO and MgO, ZnO, respectively. A new intergranular O-containing phase is formed in such alloys [150].

Pollard et al. [151] attributed the improvement in the coercivity of sintered $Fe_{74.7}Nd_{16.5}B_{7.8}Zr_1$ to the presence of Zr-containing, coherent precipitates within the hard magnetic matrix.

Using Lorentz microscopy, Parker et al. [152, 139] observed domain wall interactions with finely dispersed niobium containing coherent precipitates found in

$Nd_2Fe_{14}B$ phase which, they suggest could be responsible for coercivity improvement in Nb containing, sintered $Nd_{14.5}Dy_{1.5}Fe_{76}B_7Nb_1$ alloy.

Shu-Ming et al. [153] investigated a combination of additives and achieved good coercivity (1620 kAm^{-1}) and improved thermal stability for sintered $(Nd_{0.9}Dy_{0.1})_{16}Fe_{70}Co_5Nb_2B_7$. The Nb mainly concentrated at the grain boundaries, forming a Fe_2Nb phase which coexisted with the Nd-rich low melting phase.

Kim and Camp [154] found that the combined addition of Co (1.2%) and small amounts of Cu (0.15%) to a sintered $Nd_{30.5}Dy_{2.5}B_{1.1}Fe_{bal}$ alloy substantially increased the coercivity and corrosion resistance without J_r and T_c reduction, possibly due to a change in the grain boundary phase from Nd rich to a NdFeCoCu intermetallic phase.

Velicescu et al. [155] found that Cu and Co additions to sintered RE-Fe-B magnets refine the microstructure and replace some of the Nd-rich phase by RE-(Co,Cu) phases. Values up to 1.41 T, 1200 kAm^{-1} and 385 kJm^{-3} where achieved, respectively, for J_r, $_jH_c$ and $(BH)_{max}$ in $Nd_{13}Dy_1Co_{3.3}Cu_{0.3}B_6Fe_{bal}$ magnets.

The findings of Arai and Shibata [156] suggest that highly heat resistant sintered magnets are produced from $Nd_{16}Fe_{66}Co_{11}B_7$ alloy, when cobalt distributes only in the tetragonal hard magnetic phase. However, the squareness of the second quadrant of the loop deteriorates for Co concentrations more than 14 at.%, possibly due to the formation of a Nd-Co-B phase in the Nd rich region.

Additions of Al were reported to improve coercivity in Co-containing Nd-Fe-B alloys [157-160]. Mizoguchi et al. [157] suggested that the presence of aluminium makes the $Nd(Fe,Co)_2$ lave phase, non-magnetic; which is considered to be the cause of coercivity increase. They achieved J_r=1.32 T, $_jH_c$=875 kAm^{-1}, $(BH)_{max}$=326 kJm^{-3} and Tc=500°C for sintered $Nd_{15}Fe_{62.5}B_{5.5}Co_{16}Al_1$. Ma and Narasimhan [159] found Al to be effective in increasing $_jH_c$ of NdFeCoB sintered alloys, although it decreased the J_s and T_c of these alloys. Combined addition of Al and Mo to $Fe_{75}Nd_{18}B_7$ sintered magnets reduced the coercivity, which was considered to be due to the formation of Mo-rich inclusions, resulting in discontinuities in the isolating paramagnetic layer at the $Nd_2Fe_{14}B$ grain boundaries [160].

Kim [161] observed that sintered $(Nd_{1-x}Dy_x)_{15}Fe_{77-x}Al_yB_8$ (x=0.1-0.14, y=1-1.5) alloys, containing equal atomic proportions of Dy and Al, result in superior permanent magnetic properties. The reduction in J_r associated with the Dy addition is markedly reduced. The $_jH_c$ of the alloys increases linearly with Dy content at a rate of about 600 kAm^{-1}/at.% Dy, when the alloys contain equal atomic amounts of Dy and Al; which is approximately 1.4× the rate for (Nd,Dy)-Fe-B alloys. The increase in $_jH_c$ of the alloy lowers the irreversible losses at elevated temperatures and, consequently, the temperature range for application of the magnet can be extended with small addition of Al to (Nd,Dy)-Fe-B alloys.

It has been found that the presence of 4 at.% V (Mo) not only increases the coercivity of sintered $Nd_{16}Fe_{72}V_4B_8$, $Nd_{15}Fe_{68}Co_5V_4B_8$, $Nd_{14.4}Dy_{1.6}Fe_{72}V_4B_8$ and $Nd_{14.4}Dy_{1.6}Fe_{67}Co_5B_8V_4$ magnets but it also improves their corrosion behaviour substantially [162, 163]. Moreover, the coercivity does not decrease with Co addition as in the case of V-free samples [162].

The presence of Ti in the high corrosion resistance sintered $Nd_{15}(Fe_{0.585}Co_{0.3}Ni_{0.1}Ti_{0.015})_{77}$-$B_8$ magnets increase their intrinsic coercivity, probably due to the presence of TiB_2 precipitates, inhibiting the grain growth during sintering [164].

Small additions (1 at.%) of Cr, Sn, P, Zr, Ti and Pb have reported to inhibit the corrosion process of $Nd_{15}Fe_{76}B_8$ sintered magnets. It was established that most advantageous was the addition of 1 at.% Cr which distinctly improves the inhibition of both acidic and atmospheric corrosion processes while it did not deteriorate the magnetic characteristics of the magnet [165]. With further increase of Cr content the J_r and T_c decrease. $_jH_c$ increases up to 6 at.% Cr and then decreases rapidly [166].

2.7.12.3.2 Melt Spun Alloys

The coercivity of melt spun RE-Fe-B magnets was found to increase with small additions of Cu, Al and Zn, which reduce the grain size and modify the grain boundary structure and produce planar imperfections [167].

Nb additions to Nd-Fe-B melt spun ribbons increase their coercivity and glass forming ability and decrease T_c. Nb also has a grain refining effect which can lead to enhance remanence [111, 168].

Pollard et al. [169, 139] attributed the improvement in the coercivity of under quenched melt spun $Fe_{74.7}Nd_{16.5}B_{7.8}Nb_1$ ribbons to the presence of small (2-8 nm) Nb-rich precipitates, comparable with the domain wall width in the hard $Nd_2Fe_{14}B$ phase (~5 nm). Manaf et al. [170] also observed a second phase within $Nd_2Fe_{14}B$ and a good combination of magnetic properties for melt spun ribbons of similar composition $Nd_{18}Fe_{76}B_7Nb_1$.

Wecker and Schultz [171] observed that partial substitution of Fe by Zr or Nb increased the coercivity of melt spun $Nd_2(Fe_{1-x}M_x)_{14}B$, $Nd_2((Fe_{0.9}\text{-}Co_{0.1})_{1-x}M_x)_{14}B$ and $Nd_{15}(Fe_{1-x}M_x)_{77}B_8$ alloys by a factor up to 3. In these alloys M=Zr, Nb and x=0.05, 0.10. However, the remanence and T_c fell simultaneously, consistent with the Nb and Zr being at least partly dissolved in the tetragonal phase. Zr was also found to have a significant grain refining effect [136]. Similarly, Si and/or Al additions were found to have a grain refining effect on melt spun Nd-Fe-B alloys and enhance the remanence [7-9, 108-110].

Choi et al. [172, 173] studied melt-spun alloys $Fe_{77.5}Nd_{15}(B_{1-x}M_x)_{7.5}$ with M=C, Al and Si, and $0.1 \leq x \leq 0.4$. The crystallisation temperature of the melt-spun amorphous alloys increased with increasing concentration of the fourth elements M. T_c increased with Si, whereas it decreased with C and Al. C had little effect on ${}_jH_c$ but, in the composition range x=0.15 to x=0.25, it increased J_r significantly, and $(BH)_{max}$ was 1.6 to 1.8 times larger than that of the ternary alloy. Al and Si also increased J_r.

Ahmad et al. [174] reported enhanced ${}_jH_c$ by replacement of 2 at.% Fe by Si in melt spun $Nd_{18}Fe_{76}B_6$-based ribbons and attributed this to a grain refining effect. Further increase in ${}_jH_c$ by the addition also of 1 at.% Dy was concluded to be due largely to enhancement of the anisotropy field of the $Nd_2Fe_{14}B$ phase but also partly to reduction in the mean crystallite size. J_r was not changed significantly for Si addition,

but, as expected, was reduced by the addition of Dy due to its ferrimagnetic alignment.

Herbst et al. [175] reported a significant increase (30%) in coercive force for melt spun $(Nd_{13.5}Fe_{80.25}B_6)_{99.5}Cu_{0.5}$ ribbons with no significant decrease in remanence. Cu was reported to segregate preferentially to the grain boundaries and to decrease the melting point of the paramagnetic Nd rich phase. Chin et al. [176] found that the addition of M=Ti, V, Mo or Al to $Nd_{10.8}Fe_{84.8-x}B_{4.4}M_x$ increased the coercivity for overquenched and annealed melt spun ribbons, which was attributed to strong domain wall pinning at refined 2-14-1 grains. Fang et al. [177] showed that replacement of 3 at.% of the Fe by V or Ti effectively refined the grain size of both hard and soft magnetic phases in melt spun $Nd_6Fe_{88}B_6$ ribbons processed by rapid thermal annealing and increase the remanence ratio and energy product, although both solutes decreased J_s and J_r. However, addition of Ti increased the ${}_jH_c$ and V decreased it.

Yapp and Davies [178] found ~100°C increase in T_c for each 10 at.% cobalt substitution for iron in low Nd (9 to 10 at.%) nanocomposite melt spun alloys without unacceptable detriment to the enhanced remanence and energy product associated with the nanophase structure. Similar results were reported by Liu and Davies [134] for $Nd_9(Fe_{1-x}Co_x)_{85}B_6$.

Addition of Mo to Nd-Fe-Co-B magnets was observed to increase the coercivity [158, 160, 179], possibly as a result of grain refinement due to primary precipitation of Mo_2FeB_2 compound, in the $Nd_2Fe_{14}B$. However, J_s was also decreased [179].

Chin et al. [180] investigated melt spun alloys in the system $Nd_{13}Fe_{81-x}M_xB_6$, where M is 0.5-3 Ti, Cr, Mo, W, Mn, Co or Ni. From this they concluded that additions of Mo and Co effectively enhanced J_r, $(BH)_{max}$ and ${}_jH_c$.

2.7.12.4 Ga Substitution

Mossbauer spectra study of $Nd_2Fe_{14-x}Ga_xB$ by Xie et al. [181] showed that Ga atoms preferentially occupy the Fe k_2 sites of the $Nd_2Fe_{14}B$ structure when the Ga

content is small. However, when $x \geq 1$, they occupy the k_1 and j_1 sites, in addition to k_2 sites. They also concluded that the k_2 sites have the shortest Fe-Fe interatomic distance and thus the strongest negative exchange interaction. Therefore, when the Ga atoms preferentially replace Fe atoms at the k_2 sites, the total exchange interaction of the compound will be drastically increased, and thus T_c for the $Nd_2Fe_{14-x}Ga_xB$ compounds is increased with increasing Ga content. The anisotropy field, however, was reported to first increase and then decrease with Ga substitution. The covalent radius of Ga (0.1261 nm) is larger than that of Fe (0.117 nm); however, the Fe k_2, k_1 and j_1 sites, which are preferentially occupied by Ga atoms, are far away from the basal plane (containing the 4c iron, neodymium and boron atoms). Therefore, the a axis is little changed, but the c parameter increases with increasing Ga content.

2.7.12.4.1 Sintered Alloys

Ga decreases the melting point of the grain boundary eutectic from 720°C (ternary alloy) to 690°C [182] and also reduces the surface energy of the Nd-rich liquid phase, in sintered magnets, resulting in smoothed grain boundaries and a more uniform distribution of the Nd-rich phase [183]. Moreover, the formation of new phases at the grain boundaries may help to magnetically decouple the grains or provide pinning sites to domain wall motion, thus improving the coercivity [184-187]. However, larger Ga substitutions (> 2 at.%) are found to decrease the coercivity because of precipitation of α-Fe, together with the nonmagnetic NdGa and $NdGa_2$ [188] and magnetic $Nd_6Fe_{11}Ga_3$ [189] phases.

Knoch et al. [190] attributed enhanced coercivity of sintered Nd-Fe-B magnets by Al or Ga additions to increased wettability, which improve separation and exchange decoupling of the $Nd_2Fe_{14}B$ grains by the solidified residual liquid phase.

Pai et al. [191] observed coercivity enhancement for sintered (Nd, Dy)-(Fe, Co, Nb)-B sintered magnet at a rate of about 147 kAm^{-1}/at.% Ga. Ga was concluded to mainly exist in the Nd-rich phase and to improve its wettability.

The presence of a small amount of Ga in $Nd(Fe_{0.7}Co_{0.2}B_{0.08}Ga_{0.02})_{5.6}$ [192] and $Nd_{14.5}Fe_{bal}Co_{16}Ga_1B_x$ with x=5.5 and 9.5 [193] sintered magnets was found to increase ${}_jH_c$ and the thermal stability of the magnets considerably. Tsutai et al. [194] achieved high coercive force for x=16-30 at.% Co in the presence of 1 at.% Ga for sintered $Nd_{14.5}Fe_{76-x}Co_xGa_1B_{8.5}$ magnets.

Burkhardt et al. [195] studied the corrosion behaviour of HDDR treated powders with the compositions $Nd_{15}Fe_{77}B_8$, $Nd_{15}Fe_{77-x}B_8Zr_x$ (x=0.1, 0.5, 1.0), $Nd_{15}Fe_{77-x}B_8Ga_x$ (x=0.5, 1.0, 2.0 and 4.0). They found that alloying additions such as Zr and Ga in direct-reduced Nd-Fe-B type material lead to significantly improved corrosion resistance in dry environments but deteriorate the corrosion resistance under humid conditions due to the existence of Zr-B and Nd-Ga phases which, increase formation of local corrosion cells.

2.7.12.4.2 Melt Spun Alloys

Harland and Davies [89] observed that substitution of 30% of Nd by Dy resulted in a coercivity increase from 1590 to 3290 kA m^{-1} for melt spun $(Nd,Dy)_{18}Fe_{76}B_6$, consistent with increased anisotropy constant. However, contrary to previous suggestions [174, 196, 197], substitution of 1% of the Fe by Ga was found to have only a small influence on the magnetic properties of all the alloys in the compositional series $(Nd_{100-x}Dy_x)_{18}Fe_{76}B_6$ (x = 0-30), thus disproving the suggestion that ultra fine Ga precipitates were the source of the large ${}_jH_c$ increase.

Panagiotopoulos et al. [198] found slight increase in coercive field for directly quenched $Nd_{18}Fe_{76-x}Ga_xB_6$ (x=1 and 2) ribbons as a result of Ga presence. In samples overquenched at 60 m/s and annealed, substitution of Fe by Ga helps the formation of faceted fine (20 nm) $Nd_2Fe_{14}B$ grains and increase the coercive field; coarser equiaxed grain structure is formed in Ga free ribbons.

Combined additions of Ga and Nb were found to result in the formation of new intergranular phases and precipitates in melt spun Nd-rich $Fe_{77}Nd_{17}B_{7.5}Ga_{1.5}Nb_2$ ribbons, which improved the magnetic decoupling and thus enhancing the coercivity [199, 200]. Narrower distribution of the size and the shape of the grains and therefore,

better rectangularity of the demagnetisation curve were found in samples containing Nb and Ga, compared with samples with Ga additions alone. While, Nb or Mo were found to form domain pinning high-melting borides and precipitates in sintered magnets they acted as crystallisation nuclei in the melt-spun magnets, thus leading to a very fine-dispersed homogeneous microstructure [199].

Rieger et al. [186, 187] observed that small additions of Ga and Nb/Mo to nanocrystalline overquenched and annealed $Nd_{18}Fe_{74}B_7Ga_1$, $Nd_{17}Fe_{73}B_7Ga_1Mo_2$ and $Nd_{17}Fe_{72}B_{7.5}Ga_{1.5}Nb_2$ alloys improve the coercive field whilst the remanence remains constant.

Zhou et al. [168] investigated the melt spun $Nd_{0.15}(Fe_{0.935-x}M_xB_{0.065})_{0.85}$ system, where M=Nb, Si, and Ga, and $0 \leq x \leq 0.06$. T_c was increased on addition of Ga and Si but was decreased slightly by Nb addition. $_jH_c$ significantly increased with Ga and Nb substitution but J_s decreased monotonically. The latter was attributed to Nb and Ga acting as non-magnetic dilutant and also influencing the local Fe-Fe exchange interaction. Si addition reduced the coercivity and enhanced J_s because of the presence of α-Fe. Si and Nb increased the glass-forming ability and had a grain refining effect while little effect was observed for Ga addition.

Steel et al. [182] observed optimum magnetic properties at 1 at.% Ga addition for $Nd_{15}Fe_{79}B_6$ melt spun ribbons at which the coercivity was increased to ~1750 kAm^{-1} (c.f. 1600 kAm^{-1} without Ga). However, the remanence and the energy product decreased with increasing gallium content, whilst T_c was not dramatically altered. The optimum properties for the die-upset magnet have been established at 0.25 at.% Ga for this alloy, whereby a 25% increase in $_jH_c$ has been observed with little loss in J_r and $(BH)_{max}$.

Panchanathan and Croat [201] found that for overquenched and annealed Nd-Fe-B alloy, based on 13.9 at.% Nd and 5.5 at.% B content, J_r and $(BH)_{max}$ increase with Ga addition up to 0.6 at.% and decreases thereafter whereas; $_jH_c$ increases up to this Ga content and then remains essentially constant. They achieved optimum magnetic properties for 0.6 at.% Ga and 5.6 at.% Co.

Kim et al. [110] studied melt spun alloys in the $Nd_{12}Fe_{80}B_6M_2$ system, where M=Cu, Ti, Ga, and Nb. The addition of the element M increases the magnitude of the coercivity in the order Nb>Ga>Ti>Cu, and the remanence in the order Nb>Ti>Ga>Cu, Nb was therefore the most effective element for increasing both remanence and coercivity, to ~0.9 T and 1200 kAm^{-1}, respectively. They attribute the increases to the effects of $Nd_2Fe_{14}B$ grain refinement induced by the dopant.

Liu et al. [202] found that the addition of Ga to nanocomposite, substoichiometric melt spun $Nd_9Fe_{85}B_6$ alloys produced by direct quenching increases the mean value of remanence enhancement up to 1 at.% Ga while not significantly affecting the coercivity. This was considered to be due to increased exchange coupling resulting from grain refinement of the $Nd_2Fe_{14}B$ phase and probably also of the α-Fe second phase. On the other hand, for stoichiometric, single phase alloys, the coercivity increases up to 2 at.% Ga substitution for Fe, while leading to a slow reduction of J_r.

Small substitution of Fe by Cr and Co [203], and of Nd by Dy, and small additions of Ga, Mo, V and Nb were shown to improve the magnetic properties of nanocrystalline $Nd_2Fe_{14}B/Fe_3B$ composite melt spun alloys, by refining the grain size and changing the phase constitution [128, 204].

Sinnecker et al. [205] observed that the remanence and coercivity were improved in overquenched and annealed melt spun $Nd_4Fe_{78-x}Ga_xB_{18}$ ribbons for x = 0.5 at.%.

Kanekiyo et al. [206] investigated alloying additions for overquenched and annealed, low Nd ribbons, of composition $Nd_5F_{71.5}Co_5B_{18.5}M_1$ (where M=Al, Si, Ga, Ag, Au). The material was reported to form a nanocrystalline structure based on Fe-$(Fe,Co)_3B$-$Nd_2(Fe,Co)_{14}B$. They noted that the additions considerably reduce the grain size, resulting in improvements in the squareness of the hysteresis loop, particularly with Si and Ga additions.

2.8 Conclusions

Systematic investigation of the effects of annealing parameters and alloying additions on the microstructure and magnetic properties of stoichiometric single

phase and sub-stoichiometric two-phase melt spun Nd-Fe-B based alloys, and a comparison with the properties of corresponding directly quenched alloy, have been performed hitherto. Based on previous studies gallium appears to be a favourable solute element for improvement of magnetic properties.

Thus, the major aims of the present study are i) to determine the degree to which the enhancement of magnetic properties arising from grain refinement and consequent inter grain exchange coupling in directly quenched melt spun single phase ($Nd_2Fe_{14}B$) and two phase ($Nd_2Fe_{14}B/\alpha$-Fe) ribbon can be reproduced for corresponding overquenched and annealed ribbons and ii) to establish the effects of Ga concentration, particularly in possibly enhancing the coercivity. Particular emphasis is placed on TEM studies of the microstructure.

3. Experimental Procedures

3.1 Alloy Preparation

3.1.1 Alloy Compositions

The following alloys were investigated:

1) Near stoichiometric, $Fe_{83.2}Nd_{10.9}B_{5.9}$

2) Nominal Stoichiometric, $Fe_{82.3-x}Nd_{11.8}B_{5.9}Ga_x$, with x = 0, 0.5, 1, 1.5, 2, 2.5 and 3 at.%

3) Substoichiometric, $Fe_{85.1-x}Nd_9B_{5.9}Ga_x$, with x = 0, 0.5, 1, 1.5, 2, 2.5 and 3 at.%

3.1.2 Weighing of Alloy Components

The pure elements (Rare Earth > 99.7% purity, and non Rare Earth > 99.9% purity) were weighed out to ±0.001 g, using an Instanton C41 mechanical balance to give the required composition in each case. The results of chemical analyses of the initial samples were used as indications of losses in melting and melt spinning and appropriate adjustments were made to the charges for subsequent melts in order to try to achieve the desired compositions (Table 3- 1).

3.1.3 Alloy Preparation by Argon Arc Melting

The alloys were melted in a laboratory scale cold crucible arc furnace (Figure 3-1). Boron having a low density and high melting point, Table 3- 2, was placed at the bottom and other materials were put on top to melt first and dissolve the boron in the melt. In order to limit oxidation of the rare earth elements, the chamber pressure was first reduced to $< 50\times10^{-5}$ bar with a mechanical pump and flushed with argon. Then it was evacuated to $<10^{-4}$ mbar and finally back filled with 1/3 atm of pure argon. The total weight of the alloy for a melt was 20 g. A titanium ingot was melted before melting the alloy to react with residual oxygen. The charge was first melted to an

ingot, which was allowed to cool sufficiently so that it could be turned over. This ingot was then remelted from the other side. This process was repeated five times to improve the homogeneity of the ingot. The alloy was given enough time to cool to room temperature before removing.

3.2 Controlled Atmosphere Chill Block Melt Spinning

The alloys were rapidly solidified to thin ribbons by chill block melt spinning. Melt spinning was performed under argon in a sealed, controlled atmosphere chamber. A piece of ingot, typically 7g, was placed in a quartz crucible, with an orifice diameter of 0.50 ±0.05 mm. This was placed in the chamber, with the nozzle tip 3 mm above the copper roll, and the chamber then evacuated with a diffusion pump to better than 10^{-4} mbar, before filling with high purity argon to about 1 atmosphere. The ingot was melted by induction heating, using a power of ~5 kW for 50 seconds. The molten alloy was ejected onto the rapidly rotating copper roll by an argon over pressure of 0.4 bar applied to the melt surface. Figure 2- 17 shows a schematic of the arrangement and the actual equipment used in this study is shown in Figure 3- 2.

Various roll speeds were employed to induce different cooling rates associated with different ribbon thicknesses. The higher the roll speed the thinner the ribbon and thus the higher the cooling rate. Ribbons spun at lower speeds were relatively thick e.g. typically 85 μm at 8 m/s, whereas those melt spun at higher speeds were correspondingly thinner, typically 30 μm at 22 m/s.

3.3 Vibrating Sample Magnetometer (VSM)

An Oxford Instruments Vibrating Sample Magnetometer (VSM) coupled to a 5 T superconducting magnet was used to measure the magnetic properties of individual pieces of ribbons of premeasured thickness (Figure 3- 3). A schematic diagram of a VSM is shown in Figure 3- 4. Each ribbon, typically 10-15 mm long and 1-2 mm wide, was weighed on a Mettler mechanical balance to ±10 μg. The thickness was

measured using a point micrometer attached to a digital display transducer device, with a resolution of ±0.1 μm. The reported thickness in each case was the mean of 3 measurements. The sample was then mounted in a ceramic sample holder on the end of the sample rod, and vibrated at 66 Hz between two sense coils, in a field that was ramped up to +5 T then ramped back through zero field to -5 T and then back to zero. The signal output was amplified, filtered to remove noise, and converted to magnetic units by a microprocessor. The ribbons in this case were magnetised across their width (typically 1-2 mm), so that owing to their small thickness (typically 20-30 μm), correction for self demagnetisation was not necessary. The magnetic moment was converted from emu into gauss and a simple (J-H) loop was generated by the software. The value of $(BH)_{max}$ was computed from the product of B and H in the second quadrant using a programme written in basic. The VSM was calibrated with a length of pure nickel ribbon. At least 6 samples for each batch of ribbon were examined and the reported result is the arithmetic mean of these measurements ignoring any having very poor loop shapes (i.e. narrow loop or stepped loop). However, only a small proportion were found to be of this type and were generally due to partial or complete vitrification during melt spinning in locally thinner areas.

3.4 X-Ray Diffraction (XRD) Analysis

The X-Ray diffraction data for ribbons were analysed and indexed by comparisons with the diffraction peaks for the $Nd_2Fe_{14}B$ phase and any additional peaks were indexed with the help of the JCPDS Powder Diffraction File. A schematic representation of X-ray diffraction traces from the JCPDS Powder Diffraction File for $Nd_2Fe_{14}B$ is shown in Figure 3- 5.

An XRD line broadening technique, based on the Scherrer equation, was used to determine the mean grain size for selected samples. Pieces of ribbon were glued side by side onto a glass slide, and examined by X-ray diffraction, on a computer controlled Philips 1710 X-Ray Diffractometer, using Co $K\alpha$ radiation as a function of diffraction angle θ. Three peaks were used for line broadening analysis, in the 2θ range: 30.5-32.5°, 42.5-44.5° and 47.7-49.1° corresponding to (212), (214) and (224) reflections of the $Nd_2Fe_{14}B$ phase. Measurements were carried out on both the alloy ribbon sample and on a sample of silicon, as a standard material with unbroadened

peaks, in order to correct for instrumental broadening. To also measure the α-Fe grain size in low Nd alloy samples, Cr K_α radiation, having a longer wavelength, was used in order to separate the (110) Fe peak from adjacent $Fe_{14}Nd_2B$ peaks.

The half height peak width was used as the measure of peak breadth. This is the breadth of the peak (in radians), at exactly half the height of the peak, after subtraction of the background radiation. The values are denoted as b and b_o for the sample peak and a standard peak of similar 2θ value, respectively. Assuming a Gaussian shape for the peak then the corrected breadth B is given by:

$$B=\sqrt{(b^2-b_o^2)} \qquad (3\text{-}1)$$

The Scherrer equation then gives the mean crystallite size as:

$$t = \frac{0.9\lambda}{BCos\theta} \qquad (3\text{-}2)$$

where λ is the wavelength of radiation.

Thus t was calculated for various selected reflections [207] and the mean value calculated.

3.5 Optical Microscopy

Samples of ribbon were washed in acetone using ultrasonic cleaner, dried using an air blower, then mounted on a microscope slide with plasticine and examined in a Polivar Optical Microscope.

3.6 Scanning Electron Microscopy, SEM

A Camscan Scanning Series 2 Electron Microscope operating at 20 kV was used to examine the surface condition and fractured cross section of selected ribbon samples.

3.6.1 Specimen Preparation

Ribbon lengths were washed in acetone in a Kerry Ultrasonic bath, to remove any grease and surface debris. They were then fractured and mounted on aluminium stubs using plasticine and then silver paint was used to electrically connect ribbons to the stubs. To ensure good conduction, the ribbons were coated with a thin layer of gold (a few microns in thickness) by use of a EM Scope SC500A Sputter Coating Unit.

3.6.2 Operating Conditions

The surface features and fracture cross sections were examined. In some cases, the sample was rotated in the microscope so that both the fracture cross section and the roll contact surface could be examined simultaneously.

3.7 Conventional Transmission Electron Microscopy (TEM)

Philips EM 400T and EM 420 transmission electron microscopes were used to study the internal microstructures of selected samples, notably the phases present and their grain sizes.

3.7.1 Specimen Preparation

Pieces of ribbons, typically 20-30 μm thick, were stuck to copper slot grids and two different ion beam milling machines were used to thin the samples.

a) Gatan Duo Mill, Model 600, where the sample is tilted to the desired angle (normally 15° and then 10°), and is thinned from both sides using ionised argon, in a vacuum of $< 10^{-4}$ torr.

b) Gatan 691 PIPS™ Precision Ion Polishing System, in which the sample was attached to the specimen post using wax and thinned from one side at a desired angle (4°), and then removed, pasted to the copper grid, attached to the post and thinned from the other side until perforation occurred.

3.7.2 Use of the instrument

The foils were examined in the TEM instruments using both single-tilt and double-tilt sample holders. The latter facilitated a tilt of ±30 degrees about the Y axis, in addition to ±45 degrees about the X axis, which enabled selected area diffraction patterns to be obtained. A computer program developed by Dr. M. Al-Khafaji in the Sorby Electron Microscope Centre was used to solve these diffraction patterns. The operating voltages for the Philips 400 and 420 instruments were 100 keV and 120 keV, respectively. Selected areas of some samples were analysed for constituent elements using Energy Dispersive Spectroscopy (EDS), which was installed on the Philips 420 instrument.

3.8 High Resolution Transmission Electron Microscopy, HRTEM

High resolution TEM, (HRTEM) was carried out on selected samples with a JEOL 3010 UHR, operating at 300 keV and at a point resolution of 0.17 nm.

In the TEM, high energy electrons, typically 100-400 keV, are used to illuminate an ultra thin sample, typically <100 nm. The electrons undergo a number of different interactions during their passage through the sample, the most important of which for crystalline materials is diffraction.

In conventional TEM the diffracted beams are removed, such that the image is formed from the undeviated transmitted beam only. However, in high resolution electron microscopy (HREM), some, or all, of the diffracted beams are allowed to interfere with the transmitted beam to form the image. It is the fine detail of this interference which determines the image characteristics, and importantly, whether the image can be interpreted.

HREM is conducted at high magnifications on high quality samples in the very thinnest areas. The sample must be imaged exactly along a crystallographic zone although lower resolution alternatives exist. Under so-called "structure imaging" all diffracted beams within the point resolution of the microscope should be used. The

diffracted beams travel a different path, and therefore distance, to the transmitted beam before being recombined by the lower objective pole piece. The result is a phase difference between the two beams.

In Figure 3- 6a, a phase difference of $\pi/2$ has occurred. The diffracted beam is weak because the sample was thin. In this instance, there is no change in intensity in the sum wave compared with the transmitted beam and therefore nothing will be seen. In Figure 3- 6b, however, a phase difference of π results in a reduction in intensity in the sum wave and this will give dark atoms compared to the background. Similarly, bright atoms are obtained for a phase difference of 0 or 2π, Figure 3- 6c. The exact phase difference, and therefore atom contrast, will depend on the distance travelled by the diffracted beam, which is a function of the spacing of the atom planes.

A crystal with a range of atom spacings may therefore be imaged with a range of contrasts and this is further complicated by additional phase shifts imposed by the microscope itself. The Contrast Transfer Function (CTF) provides a measure of the atom contrast (+1, bright; 0, not seen; -1, dark) as a function of atom spacing. In the example shown in Figure 3- 7, which was produced under Scherzer defocus condition, the d spacing at this first zero is taken as the point resolution of the microscope. Under the Scherzer defocus condition, the range of atomic spacings which are imaged with the same contrast is maximised.

Moreover, by using optical diffraction, diffraction information can be obtained from the specific region of interest without the averaging effect which occurs with conventional diffraction in the microscope. With this technique a fine laser beam is passed through the high resolution negative. The diffraction which results is, in effect, equivalent to the diffraction of electrons through the sample, but on a much finer scale [208]. A simple experimental optical diffractometer is illustrated in the diagram shown in Figure 3- 8.

4. Results

4.1 Introduction

The main part of this work deals with the effect of Ga substitution for Fe in Nd-Fe-B based alloys. Two principal alloy systems were investigated: stoichiometric single phase (11.8% Nd) and substoichiometric two phase (9% Nd containing $Nd_2Fe_{14}B$ and α-Fe). Both direct quench and overquench and anneal routes were used to produce the required nanostructures. The effect of roll speed and ribbon thickness as well as Nd content on microstructure and magnetic properties were also studied.

Linear trends are represented by a line of best fit, determined statistically by the least squares method; otherwise, the data points are connected together or the best fit is drawn for clarity of observation.

4.2 Directly Quenched Ribbons

4.2.1 Ribbon Surface

In melt spinning at ambient (1 atm) pressure, trapped gas between the roll and the molten metal during the solidification process leads to localised depressions on the roll contact surface of the ribbon known as gas pockets. The same patterns of gas pockets were observed in this study for melt spun ribbons, regardless of chemical composition and roll speed down to 19 m/s. Polishing the roll surface using down to 1 μm polishing paste did not affect this pattern. The optical micrograph in Figure 4-1 shows this pattern for $Fe_{83.2}Nd_{10.9}B_{5.9}$ melt spun at 19 m/s, which is parallel to the length of the ribbon in the middle and divergent in the margin areas. $Fe_{83.2}Nd_{10.9}B_{5.9}$ ribbons spun at 8 m/s do not show gas pockets and a pattern which appears to be a replica of the roll surface is observed on the roll contact surface of these ribbons, Figure 4- 2. A similar pattern was observed for stoichiometric samples melt spun in vacuum, Figure 4- 3.

A magnified area of Figure 4- 1 is shown in Figure 4- 4. Some very coarse grains can be seen in the base of some of the gas pockets (arrowed). The free (non-contact) surface of the $Fe_{83.2}Nd_{10.9}B_{5.9}$ samples melt spun at roll speeds up to 19 m/s show a dendritic pattern as can be seen in Figure 4- 5. Samples spun at higher speeds have a smooth, featureless free surface, Figure 4- 6.

Both the roll surface and transverse cross section of the $Fe_{83.2}Nd_{10.9}B_{5.9}$ ribbon, melt spun at 22 m/s, can be seen in Figure 4- 7a. An area of coarse grains is observed in the base of one of the gas pockets (arrowed) which continues through the thickness of the ribbon to the free surface. This area is magnified in Figure 4- 7b. No coarse grains are observed in Figure 4- 8a underneath the gas pocket (arrowed) for the $Fe_{83.2}Nd_{10.9}B_{5.9}$ sample melt spun at 20 m/s. Figure 4- 8b shows fine grains underneath this gas pocket at higher magnification. A complete cross section of a $Fe_{83.2}Nd_{10.9}B_{5.9}$ ribbon melt spun at 19 m/s is shown in Figure 4- 9. Irregularity and a significant variation in the thickness is observed across the width of the ribbon. Very coarse grains are observed on the free side of the thick part of the ribbon, although, some coarse grains also exist in thinner areas. While areas of coarse grains are observed underneath some gas pockets, fine grains can be seen for others. The grain size is minimum at the roll contact surface and grow coarser towards the free surface. The grains in thicker sections of the ribbon are coarser; however, deviations from these general trends are seen in this SEM micrograph.

TEM bright field images and corresponding selected area diffraction patterns of $Fe_{79.8}Nd_{11.8}B_{5.9}Ga_{2.5}$ alloy melt spun at 22 m/s are shown in Figure 4- 10. As can be seen, a wide range of mean grain sizes are presented in this TEM sample, from ~13 nm for Figure 4- 10a to ~170 nm for Figure 4- 10f. High resolution electron micrograph for a stoichiometric sample melt spun at 22 m/s is shown in Figure 4- 11. A polygonal shape and random orientation of $Nd_2Fe_{14}B$ grains is observed.

4.2.2 Ribbon Thickness and Magnetic Properties as a Result of Roll Speed

Although in every melt spinning experiment, ribbons with a relatively wide range of thickness are produced, the mean value of the thickness is reduced with increasing

roll speed. This affects the cooling rate and thus the microstructure and grain size of the samples, which in turn determine the magnetic properties.

Figure 4- 12 shows a plot of ribbon thickness as a function of roll speed for $Fe_{83.2}Nd_{10.9}B_{5.9}$ compared to those for some other alloys reported by Vincent and Davies [57]. Ribbons spun at lower speeds are relatively thick e.g. ~100 μm for 4 m/s, whereas those melt spun at higher speed are about 30 μm thick. A value of 0.79 was obtained for the parameter "a" in equation (2-23) $t \propto V^{-a}$ for the $Fe_{83.2}Nd_{10.9}B_{5.9}$ alloy which, is within the range of values reported by Vincent and Davies i.e. a=0.75±0.08.

The mean $Nd_2Fe_{14}B$ grain size d_g of the ribbons measured by X-Ray diffraction line broadening technique as a function of roll speed is shown in Figure 4- 13 for $Fe_{83.2}Nd_{10.9}B_{5.9}$. Increasing the roll speed results in decreasing mean grain size on both surfaces of the ribbons with the values on the roll contact surface being consistently smaller than the corresponding values on the non contact surface. This difference is more pronounced for larger grain sizes and decreases with increasing roll speed. Thus, the higher roll speeds provide thinner ribbons and higher and more uniform cooling rates through the ribbon sections, i.e. the cooling becomes closer to newtonian in character and results in a more uniform grain size. This can also be seen clearly in Figure 4- 14, in which the grain size is plotted against ribbon thickness.

The average magnetic properties of $Fe_{83.2}Nd_{10.9}B_{5.9}$ melt spun at different roll speeds are presented in Figure 4- 15 and Table 4- 1. J_r has a value of around 0.65 T for roll speeds V_r between 8 and 19 m/s as a result of coarse grains but undergoes a steep increase to 0.88 T at 20 m/s, indicative of smaller and possibly more uniform, grain size in the ribbon. J_r further increases and reaches its maximum of 0.95 T at 22 m/s. This value is substantially larger than 0.8 T ($J_s/2$), the Stoner-Wohlfarth prediction for non-interacting particles; this enhancement above 0.8 T is related to the reduction in mean grain size below ~50 nm. J_r then decreases for V_r beyond 22 m/s presumably as a result of the beginning of vitrification, Figure 4- 15a.

$_jH_c$ follows almost the same pattern as J_r (Figure 4- 15b) and changes from 181 kAm^{-1} for 8 m/s to 790 kAm^{-1} for 22 m/s. For V_r>22 m/s there is a reduction in the $_jH_c$ to 590 kAm^{-1}; again because of partial vitrification. $(BH)_{max}$ chases the same

pattern as J_r and reaches its maximum of 149 kJm^{-3} at 22 m/s before reducing to 108 kJm^{-3} at 23 m/s, Figure 4- 15c.

The TEM micrograph from a coarse grained area (d_g $Nd_2Fe_{14}B$ ~170 nm; d_g α-Fe ~100 nm) for $Fe_{83.2}Nd_{10.9}B_{5.9}$ ribbon melt spun at 20 m/s, Figure 4- 16a clearly shows the grain morphology for these samples, consisting of a uniform mixture of polygonal $Nd_2Fe_{14}B$ and smaller α-Fe particles. An extensive nanostructured area for a sample melt spun at 22 m/s is shown in the TEM bright field image of Figure 4- 16b. Figure 4- 16c presents the nanostructured region for a ribbon melt spun at 23 m/s. Fine grains in amorphous matrix, which forms the other part of the microstructure of the ribbons spun at 23 m/s, can be seen in Figure 4- 16d. The inset is the selected area diffraction pattern (SADP) of this semi-amorphous microstructure.

As can be seen in Figure 4- 17, $_jH_c$ generally increases as J_r increases for ribbon samples of this alloy.

Representative hysteresis loops for near stoichiometric samples melt spun at different roll speeds are presented in Figure 4- 18. Gradual improvement in the shape of hysteresis loop in the second quadrant is observed as a result of increasing roll speed. The demagnetisation curve for the sample melt spun at 22 m/s is close to the optimum shape and is representative of a sample with very high energy product. The demagnetisation curve for the sample melt spun at 23 m/s on the other hand, shows a lower remanence and much lower intrinsic coercivity. In addition, at the start of the second quadrant there is a rather steep decrease in J_r which reflects the partial vitrification of this sample. The initial magnetization curve is missing for these loops because an initial field was used to centre the sample in the VSM "column".

X-ray diffraction traces of the "top", non-contact, surface for near stoichiometric ribbon samples spun at different speeds are shown in Figure 4- 19. Ribbons spun at higher speed reveal a crystallographically isotropic spectrum, whereas the sample spun at 4 m/s is highly textured with (001) planes parallel to the surface of the ribbon, i.e. the growth direction of columnar $Nd_2Fe_{14}B$ grains is [001], which is different from the growth direction of Nd-Fe-B ingots and die-upset forged magnets,

which is [100]. Figure 4- 20 shows columnar $Nd_2Fe_{14}B$ grains in the transverse cross section of $Fe_{83.2}Nd_{10.9}B_{5.9}$ ribbon melt spun at 4 m/s.

4.2.3 Effect of Neodymium Content

The stoichiometric (11.8% Nd) series contained only the $Nd_2Fe_{14}B$ phase, whilst the substoichiometric series contained α-Fe phase in addition to the principal hard magnetic $Nd_2Fe_{14}B$ phase and the volume fraction of α-Fe increased with decreasing Nd content. The TEM micrographs in Figure 4- 21 show typical microstructures of each alloy spun at or close to optimal V_r, together with their respective diffraction patterns. All alloys show enhanced J_r, and, for substoichiometric alloys, J_r increases progressively from the value for the stoichiometric alloy; thus J_r is 1.15, 1.09 and 0.95 T for 7, 9 and 11.76% Nd, respectively. Conversely, the highest value of $_jH_c$ 800 kAm^{-1}, was obtained for the 11.76% Nd series, compared to 500 and 318 kAm^{-1} for 9 and 7% Nd.

Figure 4- 22 shows a typical JH loop for ribbons from each series. These loops emphasise the increase in J_r and decrease in $_jH_c$ with decreasing Nd content. Figure 4- 23 shows the X-Ray diffraction traces for these alloys. As can be seen, the stoichiometric alloy has a typical single phase spectrum whilst the (110) peak of α-Fe phase becomes evident at 52.38 degrees 2θ for the 9% alloy and increases in intensity for the 7% Nd alloy.

4.2.4 Ga Addition in Stoichiometric Alloy, $Fe_{82.3-x}Nd_{11.8}B_{5.9}Ga_x$

To compare the effects of various Ga concentrations, alloys were melt spun at 22 m/s. In a few cases however, where a poor loop shape was obtained initially, another batch was produced at a different roll speed in the narrow window of 21 m/s to 23 m/s, to yield an improved loop shape.

Figure 4- 24 shows magnetic properties as a function of Ga content for $Fe_{82.3-x}Nd_{11.8}B_{5.9}Ga_x$ melt spun at optimum conditions. It may be noted that enhanced J_r is observed over the whole range of Ga contents, and that J_r increases by substituting

Ga for Fe from 0.95 T for the ternary alloy to maximum of 1.04 T for 1.5 at.% Ga and decreasing for higher Ga contents to 0.91 T for 3% Ga. $_jH_c$, however, shows relatively little dependence on Ga content increasing from 800 kAm^{-1} for the stoichiometric ternary alloy to a maximum of 835 kAm^{-1} at 2 at.% Ga and then decreasing to 812 kAm^{-1} for 3 at.%. As expected, $(BH)_{max}$ follows the trend for J_r with values of 150, 160 and 132 kJm^{-3} for 0, 1.5 and 3 at.% Ga, respectively, Table 4- 2.

Representative hysteresis loops for $Fe_{82.3}Nd_{11.8}B_{5.9}$, $Fe_{80.8}Nd_{11.8}B_{5.9}Ga_{1.5}$ and $Fe_{80.3}Nd_{11.8}B_{5.9}Ga_2$, melt spun at optimum conditions, are given in Figure 4- 25. Improved magnetic properties for Ga containing alloys with the highest J_r for 1.5% Ga and the highest $_jH_c$ for the 2% Ga sample are observed in this plot.

Figure 4- 26 shows typical microstructures for the stoichiometric alloy containing a) 1.5 at.% Ga and b) 2 at.% Ga. Slightly coarser grains for the latter are shown in Figure 4- 26c. The TEM micrograph for stoichiometric ternary alloy is shown in Figure 4- 21c. It can be seen that all these alloys are single phase, consisting of $Nd_2Fe_{14}B$ crystallites. The ternary alloy is clearly nanocrystalline, with a mean grain size of the order of ~23 nm. The mean grain size for the $Fe_{80.8}Nd_{11.8}B_{5.9}Ga_{1.5}$ is ~24 nm while $Fe_{80.3}Nd_{11.8}B_{5.9}Ga_2$ sample has a mean grain size of ~21 nm. Examination of many samples by TEM suggested that the Ga substitution had no visible systematic effect on the microstructure observed.

The magnetic properties versus ribbon thickness for all the $Fe_{82.3-x}Nd_{11.8}B_{5.9}Ga_x$ ribbons melt spun at nominally optimum V_r are given in Figure 4- 27. The best properties tend to be achieved in the range of thickness 26-38 μm. Thicknesses below that result in a higher cooling rates and probably produce partially amorphous material which has poorer properties. Larger thicknesses reduce the cooling rate and increase the mean grain size which, in turn, reduces J_r and $_jH_c$ and hence $(BH)_{max}$. There is substantial scatter of these data which emphasises the local variability of local cooling rate and differences between the samples at the start, at midstream and at the end of melt spinning run. This is more pronounced in the laboratory conditions because only small amounts of sample (~7 g) are spun in each batch and steady state conditions for heat transfer are harder to achieve.

$_jH_c$ and J_r tend to follow a general direct relation to each other with the scatter mainly arising from the effects of different Ga concentrations, Figure 4- 28.

X-ray diffraction traces for the $Fe_{82.3}Nd_{11.8}B_{5.9}$ and $Fe_{81.3}Nd_{11.8}B_{5.9}Ga$, melt spun at optimum V_r, are shown in Figure 4- 29. Table 4- 3 gives the Miller indices and d-spacings for selected traces for the $Fe_{82.3}Nd_{11.8}B_{5.9}$ and $Fe_{81.3}Nd_{11.8}B_{5.9}Ga$ ribbons, melt spun at 22 m/s and 21 m/s, respectively. The published data for $Nd_2Fe_{14}B$ phase is also given in this table.

4.2.5 Ga Addition in 9%Nd Alloy, $Fe_{85.1-x}Nd_9B_{5.9}Ga_x$

J_r, $_jH_c$ and $(BH)_{max}$ are plotted against the Ga content for $Fe_{85.1-x}Nd_9B_{5.9}Ga_x$ ribbons melt spun at optimum conditions in Figure 4- 30. As can be seen J_r remains almost unchanged from 1.09 T for the ternary alloy up to 2.5 % Ga but is slightly decreased to 1.01 T for the 3 % Ga sample. $_jH_c$ increases slightly from 500 kAm^{-1} for the ternary alloy to a maximum of 536 kAm^{-1} at 1.5 % Ga before decreasing down to 503 kAm^{-1} for the 3 % Ga sample. $(BH)_{max}$ values of 152 kJm^{-3}, 167 and 150 kJm^{-3} were achieved for the 0%, 1.5 % and 3 % Ga samples, respectively, largely reflecting the variation of J_r with Ga content, Table 4- 4.

Representative hysteresis loops for $Fe_{85.1}Nd_9B_{5.9}$ and $Fe_{83.6}Nd_9B_{5.9}Ga_{1.5}$ alloy ribbons melt spun at 22 m/s and 21 m/s, respectively, are given in Figure 4- 31. The higher $_jH_c$ and larger area enclosed by the demagnetisation curve (and thus larger $(BH)_{max}$) for the Ga containing alloy are obvious in this plot.

The TEM bright field image in Figure 4- 32a shows the dominant nanostructure for the substoichiometric $Fe_{85.1}Nd_9B_{5.9}$ ribbon melt spun at 22 m/s; this consists of a mixture of polygonal $Nd_2Fe_{14}B$ grains and α-Fe particles with mean grain sizes of ~33 nm and ~22 nm, respectively. The observed α-Fe morphology is changed from separate particles in fine grained areas to a continuous or semicontinuous phase at the grain boundary of the coarse $Nd_2Fe_{14}B$ grains for the same sample, Figure 4- 32b. The nanostructure in Figure 4- 32c contains smaller α-Fe particles, ~15 nm, for the Ga-containing $Fe_{83.6}Nd_9B_{5.9}Ga_{1.5}$ alloy, while d_g for the $Nd_2Fe_{14}B$ phase remains at

~32 nm. This finer distribution of α-Fe could be responsible for the higher coercivity of this alloy compared to ternary alloy.

The EDS spectra for a $Nd_2Fe_{14}B$ grain (continuous line) and an α-Fe particle (dashed line) in the $Fe_{83.6}Nd_9B_{5.9}Ga_{1.5}$ thin foil TEM sample are given in Figure 4-33. The Ga peak in the $Nd_2Fe_{14}B$ trace shows that Ga is mainly present in the $Nd_2Fe_{14}B$ grains at this Ga concentration. The TEM micrograph (Figure 4- 34), taken at high magnification (×800000), features (001) lattice fringes for the $Nd_2Fe_{14}B$ grain in this sample which reveals no precipitates and confirms that all the Ga content is in solid solution in the $Nd_2Fe_{14}B$ phase.

The effect of ribbon thickness on the magnetic properties of $Fe_{85.1-x}Nd_9B_{5.9}Ga_x$ ribbons melt spun at optimum conditions are shown in Figure 4- 35. The best properties are achieved in the range of 22-34 μm. There is considerably less scatter than was the case for the stoichiometric alloy samples.

The relation between remanence and coercivity for these $Fe_{85.1-x}Nd_9B_{5.9}Ga_x$ ribbons spun at optimum conditions is plotted in Figure 4- 36; it is approximately linear.

X-ray diffraction traces in Figure 4- 37 shows the presence of $Nd_2Fe_{14}B$ and α-Fe phases for directly quenched $Fe_{85.1}Nd_9B_{5.9}$ and $Fe_{82.1}Nd_9B_{5.9}Ga_3$ ribbons. No new peak, indicating any possible new phase in detectable amount, were observed for $Fe_{82.1}Nd_9B_{5.9}Ga_3$ alloy.

4.3 Over Quenched and Annealed Ribbons

4.3.1 Stoichiometric Ternary alloy, $Fe_{82.3}Nd_{11.8}B_{5.9}$

A systematic investigation of the effects of heat treatment of overquenched ternary stoichiometric alloy, melt spun at 26 m/s, was undertaken to obtain the optimum conditions for achieving the best magnetic properties.

The microstructure of the overquenched ribbons melt spun at 26 m/s consists of amorphous (Figure 4- 38a) and partly amorphous (Figure 4- 38b) regions.

The average magnetic properties and the mean grain size d_g, determined by XRD and TEM, for the ribbons from this batch, which was heat treated for 4 minutes at various temperatures in the range 600 to 900°C, are shown in Figure 4- 39. The samples annealed at 600°C have an average remanence of 0.93 T. It increases to a maximum of 0.98 T for 700°C and decreases again down to 0.69 T for 900°C. The coercivity shows a more marked dependence on annealing temperature with a peak value of 835 kAm^{-1} being achieved at 750°C. $(BH)_{max}$, as expected, follows a similar pattern to J_r with a maximum of 150 kJm^{-3} at 700°C and decreasing to 36 kJm^{-3} at 900°C. The results for d_g determined by the two methods are plotted in Figure 4-39d. They are in reasonably good agreement for temperatures up to 750°C with the minimum d_g corresponding approximately to the maximum in J_r and $(BH)_{max}$. For annealing temperatures beyond 750°C, there is increasing divergence between the d_g determined by XRD and TEM methods. It should be bore in mind that XRD line broadening analysis becomes increasingly unreliable for $d_g \geq$ 70-80 nm and is not viable in most cases for $d_g \geq 100$ nm.

Representative hysteresis loops for the as-spun sample and for those annealed for 4 minutes at various annealing temperatures are shown in Figure 4- 40. The very low, but finite, coercivity for the as-spun sample shows that the ribbon is not completely amorphous and that bulk crystallisation was initiated during spinning. Devitrification at 600°C increases both J_r and $_jH_c$ considerably and they continue to increase through 650 and 700°C. However, while $_jH_c$ continues to rise between 700°C and 750°C, J_r begins to decrease. This is accompanied by an observed increase in d_g from 26 nm to 31 nm for these temperatures.

Fine $Nd_2Fe_{14}B$ grains (~20 nm) shown in Figure 4- 41a are dominant for the stoichiometric ribbon melt spun at 26 m/s and annealed for 4 minutes at 700°C. The grain morphology, which is more clearly seen in the magnified micrograph of Figure 4- 41b, is similar to those observed for directly quenched samples. As can be seen, some block shaped grains, and a much larger d_g are developed at samples annealed in higher temperatures (850°C), Figure 4- 41c.

Figure 4- 42 shows X-ray diffraction traces for $Fe_{82.3}Nd_{11.8}B_{5.9}$ ribbons spun at 26 m/s and annealed at various temperatures. The spectrum for the as spun sample shows that it is largely amorphous; however, the existence of peaks indicates that ribbon contains some crystalline $Nd_2Fe_{14}B$ phase. The development and growth of the $Nd_2Fe_{14}B$ peaks through annealing at 550°C and higher temperatures can be seen in this Figure.

4.3.2 Ga Addition in Stoichiometric Alloy, $Fe_{82.3-x}Nd_{11.8}B_{5.9}Ga_x$

The effect of Ga concentration on the magnetic properties of $Fe_{82.3-x}Nd_{11.8}B_{5.9}Ga_x$, over quenched at 26 m/s and annealed for 4 minutes at 700°C is shown in Figure 4-43. The remanence, in general remains constant at ~0.97 T, within experimental uncertainty, up to ~1.5 at.% Ga and then decreases slightly to 0.94 T for 3 at.% Ga. However, ${}_jH_c$ increases slightly up to 2 at.% Ga at which it has a maximum value of 1000 kAm^{-1}. Beyond 2 at.% Ga, ${}_jH_c$ gradually decreases. The dependence of $(BH)_{max}$ on Ga content, as expected, largely reflects that for J_r being constant at ~150 kJm^{-3} up to 1 at.% Ga and then decreasing steadily down to 125 kJm^{-3} for 3 at.% Ga, Table 4-5.

Representative hysteresis loops for $Fe_{82.3}Nd_{11.8}B_{5.9}$ and $Fe_{80.3}Nd_{11.8}B_{5.9}Ga_2$ ribbon samples melt spun at 26 m/s and annealed for 4 minutes at 700°C are shown in Figure 4- 44. The somewhat lower remanence and the higher coercivity for the 2 at.% Ga alloy are clearly evident.

The TEM bright field image for $Fe_{80.3}Nd_{11.8}B_{5.9}Ga_2$ melt spun at 26 m/s and annealed at 700°C for 4 minutes, shown in Figure 4- 45, features single phase $Nd_2Fe_{14}B$ nanosize (~ 25 nm) grains, similar to those observed for ternary directly quenched and over quenched and annealed ribbons.

The effect of Ga content on the magnetic properties of $Fe_{82.3-x}Nd_{11.8}B_{5.9}Ga_x$ ribbon samples, prepared by optimum direct quenching are compared with those prepared by over quenching and optimum annealing in Figure 4- 46. The trend of changes in properties caused by the presence of Ga and their absolute values are broadly similar,

within the limits of experimental uncertainty. However, some significant differences exist. The maximum values for J_r and $(BH)_{max}$, were slightly larger for the directly quenched samples and were achieved at higher Ga content (1.5 vs 1.0 at.%) than for the overquenched/annealed samples. However, the maximum $_jH_c$ was larger for the overquenched/annealed samples, although the maxima occurred at the same Ga content (2 at.%) in the two cases.

4.3.3 Ga Addition in 9%Nd Alloy, $Fe_{85.1-x}Nd_9B_{5.9}Ga_x$

In order to find the best annealing temperature, over quenched $Fe_{85.1}Nd_9B_{5.9}$ ribbons, melt spun at 26 m/s, were annealed for 4 minutes at various temperatures in the range 550-850°C. The magnetic properties of samples from each batch were measured by VSM and the mean grain size was examined by X-ray diffraction line broadening. The results are plotted against annealing temperature in Figure 4- 47. As may be seen, J_r increases from 0.78 T for 550°C and reaches an impressive maximum value of 1.04 T for temperatures in the range 700-750°C then decreases with further increase in temperature down to 0.98 T for 900°C. $_jH_c$ increases with annealing temperature to a maximum of 434 kAm^{-1} at 750°C, beyond which it decreases quite rapidly. $(BH)_{max}$ values are rather modest in spite of the good enhancement of J_r, reflecting both the rather low $_jH_c$ and the relatively "flat" second quadrant loop shape. The maximum $(BH)_{max}$ of 112 kJm^{-3} achieved at 750°C is disappointing. Figure 4- 47d do not show significant change in the mean $Nd_2Fe_{14}B$ and α-Fe grain sizes between 600 and 750°C, at which the maximum J_r and $(BH)_{max}$ were achieved.

TEM examination of $Fe_{85.1}Nd_9B_{5.9}$ alloy ribbon melt spun at 26 m/s and annealed at 700°C for 4 minutes showed that the microstructure of a sample with average magnetic properties consisted of areas of fine $Nd_2Fe_{14}B$ (~37 nm) and α-Fe (~20 nm) grains (Figure 4- 48a) and also areas of coarse $Nd_2Fe_{14}B$ (~120 nm) and α-Fe (~110 nm) grains (Figure 4- 48b). Coarse grains especially for α-Fe phase seems to be responsible for low $_jH_c$ and $(BH)_{max}$ in these alloys. However, large areas of $Nd_2Fe_{14}B$/α-Fe composite structure having uniform grain sizes were observed for a sample from the same batch but having higher magnetic properties of J_r=1.1 T,

$_jH_c$=500 kAm^{-1} and $(BH)_{max}$=147 kJm^{-3} (Figure 4- 49a). The nanostructure of this ribbon, with mean $Nd_2Fe_{14}B$ and α-Fe grain sizes of ~45 nm and ~30 nm, is more clearly seen at higher magnification in Figure 4- 49b; which is similar to directly quenched ribbons.

X-ray diffraction traces of $Fe_{85.1}Nd_9B_{5.9}$, melt spun at 26 m/s and annealed for 4 minutes at different temperatures are shown in Figure 4- 50. The weak $Nd_2Fe_{14}B$ and α-Fe reflections for the as spun ribbon, on the amorphous phase background are enhanced with increasing annealing temperature as devitrification proceeds and the crystallisation would appear to be complete at 700°C.

The magnetic properties and mean grain sizes as a function of Ga content for $Fe_{85.1-x}Nd_9B_{5.9}Ga_x$, over quenched at 26 m/s and annealed for 4 minutes at 750°C, are plotted in Figure 4- 51. J_r does not change significantly with Ga content with a value of ~1 T. $_jH_c$ increases slightly from 434 kAm^{-1} for the ternary alloy to 453 kAm^{-1} for the 3 at.% Ga sample. $(BH)_{max}$ increases very slightly, from ~110 kJm^{-3} for the ternary alloy to 115 kJm^{-3} for 3 at.% Ga ribbon in spite of the constant J_r, Table 4- 6. The low values of $(BH)_{max}$, in spite of the substantially enhanced J_r and the slight increase in $_jH_c$, suggest that it is principally the poor loop shape that result in the modest values of $(BH)_{max}$ (Figure 4- 52) with probably a contribution also from the rather low $_jH_c$. From Figure 4- 51d it appears that Ga content has no significant effect on the mean $Nd_2Fe_{14}B$ and α-Fe grain sizes. Representative hysteresis loops of Figure 4- 52 for $Fe_{85.1}Nd_9B_{5.9}$ and $Fe_{82.1}Nd_9B_{5.9}Ga_3$ melt spun at 26 m/s and annealed for 4 minutes at 750°C show no significant changes in the demagnetising curve as a result of Ga substitution.

Areas of fine mixture of $Nd_2Fe_{14}B$ (~25 nm) and α-Fe (~16 nm) grains (Figure 4- 53a) and areas of coarse $Nd_2Fe_{14}B$ (~80 nm) and α-Fe (~70 nm) grains (Figure 4- 53b) were observed for $Fe_{82.1}Nd_9B_{5.9}Ga_3$ ribbon, melt spun at 26 m/s and annealed for 4 minutes at 750°C. No obvious change is observed in the microstructure of this sub-stoichiometric alloy as the result of the presence of Ga.

X-ray diffraction traces for $Fe_{85.1-x}Nd_9B_{5.9}Ga_x$ ribbons melt spun at 26 m/s and annealed for 4 minutes at 700°C is given in Figure 4- 54.

The effects of Ga additions on the optimum magnetic properties of low Nd alloy, $Fe_{85.1-x}Nd_9B_{5.9}Ga_x$, for two processing routes, i) directly quenched and ii) overquenched and annealed are compared in Figure 4- 55. All these properties, J_r, $_jH_c$ and $(BH)_{max}$, are clearly inferior for overquenched and annealed ribbons compared with the corresponding values for the direct quenching route (with the exception of J_r for the ternary alloy, for which the difference is apparently smaller).

Representative hysteresis loops for samples prepared by each of these methods are presented in Figure 4- 56. It may be observed that the directly quenched sample has higher intrinsic coercivity and closer to ideal shape (i.e. square shape) of second quadrant which leads to higher $(BH)_{max}$.

The effects of roll speed during quenching on the final magnetic properties of overquenched and optimally annealed $Fe_{82.3}Nd_{11.8}B_{5.9}$, $Fe_{79.8}Nd_{11.8}B_{5.9}Ga_{2.5}$ and also $Fe_{85.1}Nd_9B_{5.9}$ alloys are shown in Figure 4- 57. There is no significant difference between the magnetic properties of annealed ribbons melt spun at 26 m/s and those for ribbons spun at higher speeds, excepts perhaps for slightly increased $(BH)_{max}$ at the higher speed for the $Fe_{79.8}Nd_{11.8}B_{5.9}Ga_{2.5}$ and $Fe_{85.1}Nd_9B_{5.9}$ ribbons.

Figure 4- 58 shows X-ray diffraction traces indicating the effect of roll speed on the initial state of the ribbon for the stoichiometric ternary alloy. As can be seen, samples melt spun at 22 m/s (and lower) are crystalline whereas those spun at 26 m/s are mostly amorphous, with only a few small peaks representative of a small fraction of crystalline phase. Samples melt spun at 35 m/s show no peaks and are considered to be completely amorphous.

The microstructure of $Fe_{82.3}Nd_{11.8}B_{5.9}$ ribbon, melt spun at 40 m/s and annealed at 650°C for 4 minutes and consisting of $Nd_2Fe_{14}B$ grains with d_g ~27 nm, is shown in the TEM bright field image of Figure 4- 59a. Figure 4- 59b shows a region of coarser $Nd_2Fe_{14}B$ grains (~43 nm) for the same TEM foil.

4.4 Other Observations

Figure 4- 60 presents TEM bright field images for a single foil sample of $Fe_{85.1}Nd_9B_{5.9}$ alloy ribbon melt spun at 26 m/s and annealed for 4 minutes at 600 °C.

As can be seen, a wide range of grain sizes, from ~30 nm to ~300 nm for $Nd_2Fe_{14}B$ and ~15 nm to ~200 nm for α-Fe, are present over distances of a few microns in this thin foil. The grain morphologies also vary, from a fine mixture of polygonal $Nd_2Fe_{14}B$ and α-Fe grains to a petal shaped structure.

"Petal" shape structures are observed in coarse grained areas of sub-stoichiometric alloy ribbons up to 10.9 at.% Nd, which is close to the stoichiometric composition. The TEM bright field image in Figure 4- 61a shows such a structure for a $Fe_{83.2}Nd_{10.9}B_{5.9}$ ribbon melt spun at 20 m/s. Figure 4- 61b shows the micro-diffraction pattern for an α-Fe particle surrounding the $Nd_2Fe_{14}B$ grain. An indexed schematic of this diffraction pattern is produced in Figure 4- 61c.

In addition to gradual changes in the grain size such as those presented in Figure 4- 10 and Figure 4- 60, very coarse grains were also observed adjacent to very fine grains in some areas of several TEM foil samples. In Figure 4- 62a some very large $Nd_2Fe_{14}B$ grains of diameter ~1 μm are in the vicinity of fine grains having d_g~23 nm in a $Fe_{82.3}Nd_{11.8}B_{5.9}$ ribbon melt spun at 20 m/s. Coarse mixture of $Nd_2Fe_{14}B$ (d_g ~155 nm) and α-Fe (d_g ~90 nm) grains and a very large α-Fe particle at the top right hand corner of Figure 4- 62b are observed adjacent to a nanocomposite matrix of $Nd_2Fe_{14}B$ (d_g~30 nm) and α-Fe (d_g~19 nm) for a $Fe_{85.1}Nd_9B_{5.9}$ alloy melt spun at 22 m/s. Some coarse $Nd_2Fe_{14}B$ grains of diameter ~105 nm were observed within fine two phase mixtures of $Nd_2Fe_{14}B$ (d_g~22 nm) and α-Fe (d_g~17 nm) for a $Fe_{84.1}Nd_9B_{5.9}Ga$ alloy ribbon melt spun at 22 m/s, Figure 4- 62c. Such coarse structures are probably associated with areas of gas pockets on the roll contact surface in which the rate of heat transfer to the roll surface is, locally, drastically reduced.

The overquenched stoichiometric ribbons annealed at 800°C contained some slab shaped grains, Figure 4- 63a, b. The number of observed grains of this type increased on annealing at higher temperature (850°C), Figure 4- 63c. The same feature was sometimes observed in directly quenched $Fe_{85.1}Nd_9B_{5.9}$ ribbons, e.g. Figure 4- 63d for a sample spun at 22 m/s. The arrow beneath this picture, derived from superimposing the diffraction pattern from the dark grain on the bottom left side (after rotational corrections), shows that the [001] direction is perpendicular to the

length of the elongated grain, i.e. elongation occurs along the direction of fastest growth [100]/[010] as observed for dendrites on cast ingots.

In addition to polygonal shaped $Nd_2Fe_{14}B$ grains, such as those observed for ternary alloys, ribbons of Ga containing alloys may also contain some spherical shaped $Nd_2Fe_{14}B$ grains with semicontinuous α-Fe phase around them. These two types of grain morphology are shown for a $Fe_{82.6}Nd_9B_{5.9}Ga_{2.5}$ alloy ribbon melt spun at 21 m/s in Figure 4- 64a and b. Both these pictures are magnified areas of Figure 4- 64c. The coexistence of these grain morphologies can be seen in the latter.

Figure 4- 65a shows spherical grains of $Nd_2Fe_{14}B$ phase, which were also found in $Fe_{83.6}Nd_9B_{5.9}Ga_{1.5}$ ribbons. Spherical grains were also observed occasionally for substoichiometric ternary alloys. Figure 4- 65b features such grains for a $Fe_{85.1}Nd_9B_{5.9}$ alloy ribbon. Both samples were melt spun at 22 m/s. The reason for the formation of such a structure is unclear.

4.4.1 Orientation Relationship Between $Nd_2Fe_{14}B$ Matrix and α-Fe Precipitates

Finer spaced $Nd_2Fe_{14}B$ (ϕ) diffraction spots and brighter α-Fe spots are seen in superimposed diffraction patterns of Figure 4- 66a taken from a thin TEM sample of a $Fe_{80.2}Nd_{10.9}B_{5.9}Ga_3$ alloy ribbon, melt spun at 4 m/s (deliberately low to yield coarse grains). The indexed schematic of these diffraction patterns is shown in Figure 4- 66b. The orientation relationship between these two phases can be shown to be 209:

$$[001]_{\phi} \,||\, [1\bar{1}\bar{1}]_{\alpha\text{-Fe}} \qquad \text{and} \qquad (110)_{\phi} \,||\, (101)_{\alpha\text{-Fe}}$$

The diffraction pattern in Figure 4- 67a, also shows that the [010] zone axis for $Nd_2Fe_{14}B$ is almost parallel to the $[\bar{1}\bar{3}5]$ zone axis for the α-Fe. Also diffraction pattern in Figure 4- 67b shows that the $[\bar{1}11]$ zone axis for $Nd_2Fe_{14}B$ is almost parallel to the $[\bar{3}2\bar{1}]$ zone axis for the α-Fe phase.

Bright α-Fe precipitates of identical brightness in the dark field TEM micrograph shown in Figure 4- 67c, taken from the same ribbon sample, using the (110) diffraction spot of α-Fe, indicate that these precipitates have identical orientation.

4.4.2 Additional Phases in $Fe_{85.1}Nd_{10.9}BGa_3$ Alloy Ribbons

In an attempt to investigate possible extra phases present in samples containing higher amounts of Ga, $Fe_{80.2}Nd_{10.9}B_{5.9}Ga_3$ alloy was melt spun at 4 m/s. In addition to $Nd_2Fe_{14}B$ and α-Fe, two new phases were observed in the form of precipitates within large $Nd_2Fe_{14}B$ grains, often adjacent to each other, top right and bottom left corners of Figure 4- 68a. One area is magnified in Figure 4- 68b. Fine stripes are evident in phase A and some bands are observed in phase B. The fine modulated structure within phase A is shown more clearly in the bright field and dark field images of Figure 4- 68c and d, respectively. Four fold symmetry in the convergent beam diffraction pattern of phase A could be either from a cubic or tetragonal structure, Figure 4- $69a_1$. From the nanodiffraction patterns, Figure 4- $69a_1$, a_2 and a_3, and the $1/d^2$ ratios of Table 4- 7, a body centred cubic (b.c.c.) structure with a lattice parameter a_o= 0.7255 nm or a tetragonal structure with lattice parameters of: a=0.5130 nm and c= 0.7246 nm can be suggested for phase A. Orthogonal (90°) arrays of spots in the micro diffraction pattern of Figure 4- $69b_3$, suggest a cubic, tetragonal or orthorhombic structure for phase B [210]. EDS analysis of these phases gives the approximate chemical composition of 77 at.% Fe, 22.8 at.% Nd and 0.2 at.% Ga for phase A and 8.7 at.% Fe, 63.4 at.% Nd and 27.9 at.% Ga for phase B, bearing in mind that boron (B) does not appear in EDS analysis (Figure 4- 70 and Figure 4- 71).

Features, having the characteristics of dislocations, were observed occasionally within coarse $Nd_2Fe_{14}B$ grains in various alloy ribbon samples. In the TEM bright field (BF) image of Figure 4- 72a for a $Fe_{83.2}Nd_{10.9}B_{5.9}$ ribbon melt spun at 23 m/s, such features are seen in the large $Nd_2Fe_{14}B$ grain in the both ends of the α-Fe precipitate (arrowed). Weak beam dark field (WBDF) image for a $Fe_{82.3}Nd_{11.8}B_{5.9}$ ribbon sample melt spun at 26 m/s and annealed for 4 minutes at 800°C, also contain such features (Figure 4- 72b). TEM bright field (BF) image for a $Fe_{83.2}Nd_{10.9}B_{5.9}$

ribbon melt spun at 23 m/s, Figure 4- 72c, contains some needle shape features lying in the (001) plane of the $Nd_2Fe_{14}B$ grain. Figure 4- 72d, taken at higher magnification, contains such features and parallel (001) lattice fringes.

A High Resolution Electron Micrograph for a $Fe_{83.2}Nd_{10.9}B_{5.9}$ ribbon sample melt spun at 23 m/s shows one of these needles (Figure 4- 73). An optical diffraction pattern shown in Figure 4- 74 was used to index this HREM micrograph. Although the exact nature of this feature is not yet known, the closure failure around this feature clearly shows the presence of two extra $(\bar{1}10)$ half planes and two extra (101) half planes.

5. Discussion

5.1 Effect of Roll Speed on Thickness, Microstructure and Magnetic Properties of Directly Quenched Ribbons

For Nd-Fe-B alloys produced under constant melt spinning conditions, a decrease in ribbon thickness leads to an increase in cooling rate, and thus to a refinement of mean grain size d_g [211, 212]. Figure 4- 12 and Figure 4- 13 show the ribbon thickness and grain size as a function of roll speed for $Fe_{83.2}Nd_{10.9}B_{5.9}$, where it is observed that both the ribbon thickness and d_g are reduced with increasing roll speed. In fact, increasing the roll speed leads to increased cooling rate of the melt, both because of a change in ribbon thickness and because of an increase in the interfacial heat transfer coefficient since the higher is the roll speed, the more frequently any point on the roll surface encounters the melt and hence the hotter it runs at its surface [213]. The higher the cooling rate, the greater the undercooling (for a constant number density of heterogeneous nucleants) and hence the higher the nucleation frequency and thus the finer the crystallite diameter (i.e. the smaller is d_g). The mean grain size adjacent to the roll contact surface of the ribbon tends to be slightly smaller than that adjacent to the free side, because the cooling rate is higher at smaller distances to the heat sink for non-Newtonian cooling conditions. As the roll speed increases to 23 m/s the ribbon is beginning to vitrify, and so it may be concluded that, for this composition under chosen melt spinning conditions (chapter 3), the optimum roll speed for minimising the crystallite size is 22 m/s. Ribbons spun at this speed had a thickness of around 34 μm in the present study and a grain size of the order of 30 nm.

Figure 4- 14 shows d_g as a function of ribbon thickness for $Fe_{83.2}Nd_{10.9}B_{5.9}$ melt spun at different roll speeds. A thinner ribbon provides a higher cooling rate throughout the ribbon's thickness and creates smaller and more uniform grain size. The fact that the thickness is not uniform and varies significantly along both the

length and the width of the ribbon, and therefore do the cooling rate and d_g, could largely explain the scatter in the data.

For the majority of directly quenched ribbons examined by TEM, large ranges of local grain sizes were present, even within the very small, electron transparent, region of the TEM foil. However, it must be noted that there is the tendency for TEM samples to have disproportionately large regions of larger grains, due to the fact that the ribbon will be thinner at these points, and thus it will tend to perforate first adjacent to these larger grains during sample preparation. Thus, the volume fraction of larger grains is usually smaller than apparent by TEM investigations as compared to the mean grain sizes estimated by XRD line broadening. The d_g for optimally quenched ribbons were in general of the order of ~30 nm; however, nearly always areas were observed within these ribbons with significantly larger grains, often up to ~100 nm in diameter, and sometimes up to ~300 nm. Wecker and Schultz [212] also comment that, even in optimally quenched ribbon, they observe a large range of grain sizes. In $Nd_{15}Fe_{77}B_8$ alloy ribbons they observe $Nd_2Fe_{14}B$ grains in the centre of the ribbon ranging between 20 and 200 nm, and at the free surface, which has experienced lower quenching rates, some grains are up to 500 nm in diameter. Koestler et al. [121] also observe grains in $Nd_{15}(Fe_{1-x}Co_x)_{77}B_8$ alloys ranging from 40 to >300 nm.

Figure 4- 15 shows that as the roll speed increases (i.e. the ribbon thickness and the mean grain size decrease) the magnetic properties, J_r, $_jH_c$ and $(BH)_{max}$ are improved and all reach optimum values at 22 m/s. It should be noted that at higher speeds (>20 m/s), J_r is larger than that predicted by the Stoner-Wohlfarth theory [14] for an assembly of uniaxial non-interacting grains which, for stoichiometric Nd-Fe-B would be 0.8 T, given that J_s=1.6 T. This increase may be attributed to the fact that as the roll speed increases, d_g is refined and, as can be seen in Figure 4- 13, the mean grain size of ribbons spun at 22 m/s has a close range of about 30 to 40 nm throughout the thickness which provides the necessary condition for remanence enhancement through exchange interaction between $Nd_2Fe_{14}B$ grains.

Croat et al. [2, 211] demonstrated that both $_jH_c$ and $(BH)_{max}$ increased steeply with increasing roll speed, which they attributed to a progressively decreasing grain size

resulting from the increased cooling rate. This behaviour occurred up to a maximum point, where the alloy began to become amorphous, and beyond this point the properties then decreased with roll speed, as the alloy contained a progressively increasing amount of amorphous phase. Enhanced remanence, $J_r > J_s/2$, is observed for the smaller grain sizes, ~35 nm, and the attainment of values of J_r which are greater than $J_s/2$ is in agreement with the results obtained by Manaf et al. [10] for single phase $Nd_2Fe_{14}B$. However, the studies of Croat et al. were not undertaken in sufficient detail in the critical range for exchange enhancement to gain a clear perspective on the influence of roll speed on $_jH_c$.

Figure 4- 10 illustrates the range of grain sizes found within one individual ribbon of $Fe_{79.8}Nd_{11.8}B_{5.9}Ga_{2.5}$ melt spun at 21.5 m/s. Ribbons from this particular batch nominally had d_g of ~28 nm as estimated by x-ray diffraction line broadening analysis; however, the micrographs for this ribbon show grains ranging in diameter from less than 13 nm (Figure 4- 10a) up to ~170 nm (Figure 4- 10f), a diameter more than 10 times larger. Given that the magnetic properties in melt spun ribbons are, to some extent, grain size dependent, this range of grain size may account for some of the scatter of the values for magnetic properties of ribbons which are nominally the same, i.e. of the same thickness and composition and produced under the same conditions. This range in grain size is indicative of variable cooling rates, and probably related to locally varying thickness of the ribbon. For this reason the reported ribbon thickness, although measured relatively accurately, is not always representative of the true local thickness of the ribbon, and thus is not a completely reliable guide to the mean cooling rate of the ribbon. In addition, longer range variations in thickness also occur. SEM micrograph of Figure 4- 9, showing a transverse cross section of $Fe_{83.2}Nd_{10.9}B_{5.9}$ alloy melt spun at 19 m/s, confirms this by showing the variation in ribbon thickness that can occur, in this case an increase of about two fold, over a relatively short distance. The very large variation in grain size observed by TEM may not be entirely due to a variation in overall thickness but rather to problems with local gas pockets and the tendency to perforate first at these pockets in TEM sample preparation where the grain size can be substantially coarser. Thus, it is not surprising to find grains of significantly different dimensions within one ribbon, especially if it has a profile such as that shown in Figure 4- 9.

It is also should be borne in mind that, for short melt spinning runs of the order of grams of melt without internal water cooling of the roll, steady state conditions are not achieved and hence ribbons from the initial part of a run will tend to have undergone solidification at a lower cooling rate and thus have a larger mean grain size than material quenched in the latter part of the run. This is in addition to any variations arising from the presence of gas pockets on the roll contact side of the ribbon.

5.2 Effect of Annealing Temperature on Grain Size and Magnetic Properties of Over-quenched Stoichiometric Alloy

The X-Ray diffraction traces of Figure 4- 42 confirm the evolution of the structure for stoichiometric ribbons for various heat treatment temperatures. It is evident that, ribbon heat treated for 4 minutes at 600°C is strongly crystalline but, on the other hand, the magnetic property measurements (Figure 4- 39) show that some untransformed amorphous phase, probably as a thin layer at the grain boundaries, is still present since J_r, $_jH_c$ and $(BH)_{max}$ are low. The best magnetic properties, suggesting complete recrystallisation, was realised for samples annealed at 700°C. The d_g remains almost unchanged up to 750°C but increases at higher temperatures.

Wecker and Schultz [212] reported that $_jH_c$ values for Nd rich alloys obtained through crystallisation of amorphous ribbons did not significantly depend on annealing temperature in the range 630 to 700°C, but more crucially on the composition.

Davies et al. [145] report that for $Nd_{14.2}Fe_{77.9}B_{7.8}$, after an initial increase, corresponding to the devitrification process at 700°C, the mean grain size of $Nd_2Fe_{14}B$ remains almost independent of annealing time, at least up to 30 minutes. Cochet-Munchy and Paidassi [214] also noted that , for longer annealing times for $Nd_2Fe_{14}B$ based alloys, the increase in grain size was relatively shallow, but nevertheless, they concluded that long annealing times should be avoided, since the

ribbon surfaces are very reactive towards oxygen at typical heat treatment temperatures. Thus, minimising the heat treatment time, and ensuring an oxygen free environment reduces the possibility of forming magnetically soft surface layers (neodymium oxides and α-Fe).

5.3 Effect of Nd Content on Hysteresis Loop

The results obtained for the effects of varying the Nd concentration on the microstructure and magnetic properties are in agreement with the published data by Manaf et al. [11]. As the Nd level in the alloy is decreased, there is surplus Fe, and so a two phase structure of $Nd_2Fe_{14}B$ and α-Fe is formed. The soft magnetic α-Fe has a saturation polarisation of ~2.2 T, whilst that of the hard magnetic $Nd_2Fe_{14}B$ phase is ~1.6 T. Thus, by increasing the proportion of α-Fe in the alloy, J_s is increased, and consequently the value of J_r for the alloy is also increased. For the stoichiometric alloys, a saturation of 1.6 T would be predicted. The 9%Nd alloy (i.e. $Nd_9Fe_{85}B_6$) has between 20 and 26 (~23) volume% of α-Fe [215], and so this value would be increased to ~1.74 T, and to ~ 1.84 T for the 7%Nd series, where there is estimated to be ~40 volume% α-Fe present. Thus the threshold value of J_r for enhanced remanence should be ~0.87 T for 9%Nd alloys, and ~0.92 T for 7%Nd alloys. Manaf et al. [114] showed that the $(BH)_{max}$ closely mirrors the behaviour of J_r initially; however, the presence of the soft magnetic α-Fe phase within the alloy causes a decrease in the coercivity and at high volume fraction of the α-Fe, the decrease in $_jH_c$ becomes so large that it leads to a non-linear B-H characteristic, so that in spite of the high J_r, $(BH)_{max}$ is reduced Figure 2- 27.

Representative hysteresis loops for stoichiometric, 9%Nd and 7%Nd are plotted in Figure 4- 22. It may be observed that the highest value of J_r (1.15 T) is attained for the alloy with the lowest Nd level, 7%Nd. Conversely, for $_jH_c$ the highest value (800 kAm^{-1}) is observed in the stoichiometric alloy, and the value decreases with decreasing concentration of Nd in the alloy, and thus is lowest (318 kAm^{-1}) for the 7%Nd alloy. It is noted that for all these alloys enhanced remanence is observed as a consequence of the nanocrystalline structure but that the presence of nanoscale α-Fe grains (~15 nm) further enhances J_r since they are completely coupled to their

neighbouring $Nd_2Fe_{14}B$ grains and have a larger J_s than the latter [13]. This enhancement of the remanence also contributes to increasing $(BH)_{max}$.

The X-Ray diffraction traces of Figure 4- 23 confirm the presence of the α-Fe in the sub-stoichiometric alloys. Although the α-Fe (110) peak partly overlaps with the $Nd_2Fe_{14}B$ (314) peak, its existence may be confirmed by comparing the ratio of the intensity of this peak with that of the $Nd_2Fe_{14}B$ (410) peak. For the sub-stoichiometric alloys this ratio is much higher, confirming the presence of the additional α-Fe peak in these alloys.

5.4 Effect of Ga Content on Magnetic Properties of Stoichiometric Alloy

Two separate routes were chosen to investigate of the effect of Ga substitution for Fe in $Fe_{82.3-x}Nd_{11.8}B_{5.9}Ga_x$ alloys; melt spinning at optimum conditions and overquenching and annealing. Processing parameters were carefully controlled to achieve nanostructured samples. As can be seen from Table 4- 2, the enhanced remanence of 0.95 T, ${}_jH_c$=800 kAm^{-1} and $(BH)_{max}$=150 kJm^{-3} were achieved for the ternary alloy (x=0) melt spun at 22 m/s. The data in Table 4- 5 show that similar values of J_r=0.97 T, ${}_jH_c$=810 kAm^{-1} and $(BH)_{max}$=150 kJm^{-3} are realised for the stoichiometric alloy through over-quenching at 26 m/s and annealing at 700°C for 4 minutes. As the processing parameters for the over-quench and anneal route are easier to control and the product is more consistent compared to single stage direct melt spinning route, achieving comparable, or even better magnetic properties for the former is very important. A typical microstructure for the directly quenched ternary alloy (x=0) is shown in Figure 4- 21c. The nanostructure of this ribbon consists of polygonal $Nd_2Fe_{14}B$ grains with a mean grain size of ~23 nm. No other phases were observed for this alloy. The dominant nanostructure for the same alloy prepared by the over-quench and anneal route is similar to this with a mean grain size of ~20 nm, Figure 4- 41a and b, consistent with the very similar magnetic properties.

Some investigators observed different magnetic properties for direct quenched and overquenched and annealed ribbons of the same composition. Jeung et al. [216] noted

that the magnetic properties of their heat treated ribbons were inferior to those ribbons optimally quenched from the melt and, even for the most favorable heat treatment (30 minutes, 800°C, for $Pr_{12.5}Fe_{80.5}B_{5.5}Zr_{1.5}$), they achieved $_jH_c$ of only 986 kAm^{-1} (c.f. 1225 kAm^{-1} by direct quenching) and $(BH)_{max}$=89 kJm^{-3} (c.f. 97 kJm^{-3} by direct quenching). Wecker and Schultz [212] also noted this difference. They reported that for $Nd_{15}Fe_{77}B_8$, the best properties were obtained at a temperature of 675°C, but even here $_jH_c$ was 1392 kAm^{-1}, compared with 1790 kA^{-1} for directly quenched material of the same composition.

The effect of Ga content on the magnetic properties of the $Fe_{82.3-x}Nd_{11.8}B_{5.9}Ga_x$ alloys melt spun at optimum conditions for a maximising J_r and $(BH)_{max}$ (directly quenched samples) are given in Figure 4- 24 and Table 4- 2. Corresponding data for overquenched and annealed samples are shown in Figure 4- 43 and Table 4- 5. Both sets of data are included and can be compared in Figure 4- 46. As can be seen in this figure, the values of the magnetic properties achieved for samples prepared by these two methods are the same, within experimental error, for the lower Ga concentrations but there is significant divergence beyond 1 at.% Ga, especially for $(BH)_{max}$.

J_r increases for directly quenched alloys by substituting Ga for Fe up to a maximum of 1.04 T for 1.5 at.% Ga and decreases for higher Ga contents down to 0.91 T for 3% Ga probably due partly to Ga being nonmagnetic and diluting the magnetic $Nd_2Fe_{14}B$ phase. For overquenched/annealed samples, J_r also increases initially but decreases more rapidly with further increase in Ga down to 0.89 T for 2 at.% Ga. $_jH_c$, remains remarkably constant within the range 800-835 with increasing Ga for both series of alloys except for a significantly larger value of 1000 kAm^{-1} for the OQ/anneal 2 at.% Ga sample. As expected, $(BH)_{max}$ follows partly the trend for J_r, the maximum value of 160 kJm^{-3} being achieved for the directly quenched sample containing 1.5 at.% Ga. Beyond 1.5 at.% Ga $(BH)_{max}$ decreases but the values for the OQ/anneal samples are significantly smaller than for the directly quenched samples in this range which reflects partly the lower J_r but also a somewhat poorer loop shapes for the former. This probably results from a broader grain size distribution.

Effect of gallium addition on the remanence and coercivity of directly quenched $Nd_{11.8}Fe_{82.36-x}B_{5.88}Ga_x$ ribbons together with those values obtained by Liu et al. [202]

for the same alloys melt spun at 20 m/s are compared in Figure 5- 1. These investigators found that the substitution of Ga for Fe in nanocrystalline melt spun stoichiometric alloys increases the coercivity to higher levels than those observed in this study up to 2 at.% Ga, while leading to a slow reduction of J_r without the maximum value observed at 1.5 at.% Ga in this study. The magnetic properties of J_r=0.98 T, $_jH_c$=1056 kAm^{-1} and $(BH)_{max}$=175 kJm^{-3} were realised for this composition. The combination of possible presence of second phase and the observed grain refinement was suggested to be responsible for these changes.

Representative hysteresis loops in Figure 4- 25 show the improved second quadrant for Ga substituted directly quenched alloys compared to ternary $Fe_{82.3}Nd_{11.8}B_{5.9}$ alloy, with higher J_r for $Fe_{80.8}Nd_{11.8}B_{5.9}Ga_{1.5}$ and higher $_jH_c$ for the $Fe_{80.3}Nd_{11.8}B_{5.9}Ga_2$ alloy. Representative hysteresis loops for overquenched and annealed $Fe_{82.3}Nd_{11.8}B_{5.9}$ and $Fe_{80.3}Nd_{11.8}B_{5.9}Ga_2$ are shown in Figure 4- 44. The lower remanence and higher coercivity for the 2 at.% Ga alloy are clearly evident, suggesting that the Ga enhances the anisotropy field for the $Nd_2Fe_{14}B$ phase.

Examination of many samples by TEM showed that no obvious changes in the nanostructure were observed with Ga substitution or production routes for stoichiometric i.e. 11.8 at.% Nd alloys. Figure 4- 26a shows a typical microstructure for the directly quenched stoichiometric alloy containing 1.5 at.% Ga. Figure 4- 26b is a typical microstructure for the directly quenched $Fe_{80.3}Nd_{11.8}B_{5.9}Ga_2$ alloy and Figure 4- 26c is taken from a region of slightly coarser grains of the same TEM sample. Comparing with the TEM micrograph for the directly quenched stoichiometric ternary alloy of Figure 4- 21c, it can be seen that the ternary and Ga containing alloys are all nanocrystalline, single phase, consisting of $Nd_2Fe_{14}B$ crystallites. Similar mean grain sizes of the order of ~23 nm, ~24 and ~21 nm are observed for the stoichiometric $Fe_{82.3}Nd_{11.8}B_{5.9}$, $Fe_{80.8}Nd_{11.8}B_{5.9}Ga_{1.5}$ and $Fe_{80.3}Nd_{11.8}B_{5.9}Ga_2$ alloy samples, respectively. The dominant nanostructure for the corresponding overquenched/annealed stoichiometric ternary alloy is similar to these, with a mean grain size of ~20 nm (Figure 4- 41a and b). Figure 4- 45 reveals the nanostructure for the overquench/anneal $Fe_{80.3}Nd_{11.8}B_{5.9}Ga_2$ alloy with a d_g of ~25 nm.

It has been reported in the literature that for a small addition of Ga, the coercivity usually increases for sintered as well as for melt spun alloys. Some investigators, especially for alloys containing high Nd contents, attributed this to the Ga role in decoupling the $Nd_2Fe_{14}B$ grains by modifying the Nd-rich grain boundary phase [183, 190, 191] or in forming new grain boundary phases [184, 185, 186, 187]. A grain refining effect is also reported by some investigators [110, 198, 202, 206]. Increases in remanence [110, 202, 201] and Curie temperature [168, 181] have also been observed in some cases.

According to Xie et al. [181], when the Ga content is low, Ga atoms preferentially occupy the K_2 sites of the $Nd_2Fe_{14}B$ structure which have the shortest Fe-Fe interatomic distance and thus the strongest negative exchange interaction. Therefore, the total exchange interaction of the compound will be drastically increased. Thus, better magnetic properties could be expected for small substitutions of Ga for Fe. The anisotropy field, was reported to increase and then to decrease with increasing Ga substitution which is consistent with the previous observations for the 2 at.% Ga alloy.

The magnetic properties versus ribbon thickness for $Fe_{82.3-x}Nd_{11.8}B_{5.9}Ga_x$ alloy ribbons directly quenched at optimum conditions are given in Figure 4- 27. Optimum properties are achieved in the range of between 26-38 μm thickness. Thicknesses below this range result in cooling rates that are sufficiently high to produce amorphous or partially amorphous material which has poorer properties. Larger thicknesses reduce the cooling rate and increase the grain size which, in turn, reduces J_r and ${}_jH_c$ and hence $(BH)_{max}$. The presence of significant scatter in these data is probably arises from the fact that the cooling condition are different at the start and end of each melt spinning run and also at midstream. This is more pronounced in laboratory conditions because only a small amount of sample (~7 g) is spun in each batch and steady state conditions for heat transfer are not achieved.

5.5 Effect of Ga Content on the Magnetic Properties of Substoichiometric Alloys

The effect of Ga content on the magnetic properties of $Fe_{85.1-x}Nd_9B_{5.9}Ga_x$ alloys melt spun at optimum conditions (i.e. to produce the best properties) is shown in Figure 4- 30 and Table 4- 4 and the corresponding effect on similar alloys, over quenched at 26 m/s and annealed for 4 minutes at 750°C, are plotted in Figure 4- 51 and Table 4- 6. A plot containing both sets of data is also given in Figure 4- 55. Large enhancements of J_r are achieved in the heat treated $Fe_{85.1}Nd_9B_{5.9}$ ribbons, (to around 1 T) which, is still lower than the ~1.1 T achieved for the directly quenched alloys of the same composition. However, the loop shapes of the majority of the heat treated ribbons were poor, Figure 4- 56, with relatively low values of ${}_jH_c$ (~430 kAm^{-1} compared to >500 kAm^{-1} for directly quenched samples), thus leading to poor values of $(BH)_{max}$, ~110 kJm^{-3}, compared with those for directly quenched ribbons of the same alloy, which were >150 kJm^{-3}.

Typical microstructure of over quenched and annealed substoichiometric ribbons were observed to be consist of areas of fine $Nd_2Fe_{14}B$ (~37 nm) and α-Fe (~20 nm) grains (Figure 4- 48a) and also areas of coarse $Nd_2Fe_{14}B$ (~120 nm) and α-Fe (~110 nm) grains (Figure 4- 48b). Coarse grains of magnetically soft α-Fe phase, in particular, facilitate the magnetisation reversal and reduced ${}_jH_c$ and $(BH)_{max}$. However, for a sample from the same batch but having higher magnetic properties of J_r=1.1 T, ${}_jH_c$=500 kAm^{-1} and $(BH)_{max}$=147 kJm^{-3}, similar to those for directly quenched ribbons, large areas of $Nd_2Fe_{14}B$/α-Fe composite structure having uniform grain sizes ($d_{g(\phi)}$=~45 nm and $d_{g(\alpha\text{-}Fe)}$=~30 nm) were observed (Figure 4- 49a and Figure 4- 49b) which are also similar to those observed for directly quenched ribbons in Figure 4- 32a ($d_{g(\phi)}$=~33 nm and $d_{g(\alpha\text{-}Fe)}$=~22 nm). Thus, achieving a uniform, nanosize mixture of $Nd_2Fe_{14}B$ and α-Fe phases seems to be the key for obtaining high ${}_jH_c$ and a good (close to ideal) second quadrant loop shape and therefore $(BH)_{max}$. As mentioned earlier, such structures were observe occasionally for over quenched and annealed ribbons and suitable dopants should be used to ensure it for

the majority of ribbons by providing nucleation sites and/or inhibiting grain growth during devitrification process.

Inoue et al. [217] heat treated $Nd_8Fe_{88}B_4$ between 1 and 5 minutes at 650-750°C, obtaining the best values of J_r=1.22 T, $_jH_c$=240 kAm^{-1} and $(BH)_{max}$=130 kJm^{-3}, the relatively low coercivity in this case being due to a higher volume fraction of α-Fe phase and resulting in a lower $(BH)_{max}$ than suggested by the high J_r obtained. It was observed that some untransformed phase was present in the alloy, which was suggested to be beneficial, since the disappearance of the amorphous phase by annealing for longer times, or at higher temperatures) led to grain growth of the α-Fe and $Nd_2Fe_{14}B$ Phases. It was proposed that this grain growth resulted in a decreased fraction of inter phase coupled material, and that this was responsible for the decreased J_r and $_jH_c$.

Panagiotopoulos et al. [198] found that, in samples of $Nd_{18}Fe_{76-x}Ga_xB_6$ alloys, overquenched at 60 m/s and subsequently annealed, gallium substitution for iron helps the formation of faceted fine (20 nm) $Nd_2Fe_{14}B$ grains, compared with coarser, equiaxed grains for ternary alloy samples which leads to lower coercivity. Branagan and McCallum [69] have shown that, with TiC addition to stoichiometric $Nd_2Fe_{14}B$ alloy, the properties of material crystallised from the glass can be significantly enhanced due to a combined effect of increases in the crystallisation temperature and inoculation of nucleation.

Goll and Kronmuller [136] found that the inferior hard magnetic properties of overquenched and annealed, exchange coupled, Pr ribbons improves significantly by addition of Zr. They attributed this to grain growth inhibition effects of precipitates formed in these alloys.

As can be seen in Figure 4- 55, for directly quenched alloys, J_r remains almost constant at around 1.1 T but slightly decreases to 1.01 T for the 3 % Ga sample. J_r does not change significantly with Ga content for overquenched and annealed alloys and is practically constant at around 1 T. For directly quenched alloys, $_jH_c$ increases slightly from 500 kAm^{-1} for the ternary alloy to a maximum of 536 kAm^{-1} at 1.5 % Ga before decreasing down to 503 kAm^{-1} for the 3 % Ga sample. $_jH_c$ for annealed

alloys starts at much lower value of 434 kAm^{-1} for the ternary alloy and increases slightly to 453 kAm^{-1} for the 3 at.% Ga sample. The maximum $(BH)_{max}$ value of 167 kJm^{-3} was achieved for the directly quenched sample containing 1.5 % Ga. $(BH)_{max}$ increases slightly for the overquenched and annealed ribbons, from 112 kJm^{-3} for the ternary alloy (compared to 152 kJm^{-3} for the directly quenched sample) to 115 kJm^{-3} for 3 at.% Ga substitution. These low values of $(BH)_{max}$, in spite of the substantially enhanced J_r, are mainly due to an inferior loop shape, indicative of rather coarse α-Fe grain size.

Liu et al. [202] found that the addition of Ga to nanocrystalline, directly quenched $Nd_9Fe_{85-x}B_6Ga_x$ increases the mean value of enhanced remanence up to 1 at.% Ga with the values in the range obtained in this study, while not significantly affecting the coercivity values, which were lower than those achieved in this study (Figure 5-2). They achieved J_r=1.2 T, $_jH_c$=440 kAm^{-1} and $(BH)_{max}$=160 kJm^{-3} for this composition. The J_r enhancement of Ga containing ribbons was considered to be due to increased exchange coupling resulting from grain refinement of $Nd_2Fe_{14}B$ grains and the presence of ultra fine α-Fe second phase grains.

Representative hysteresis loops for directly quenched $Fe_{85.1}Nd_9B_{5.9}$ and $Fe_{83.6}Nd_9B_{5.9}Ga_{1.5}$ alloys melt spun at 22 m/s and 21 m/s, respectively, are given in Figure 4- 31. The higher $_jH_c$ and larger surface area under the demagnetisation curve in the Ga containing alloy are obvious in this plot. Representative hysteresis loops of Figure 4- 52 for $Fe_{85.1}Nd_9B_{5.9}$ and $Fe_{82.1}Nd_9B_{5.9}Ga_3$ melt spun at 26 m/s and annealed for 4 minutes at 750°C are rather flat, i.e. lacking squareness, and show no significant improvement in the demagnetising curve as a result of Ga substitution.

The TEM bright field image in Figure 4- 32a shows the nanostructure of $Fe_{85.1}Nd_9B_{5.9}$ ribbon directly quenched at 22 m/s, consisting of a mixture of polygonal $Nd_2Fe_{14}B$ grains and α-Fe particles with mean grain size of ~33 nm and ~22 nm, respectively. The observed α-Fe morphology is changed from separate particles in fine grained areas to a continuous or semicontinuous phase at the grain boundary of the coarse $Nd_2Fe_{14}B$ grains, which were observed in few isolated areas, for the same sample (Figure 4- 32b). The nanostructure for directly quenched $Fe_{83.6}Nd_9B_{5.9}Ga_{1.5}$ alloy (Figure 4- 32c) contains smaller α-Fe particles, ~15 nm, than

for the corresponding ternary alloy (Figure 4- 32a), while the mean grain size for the $Nd_2Fe_{14}B$ phase is of the same order, ~32 nm. This finer distribution of α-Fe soft magnetic phase, could be responsible for the higher coercivity of this alloy compared to ternary alloy although Ga probably also results in increased an anisotropy constant of the $Nd_2Fe_{14}B$ phase. Areas of fine mixture of $Nd_2Fe_{14}B$ (~25 nm) and α-Fe (~16 nm) grains (Figure 4- 53a) and areas of coarse $Nd_2Fe_{14}B$ (~80 nm) and α-Fe (~70 nm) grains (Figure 4- 53b) were observed for $Fe_{82.1}Nd_9B_{5.9}Ga_3$ ribbon, melt spun at 26 m/s and annealed for 4 minutes at 750°C. As in the case of directly quenched samples some grain refinement is evident by TEM especially for α-Fe particles as a result of Ga substitution for Fe, although on the other hand, from Figure 4- 51d the XRD line broadening analysis indicates that the Ga content has overall, no significant effect on the mean $Nd_2Fe_{14}B$ and α-Fe grain sizes. No obvious change in the grain morphology is observed in the microstructure of this sub-stoichiometric alloy as the result of the processing route, i.e. direct quenching or overquenching and annealing except for coarser $Nd_2Fe_{14}B$ and α-Fe grains for the latter. The EDS spectra for a $Nd_2Fe_{14}B$ grain and an α-Fe particle in a $Fe_{83.6}Nd_9B_{5.9}Ga_{1.5}$ thin foil TEM sample shown in Figure 4- 33 indicates that the Ga (solid line trace) is mainly present in the $Nd_2Fe_{14}B$ grains, at least at this Ga concentration. The TEM micrograph in Figure 4- 34, taken at high magnification (×800000), features (001) lattice fringes for the $Nd_2Fe_{14}B$ grain in this sample. This reveals no precipitates and suggests therefore that all the Ga content is in solid solution in the $Nd_2Fe_{14}B$ phase.

In addition to polygonal shaped $Nd_2Fe_{14}B$ grains, such as those observed for ternary alloys, ribbons of Ga containing alloys may contain some spherical shaped $Nd_2Fe_{14}B$ grains with semicontinuous α-Fe phase around them. These two types of grain morphology are pictured for a $Fe_{82.6}Nd_9B_{5.9}Ga_{2.5}$ alloy ribbon, directly quenched at 21 m/s, in Figure 4- 64a and b. Both these micrographs are magnified sections of Figure 4- 64c. The coexistence of these two grain morphologies is seen in the latter in which the spherical $Nd_2Fe_{14}B$ grains occupy the bottom left hand section of the micrograph. Figure 4- 65a also shows spherical $Nd_2Fe_{14}B$ grains, which were observed in a $Fe_{83.6}Nd_9B_{5.9}Ga_{1.5}$ ribbon. Spherical grains were also observed occasionally for substoichiometric ternary (i.e. Ga free) alloys. Figure 4- 65b features such grains for a $Fe_{85.1}Nd_9B_{5.9}$ ribbon. Both samples were melt spun at 22 m/s. Ga

has been reported to decrease the surface energy and increase the "wettability" of the Nd rich grain boundary phase (in high Nd content alloys) [182, 190] although the true meaning of this term in the context of these two phase ($Nd_2Fe_{14}B$ and α-Fe) nanocomposite alloys is unclear. It would appear for the present observations that Ga has a tendency to increase the interfacial energy between $Nd_2Fe_{14}B$ crystals, which evidently form first, and the residual liquid phase which results in minimisation of the interfacial area, i.e. in spheroidal grains. The liquid phase then transforms into a semicontinuous layer of "intergranular" α-Fe phase, in contrast to the discrete particles of α-Fe interspersed between polygonal $Nd_2Fe_{14}B$ grains, as exemplified in for instance Figure 4- 64 and Figure 4- 32a. Although the sample ($Fe_{82.6}Nd_9B_{5.9}Ga_{2.5}$) shown in Figure 4- 64 containing spherical grains, had a good (close to ideal) loop shape and $(BH)_{max}$=189 kJm^{-3}, much higher than the average 165 kJm^{-3}, more TEM study is needed to draw a conclusion on the effect of grain morphology on magnetic properties of Ga containing substoichiometric alloys.

The effect of ribbon thickness on magnetic properties of $Fe_{85.1-x}Nd_9B_{5.9}Ga_x$ melt spun at optimum conditions can be seen in Figure 4- 35. The best properties are achieved in the range of 22-34 μm. There is considerably less scatter than was the case for the stoichiometric samples.

5.6 Effect of Roll Speed on Magnetic Properties of Overquenched and Annealed Ribbons

In order to investigate the effect of initial state of the ribbon dictated by the roll speed on the final magnetic properties, samples of stoichiometric alloy were spun at 35 and 40 m/s in addition to the samples spun earlier at 26 m/s. The x-ray diffraction traces in Figure 4- 58 show that ribbon spun at 35 m/s is fully amorphous, whilst that spun at 26 m/s is partly crystalline. The sample spun at the optimum speed of 22 m/s shows diffraction spectrum typical of fully crystalline $Nd_2Fe_{14}B$ single phase. J_r, $_JH_c$ and $(BH)_{max}$ for stoichiometric samples spun at 26, 35 and 40 m/s are presented in Figure 4- 57. As may be seen there is little change in property values with change in the initial roll speed. Samples of two other compositions, $Fe_{79.8}Nd_{11.8}B_{5.9}Ga_{2.5}$ and $Fe_{85.1}Nd_9B_{5.9}$, were also spun at 35 m/s and the magnetic properties are compared

with those of corresponding samples spun at 26 m/s in Figure 4- 57. These do indicate slight increase in J_r and $(BH)_{max}$ for the higher speed. Thus, it appears that the magnitude of the roll speed has either no effect or only a small effect on the best magnetic properties for a particular composition.

The microstructure of $Fe_{82.3}Nd_{11.8}B_{5.9}$ ribbon, melt spun at 40 m/s and annealed at 650°C for 4 minutes, consisting of $Nd_2Fe_{14}B$ grains with d_g~27 nm, is shown in the TEM bright field image of Figure 4- 59a. Figure 4- 59b is taken from a region of coarser $Nd_2Fe_{14}B$ grains (~43 nm) for the same TEM sample. Hence, it is apparent that even for a high roll speed, where the ribbon is cast into an apparently fully amorphous state, there is sufficient reduction in cooling rate adjacent to gas pockets to result in the formation of local crystal nuclei during the quench.

5.7 B-H relationship

It has been reported that overall there is an approximate inverse linear relationship between J_r and $_jH_c$ over a wide range of $_jH_c$, with a general pattern of enhancing one property at the expense of the other as the $Nd_2Fe_{14}B$ grain size [59] and/or the Nd:Fe ratio [114, 218] are changed. However, in the present study, it appears that, for near stoichiometric alloy ($Fe_{83.2}Nd_{10.9}B_{5.9}$), the enhancement or decrease of remanence resulting from a change in $Nd_2Fe_{14}B$ grain size is generally accompanied the same trend for the coercivity. $_jH_c$ is plotted against J_r for batches of $Fe_{83.2}Nd_{10.9}B_{5.9}$ ribbons melt spun at different roll speeds in Figure 4- 17. This direct as opposed to inverse relationship between $_jH_c$ and J_r is also evident in Figure 4- 28 and Figure 4- 36 for Ga containing alloys. It is not surprising that this is the case for the data for the substoichiometric nanocomposite alloy shown in Figure 4- 36 but the data for the single phase stoichiometric alloy in Figure 4- 28 run contrary the model conceived originally. The hysteresis loops in Figure 4- 18 and Figure 4- 40, for directly quenched and overquench and annealed samples, also indicate that coarser grains due to a lower roll speed or a higher annealing temperature, leads to both lower J_r and lower $_jH_c$. In these cases reducing the mean grain size by either melt spinning at higher roll speeds or annealing at lower temperatures improves both properties.

It is proposed that by decreasing the grain size to a nanoscale regime, the exchange alignment increases the remanence but at the same time tends to reduce the resistance to reverse magnetisation [110, 112]. On the other hand, as the grain size decreases the number of grain boundaries and thus, the number of pinning sites increases which, conventionally, increase the coercivity. Thus there may be two competing effects of decreasing the grain size which may influence the coercivity change differently in different alloys and for different processing routes.

Simultaneous increase of both J_r and $_jH_c$ with decreasing d_g has also been observed for nanocomposite ribbon of misch metal-iron-boron, by Dobson et al. [118] and of some ternary Nd-Fe-B alloys by Zhang and Davies [202] for the same batch of ribbons. Liu et al. [202] also observed that in Ga containing stoichiometric and substoichiometric melt spun Nd-Fe-B alloys both the remanence and coercivity increase together for ribbon samples of various thicknesses in any batch cast at a given velocity.

According to Schrefl et al. [113], the inhomogeneous ground state favours the nucleation of reversed domains leading to a reduction of the coercive field with decreasing grain size. The absolute value of the stray field reaches its maximum near grain boundary junctions of strongly misoriented grains. The increased stray fields considerably reduce the coercivity of nanocrystalline magnets with inhomogeneous grain structure. However, a uniform grain structure with a very small range in grain size avoids large demagnetising fields and thus preserves a high coercivity. They predicted that in order to achieve a significant enhancement of the remanence and to preserve a high coercive field in isotropic nanocrystalline $Nd_2Fe_{14}B$-based magnets, a mean grain size $d < 20$ nm and a homogeneous microstructure with a very small range in grain size are required.

5.8 Ribbon's Roll Contact Surface Condition

Gas pockets on the roll contact surface were observed for all the melt spun ribbons, regardless of the alloy composition and roll surface condition, Figure 4- 1. The only exceptions were those ribbons spun at very low speed of 8 m/s, Figure 4- 2,

and the samples melt spun in vacuum, Figure 4- 3. These pockets prevent the close contact between the ribbon and roll surface and thus impede the heat transfer from ribbon to roll surface, which is crucial to rapid solidification and can lead to regions of very coarse grains (Figure 4- 4) depending on the size and depth of the pocket.

Lower ambient argon gas pressure, or the use of a low atomic weight gas (such as helium) were reported [62, 63, 219] to lead to an improvement in the surface quality of the ribbons. Yapp et al. [64] also observed that quenching at a reduced pressure of argon (<0.5 atmosphere) leads to more uniform magnetic properties within ribbon segments and more consistent properties between ribbons for nanophase materials. They also noted that, consistent with the better magnetic properties, the grain size is consistently small and uniform in ribbons optimally quenched at 380 torr.

This supports the suggestion made by Matsuura et al. [65] and Luborsky et al. [66] for soft magnetic materials, that when the surface of the ribbon is of good quality (as a result of a low ambient gas pressure, or fabrication in helium) this leads to more uniform cooling. In ribbons fabricated at higher pressures (e.g. 760 torr argon), it had been speculated that coarse grains formed adjacent to gas pockets due to lower localised cooling rate, compared to area of ribbon in intimate contact with the substrate (roll surface). This is corroborated in the present study from Figure 4- 4.

5.9 Texture

Comparison of x-ray diffraction patterns for samples of a near stoichiometric alloy, melt spun at various roll speeds, reveals the presence of texture in the ribbons spun at very low roll speed of 4 m/s, with the c-axis (the easy magnetic direction) being perpendicular to the surface, Figure 4- 19. This was also reported in the studies of Wecker and Schultz [220], and of Ahmad [221] who noted that strong texture was generally observed on both the free and roll contact surfaces of the ribbons, produced at lower roll speeds. Tu et al. also [222] reported preferred orientation on the roll contact surface of ribbons for slow quenches (velocity<15 m/s), and Coehoorn and Duchateau [223] also found texture most pronounced at low roll speeds. It would follow in from this that individual ribbons which had some degree of texture present

would not have isotropic magnetic properties. However, in the present study, the majority of ribbons were spun at speeds sufficiently high to avoid strong preferred orientation, and the batches of ribbon were assumed to be isotropic. No property measurement were performed in a direction perpendicular to the plane of the ribbon for which there could be a large correction for self demagnetisation.

5.10 Orientation Relationship of α-Fe Precipitates and $Nd_2Fe_{14}B$ Grains

The selected area diffraction pattern in Figure 4- 66a shows combined diffraction patterns for $Nd_2Fe_{14}B$ and α-Fe precipitate for $Fe_{80.2}Nd_{10.9}B_{5.9}Ga_3$ alloy, melt spun at 4 m/s. The spots with the finer spacing belong to the $Nd_2Fe_{14}B$ (ϕ) phase and the brighter spots are due to the α-Fe phase. The diffraction vectors $[110]_{\phi}$ and $[101]_{\alpha\text{-Fe}}$ are also parallel in the two patterns so it follows that these two sets of planes are parallel. Therefore, the orientation relationship between these two phases is [209]:

$$[001]_{\phi} \,||\, [1\bar{1}\bar{1}]_{\alpha\text{-Fe}} \qquad \text{and} \qquad (110)_{\phi} \,||\, (101)_{\alpha\text{-Fe}}$$

It can be observed from the indexed schematic diffraction pattern in Figure 4- 66b that the (101) diffraction spot of α-Fe is superimposed on the (330) diffraction spot of $Nd_2Fe_{14}B$ phase. The d spacing of these two set of planes are almost identical and are 0.2027 nm and 0.2075 nm, respectively.

The diffraction patterns in Figure 4- 67a, also show that the [010] zone axis of $Nd_2Fe_{14}B$ is almost parallel to the $[\bar{1}35]$ zone axis of α-Fe precipitate and diffraction patterns in Figure 4- 67b show that the $[\bar{1}11]$ zone axis of $Nd_2Fe_{14}B$ is almost parallel to the $[\bar{3}2\bar{1}]$ zone axis of the α-Fe precipitate.

Figure 4- 67c is a dark field image of α-Fe precipitates in a very large $Nd_2Fe_{14}B$ grain in a $Fe_{80.2}Nd_{10.9}B_{5.9}Ga_3$ alloy ribbon, melt spun at 4 m/s. It was taken using a (110) reflection of the $[1\bar{1}\bar{1}]$ zone axis. It can be seen that α-Fe precipitates appear bright across this image which suggests that they have a common orientation. This

further supports the belief that the α-Fe precipitates have a discrete orientation relationship with the $Nd_2Fe_{14}B$ grains.

Fidler and Tawara [100] found 3 types of α-Fe in $Nd_{15}Fe_{77}B_8$ sintered magnets: a) separated α-Fe regions (<1 μm) at the 2-14-1 grain edges, the interiors of which, were heavily faulted and contained high densities of dislocations; b) α-Fe precipitates (up to 10 nm diameter) within individual 2-14-1 grains; in dark field electron micrographs, taken with the (011) reflection of iron phase, some of these precipitates are bright; c) individual 2-14-1 grains with high number densities of α-Fe precipitation.

5.11 Additional Phases in $Fe_{80.2}Nd_{10.9}B_{5.9}Ga_3$ Alloy Ribbons

In addition to $Nd_2Fe_{14}B$ and α-Fe, two new phases were observed in the $Fe_{80.2}Nd_{10.9}B_{5.9}Ga_3$ alloy, melt spun at 4 m/s, in the form of precipitates within large $Nd_2Fe_{14}B$ grains, often occurring adjacent to each other. They can be seen at the top right and bottom left corners of Figure 4- 68a, and at higher magnification in Figure 4- 68b. Fine stripes in phase A and some bands in phase B are observed. The fine modulated structure within phase A is shown more clearly in the bight field and dark field images in Figure 4- 68c and d, respectively. Kikuchi lines in the convergent beam diffraction pattern of Figure 4- $69a_1$ show four fold symmetry for phase A, which suggests that its structure is either cubic or tetragonal. $1/d^2$ values were determined for the spots in the various diffraction patterns of phase A, Figure 4- $69a_1$ and a_2 and a_3, and sorted in ascending order. These values, together with the $1/d^2$ ratios, are presented in Table 4- 7. The $1/d^2$ ratios in column 2 match the allowed $N=h^2+k^2+l^2$ values for the b.c.c. structure, 2, 4, 6, 8, 10, 12, 14, 16, 18, 20, ... [210]. Assuming this structure, the lattice parameter, a, calculated using equation 5-1:

$$\frac{1}{d^2} = \frac{h^2+k^2+l^2}{a^2} = \frac{N}{a^2} \qquad (5\text{-}1)$$

is determined as 0.7255 nm.

The other possibility is a tetragonal structure; the $1/d^2$ ratios of column 3 of Figure 4- 7 are compared with the possible values for $M= h^2+k^2$, 1, 2, 4, 5, 8, 9, 10, 13, 16, 17, 18, 20, ... The d-spacings from the $1/d^2$ values with a 2:1 ratio are from the {hk0} reflections, and these d-spacings were used to solve for h, k and a, while other d-spacings not fitting the 2:1 ratio pattern, are from {hkl} reflections and were used to solve for l and c using the following equation:

$$\frac{1}{d^2} = \frac{h^2+k^2}{a^2} + \frac{l^2}{c^2} = \frac{M}{a^2} + \frac{l^2}{c^2} \qquad (5\text{-}2)$$

Values of a = 0.5130 nm and c = 0.7246 nm were calculated as the lattice parameters for this structure.

Orthogonal (90^0) arrays of spots in the diffraction pattern of Figure 4- $69b_3$, suggest a cubic, tetragonal or orthorhombic structure for phase B [210].

It worth of note that it was not possible to go from one zone axis to another by tilting the specimen for either phase A or phase B. This suggests that these phases, in contrast to $Nd_2Fe_{14}B$, should have simple unit cells with small numbers of atoms.

EDS analysis of these phases (Figure 4- 70 and Figure 4- 71) gives the approximate chemical composition of 77at.% Fe, 22.8at.% Nd and 0.2at.% Ga for phase A and 8.7at.% Fe, 63.4at.% Nd and 27.9at.% Ga for phase B. The possible boron (B) content of these phases can not be measured by EDS analysis technique. No phase containing these elements was found to match the chemical composition and calculated lattice parameters for any of these two phases.

5.12 Observation of Additional Features in $Nd_2Fe_{14}B$ Phase

Some slab or platelet shaped $Nd_2Fe_{14}B$ grains were observed largely in the over quenched stoichiometric ribbons, annealed at temperatures ≥ 800°C, Figure 4- 63a, b and c. However, they were also found in directly quenched (at 22 m/s) $Fe_{85.1}Nd_9B_{5.9}$ ribbons (Figure 4- 63d). Although the reason for this morphology is not clear, it was found that the elongated face is the (001) plane. This suggests that the (001) face has

the lowest surface energy for these grains. Al-Khafaji et al. [120], reported ~ 20 nm platelet shaped grains for directly quenched, Nd-rich $Nd_{18}Fe_{76}B_6$ alloy ribbons. Panagiotopoulos et al. [198] also observed the formation of faceted fine (20 nm) $Nd_2Fe_{14}B$ grains in $Nd_{18}Fe_{76-x}Ga_xB_6$ alloys overquenched at 60 m/s and annealed.

Dislocation type features were observed occasionally in coarse $Nd_2Fe_{14}B$ grains of various alloys. In the TEM bright field (BF) image of Figure 4- 72a for $Fe_{83.2}Nd_{10.9}B_{5.9}$ ribbon, melt spun at 23 m/s such features are seen within the large $Nd_2Fe_{14}B$ grain at both ends of the α-Fe second phase particle. A weak beam dark field (WBDF) image of a $Fe_{82.3}Nd_{11.8}B_{5.9}$ ribbon sample, melt spun at 26 m/s and annealed for 4 minutes at 800°C, also showed such features, Figure 4- 72b. A TEM bright field (BF) image for $Fe_{83.2}Nd_{10.9}B_{5.9}$, melt spun at 23 m/s, Figure 4- 72c, contained some needle shape features lying in the (001) plane of the $Nd_2Fe_{14}B$ grain. Figure 4- 72d, taken at higher magnification, contains such features and parallel (001) lattice fringes. The small sizes of these features, compared to the probe dimensions, prevents EDS chemical analysis. Pollard et al. [151] observed similar features for Zr-containing needle shaped coherent precipitates in sintered $Fe_{74.7}Nd_{16.5}B_{7.8}Zr_1$ alloy, which appeared to be growing parallel to the (011) lattice planes of the matrix. Coherency strains were clearly visible around precipitates. A high resolution electron micrograph for a $Fe_{83.2}Nd_{10.9}B_{5.9}$ ribbon, melt spun at 23 m/s, taken from the $[11\bar{1}]$ zone axis, shows one of these needles. The optical diffraction pattern of Figure 4- 74 was used to index this HREM micrograph. Although the exact nature of this feature is not yet known, the closure failure around this feature clearly shows the presence of two extra $(\bar{1}10)$ half planes and two (101) half planes. $(\bar{1}10)$ half planes match the $[\bar{1}10]$ slip direction in the $Nd_2Fe_{14}B$ primary (001) slip plane [224].

The study of dislocations is important because of their possible role in plastic deformation during die-upset forging in which, the hot pressed block is plastically deformed at high temperature by compressing it to below 50% of its thickness in a die cavity of larger diameter. Mechanisms such as grain boundary sliding [75], diffusion slip [76], dissolving of misaligned grains and growth of the favourably

oriented crystallites [77] are suggested for deformation, some of which are mainly based on the presence of Nd rich grain boundary phase, which is liquid at the forming temperature. However, it has been shown that, although anisotropy was only developed in the presence of the grain boundary liquid phase, plastic deformation also occurred in the absence of liquid phase for substoichiometric Nd-Fe-B [78] and Pr-Fe-B [79] alloy samples.

Although dislocations are rarely (if any) reported to be seen in $Nd_2Fe_{14}B$ structure, it is suggested that dislocations are generated and move at high temperatures but are annihilated on cooling to room temperature [74]. Kuhrt et al. [224] performed some high temperature plastic deformation on $Nd_2Fe_{14}B$ single crystal cubes which were crystallographically oriented with the (001) plane at an angle of 45° to the sample's axis so that the maximum resolved stress was initially on the (001) plane, which is the only primary slip plane in the tetragonal $Nd_2Fe_{14}B$ phase. The slip directions in this plane are [110] and $[\bar{1}10]$. For a strain rate of 5×10^{-5} s^{-1} and temperatures of 1000-1050°C they observed pronounced yield points and that the monotonic stress decreased until fracture. This suggests that, because of the lack of dislocations in the $Nd_2Fe_{14}B$ phase, a high stress is needed to generate and accelerate dislocations, which move on the only operative slip plane until fracture, without being hindered by forest dislocations of a second slip system. They also observed that, if a sample is deformed partially at 1000°C and stopped and then continued at 900°C, the critical stress is considerably lowered by the first higher temperature deformation. This suggests that, after dislocations are generated at the higher temperature, they are numerous and mobile enough to provide considerable ductility at the lower temperature. However, lower temperatures (700-800°C) and higher strain rates (10^{-3}-10^{-2} s^{-1}) are generally used in the die-upsetting process in which, the $Nd_2Fe_{14}B$ single crystal would not have substantial ductility.

6. Summary and Conclusions

1. The optimum roll speed required to achieve the largest J_r and $(BH)_{max}$ enhancement was found to be 22 m/s for both stoichiometric ($Fe_{82.3}Nd_{11.8}B_{5.9}$) and substoichiometric ($Fe_{85.1}Nd_9B_{5.9}$) alloys. The substitution of Ga did not significantly alter the optimum V_r.

2. Enhanced remanence above the value predicted by Stoner-Wohlfarth model, for randomly oriented, non-interacting single domain particles, was obtained for $Fe_{83.2}Nd_{10.9}B_{5.9}$, when melt spun at roll speeds in the range of 20-22 m/s. J_r=0.95 T, ${}_jH_c$=790 kAm^{-1} and $(BH)_{max}$=149 kJm^{-3} were achieved for ribbons spun at 22 m/s.

3. Enhanced remanence was also obtained for stoichiometric ($Fe_{82.3}Nd_{11.8}B_{5.9}$) samples directly quenched at 22 m/s (J_r=0.95 T) and also for those melt spun at 26 m/s and annealed for 4 minutes at 600 to 850°C. J_r=0.97 T was obtained for samples annealed at 700°C. Annealed ribbon samples, melt spun at roll speeds of 30 and 40 m/s, also showed similar enhanced remanence values of 0.98 and 0.97 T, respectively.

4. Mean values of $(BH)_{max}$ as high as 150 kJm^{-3} were achieved for optimally quenched $Fe_{82.3}Nd_{11.8}B_{5.9}$ alloy ribbons, although individual values as high as 160 kJm^{-3} were obtained for a sample of thickness ~32 μm.

5. Randomly oriented, fine $Nd_2Fe_{14}B$ grains of mean diameter ~30 nm and with polygonal shapes were the dominant microstructural features of optimally quenched stoichiometric ribbons.

6. The coercivity of optimally quenched stoichiometric alloys (800 kAm^{-1}) increased slightly with Ga additions up to 2 at.% Ga (835 kAm^{-1}), while the remanence increased up to 1.5 at.% Ga (1.04 T) but decreased for higher Ga contents. The best $(BH)_{max}$ value of 160 kJm^{-3} averaged over several ribbon samples was obtained for optimally quenched $Fe_{80.8}Nd_{11.8}B_{5.9}Ga_{1.5}$ ribbons, with values as high as 173 kJm^{-3} for individual ribbon samples of thickness 28 μm.

7. Mean and maximum $(BH)_{max}$ values of 150 and 158 kJm^{-3}, respectively, similar to those for directly quenched ribbons, were achieved for stoichiometric $Fe_{82.3}Nd_{11.8}B_{5.9}$ ribbons overquenched at 26 m/s and optimally annealed at 700°C. $_jH_c$=810 kAm^{-1} was also achieved for these ribbons. These are potentially useful for practical application in large scale melt spinning of these alloys.

8. Overquenched and annealed stoichiometric ribbon samples containing Ga show generally slightly lower remanence and energy product than the ternary alloy ribbon, except for a small increase for 1 at.% Ga substitution (0.99 T). The coercivity did not change significantly except for an apparently "local" increase at 2 at.% Ga (1000 kAm^{-1}) accompanied by a reduction in remanence (089 T). Thus, for overquenched and optimally annealed $Fe_{81.3}Nd_{11.8}B_{5.9}Ga_1$ alloy, average and maximum $(BH)_{max}$ values of 155 kJm^{-3} and 157 kJm^{-3}, respectively, were achieved. The narrow spread of the values of magnetic properties for these overquenched and annealed samples is notable and emphasises the advantage of this process route over direct quenching.

9. Good magnetic properties ($(BH)_{max}$~150 kJm^{-3}) were obtained for overquenched and annealed stoichiometric alloy ribbons for a wide range of roll speeds (26-40 m/s). The results of grain size measurements by XRD line broadening and TEM, were in good agreement for samples annealed at temperatures up to 750°C and show that the $Nd_2Fe_{14}B$ grains have a good resistance to grain growth, on annealing below this temperature.

10. The addition of Ga does not appear to change the morphology of the $Nd_2Fe_{14}B$ nanograins for the stoichiometric alloy, in the directly quenched condition. Overquenched and annealed samples also have similar grain morphologies.

11. Remanence was further enhanced to 1.09 T for directly quenched $Fe_{85.1}Nd_9B_{5.9}$ alloy ribbons due to the presence of α-Fe nano-particles. $_jH_c$ however, decreased to 500 kAm^{-1}.

12. Average values of $(BH)_{max}$ up to 152 kJm^{-3} were achieved for $Fe_{85.1}Nd_9B_{5.9}$ alloy ribbons directly quenched under optimal conditions, although single values as high as 174 kJm^{-3} were obtained for a sample about 21 μm thick.

13. The influence of up to 1.5 at.% Ga addition for optimally quenched, low Nd (9at.%) nanocomposite alloys was to increase the coercivity (by ~ %10) and energy product (up to 167 kJm^{-3}) while remanence remained almost unchanged. The highest J_r (=1.13 T) and $(BH)_{max}$ were realised for 0.5 at.% Ga substitution. Mean $(BH)_{max}$ of 169 kJm^{-3} and single values as high as 180 kJm^{-3} were achieved for this alloy. EDS analysis showed that the Ga is mainly contained in the $Nd_2Fe_{14}B$ phase while TEM indicated that the Ga is in solid solution and does not form precipitates.

14. The best magnetic properties for overquenched and annealed ternary nanocomposite alloy samples of $Nd_9Fe_{85.1}B_{5.9}$ were achieved on annealing in the temperature range 700-750°C. In contrast to stoichiometric alloy ribbons, large differences between the magnetic properties of optimum directly quenched samples and those of overquenched and annealed samples were observed and mainly reflect inferior loop shapes, (due to the presence of locally coarse grains), and the lower coercivity of the latter (~430 kAm^{-1} compared to ~ 500 kAm^{-1} for directly quenched ribbons). These factors, together with the somewhat lower remanence (1.04 T compared to 1.09 T for directly quenched ribbons), result in much lower energy products (~110 kJm^{-3} compared to ~150 kJm^{-3} for directly quenched ribbons).

15. The magnetic properties of overquenched and annealed, low Nd samples do not change substantially with the addition of Ga and neither do the mean $Nd_2Fe_{14}B$ and α-Fe grain sizes. Average and maximum values of 115 kJm^{-3} and 135 kJm^{-3} were achieved for $(BH)_{max}$ for overquenched and optimally annealed $Fe_{82.1}Nd_9B_{5.9}Ga_3$ ribbons.

16. Randomly oriented, fine polygonal $Nd_2Fe_{14}B$ grains (30-40 nm), together with evenly distributed 10-20 nm diameter α-Fe grains, form the dominant microstructure of low Nd directly quenched ribbons. Overquenched and annealed samples show similar but rather coarse, microstructures which partly account for their inferior properties compared with directly quenched alloys. Although some areas of spherical $Nd_2Fe_{14}B$ grains and elongated Fe phase at the $Nd_2Fe_{14}B$ grain boundaries were found in Ga-containing samples, suggesting an influence of Ga on the $Nd_2Fe_{14}B$-liquid interfacial energy, it appears that, in most areas of the TEM foil, samples the microstructures were very similar to those of ternary alloys. Moreover, a few areas of

spherical $Nd_2Fe_{14}B$ grains were also found in some of the substoichiometric ternary alloys.

17. The following orientation relationship was found between $Nd_2Fe_{14}B$ and α-Fe precipitates for coarsed grained samples spun at low roll speed:

$$[001]_\phi \,||\, [1\bar{1}\bar{1}]_{\alpha\text{-Fe}} \qquad \text{and} \qquad (110)_\phi \,||\, (101)_{\alpha\text{-Fe}}$$

Dark field TEM also showed that some of the α-Fe precipitates had identical orientation.

18. Two phases (often adjacent to each other), in addition to $Nd_2Fe_{14}B$ and α-Fe, were found in the 10.9% Nd sample containing 3% Ga melt spun at 4 m/s. Four-fold symmetry in convergent beam electron diffraction patterns taken from phase A, suggests that this phase has a cubic or tetragonal crystal structure. Orthogonal (90°) arrays of spots in the diffraction pattern suggest a cubic, tetragonal or orthorhombic structure for phase B [210]. EDS analysis revealed a composition of 77at.%Fe, 22.8at.% Nd and 0.2at.% Ga for the phase A, and 8.6 at.% Fe, 63.5at.% Nd and 27.9at.% Ga for the phase B.

19. Some plate-like grains were found in low Nd samples melt spun at 22 m/s. The plane of the edges of these grains was found to be (001). Similar grains were found in stoichiometric samples annealed at 800 - 850°C.

20. Dislocation-type and some needle-shaped features were observed in some coarse $Nd_2Fe_{14}B$ grains.

7. Suggestions for Further Work

Although excellent $(BH)_{max}$ values were achieved for directly quenched nanocomposite alloys containing 9 at.% Nd, it could prove worthwhile to study the possibility of increasing ${}_jH_c$ without significant loss in J_r for this alloy and those containing smaller amounts of Nd and to combine the improved magnetic properties with the lower cost, better corrosion resistance, formability and thermal stability, associated with the low Nd nanocomposite alloys.

It is suggested that the effects of solute additions on the vitrification and crystallisation behaviour be investigated for overquenched and annealed substoichiometric alloy ribbons to try to develop a uniform, nanoscale grain size for $Nd_2Fe_{14}B$ and α-Fe phases in order to achieve an improved second quadrant hysteresis loop and therefore, higher $(BH)_{max}$ close to values obtained for directly quenched ribbons of similar compositions.

A study of the effect of combined additions of dopants such as Dy and Al on the microstructure and magnetic properties of stoichiometric and substoichiometric melt spun alloys could be useful.

Further TEM study of the substoichiometric alloys containing Ga should be undertaken to establish the relationship between grain morphology and magnetic properties.

HREM of overquenched ribbons spun at roll speeds greater than 26 m/s should be performed in order to establish more clearly the threshold speed for producing a fully amorphous ribbon, free of crystal nuclei.

Further HREM study of Ga-containing substoichiometric alloys is recommended to investigate more fully the formation of phases A and B in nanocrystalline samples, spun at high roll speeds, to complement the studies of microcrystalline samples spun at lower roll speeds in the present study.

References

1. R.J. Parker, Advances on Permanent Magnetism. 1990, New York: John Wiley & Sons.

2. J.J. Croat, J.F. Herbst, R.W. Lee and F.E. Pinkerton, J Appl Phys, 1984, **55**, 6, pp. 2078-2082.

3. M. Sagawa, S. Fujimura, N. Togawa, H. Yamamoto and Y. Matsuura, J Appl Phys, 1984, **55**, 6, pp. 2083-2087.

4. S. Hirosawa and Y. Kaneko, Proc 15th Intl Wkshop on RE Magnets and their Applicns, Dresden, Germany, 1998, pp. 43-53.

5. R.K. Mishra, Mat. Researc Soc., 1987, **96**, pp. 83.

6. P. Campbell, Proc 15th Intl Wkshop on RE Magnets and their Applicns, Dresden, Germany, 1998, pp. 681-687.

7. A.M. Kadin, R.W. McCallum, G.B. Clemente and J.E. Keem, Materials Research Society, 1986, pp. 385-394.

8. R.W. McCallum, A.M. Kadin, G.B. Clemente and J.E. Keem, J Appl Phys, 1987, **61**, 8, pp. 3577-3579.

9. G.B. Clemente, J.E. Keem and J.P. Bradley, J Appl Phys, 1988, **64**, **10**, pp. 5299-5301.

10. A. Manaf, M. Leonowicz, H.A. Davies and R.A. Buckley, Mater Lett, 1992, **13**, **4-5**, pp. 194-198.

11. A. Manaf, R.A. Buckley and H.A. Davies, J Magn Magn Mater, 1993, **128**, 3, pp. 302-306.

12. A. Manaf, M. Alkhafaji, P.Z. Zhang, H.A. Davies, R.A. Buckley and W.M. Rainforth, J Magn Magn Mater, 1993, **128**, **3**, pp. 307-312.

13. H.A. Davies, A. Manaf, M. Leonowicz, P.Z. Zhang, S.J. Dobson and R.A. Buckley, Nanostr Mater, 1993, **2**, pp. 197-203.

14. E.C. Stoner and E.P. Wohlfarth, IEEE Trans Magn, 1991, **27**, **4**, pp. 3475-3518.

15. R. Coehoorn, D.B. Demooij and C. Dewaard, J Magn Magn Mater, 1989, **80**, **1**, pp. 101-104.

16. J.J. Croat, Proc 13th Intl Wkshop on RE Magnets and their Applicns, Birmingham, 11-14 Sept , 1994, pp. 65-78.

17. D. Jiles, Introduction to Magnetism and Magnetic Materials. 1994, London: Chapman & Hall.

18. J.P. Jakubovics, Magnetism and Magnetic Materials. 1994, Cambridge: The University Press.

19. R. Skomski and J.M.D. Coey, Permanent Magnetism. 1999, Bristol: Institute of Publishing.

20. H. Kronmuller, J Magn Magn Mater, 1995, **144, Pt1**, pp. 25-28.

21. M. Sagawa, S. Fujimura, H. Yamamoto, Y. Matsuura and K. Hiraga, IEEE Trans Magn, 1984, **20, 5**, pp. 1584-1589.

22. S. Sinnema, R.J. Radwanski, J.J.M. Franse, D.B. Demooij and K.H.J. Buschow, J Magn Magn Mater, 1984, **44, 3**, pp. 333-341.

23. E. Burzo, E. Oswald, M.Q. Huang, E. Boltich and W.E. Wallace, J Appl Phys, 1985, **57, 8**, pp. 4109-4111.

24. M. McCaig and A.G. Clegg, Permanent Magnets in Theory and Practice. 1987, London: Pentec Press.

25. J.S. Cook and P.L. Rossiter, Critical Reviews in Solid State and Materials Sciences, Boca Raton, Florida, CRC Press, Inc., 1989, **15, 6**, pp. 509-547.

26. B.D. Cullity, Introduction to Magnetic Materials. 1972, U.S.A.: Addison-Wesley.

27. H. Kronmuller, T. Schrefl, R. Fischer and J. Fidler, Proc 8th Intl Symp Magn Anisot and Coerc in RE-TM Alloys, Birmingham, UK, 1994, pp. 1-24.

28. H. Kronmuller and T. Schrefl, J Magn Magn Mater, 1994, **129, 1**, pp. 66-78.

29. Rare-Earth Iron Permanent Magnets, ed. J.M.D. Coey. 1996, New York: Oxford University Press.

30. M. Sagawa, S. Hirosawa, H. Yamamoto, S. Fujimura and Y. Matsuura, Japn J Appl Phys, Part 1, 1987, **26, 6**, pp. 785-800.

31. G.C. Hadjipanayis and A. Kim, J Appl Phys, 1988, **63, 8**, pp. 3310-3315.

32. K.H.J. Buschow, J Magn Magn Mater, 1989, **80, 1**, pp. 1-8.

33. A. Hutten, J Metals, 1992, **44, 3**, pp. 11-15.

34. J.F. Herbst, J.J. Croat, F.E. Pinkerton and W.B. Yelon, Phys Rev B, 1984, **29, 7**, pp. 4176-4178.

35. R.W. Lee, App Phys Lett, 1985, **46, 8**, pp. 790-791.

36. C.B. Shoemaker, D.P. Shoemaker and R. Fruchart, Acta Crystal C, 1984, **40, OCT**, pp. 1665-1668.

37. D. Givord, H.S. Li and J.M. Moreau, Solid State Commu, 1984, **50, 6**, pp. 497-499.

38. H. Boller and H. Oesterreicher, J Less Comm Mater, 1984, **105**, pp. L5-L8.

39. Y. Matsuura, S. Hirosawa, H. Yamamoto, S. Fujimura, M. Sagawa and K. Osamura, Japn J Appl Phys, Part 2, 1985, **24**, 8, pp. L635-L637.

40. K.G. Knoch, B. Reinsch and G. Petzow, Zeitschrift Fur Metallkunde, 1994, **85**, 5, pp. 350-353.

41. G.C. Hadjipanayis, T.Y. F. and I.K. R., Proc 8th Intl Wkshop RE Magnets and their Applicns, Dayton, Ohio, 1985, pp. 657-668.

42. J. Fidler, IEEE Trans Magn, 1987, **23**, 5, pp. 2106-2108.

43. J. Fidler and K.G. Knoch, J Magn Magn Mater, 1989, **80**, 1, pp. 48-56.

44. J. Fidler, K.G. Knoch, H. Kronmuller and G. Schneider, J Mater Research, 1989, **4**, 4, pp. 806-814.

45. K. Hiraga, M. Hirabayashi, M. Sagawa and Y. Matsuura, Japn J Appl Phys, Part 2, 1985, **24**, 1, pp. L 30-L 32.

46. M. Tokunaga, M. Tobise, N. Meguro and H. Harada, IEEE Trans Magn, 1986, **22**, 5, pp. 904-909.

47. R. Ramesh, J.K. Chen and G. Thomas, J Appl Phys, 1987, **61**, 8, pp. 2993-2998.

48. I.R. Harris, C. Noble and T. Bailey, J Less Comm Metals, 1985, **106**, pp. L1-L4.

49. I.R. Harris, J Less Comm Metals, 1987, **131**, **MAR**, pp. 245-262.

50. Y. Bogatin, J Appl Phys, 1990, **67**, 9, pp. 4625-4625.

51. Mtals Handbook, Ninth Edition, Volume 8, Mechanical Testing, ed. J.e.a. Newby. 1985, Metals Park, Ohio, USA: American Society for Metals.

52. P.J. McGuiness and I.R. Harris, J Appl Phys, 1988, **64**, **10**, pp. 5308-5310.

53. I.R. Harris and P.J. McGuiness, J Less Comm Metals, 1991, **172**, **SEP**, pp. 1273-1284.

54. X.J. Zhang, P.J. McGuiness and I.R. Harris, J Appl Phys, 1991, **69**, 8, pp. 5838-5840.

55. D. Book and H.I. R., Proc 8th Intl Symp Magn Anisot and Coerc in RE-TM Alloys, Birmingham, UK, 1994, pp. 205-214.

56. K.H.J. Buschow, IEEE Trans Magn, 1994, **30**, **2 Pt2**, pp. 565-570.

57. J.H. Vincent and H.A. Davies, Proc Intl Conf of the Appl Metal and Metals Tech Group of the Met Soci , 1980, pp. 153-158.

58. H. Hillman and H.R. Hilzinger, London, The Chameleon Press Ltd., 1988, pp. 22-29.

59. A. Manaf, R.A. Buckley, H.A. Davies and M. Leonowicz, J Magn Magn Mater, 1991, **101, 1-3**, pp. 360-362.

60. R. Coehoorn and J. Duchateau, Mater Sci Eng , 1988, **99, MAR**, pp. 131-135.

61. L.J. Eshelman, K.A. Young, V. Panchanathan and J.J. Croat, J Appl Phys, 1988, **64, 10**, pp. 5293-5295.

62. H.H. Liebermann, Rapidly Quenched Metals III, London, The Metals Society, 1978, pp. 34-40.

63. S.C. Huang and H.C. Fidler, Mater Sci Eng A, 1981, **51**, pp. 39-46.

64. R. Yapp, H.A. Davies, F. Leccabue and B.E. Watts, Mater Lett, 1999, **38, 1**, pp. 33-38.

65. M. Matsuura, M. Kikuchi, M. Yagi and K. Suzuki, Japn J Appl Phys, 1980, **19**, pp. 1781-1787.

66. F.E. Luborsky, S.C. Huang and H.C. Fiedler, IEEE Trans Magn, 1981, **17**, pp. 3463-3466.

67. C. Harland and H.A. Davies, Proc 15th Intl Wkshop on RE Magnets and their Applicns, Dresden, Germany, 1998, pp. 263-269.

68. A. Jha, H.A. Davies and R.A. Buckley, J Magn Magn Mater, 1989, **80, 1**, pp. 109-114.

69. D.J. Branagan and R.W. McCallum, J Magn Magn Mater, 1995, **146, 1-2**, pp. 89-102.

70. R.K. Mishra, J Magn Magn Mater, 1986, **54, 7**, pp. 450-456.

71. J.J. Croat, J Appl Phys, 1997, **81, 8 Pt2B**, pp. 4804-4809.

72. V. Panchanathan and K. Sparwasser, Proc 15th Intl Wkshop on RE Magnets and their Applicns, Dresden, Germany, 1998, pp. 671-679.

73. P.B. Gwan, J.P. Scully, D. Bingham, J.S. Cook, R.K. Day, J.B. Dunlop and R.G. Heydon, Proc. 9th Intl Workshop on Rare-Earth Magnets and their Applns, Bad Soden, FRG, DPG-GmbH, 1987, pp. 295-300.

74. L. Li and C.D. Graham, J Appl Phys, 1990, **67, 9**, pp. 4756-4758.

75. R.K. Mishra, T.Y. Chu and L.K. Rabenberg, J Magn Magn Mater, 1990, **84, 1-2**, pp. 88-94.

76. R.K. Mishra, J Appl Phys, 1987, **62, 3**, pp. 967-971.

77. L. Li and C.D. Graham, IEEE Trans Magn, 1992, **28, 5 Pt2**, pp. 2130-2132.

78. M. Leonowicz and H.A. Davies, Mater Lett, 1994, **19, 5-6**, pp. 275-279.

79. G. Mendoza, H. A. Davies and M. Leonowicz, Proc 14th Intl Conf on RE Magnets and their Applicns, São Paulo, Brazil, 1996, pp. 556-562.

80. A. Kirchner, W. Grunberger, O. Gutfleisch, V. Neu, K.H. Muller and L. Schultz, Proc 15th Intl Wkshop on RE Magnets and their Applicns, Dresden, Germany, 1998, pp. 373-380.

81. L. Schultz, J. Wecker and E. Hellstern, J Appl Phys, 1987, **61, 8**, pp. 3583-3585.

82. L. Schultz, K. Schnitzke, J. Wecker, M. Katter and C. Kuhrt, J Appl Phys, 1991, **70, 10**, pp. 6339-6344.

83. J.P. Nozieres and R.P. Delabathie, IEEE Trans Magn, 1989, **25, 5**, pp. 4117-4119.

84. T. Shimoda, K. Akioka, O. Kobayashi and T. Yamagami, J Appl Phys, 1988, **64, 10**, pp. 5290-5292.

85. W.C. Chang, C.R. Paik, H. Nakamura, N. Takahasi, S. Sugimoto, M. Okada and M. Homma, IEEE Trans Magn, 1990, **26, 5**, pp. 2604-2606.

86. T. Shimoda, K. Akioka, O. Kobayashi, T. Yamagami, T. Ohki, M. Miyagawa and T. Yuri, IEEE Trans Magn, 1989, **25, 5**, pp. 4099-4104.

87. G.C. Hadjipanayis, R.C. Hazelton and K.R. Lawless, J Appl Phys, 1984, **55, 6**, pp. 2073-2077.

88. Y.L. Chen, IEEE Trans Magn, 1985, **Mag, 21**, pp. 1967-1969.

89. C.L. Harland and H.A. Davies, J Alloys Compounds, 1998, **281, 1**, pp. 37-40.

90. J. Fidler and P. Skalicky, Mikrochimica Acta, 1987, **1**, pp. 115-124.

91. A.S. Kim and F.E. Kamp, Proc 14th Intl Conf on RE Magnets and their Applicns, São Paulo, Brazil, 1996, pp. 678-688.

92. J.F. Herbst, Reviews Of Modern Physics, 1991, **63, 4**, pp. 819-898.

93. K. Hiraga, M. Hirabayashi, M. Sagawa and Y. Matsuura, Japn J Appl Phys, Part 1, 1985, **24, 6**, pp. 699-703.

94. G.C. Hadjipanayis, K.R. Lawless and R.C. Dickerson, J Appl Phys, 1985, **57, 8**, pp. 4097-4099.

95. K.D. Durst and H. Kronmuller, J Magn Magn Mater, 1987, **68, 1**, pp. 63-75.

96. K.H.J. Buschow, Materials Science Reports, 1986, **1**, pp. 1-64.

97. M. Sagawa, S. Hirosawa, H. Yamamoto, Y. Matsuura, S. Fujimura, H. Tokuhara and K. Hiraga, IEEE Trans Magn, 1986, **22, 5**, pp. 910-912.

98. K.J. Strnat, H.F. Mildrum, M. Tokunaga and H. Harada, J Appl Phys, 1988, **63, 8**, pp. 3321-3323?

99. J. Holc, S. Besenicar and D. Kolar, J Mater Sci, 1990, **25, 1A**, pp. 215-219.

100. J. Fidler and Y. Tawara, IEEE Trans Magn, 1988, **24, 2**, pp. 1951-1953.

101. B. Grieb, E.T. Henig, G. Schneider, G. Knoch, G. Petzow and D. Demooij, Powder Metal, 1992, **35, 3**, pp. 221-227.

102. K.G. Knoch, G. Schneider, J. Fidler, E.T. Henig and H. Kronmuller, IEEE Trans Magn, 1989, **25, 5**, pp. 3426-3428.

103. R. Ramesh and G. Thomas, Acta Met, 1988, **36, 12**, pp. 3137-3147.

104. G.C. Hadjipanayis, R.C. Dickenson and K.R. Lawless, J Magn Magn Mater, 1986, **54, 7**, pp. 557-558.

105. M. Leonowicz, A. Manaf and H.A. Davies, Mater Lett, 1992, **14**, pp. 277-280.

106. M.T. Claveguera-Mora, J.A. Diego, M.D. Baro, S. Surinach, A. Hernando, P. Crespo and G. Rivero, J Magn Magn Mater, 1993, **119**, pp. 289-293.

107. F.E. Pinkerton, IEEE Trans Magn, 1986, **22, 5**, pp. 922-924.

108. G.C. Hadjipanayis and W. Gong, J Appl Phys, 1988, **64, 10**, pp. 5559-5561.

109. F. Matsumoto, H. Sakamoto, M. Komiya and M. Fujikura, J Appl Phys, 1988, **63, 8**, pp. 3507-3509.

110. Y.B. Kim, K.W. Lee, C.S. Kim, H.C. Shin, T.K. Kim, M. Okada and M. Homma, J Appl Phys, 1991, **70, 10**, pp. 6477-6479.

111. J.E. Keem, G.B. Clemente, A.M. Kadin and R.W. McCallum, Proc of ASM Mater Week Symp, ASM, 1987, pp. .

112. A. Manaf, M. Leonowicz, H.A. Davies and R.A. Buckley, Proc 12th Intl Wkshop on RE Magnets and their Applicns, Canberra, Australia, 1992, pp. .

113. T. Schrefl, J. Fidler and H. Kronmuller, Phys Rev B, 1994, **49, 9**, pp. 6100-6110.

114. A. Manaf, P.Z. Zhang, I. Ahmad, H.A. Davies and R.A. Buckley, IEEE Trans Magn, 1993, **29, 6 Pt1**, pp. 2866-2868.

115. M.R.J. Gibbs, M.A. Alkhafaji, W.M. Rainforth, H.A. Davies, K. Babcock, J.N. Chapman and L.J. Heyderman, IEEE Trans Magn, 1995, **31, 6 Pt1**, pp. 3349-3351.

116. A. Manaf, M. Leonowicz, H.A. Davies and R.A. Buckley, J Appl Phys, 1991, **70, 10**, pp. 6366-6368.

117. A. Manaf, H.A. Davies, R.A. Buckley and M. Leonowicz, J Magn Magn Mater, 1992, **104, Pt2**, pp. 1145-1146.

118. S.J. Dobson, R.A. Buckley and H.A. Davies, Proc 12th Intl Wkshop on RE Magnets and their Applicns, Canberra, Australia, Univ. W. Australia, 1992, pp. 92-101.

119. M.W. Crabbe, H.A. Davies and R.A. Buckley, IEEE Trans Magn, 1994, **30, 2**, pp. 696-698.

120. M.A. Al-Khafaji, A. Manaf, P. Zhang, I. Ahmed, W.M. Rainforth and H.A. Davies, Institute Of Physics Conference Series, 1993, **138**, pp. 457-460.

121. C. Koestler, R. Ramesh, C.J. Echer, G. Thomas and J. Wecker, Acta Met, 1989, **37, 7**, pp. 1945-1955.

122. E. Girt, K.M. Krishnan, G. Thomas, Z. Altounian and M. Dikeakos, J Appl Phys, , **88, 9**, pp. 5311-5314.

123. R.K. Mishra, E.G. Brewer and R.W. Lee, J Appl Phys, 1988, **63, 8**, pp. 3528-3530.

124. I. Ahmad, H.A. Davies and R.A. Buckley, J Magn Magn Mater, 1996, **158**, pp. 31-32.

125. G.C. Hadjipanayis, L. Withanawasam and R.F. Krause, IEEE Trans Magn, 1995, **31, 6**, pp. 3596-3601.

126. A. Inoue, A. Takeuchi, A. Makino and T. Masumoto, IEEE Trans Magn, 1995, **31, 6 Pt2**, pp. 3626-3628.

127. L. Withanawasam, A.S. Murthy and G.C. Hadjipanayis, IEEE Trans Magn, 1995, **31, 6 Pt2**, pp. 3608-3610.

128. S. Hirosawa and H. Kanekiyo, Mater Sci Eng A, 1996, **217**, pp. 367-370.

129. H. Kronmuller, R. Fischer, M. Seeger and A. Zern, J Phys D-Appl Phys, 1996, **29, 9**, pp. 2274-2283.

130. Y.S. Cho, Y.B. Kim and T.K. Kim, IEEE Trans Magn, 1996, **32**, pp. 1964-1966.

131. T. Schrefl, H. Kronmuller and J. Fidler, J Magn Magn Mater, 1993, **127, 3**, pp. L 273-L 277.

132. R. Skomski, J Appl Phys, 1994, **76, 10 Pt2**, pp. 7059-7064.

133. L. Withanawasam, G.C. Hadjipanayis and R.F. Krause, J Appl Phys, 1994, **75, 10 Pt2B**, pp. 6646-6648.

134. J.F. Liu and H.A. Davies, J Magn Magn Mater, 1996, **158**, pp. 29-30.

135. G. Mendoza Suarez and H.A. Davies, J Alloys Compounds, 1998, **281, 1**, pp. 17-22.

136. D. Goll and H. Kronmuller, Proc 15th Intl Wkshop on RE Magnets and their Applicns, Dresden, Germany, 1998, pp. 189-198.

137. L. Folks, R. Street, R.C. Woodward, S. Hirosawa and H. Kanekiyo, J Magn Magn Mater, 1995, **147, 3**, pp. 360-366.

138. J.D. Livingston, Proc 8th Intl Wkshop RE Magnets and their Applicns, Dayton, Ohio, 1985, pp. 423-440.

139. S.F.H. Parker, R.J. Pollard, D.G. Lord and P.J. Grundy, IEEE Trans Magn, 1987, **23, 5**, pp. 2103-2105.

140. D.R. Gauder, M.H. Froning, R.J. White and A.E. Ray, J Appl Phys, 1988, **63, 8**, pp. 3522-3524.

141. Y. Xiao, S. Liu, H.F. Mildrum, K.J. Strnat and A.E. Ray, J Appl Phys, 1988, **63, 8**, pp. 3516-3518.

142. M. Seeger, D. Kohler and H. Kronmuller, J Magn Magn Mater, 1994, **130, 1-3**, pp. 165-172.

143. H. Yamamoto, M. Nagakura, Y. Ozawa and T. Katsuno, IEEE Trans Magn, 1989, **25, 5**, pp. 4123-4125.

144. W.P. Sequeira, S.J. Dobson, R.A. Buckley and H.A. Davies, Mater Lett, 1993, **15, 5-6**, pp. 376-378.

145. H.A. Davies, K.J.A. Mawella, R.A. Buckley, G.E. Carr, A. Manaf and A. Jha, Concerted European Action on Magnets, eds. I V Mitchell et al, Elsevier Applied Science, London, Elsevier Applied Science, 1988, pp. 543-557.

146. H. Yamamoto, S. Hirosawa, S. Fujimura, K. Tokuhara, H. Nagata and M. Sagawa, IEEE Trans Magn, 1987, **23, 5**, pp. 2100-2102.

147. S. Hirosawa, Y. Yamaguchi, K. Tokuhara, H. Yamamoto, S. Fujimura and M. Sagawa, IEEE Trans Magn, 1987, **23, 5**, pp. 2120-2123.

148. J. Fidler, Proc 7th Intl Symp Magn Anisot and Coerc in RE-TM Alloys, 1992, pp. 11-22.

149. Z.M. Chen, N.X. Wang, X.P. Song and X.T. Wang, IEEE Trans Magn, 1995, **31, 3 Pt2**, pp. 2215-2219.

150. Z.M. Chen, A. Yan and X.T. Wang, J Magn Magn Mater, 1996, **162, 2-3**, pp. 307-313.

151. R.J. Pollard, P.J. Grundy, S.F.H. Parker and D.G. Lord, IEEE Trans Magn, 1988, **24, 2**, pp. 1626-1628.

152. S.F.H. Parker, P.J. Grundy and J. Fidler, J Magn Magn Mater, 1987, **66, 1**, pp. 74-78.

153. P. Shu-Ming, X.D.Y.N. Xiang, M. Ru-Zhang and P. Feng, Proc 13th Intl Wkshop on RE Magnets and their Applicns, Birmingham, 11-14 Sept , 1994, pp. 435-438.

154. A.S. Kim and F.E. Camp, IEEE Trans Magn, 1995, **31, 6 Pt2**, pp. 3620-3622.

155. M. Velicescu, W. Fernengel, W. Rodewald, P. Schrey and B. Wall, J Magn Magn Mater, 1996, **158**, pp. 47-48.

156. S. Arai and T. Shibata, IEEE Trans Magn, 1985, **21, 5**, pp. 1952-1954.

157. T. Mizoguchi, I. Sakai, H. Niu and K. Inomata, IEEE Trans Magn, 1986, **22, 5**, pp. 919-921.

158. V. Sinka, M. Ferrante, T. Kvackaj and G. Janak, Proc 14th Intl Conf on RE Magnets and their Applicns, São Paulo, Brazil, 1996, pp. 168-173.

159. B.M. Ma and K. Narasimhan, IEEE Trans Magn, 1986, **22, 5**, pp. 916-918.

160. M. Leonowicz and W. Kaszuwara, Proc 14th Intl Conf on RE Magnets and their Applicns, São Paulo, Brazil, 1996, pp. 148-157.

161. A.S. Kim, J Appl Phys, 1988, **63, 8**, pp. 3519-3521.

162. M. Sagawa, P. Tenaud, F. Vial and K. Hiraga, IEEE Trans Magn, 1990, **26, 5**, pp. 1957-1959.

163. S. Hirosawa, H. Tomizawa, S. Mino and A. Hamamura, IEEE Trans Magn, 1990, **26, 5**, pp. 1960-1962.

164. Y. Kitano, J. Shimomura and M. Shimotomai, J Appl Phys, 1991, **69, 8**, pp. 6055-6057.

165. H. Bala, G. Pawlowska, S. Szymura, V.V. Sergeev and Y.M. Rabinovich, J Magn Magn Mater, 1990, **87, 3**, pp. L 255-L 259.

166. S. Szymura, H. Bala, Y.M. Rabinovich, V.V. Sergeev and G. Pawlowska, J Magn Magn Mater, 1991, **94, 1-2**, pp. 113-118.

167. G.C. Hadjipanayis, Y.J. Zhang and L. Withanawasam, Proc 7th Intl Symp Magn Anisot and Coerc in RE-TM Alloys, 1992, pp. 151-161.

168. S.X. Zhou, P. Johansson, S.J. Savage and L.Y. Cui, IEEE Trans Magn, 1990, **26, 5**, pp. 1739-1741.

169. R.J. Pollard, S.F.H. Parker and P.J. Grundy, J Magn Magn Mater, 1988, **75, 3**, pp. 239-242.

170. A. Manaf, M. Leonowicz, H.A. Davies and R.A. Buckley, J Appl Phys, 1993, **73, 10**, pp. 6473-6475.

171. J. Wecker and L. Schultz, J Magn Magn Mater, 1990, **83, 1-3**, pp. 189-191.

172. P. Choi, H. Ino and G. Kido, Journal Of the Japan Institute Of Metals, 1992, **56, 8**, pp. 952-959.

173. P. Choi and H. Ino, Mater Sci Eng A, 1994, **182**, pp. 1004-1009.

174. I. Ahmad, M.A. Alkhafaji, H.A. Davies, R.A. Buckley and W.M. Rainforth, Proc 8th Intl Symp Magn Anisot and Coerc in RE-TM Alloys, Birmingham, UK, 1994, pp. 145-153.

175. J.F. Herbst, C.D. Fuerst, R.K. Mishra, C.B. Murphy and D.J. Vanwingerden, J Appl Phys, 1991, **69, 8**, pp. 5823-5825.

176. T.S. Chin, C.H. Lin, S.H. Huang, J.M. Yau, T.Y. Chu and C.D. Wu, Japn J Appl Phys, Part 1, 1992, **31, 10**, pp. 3323-3327.

177. J.S. Fang, T.S. Chin and S.K. Chen, IEEE Trans Magn, 1996, **32, 5 Pt2**, pp. 4401-4403.

178. R. Yapp and H.A. Davies, Proc 15th Intl Wkshop on RE Magnets and their Applicns, Dresden, Germany, 1998, pp. 315-321.

179. W. Rodewald and P. Schrey, IEEE Trans Magn, 1989, **25, 5**, pp. 3770-3772.

180. T.S. Chin, S.H. Huang and J.M. Yau, IEEE Trans Magn, 1993, **29, 6 Pt1**, pp. 2791-2793.

181. J.Q. Xie, C.H. Wu, Y.C. Chuang and F.M. Yang, J Appl Phys, , **68, 8**, pp. 4208-4213.

182. D.T. Steel, M. Leonowicz and H.A. Davies, Mater Lett, 1995, **23, 1-3**, pp. 43-46.

183. W.C. Chang, C.H. Lin, K.D. Lin, Y.M. Chien and S.K. Chen, Proc 10th Intl Wkshop on RE Magnets and their Applicns, Kyoto, Japan, 1989, pp. 509.

184. P. Shuming and M. Ruahang, Proc 10th Intl Wkshop on RE Magnets and their Applicns, Kyoto, Japan, 1989, pp. 537-544.

185. M. Leonowicz, J Magn Magn Mater, 1990, **83, 1-3**, pp. 211-213.

186. G. Rieger, M. Seeger, L. Sun and H. Kronmuller, J Magn Magn Mater, 1995, **151, 1-2**, pp. 193-201.

187. G. Rieger, J. Bauer, M. Seeger and H. Kronmuller, Nanostr Mater, 1995, **6, 5-8**, pp. 953-956.

188. J. Fidler, C. Groiss and M. Tokunaga, IEEE Trans Magn, 1990, **26, 5**, pp. 1948-1950.

189. H.S. Li, B.P. Hu, J.M. Cadogan, J.M.D. Coey and J.P. Gavigan, J Appl Phys, 1990, **67, 9**, pp. 4841-4843.

190. K.G. Knoch, B. Grieb, E.T. Henig, H. Kronmuller and G. Petzow, IEEE Trans Magn, 1990, **26, 5**, pp. 1951-1953.

191. Z. Pai, Q. Tiangang, S. Xiaoping, M. Baotian and W. Xiaotian, Proc 12th Intl Wkshop on RE Magnets and their Applicns, Canberra, Australia, 1992, pp. 277-281.

192. M. Endoh, M. Tokunaga and H. Harada, IEEE Trans Magn, 1987, **23, 5**, pp. 2290-2292.

193. A. Tsutai, I. Sakai, T. Mizoguchi and K. Inomata, App Phys Lett, 1987, **51, 13**, pp. 1043-1045.

194. A. Tsutai, I. Sakai, M. Sahashi and K. Inomata, J Appl Phys, 1990, **67, 9**, pp. 4777-4777.

195. C. Burkhardt, I.R. Harris, S. Kobe, L. Vehovar and M. Steinhorst, Proc 14th Intl Conf on RE Magnets and their Applicns, São Paulo, Brazil, 1996, pp. 689-697.

196. I. Ahmad, H.A. Davies and R.A. Buckley, Mater Lett, 1994, **20, 3-4**, pp. 139-142.

197. I. Ahmad, M.A. Alkhafaji, H.A. Davies, W.M. Rainforth and R.A. Buckley, J Magn Magn Mater, 1995, **145, 1-2**, pp. L 19-L 22.

198. I. Panagiotopoulos, A.S. Murthy and G.C. Hadjipanayis, IEEE Trans Magn, 1995, **31, 6 Pt2**, pp. 3617-3619.

199. J. Bauer, M. Seeger, G. Rieger, H. Kronmuller, J. Bernardi and J. Fidler, Proc 8th Intl Symp Magn Anisot and Coerc in RE-TM Alloys, Birmingham, UK, 1994, pp. 405-413.

200. M. Seeger, J. Bauer, G. Rieger, H. Kronmuller, J. Bernardi and J. Fidler, J Magn Magn Mater, 1995, **144, Pt2**, pp. 1059-1060.

201. V. Panchanathan and J.J. Croat, IEEE Trans Magn, 1989, **25, 5**, pp. 4111-4113.

202. J.F. Liu, H.A. Davies and R.A. Buckley, Proc 13th Intl Wkshop on RE Magnets and their Applicns, Birmingham, 11-14 Sept , 1994, pp. 79-86.

203. S. Hirosawa and H. Kanekiyo, Proc 13th Intl Wkshop on RE Magnets and their Applicns, Birmingham, 11-14 Sept , 1994, pp. 87-94.

204. V. Panchanathan, IEEE Trans Magn, 1995, **31, 6 Pt2**, pp. 3605-3607.

205. E. Sinnecker, E. Ferrara, P. Tiberto, M. Baricco and F. Vinai, J Magn Magn Mater, 1999, **197**, pp. 291-292.

206. H. Kanekiyo, M. Uehara and S. Hirosawa, IEEE Trans Magn, 1993, **29, 6 Pt1**, pp. 2863-2865.

207. G.E. Carr, H.A. Davies and R.A. Buckley, Mater Sci Eng , 1988, **99, MAR**, pp. 147-151.

208. W.M. Rainforth, Materials World, 1994, **2, 10**, pp. 527-530.

209. M.H. Loretto, Electron Beam Analysis of Materials. 1984, London: Chapman and Hall.

210. B.E.P. Beeston, R.W. Horne and R. Markham, Electron Diffraction and Optical Diffraction Techniques, ed. A.M. Glauert. 1973, Netherlands: North-Holland Publishing Company.

211. J.J. Croat, J.F. Herbst, R.W. Lee and F.E. Pinkerton, App Phys Lett, 1984, **44, 1**, pp. 148-149.

212. J. Wecker and L. Schultz, J Appl Phys, 1987, **62, 3**, pp. 990-993.

213. H.A. Davies, J.F. Liu and G. Mendoza, Proc 9th Intl Symp Magnetic Aniso Coercivity RE Trans Metal Alloys,São Paulo, Brazil, Word. Scientific, 1996, **2**, pp. 251-267.

214. D. Cochet-Muchy and S. Paidassi, Intl J Rapid Solidificn, 1989, **5, 1**, pp. 11-31.

215. M.N.K. Willcox, J.M. Williams, M. Leonowicz, A. Manaf and H.A. Davies, Proc 13th Intl Wkshop on RE Magnets and their Applicns, Birmingham, 11-14 Sept , 1994, pp. 443-453.

216. W.Y. Jeung, I.K. Kang, J.O. Choi and J.J. Lee, IEEE Trans Magn, 1990, **26, 5**, pp. 1733.

217. A. Inoue, A. Takeuchi, A. Makino and T. Masumoto, Mater Trans, Jim, 1995, **36, 7**, pp. 962-971.

218. H.A. Davies, A. Manaf and P.Z. Zhang, J Mater Eng Perfor, 1993, **2, 4**, pp. 579-587.

219. T.R. Anthony and H.E. Cline, J Appl Phys, 1979, **50**, pp. 245-254.

220. J. Wecker and L. Schultz, App Phys Lett, 1987, **51, 9**, pp. 697-699.

221. I. Ahmad, Sheffield University, Thesis, 1996, pp. .

222. G.H. Tu, Z. Altounian, D.H. Ryan and J.O. Strom-Olsen, J Appl Phys, 1988, **63, 8**, pp. 3330-3332.

223. R. Coehoorn, D.B. Demooij, J. Duchateau and K.H.J. Buschow, J De Phys, Paris, 1988, **49, C-8**, pp. 669-670.

224. C. Kuhrt, L. Schultz, K. Schnitzke, S. Hock and R. Behrensmeier, App Phys Lett, 1991, **59, 12**, pp. 1418-1420.

225. Mtals Handbook, Ninth Edition, Volume I Properties and Selection: Irons and Steels, ed. B. Bardes. 1978, Metals Park, Ohio, USA: American Society for Metals.

226. Mtals Handbook, Ninth Edition, Volume 2, Properties and Selection: Nonferrous Alloys and Pure Metals, ed. H.e.a. Baker. 1979, Metals Park, Ohio, USA: American Society for Metals.

227. H. Davies, Phys World, 1994, **7, 11**, pp. 40-43.

Tables

Table 2- 1: Magnetic units [19].

SI	cgs relation
$B=\mu_o(H+M)=\mu_oH+J$	$B=H+4\pi M=H+I$
B=1 T (Tesla)	B=10 kG (k Gauss)
M=1 kA m^{-1}	M=1 emu cm^{-1}
$J=\mu_oM=1$ T	$4\pi M=10$ kG
H=1 kA m^{-1}	$H=4\pi$ Oe (Oersted)
$(BH)_{max}=1$ MJ m^{-3}	$(BH)_{max}=40\pi$ MG Oe

Table 2- 2: The most useful conversion factors between SI and cgs units in magnetism [19].

SI	cgs
1 T	10 kG
1 kA m^{-1}	12.57 (≈12.5) Oe
1 MJ m^{-3}	125.7 MG Oe
0.1 mT	1 G
79.8 (≈80) Am^{-1}	1 Oe
7.96 kJm^{-3}	1 MG Oe

Table 2- 3: Reactions in the ternary system Nd-Fe-B [40], Figure 2- 15.

Symbol	Reaction	T (°C)
P_1	$l+\delta Fe \rightarrow \gamma Fe$	1392
P_2	$l+\gamma Fe \rightarrow \psi$	1185
P_3	$l+\psi \rightarrow Nd_5Fe_{17}$	780
P_4	$l+\beta Nd \rightarrow \alpha Nd$	856
P_5	$l+\delta Fe \rightarrow \gamma Fe$	1381
P_6	$l+FeB \rightarrow Fe_2B$	1389
P_7	$l+\gamma Fe \rightarrow \phi$	1180
P_8	$l+NdB_4 \rightarrow \eta$	1345
e_1	$l \rightarrow Nd_5Fe_{17}+Nd$	685
e_2	$l \rightarrow \gamma Fe+Fe_2B$	1177
e_3	$l \rightarrow Nd+Nd_2B_5$	1000
e_4	$l \rightarrow \eta+\phi$	1115
e_5	$l \rightarrow Fe_2B+\phi$	1110
U_1	$L+FeB \rightarrow Fe_2B+NdB_4$	?
U_2	$L+NdB_4 \rightarrow \eta+Fe_2B$	?
U_3	$L+\gamma Fe \rightarrow \phi+\psi$	1130
U_4	$L+Nd_2B_5 \rightarrow Nd+\rho$	?
U_5	$L+\rho \rightarrow Nd+\eta$	(745)
U_6	$L+\eta \rightarrow Nd+\phi$	710
E_1	$L \rightarrow \phi+\gamma Fe+Fe_2B$	1105
E_2	$L \rightarrow \eta+\phi+Fe_2B$	1095

Table 2- 4: Chemical composition of the symbols used in Figure 2- 15 and Figure 2- 16 [40].

Symbol	Composition
ψ	Nd_2Fe_{17}
ϕ	$Nd_2Fe_{14}B$
η	$Nd_{1.1}Fe_4B_4$
ρ	$Nd_5Fe_2B_6$

Table 2- 5: Reaction regions of CCT diagram (Figure 2- 19) [69].

Region	Reaction	Type	Description
1	$L>Fe+L_1$	Peritectic	Properitectic iron reaction
2	$L>T_1$	Transition	Direct crystallisation
3	$L+Fe>T_1$	Peritectic	Peritectic reaction
4	$L>T_1+L_1$	Peritectic	Hyperperitectic reaction
5	$L>T_1+T_2+L_1$	Eutectic	Proeutectic reaction
6	$L>T_1+T_2+Nd$	Eutectic	Ternary eutectic reaction
7	L>Glass	Transition	Liquid to glass transition

Table 2- 6: Quantitative effect of substitution of transition metals (T) in $Nd_2Fe_{14}B$ on Curie temperature (ΔT_o), magnetisation at 300 K ($\Delta M(300)$) and anisotropy field at 300 K ($\Delta H_A(300)$). The second column indicates the site preference of the T atoms 56.

T	Site	ΔT_o	$\Delta M(300)$	$\Delta H_A(300)$
Ti		-	-	-
V		-	-	-
Cr	$8j_2$	-	-	-
Mn	$8j_2$	-	-	-
Co	$16K_2$, $8j_1$	+	-	-
Ni	$18K_2$, $8j_2$	+	-	-
Cu		+	-	-
Zr		-	-	-
Nb		-	-	+
Mo			-	-
Ru		-		-
W		-		
Al	$8j_2$, $16K_2$	-	-	+
Ga	$8j_1$, 4c, $16K_2$	+	-	+
Si	$4c(16K_2)$	+	-	+

Table 3- 1: Chemical analyses for initial and corrected stoichiometric alloy samples, compared to nominal composition.

	Stoichiometric		Near Stoichiometric		Corrected Samples	
	at.%	wt%	at.%	wt%	at.%	wt%
Fe	82.3	72.25	83.2	73.96	82.3±0.3	72.25±0.5
Nd	11.8	26.75	10.9	25.02	11.8±0.3	26.75±0.5
B	5.9	1.00	5.9	1.02	5.9± 0.02	1.00±0.03

Table 3- 2: Melting point and density of the elements used to make alloys in argon arc furnace [225, 226].

Element	Melting Point, °C	Density, gcm^{-3}
Fe	1538	7.87
Nd	1021	7.008
B	2300	2.3
Ga	29.78	5.907

Table 4- 1: Average values of magnetic properties as a function of roll speed for melt spun $Fe_{83.2}Nd_{10.9}B_{5.9}$ alloy (Figure 4- 15).

Roll Speed, m/s	J_r, T	$_jH_c$, kAm^{-1}	$(BH)_{max}$, kJm^{-3}
8	0.64	181	22
19	0.66	213	34
20	0.88	393	101
21	0.94	769	128
22	0.95	790	149
23	0.91	590	108

Table 4- 2: Average values of magnetic properties as a function of Ga content for stoichiometric alloy, melt spun at optimum conditions (Figure 4- 24).

Ga Content, at.%	J_r, T	$_jH_c$, kAm^{-1}	$(BH)_{max}$, kJm^{-3}
0	0.95	800	150
0.5	0.98	802	148
1	0.98	812	154
1.5	1.04	810	160
2	0.98	835	149
2.5	0.93	830	140
3	0.91	812	132

Table 4- 3: X-Ray diffraction data for $Fe_{82.3}Nd_{11.8}B_{5.9}$ and $Fe_{81.3}Nd_{11.8}B_{5.9}Ga$, melt spun at 22 m/s and 21 m/s, respectively, compared to the data from Powder Diffraction File (PDF), Figure 4- 29.

	PDF	PDF	$Fe_{82.3}Nd_{11.8}B_{5.9}$	$Fe_{81.3}Nd_{11.8}B_{5.9}Ga$
hkl	2θ°	d A	d A	d
002	16.87	6.100	6.114	6.174
210	26.27	3.936	3.929	3.961
202	29.03	3.569	3.561	3.592
212	31.38	3.308	3.299	3.326
311	38.49	2.714	2.709	2.721
214	43.54	2.412	2.409	2.418
313	45.83	2.197	2.295	2.304
224	48.48	2.179	2.176	2.183
410	49.53	2.135	2.131	2.139
314	51.56	2.057	2.053	2.06
413	56.47	1.891	1.888	1.895
511	63.08	1.710	1.709	1.713
008	71.79	1.526	1.525	1.53
515	78.76	1.410	1.409	1.413
622	82.44	1.357	1.355	1.357

Table 4- 4: Average values of magnetic properties as a function of Ga content for $Fe_{85.1-x}Nd_9B_{5.9}Ga_x$ alloy, melt spun at optimum conditions (Figure 4- 30).

Ga Content, at.%	J_r, T	$_jH_c$, kAm^{-}	$(BH)_{max}$, kJm^{-3}
0	1.09	500	152
0.5	1.13	497	169
1	1.09	515	163
1.5	1.09	536	167
2	1.11	533	164
2.5	1.13	506	165
3	1.01	503	150

Table 4- 5: Average values of magnetic properties as a function of Ga content for stoichiometric alloy, overquenched by melt spinning at 26 m/s followed by annealing for 4 minutes at 700°C (Figure 4- 43).

Ga Content, at.%	J_r, T	$_jH_c$, kAm^{-1}	$(BH)_{max}$, kJm^{-3}
0	0.97	810	150
0.5	0.95	750	140
1	0.99	830	155
1.5	0.97	820	141
2	0.89	1000	124
2.5	0.92	844	121
3	0.94	780	125

Table 4- 6: Average values of magnetic properties as a function of Ga content for $Fe_{85.1-x}Nd_9B_{5.9}Ga_x$ alloy, melt spun at 26 m/s and annealed for 4 minutes at 750°C (Figure 4- 51).

Ga Content, at.%	J_r, T	$_jH_c$, kAm^{-1}	$(BH)_{max}$, kJm^{-3}
0	1.04	434	112
0.5	0.95	405	105
1	0.98	434	96
1.5	1.03	441	105
2	1.01	445	114
2.5	1.00	429	104
3	1.01	453	115

Table 4- 7: $1/d^2$ values obtained from different spots in the various phase A diffraction patterns (Figure 4- 69a), in ascending order.

$1/d^2$	$1/d^2$	$1/d^2$ Ratio
0.038	2	1
0.077	4	2
0.112	6	3
0.192	10	5
0.267	14	7
0.346	18	9
0.380	20	10
0.495	26	13
0.576	30	15
0.755	40	20

Figures

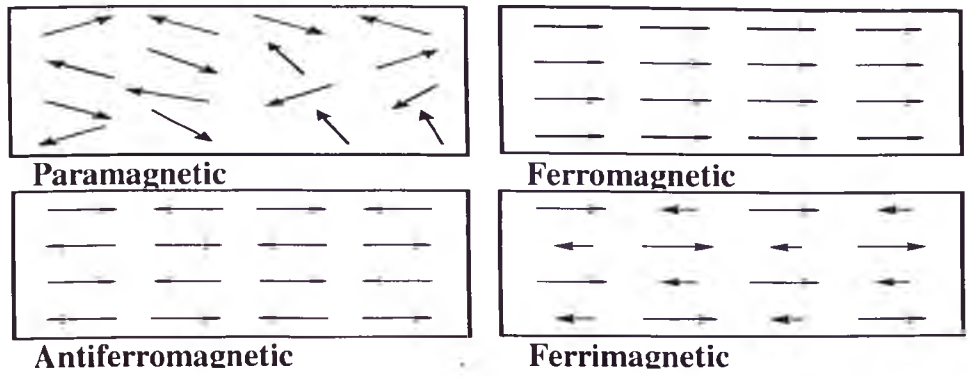

Figure 2- 1: Schematic diagrams of the alignment of magnetic moments in different type of materials [18].

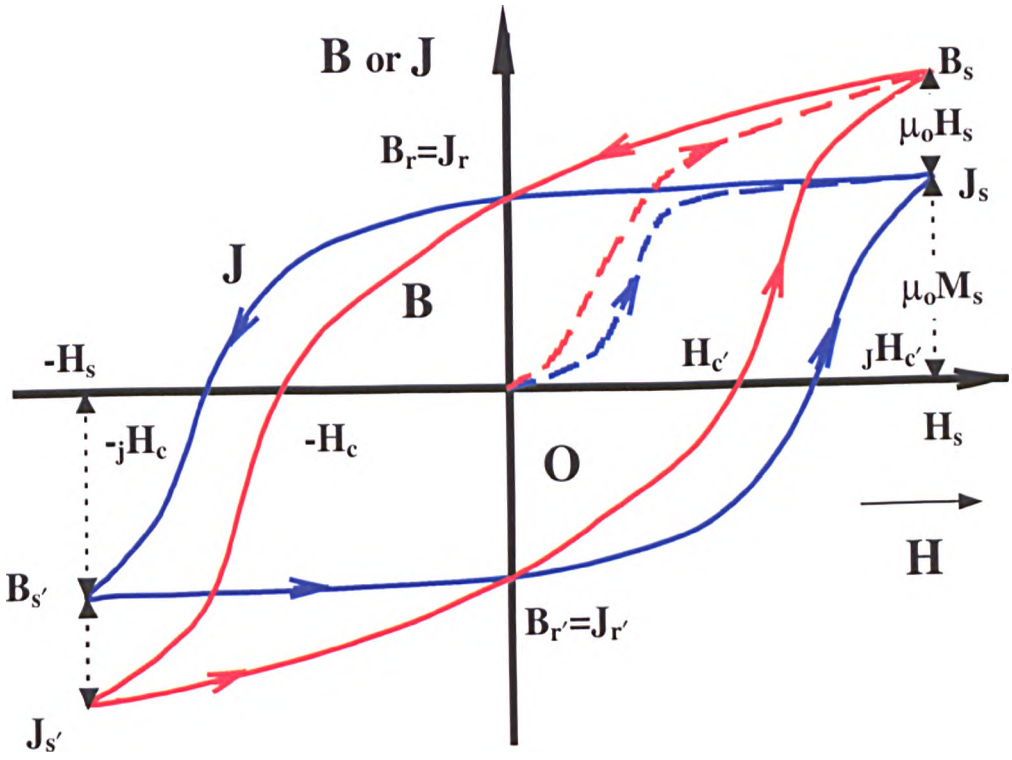

$$B = \mu_o H + \mu_o M, \qquad J = \mu_o M,$$

$$B = 0 \rightarrow H = H_c, \qquad \mu_o M = 0 \rightarrow H = {}_jH_c$$

Figure 2- 2: The Hysteresis Loop [1].

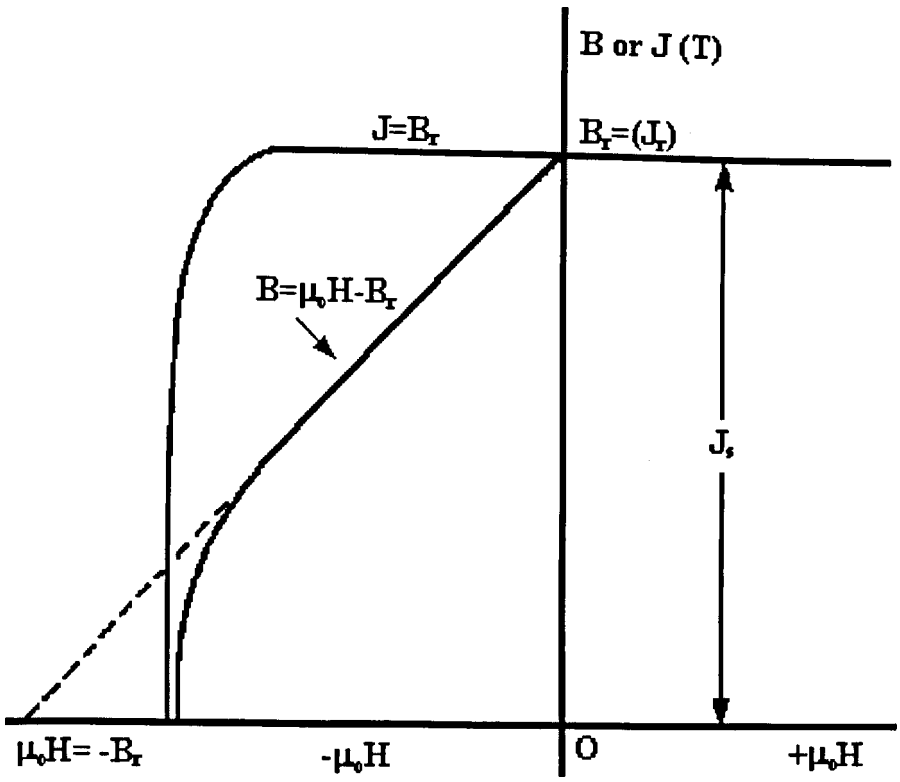

Figure 2- 3: Idealised J versus $\mu_0 H$ and B versus $\mu_0 H$ curves. The equations $J=B_r$ and $B=\mu_0 H+B_r$ are for the linear parts of the demagnetisation curves [24].

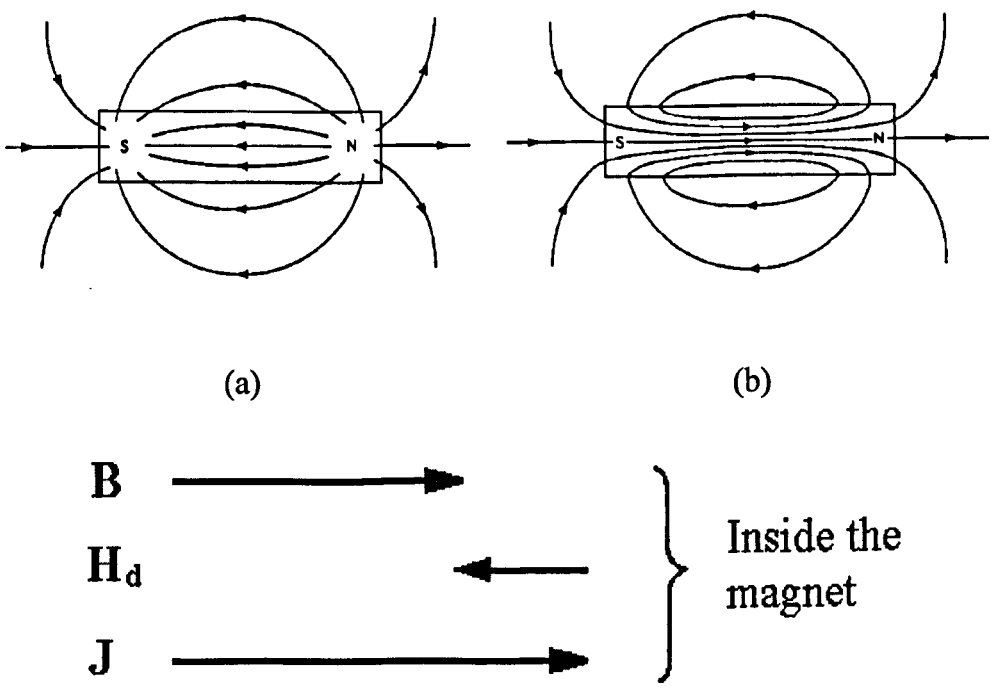

Figure 2- 4: a) Magnetic field H both inside and outside a bar magnet, b) Magnetic induction B both inside and outside a bar magnet [17].

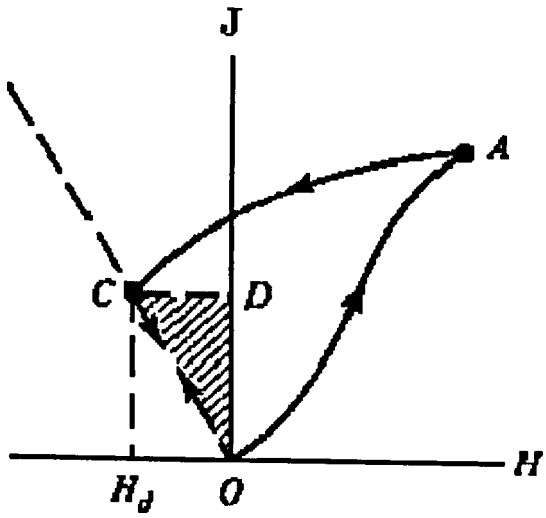

Figure 2- 5: Magnetostatic energy of a magnetised body in zero applied field [26].

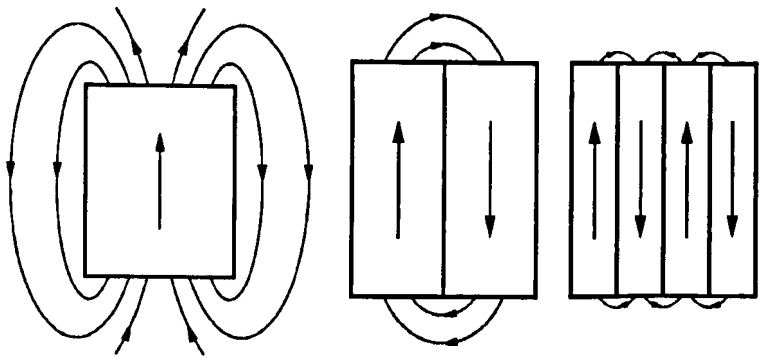

(a) (b) (c)

Figure 2- 6: The stray field of a) a uniformly magnetised specimen, and of a specimen divided into b) two, and c) four domains [18].

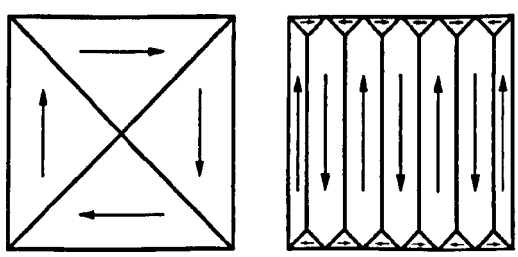

(a) (b)

Figure 2- 7: Two possible domain structures in a cubic single crystal [18].

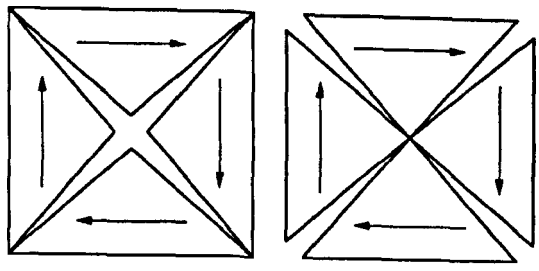

(a) (b)

Figure 2- 8: Possible elastic distortions in materials with a) positive and b) negative magnetostriction [18].

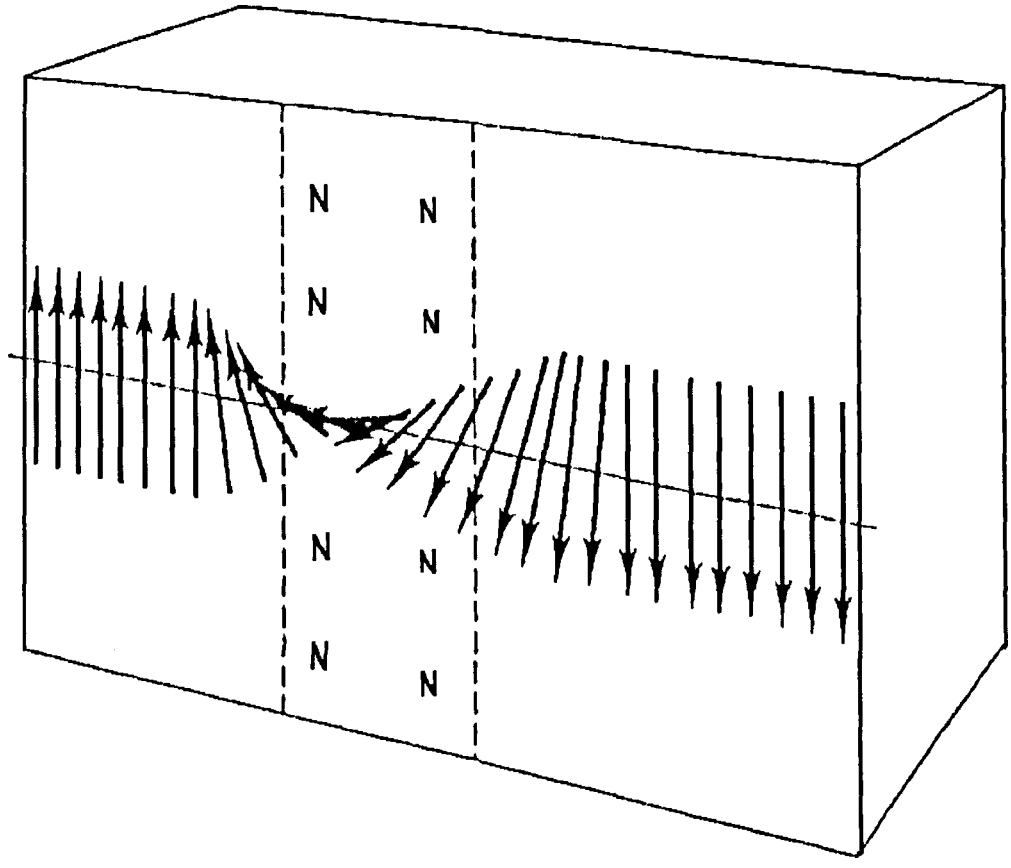

Figure 2- 9: Schematic of the alignment of individual magnetic moments within a 180° domain wall [17].

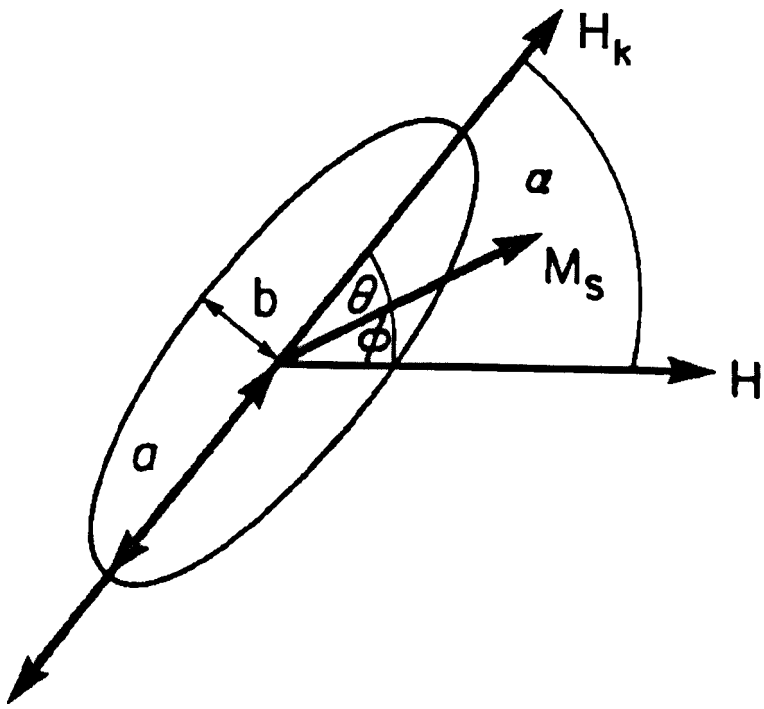

Figure 2- 10: Shape anisotropy of an ellipsoidal single-domain particle assumed to have neither crystal or stress anisotropy. The particle has higher demagnetising factor N_d along the short axis than along the long axis. This leads to shape anisotropy [17].

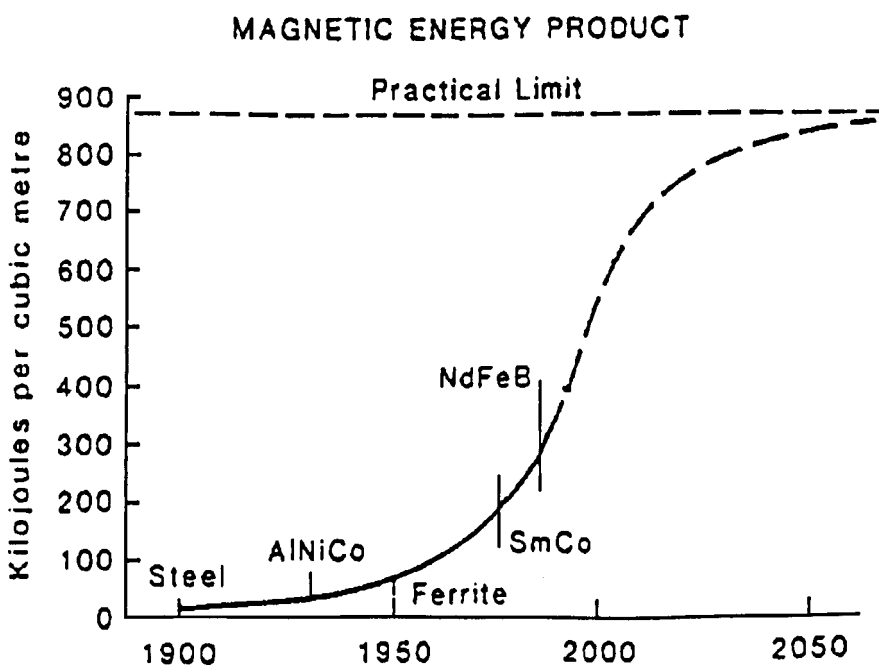

Figure 2- 11: Increase in the strength of magnets during this century, and a projection of how the limit for iron-based magnets may be approached [25].

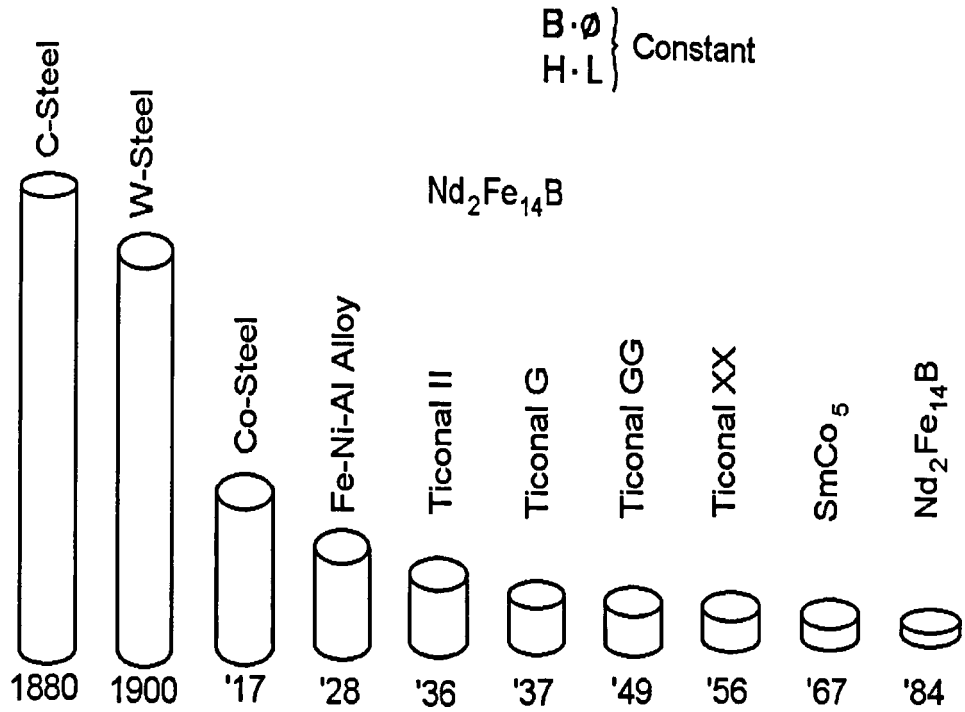

Figure 2- 12: Schematic representation of the strengths of different types of magnet material. The energy product increases steadily from left to right. The year of discovery is indicated at the bottom of the magnets [32].

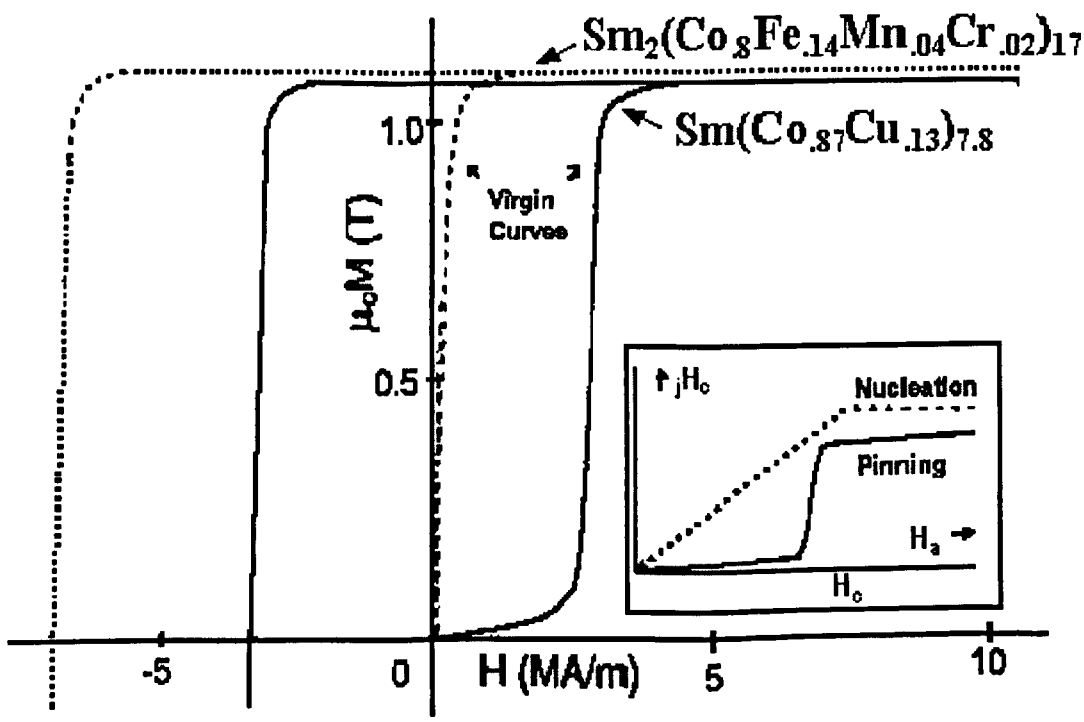

Figure 2- 13: Initial magnetisation curves and field dependence of coercivity in "nucleation" and "pinning"-type permanent magnets [29].

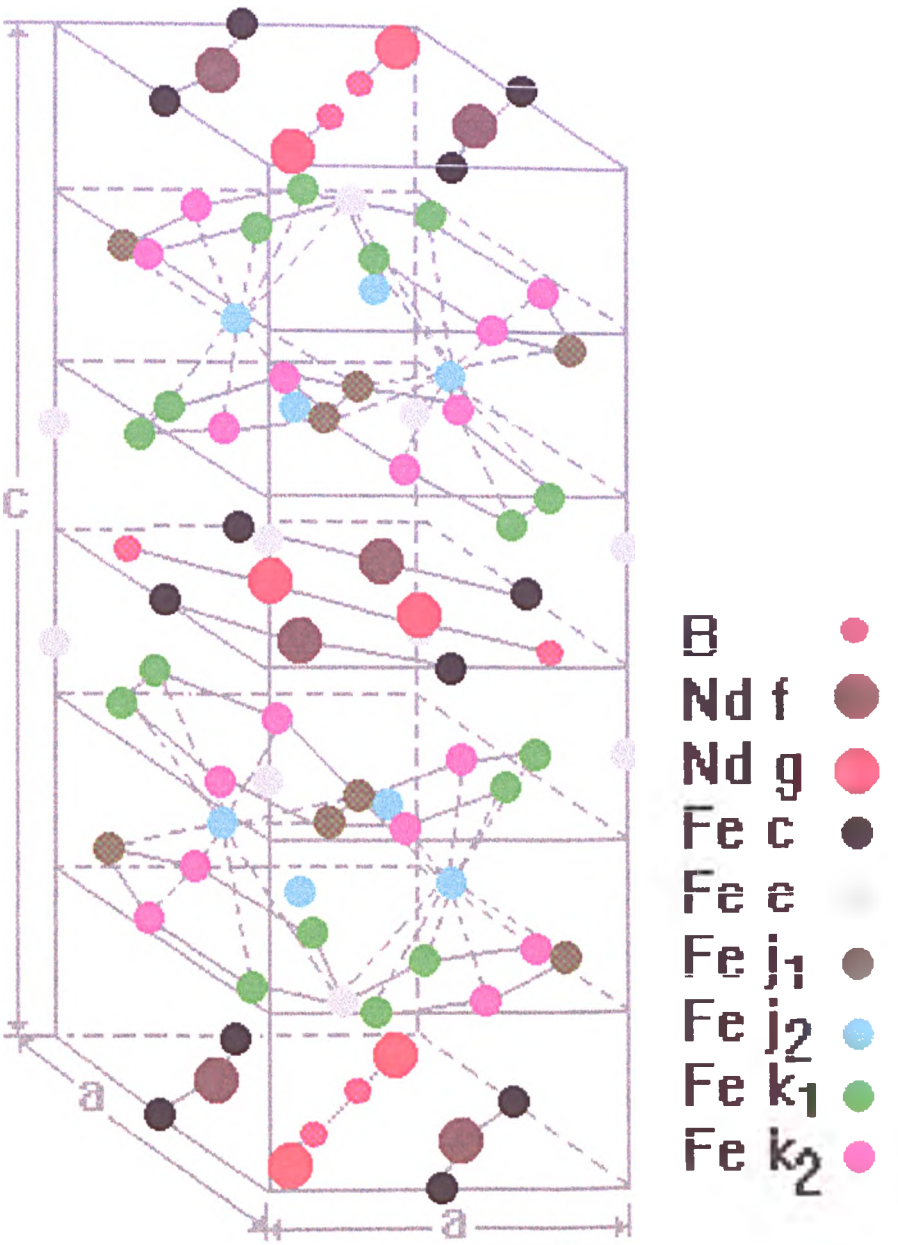

Figure 2- 14: Unit cell of $Nd_2Fe_{14}B$. The c/a ratio is exaggerated to emphasise the puckering of the hexagonal iron nets [2].

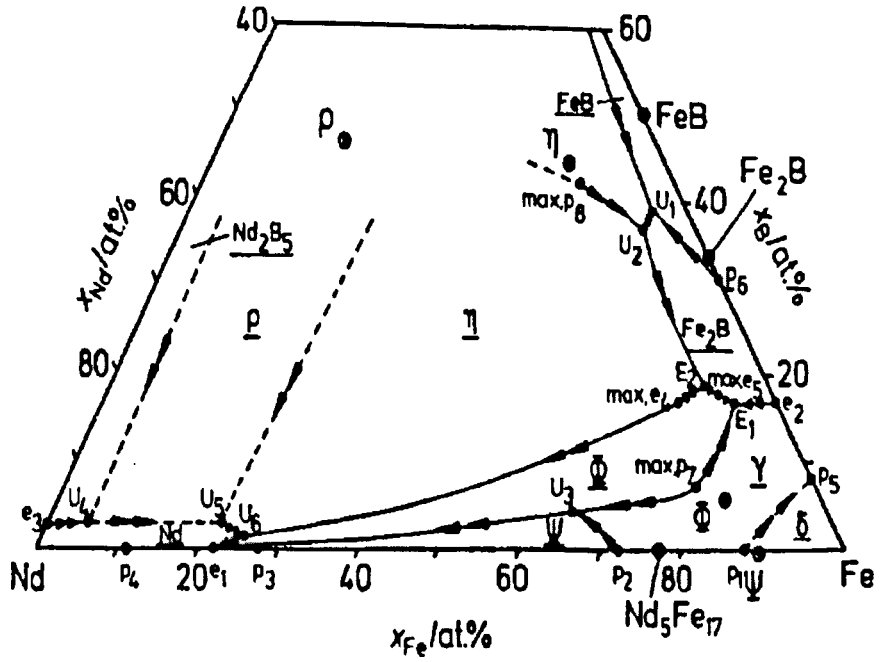

Figure 2- 15: Liquidus projection of the ternary phase diagram Nd-Fe-B (ϕ=$Nd_2Fe_{14}B$, η= $Nd_{1.1}Fe_4B_4$, ρ=$Nd_5Fe_2B_6$ and ψ=Nd_2Fe_{17}) [40].

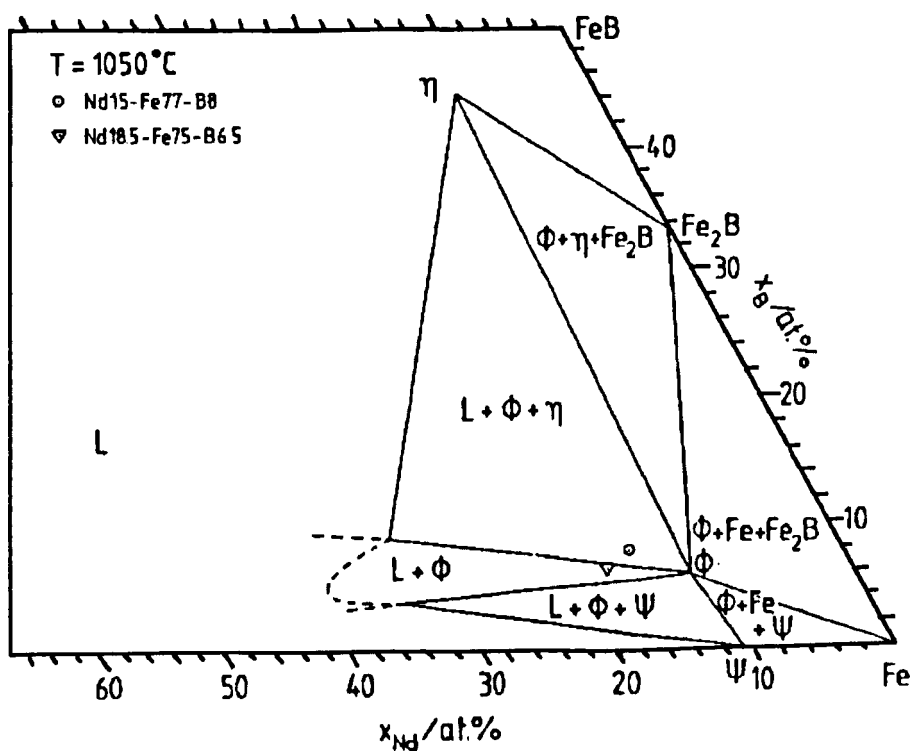

Figure 2- 16: Isothermal section of the Nd-Fe-B phase diagram at 1050°C [40].

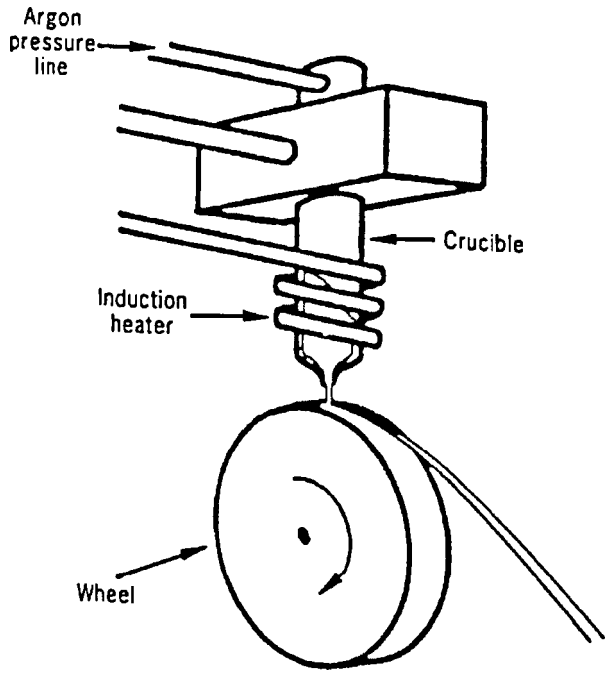

Figure 2- 17: A schematic of the rapid solidification process [1].

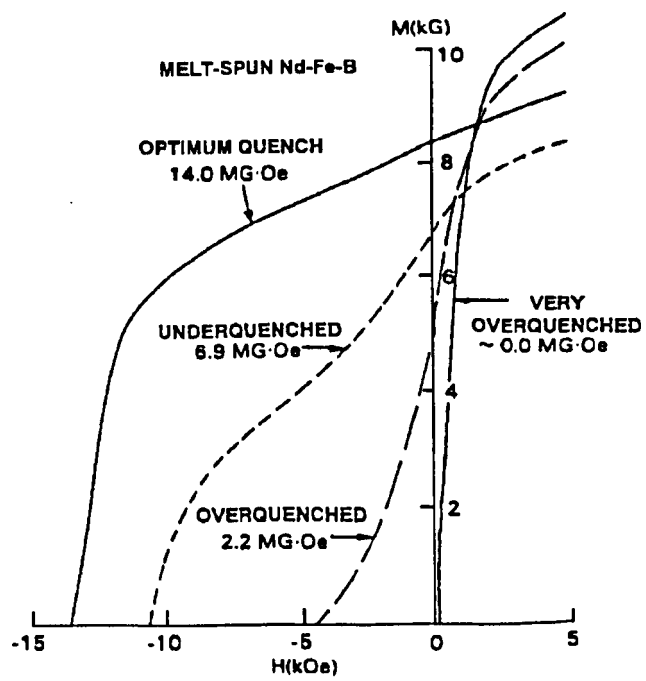

Figure 2- 18: Demagnetisation behaviour versus roll speed for melt-spun Nd-Fe-B ribbons [16].

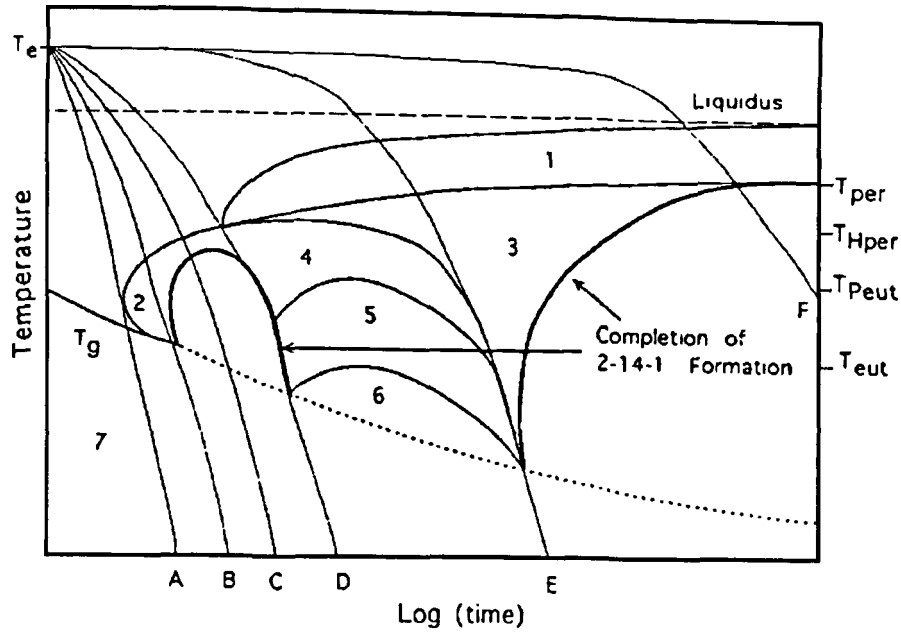

Figure 2- 19: Model CCT diagram for stoichiometric $Nd_2Fe_{14}B$. The reaction regions are labelled A-E are shown. Temperatures corresponding to the phase diagram of Figure 2- 20 are labelled on the Y-axis [69].

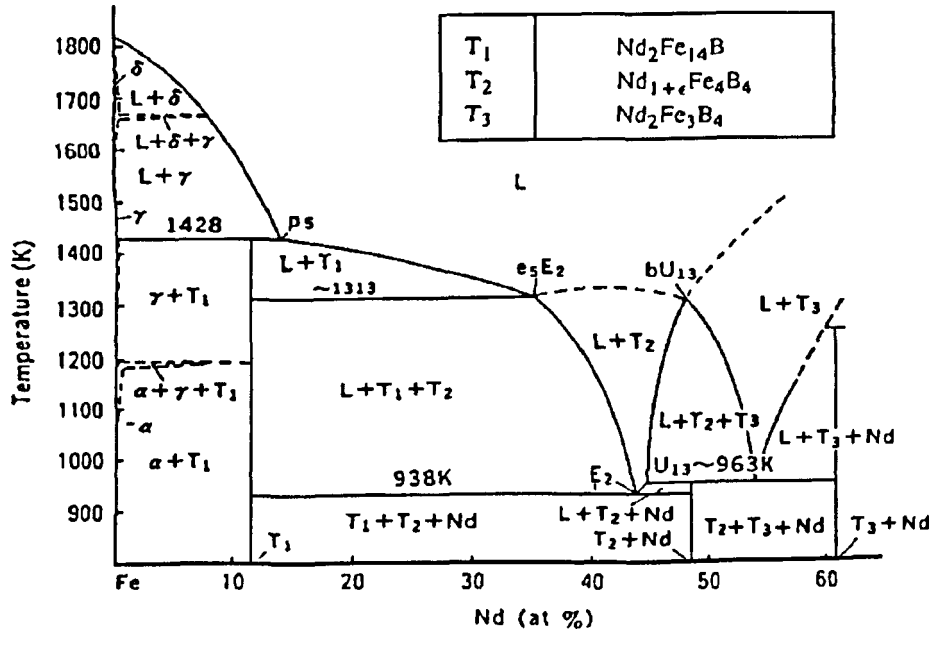

Figure 2- 20: A vertical section of the Nd-Fe-B phase diagram along the tie-line between Fe and T_1 [30].

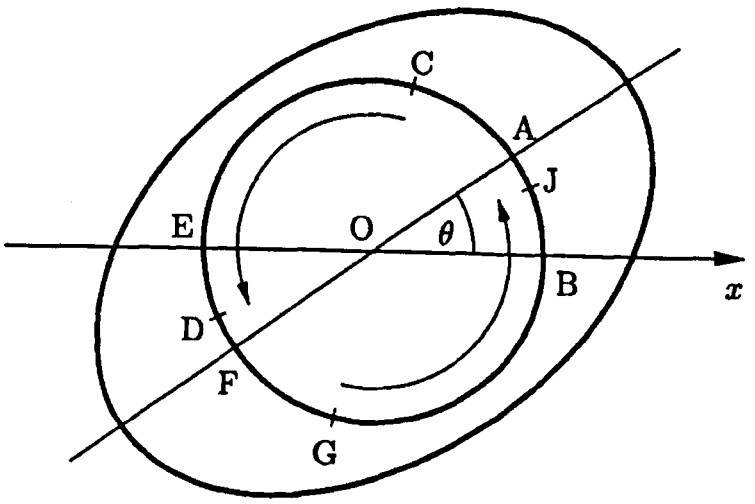

(a)

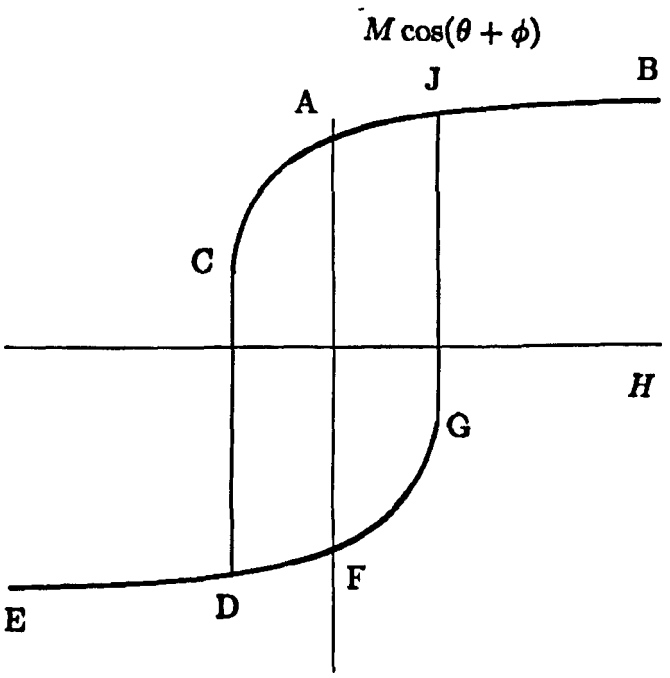

(b)

Figure 2- 21: a) Rotation of the magnetisation of a spheroidal particle in an applied field. b) The resulting magnetisation curve [18].

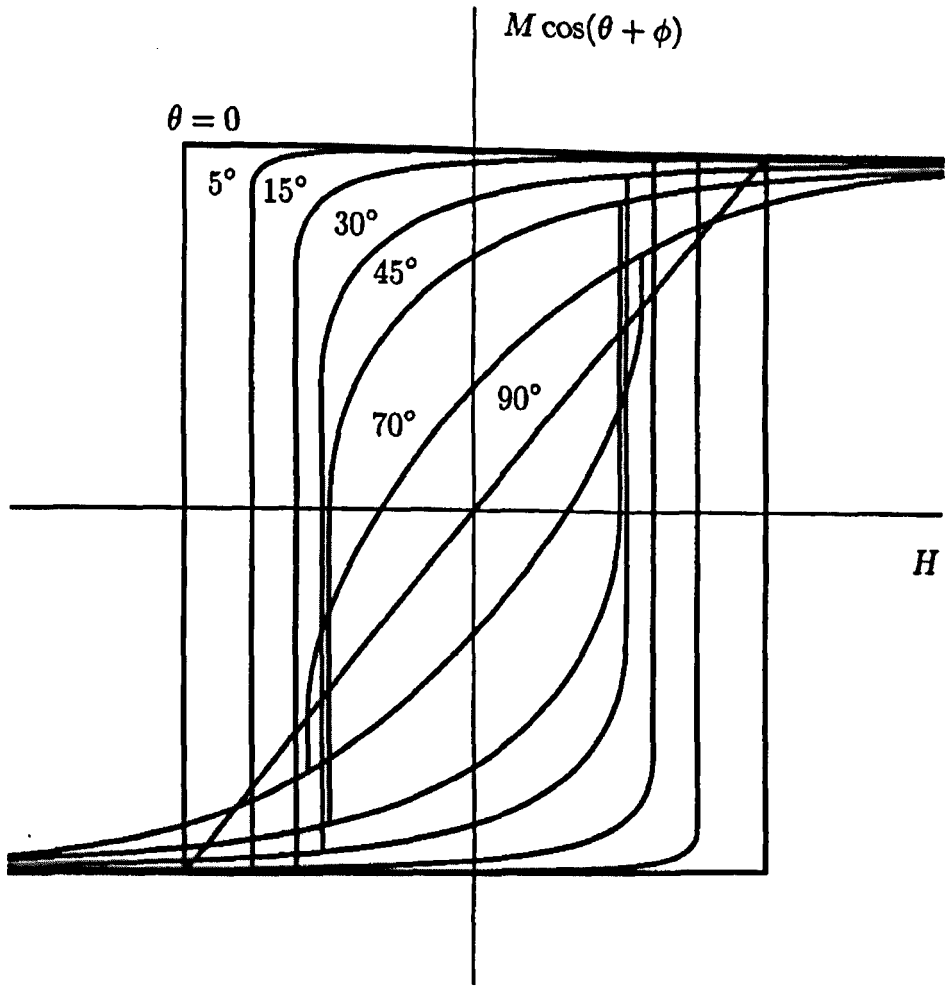

Figure 2- 22: Magnetisation curves for various values of the angle θ between the direction of the applied field and the easy axis, for coherent magnetisation rotation 18.

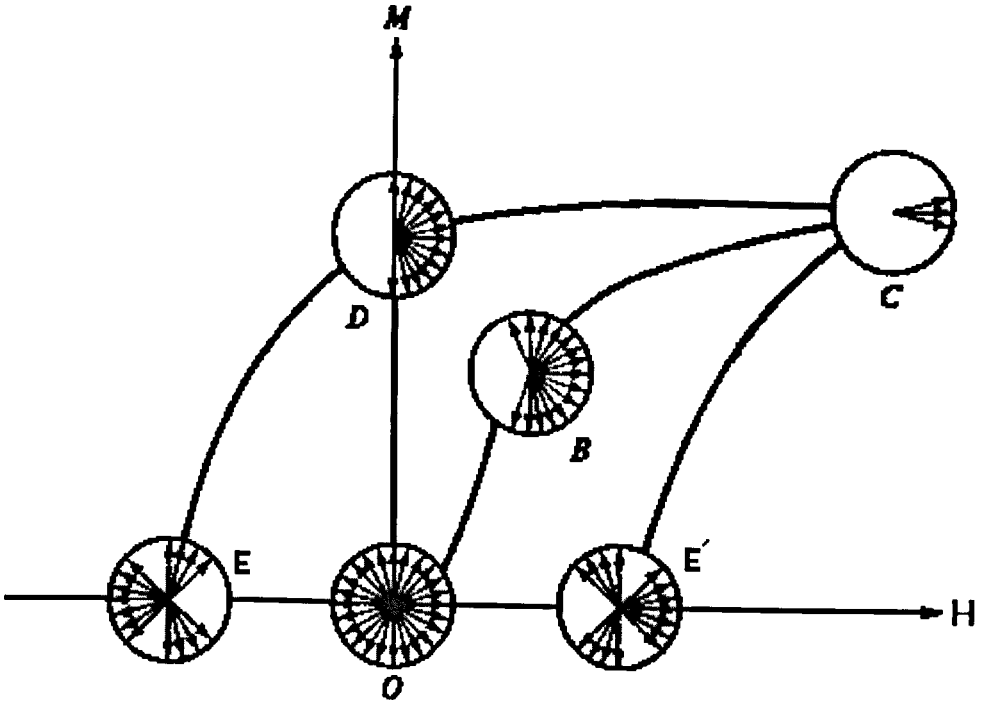

(a)

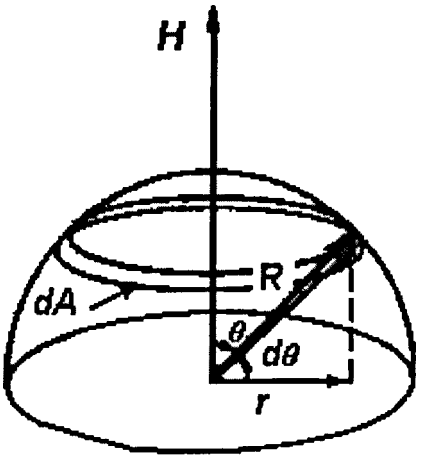

(b)

Figure 2- 23: Domain arrangements for various states of magnetisation [26].

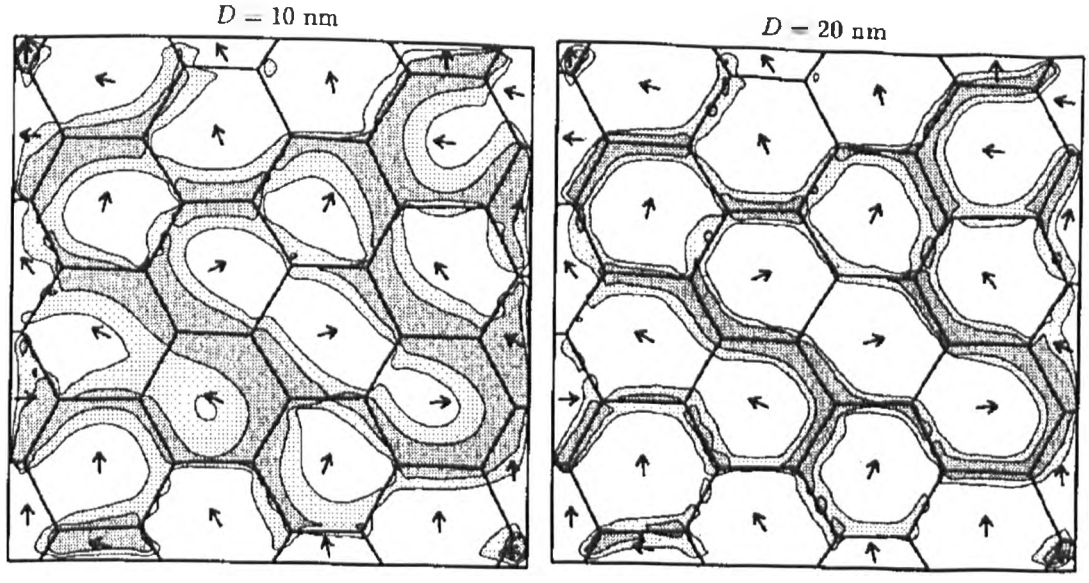

Figure 2- 24: Inhomogeneous regions along the grain boundaries. The arrows indicate the direction of the easy axes. The shaded areas denote the regions where the magnetic polarisation deviates from the local easy axis by more than 10° and 20°, respectively [113].

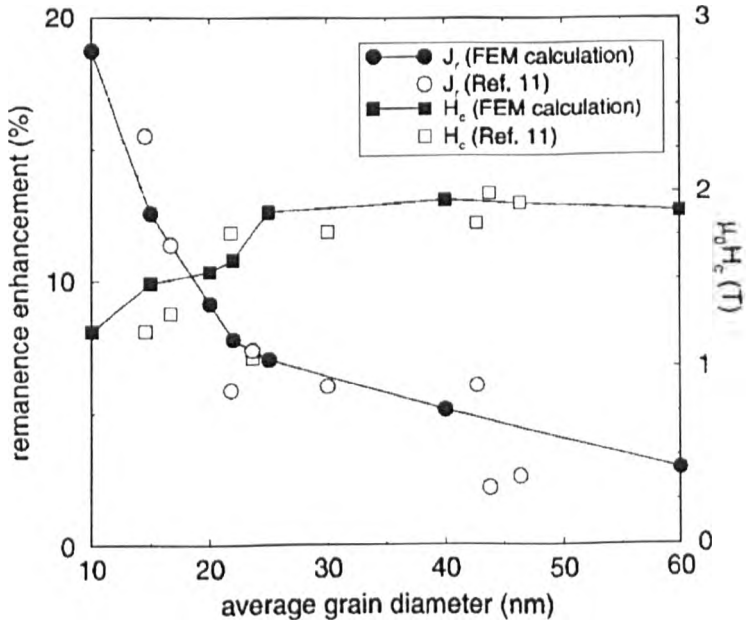

Figure 2- 25: Remanence and coercivity as a function of grain size. The remanence enhancement is given with respect to the theoretical limit for noninteracting particles. Circles: remanence enhancement; squares: coercive field. The open symbols refer to experimental values obtained by Manaf et al. [59] for $Nd_{13.2}Fe_{79.6}B_6Si_{1.2}$ melt spun ribbons [113].

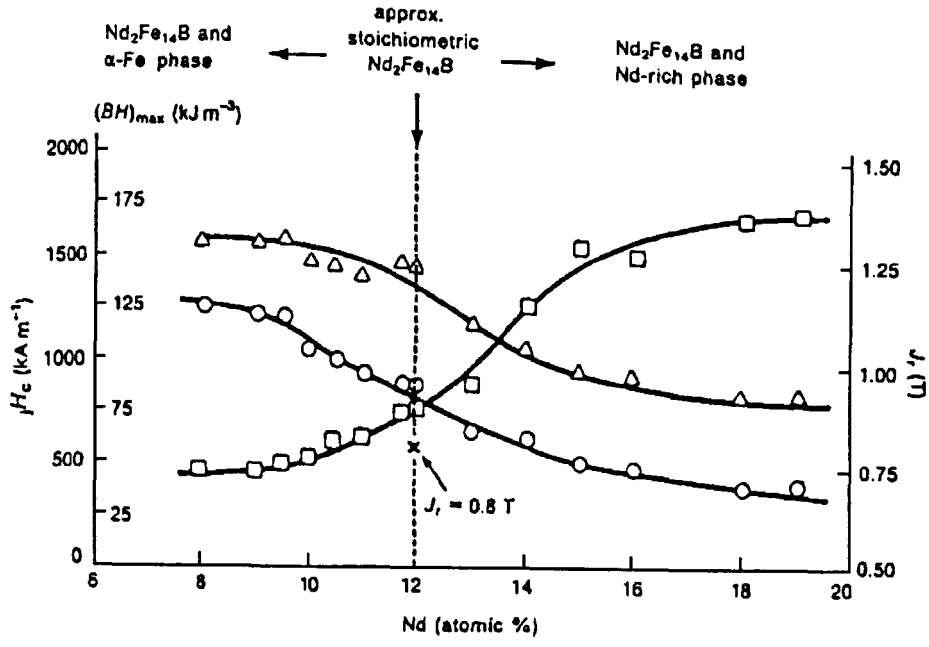

Figure 2- 26: The effect of neodymium content (8-19 at.%) on the magnetic properties of nanophase melt-spun neodymium-iron-boron alloy (with 6 at.% B). =coercivity, o= remanent polarisation and $\Delta=(BH)_{max}$. Mean $Nd_2Fe_{14}B$ crystallite size ~26-30 nm [227].

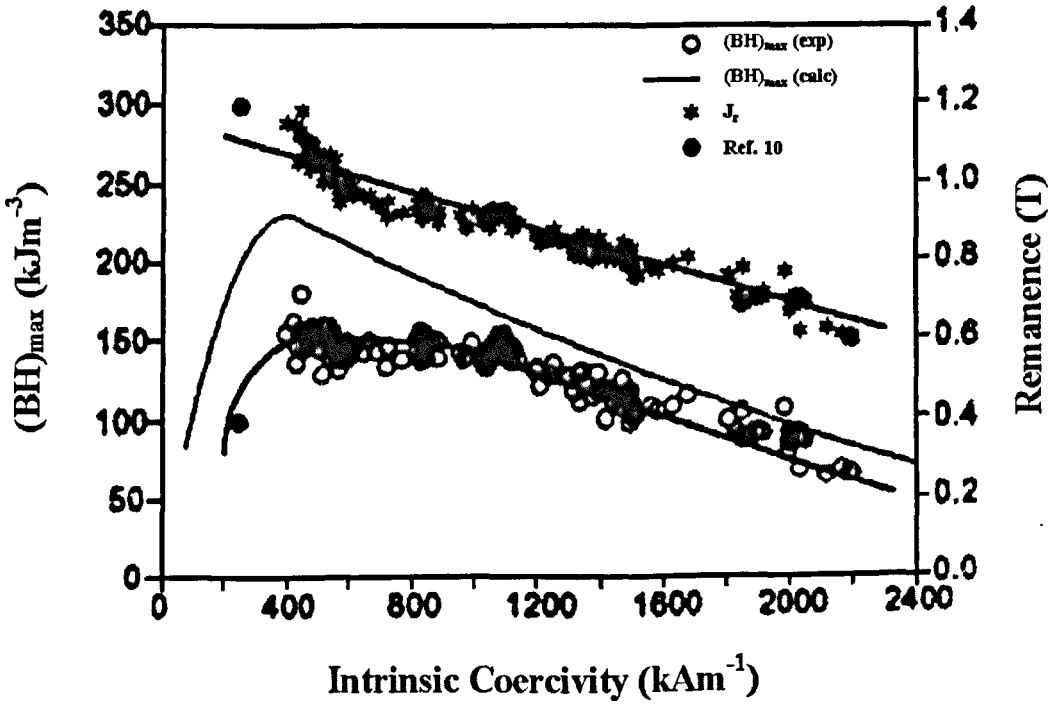

Figure 2- 27: Correlation between J_r and $_jH_c$ for a wide range of as-cast ribbons. The lowest coercivity point (Ref. 10) appertaining to a very low Nd containing $Nd_4Fe_{78}B_{18}$ alloy is included from the work of Coehoorn et al. [15]. Data $_jH_c$<1600 kAm^{-1} represent alloy $Fe_{79.6}Nd_{13.2}B_6Si_{1.2}$ while those for <500 kAm^{-1} and >1600 kAm^{-1} represent alloys of typical compositions $Fe_{85}Nd_9B_6$ and $Fe_{76}Nd_{18}B_6$, respectively [114].

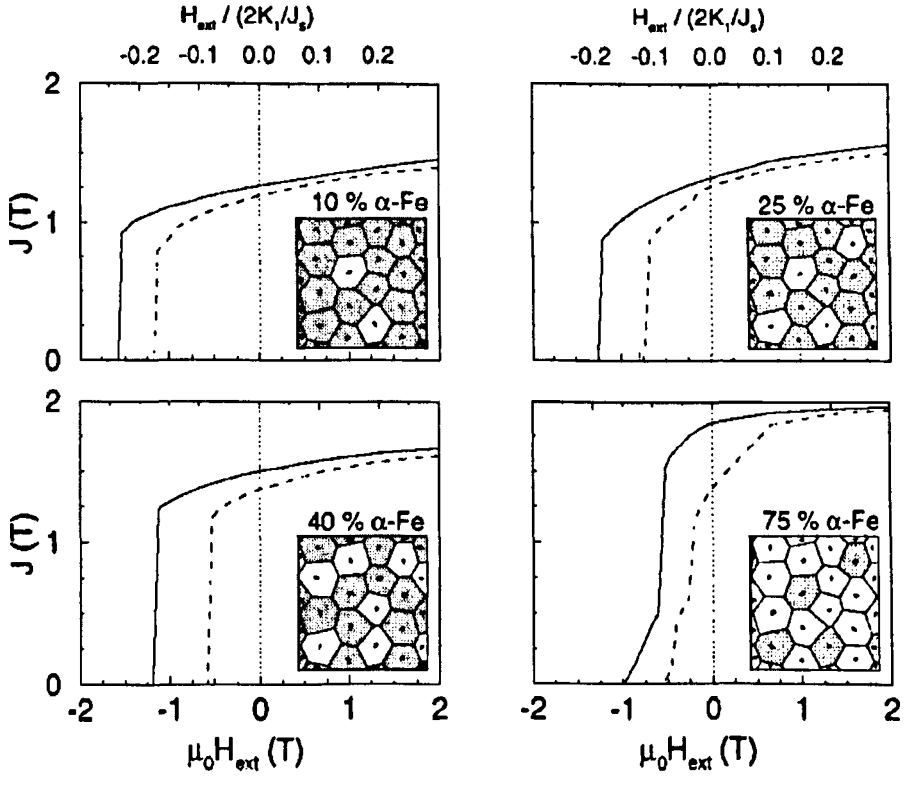

Figure 2- 28: Demagnetisation curves of isotropic two-phase permanent magnets. The insets show the corresponding microstructures. The arrows indicate the direction of the easy axes. The open and shaded grains denote the soft and hard magnetic phases, respectively. Continuous and dashed curves correspond to 10 and 20 nm mean grain sizes, respectively [113].

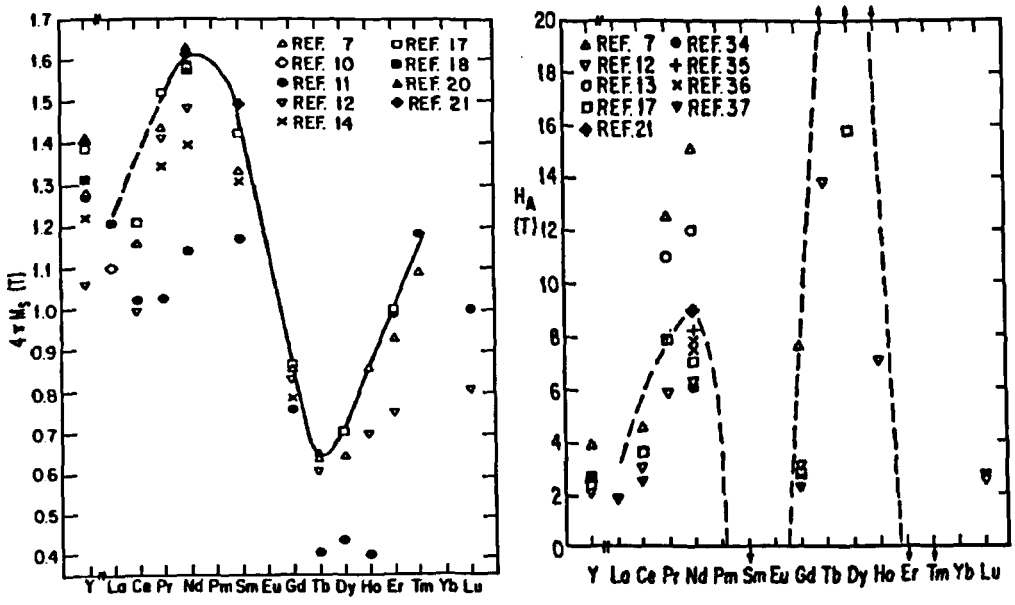

(a) (b)

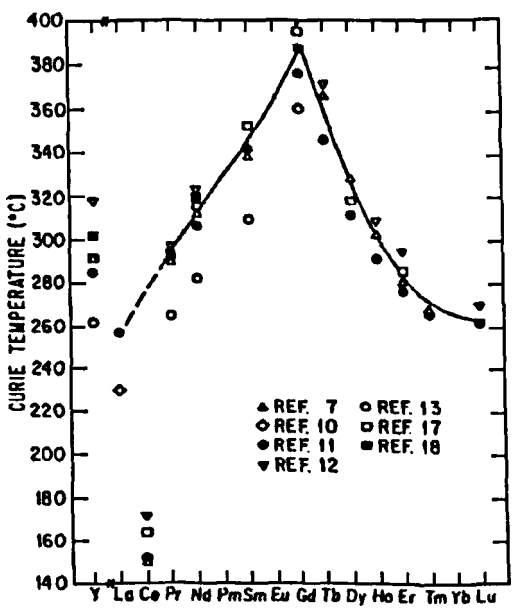

(c)

Figure 2- 29: Reported a) magnetisations, b) anisotropy fields and c) Curie temperatures of $Fe_{14}R_2B$ compounds [138].

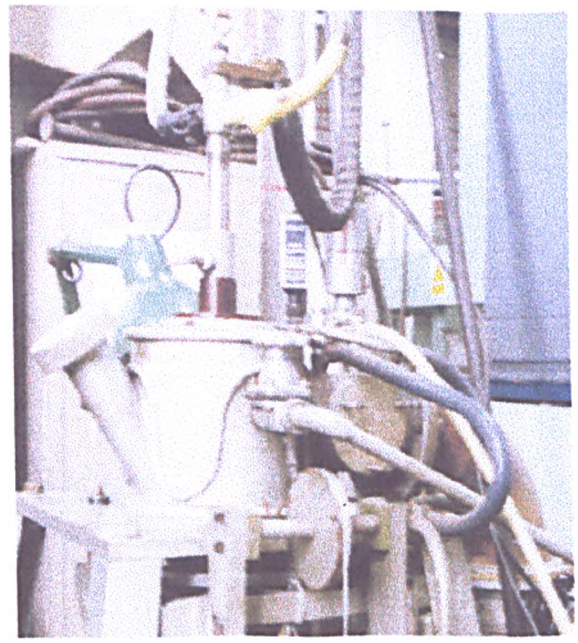

Figure 3- 1: A laboratory scale argon arc melting furnace.

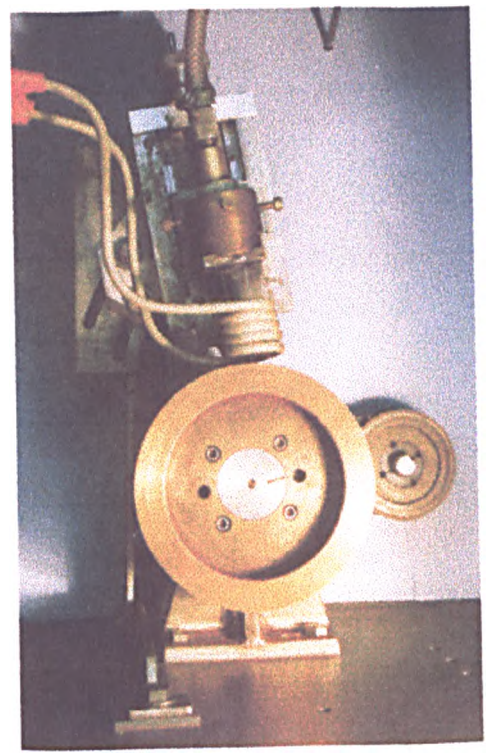

Figure 3- 2: Chill block melt-spinner.

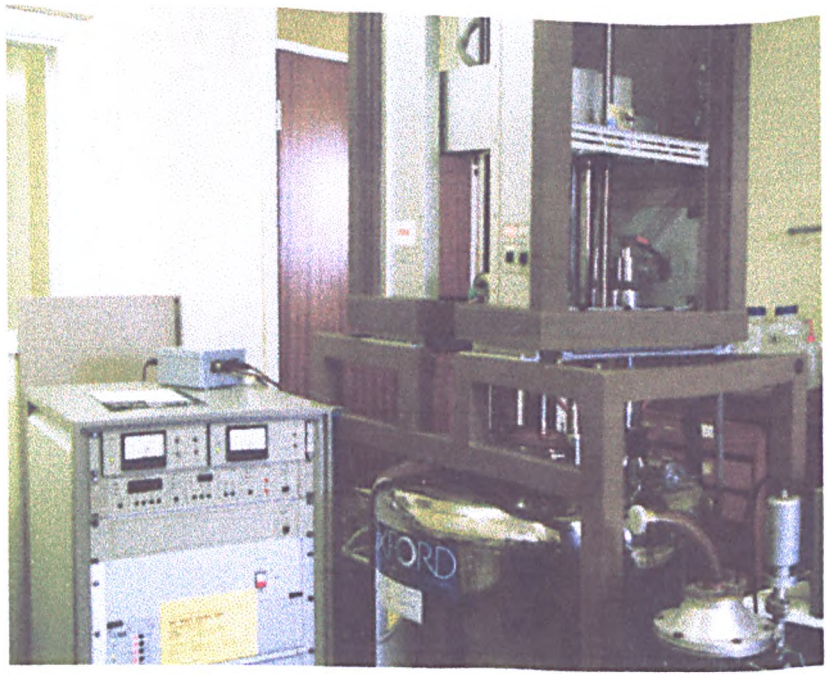

Figure 3- 3: Vibrating sample magnetometer.

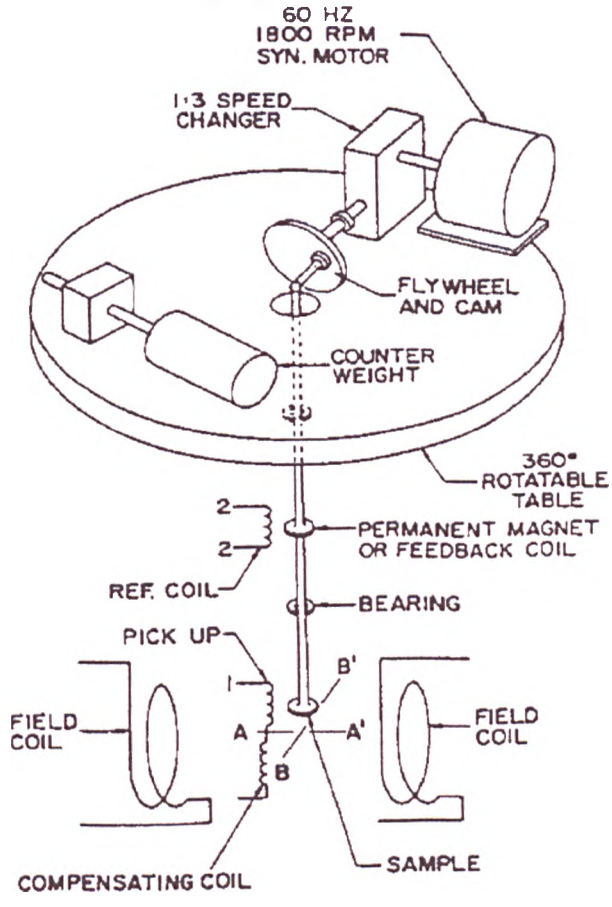

Figure 3- 4: Schematic diagram of a vibrating sample magnetometer (VSM.) [17].

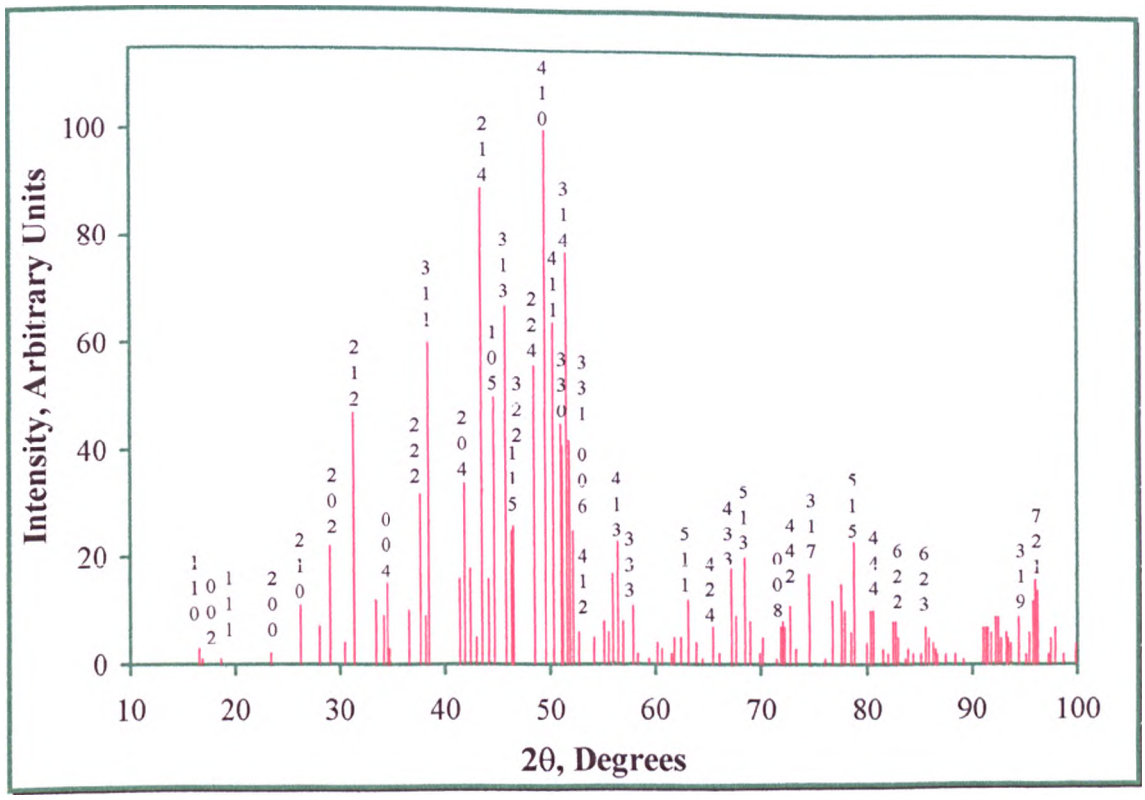

Figure 3- 5: Schematic representation of X-ray diffraction traces from JCPDS Powder Diffraction File for $Nd_2Fe_{14}B$.

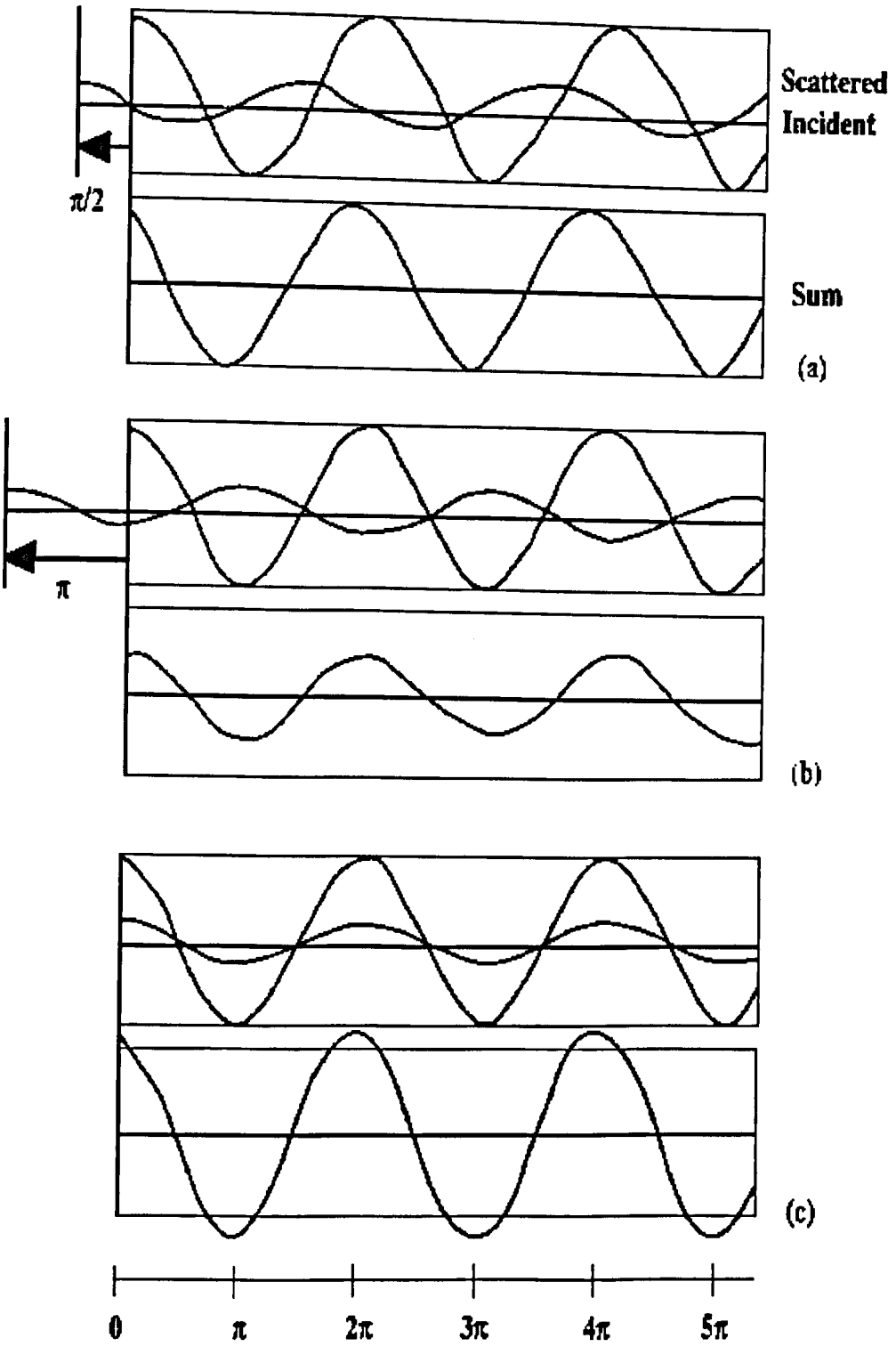

Figure 3- 6: The effect of the phase difference between transmitted and scattered beams when recombined by the objective lens: a) a phase difference of $\pi/2$ gives a sum wave with the same intensity as the transmitted wave, and therefore no contrast, b) a phase difference of π gives a reduced sum wave intensity and consequently the atoms appear black, c) a phase difference of 2π or 0 gives bright atoms [208].

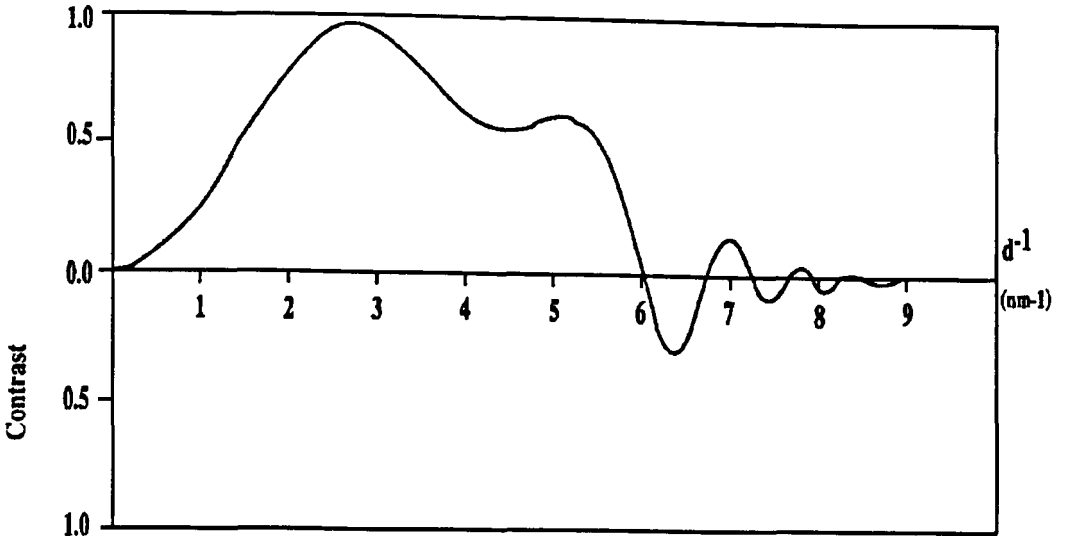

Figure 3- 7: Computer generated contrast transfer function for a Jeol 3010-UHR for the Scherzer defocus. The first zero indicates a point resolution of 0.17 nm, which can be verified using optical diffraction of a HREM negative taken from an amorphous thin film under ideal conditions [208].

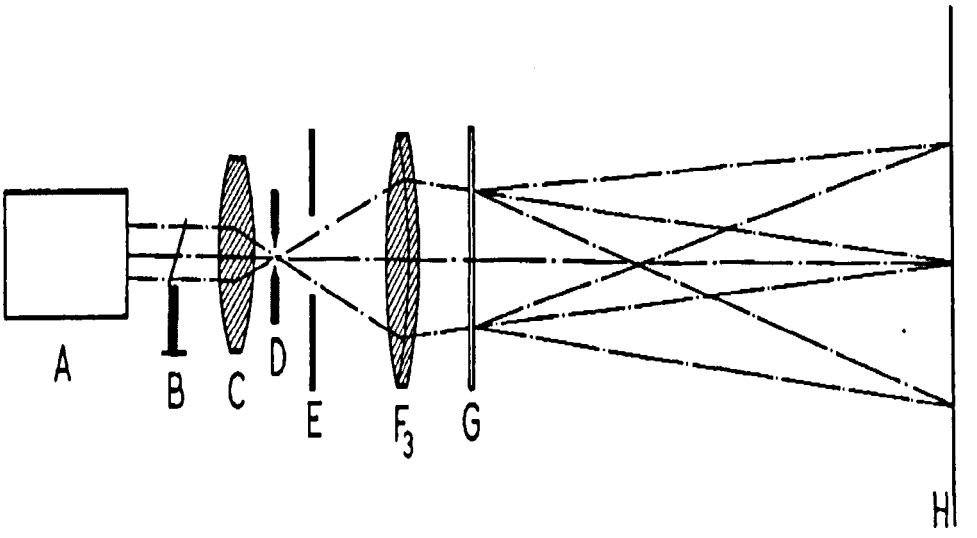

Figure 3- 8: Simple optical diffractometer. The diagram shows the arrangement of the components used to construct a simple optical diffractometer. A, laser; B, shutter; C, beam expanding lens; D, pinhole; E, adjustable diaphragm; F, diffraction lens; G, electron micrograph; and H, viewing screen or camera [210].

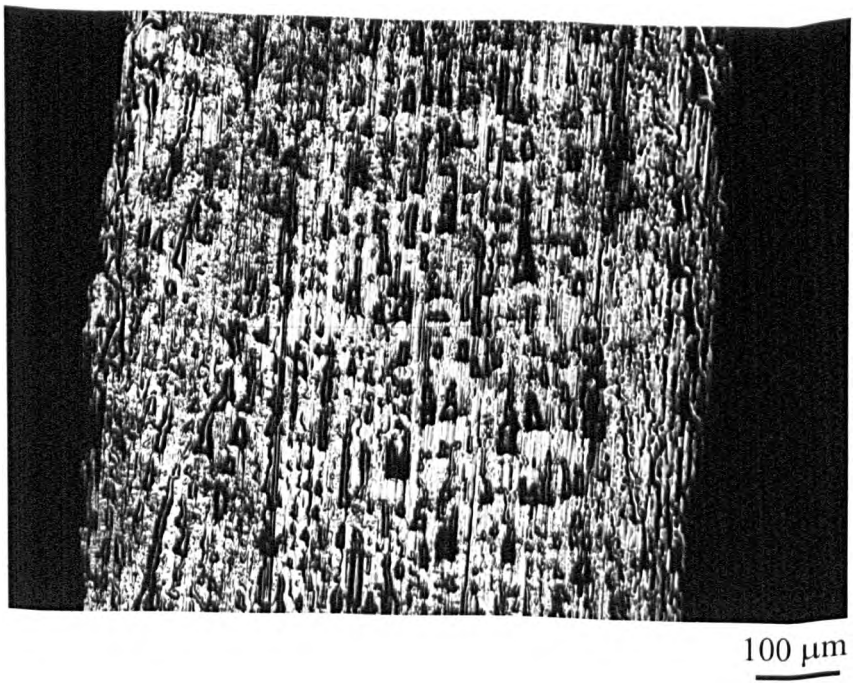

Figure 4- 1: Optical micrograph of roll contact surface of $Fe_{83.2}Nd_{10.9}B_{5.9}$ alloy melt spun at 19 m/s.

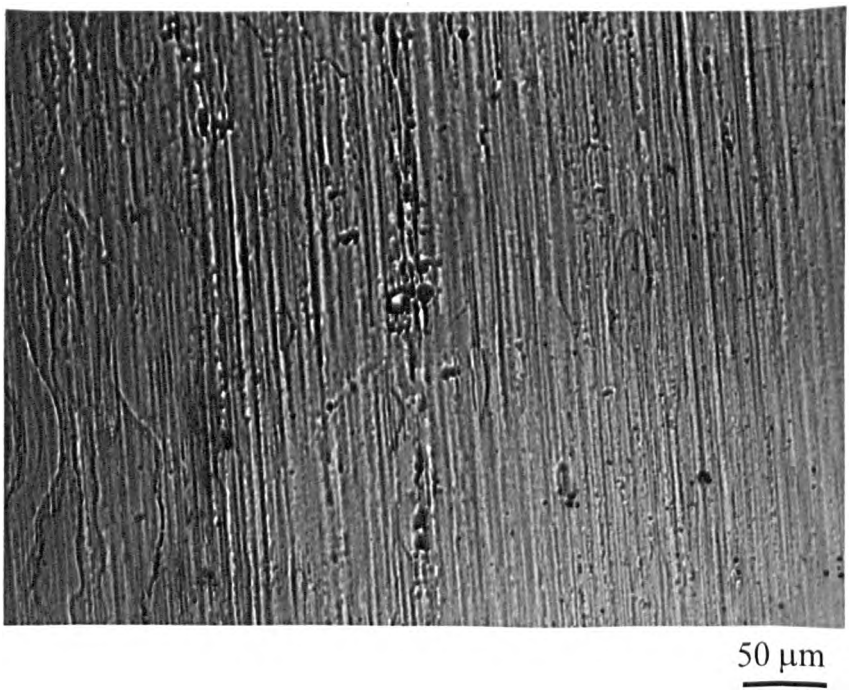

Figure 4- 2: Optical micrograph of roll contact surface of $Fe_{83.2}Nd_{10.9}B_{5.9}$ alloy melt spun at 8 m/s.

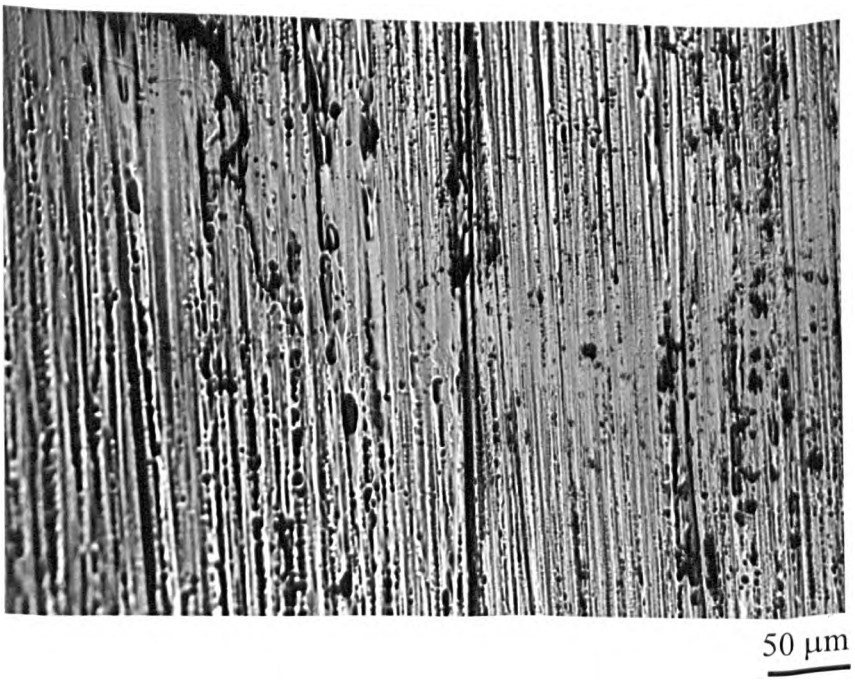

Figure 4- 3: Optical micrograph of roll contact surface of stoichiometric alloy melt spun at 20 m/s in vacuum.

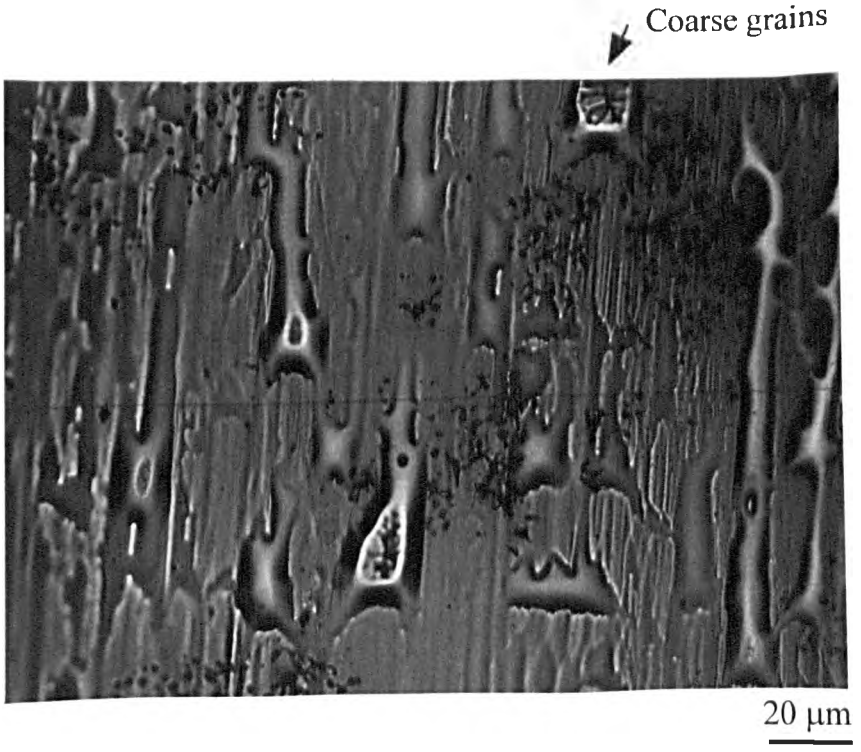

Figure 4- 4: Optical micrograph of roll contact surface of $Fe_{83.2}Nd_{10.9}B_{5.9}$ alloy melt spun at 19 m/s.

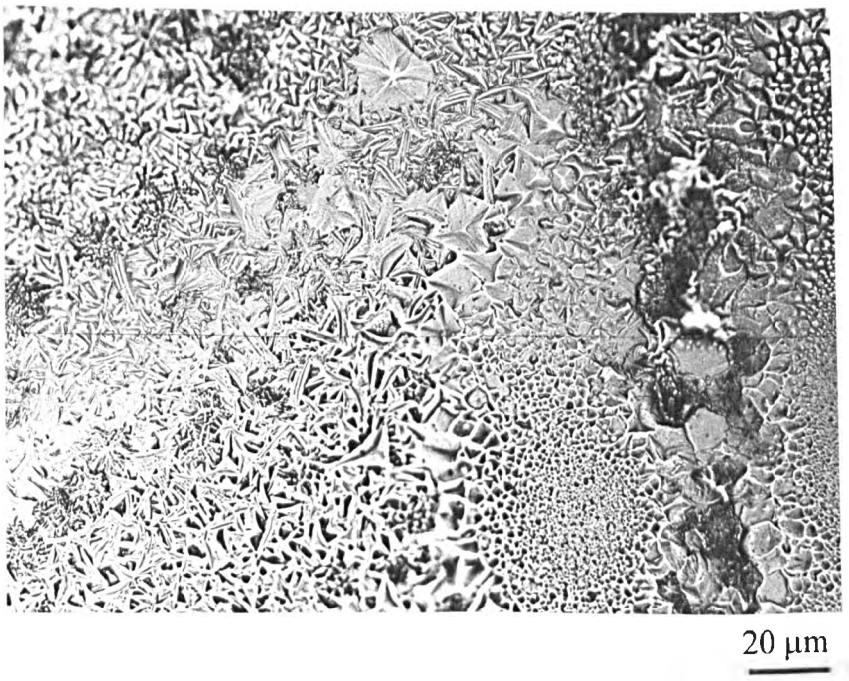

Figure 4- 5: Optical micrograph of free (non-contact) surface of $Fe_{83.2}Nd_{10.9}B_{5.9}$ alloy melt spun at 19 m/s.

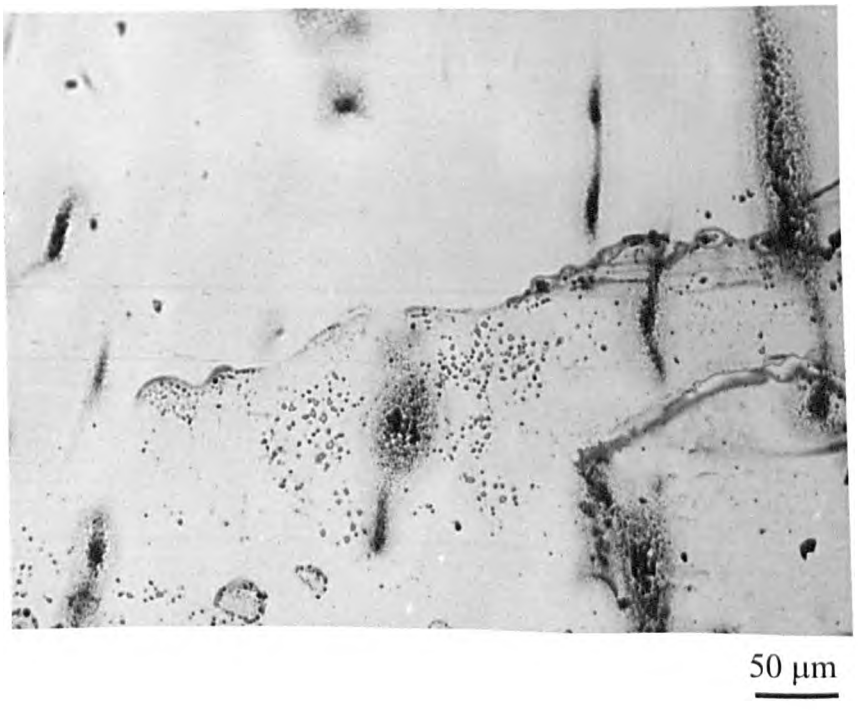

Figure 4- 6: Optical micrograph of free (non-contact) surface of $Fe_{83.2}Nd_{10.9}B_{5.9}$ alloy melt spun at 20 m/s.

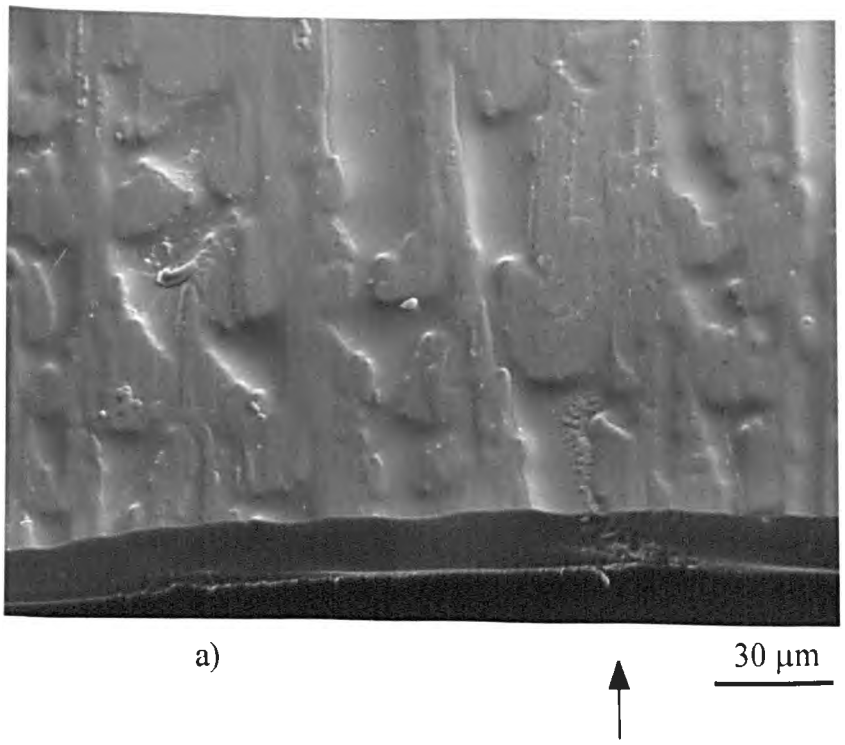

Figure 4- 7: a) SEM micrograph of roll contact surface and transverse cross section of $Fe_{83.2}Nd_{10.9}B_{5.9}$ alloy melt spun at 22 m/s, b) the area underneath the gas pocket at higher magnification.

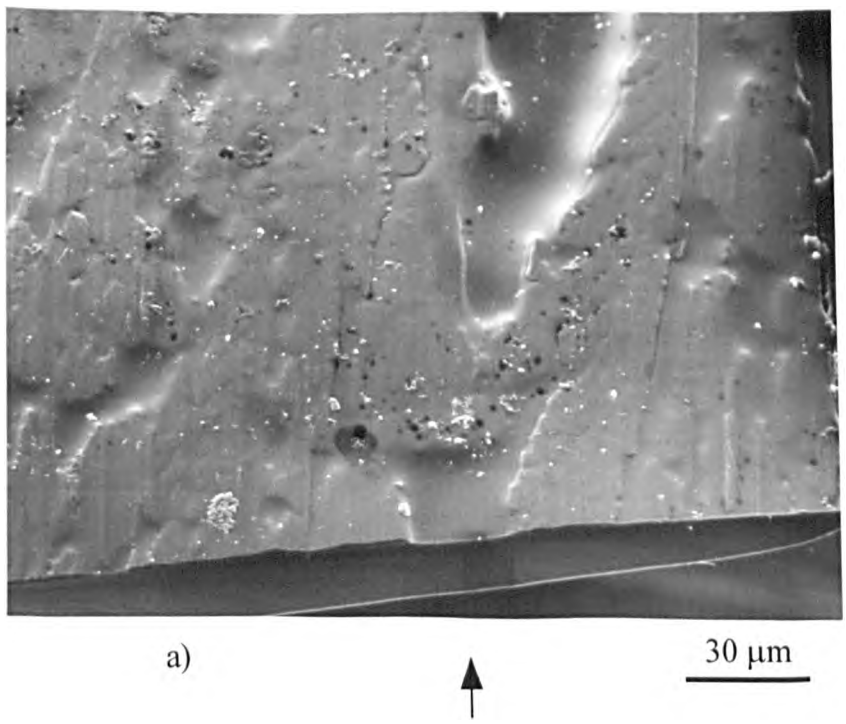

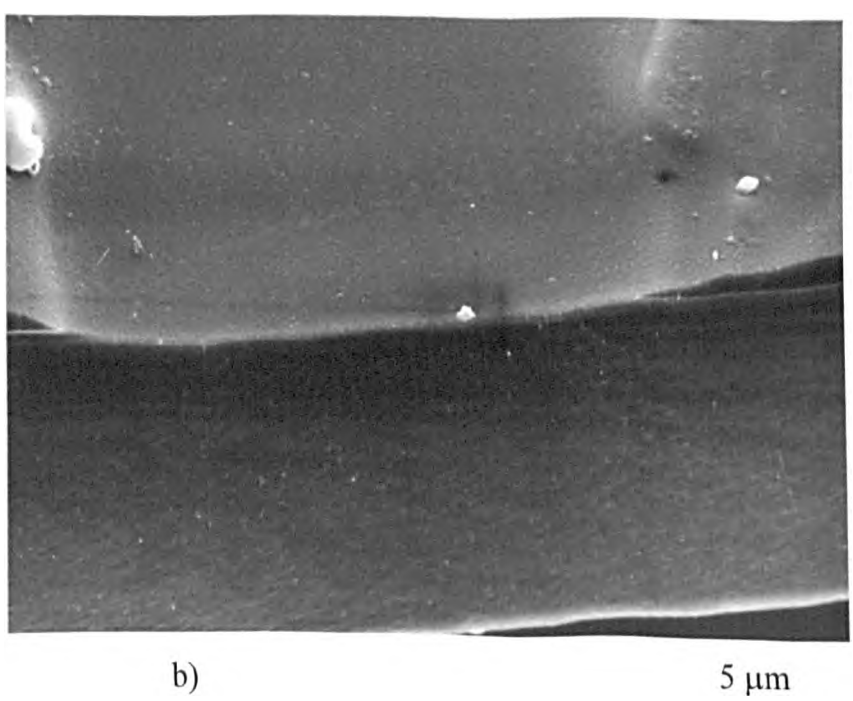

Figure 4- 8: a) SEM micrograph of roll contact surface and transverse cross section of $Fe_{83.2}Nd_{10.9}B_{5.9}$ alloy melt spun at 20 m/s, b) the area underneath the gas pocket at higher magnification.

Figure 4- 9: SEM micrograph of roll contact surface and transverse cross section of $Fe_{83.2}Nd_{10.9}B_{5.9}$ alloy melt spun at 19 m/s.

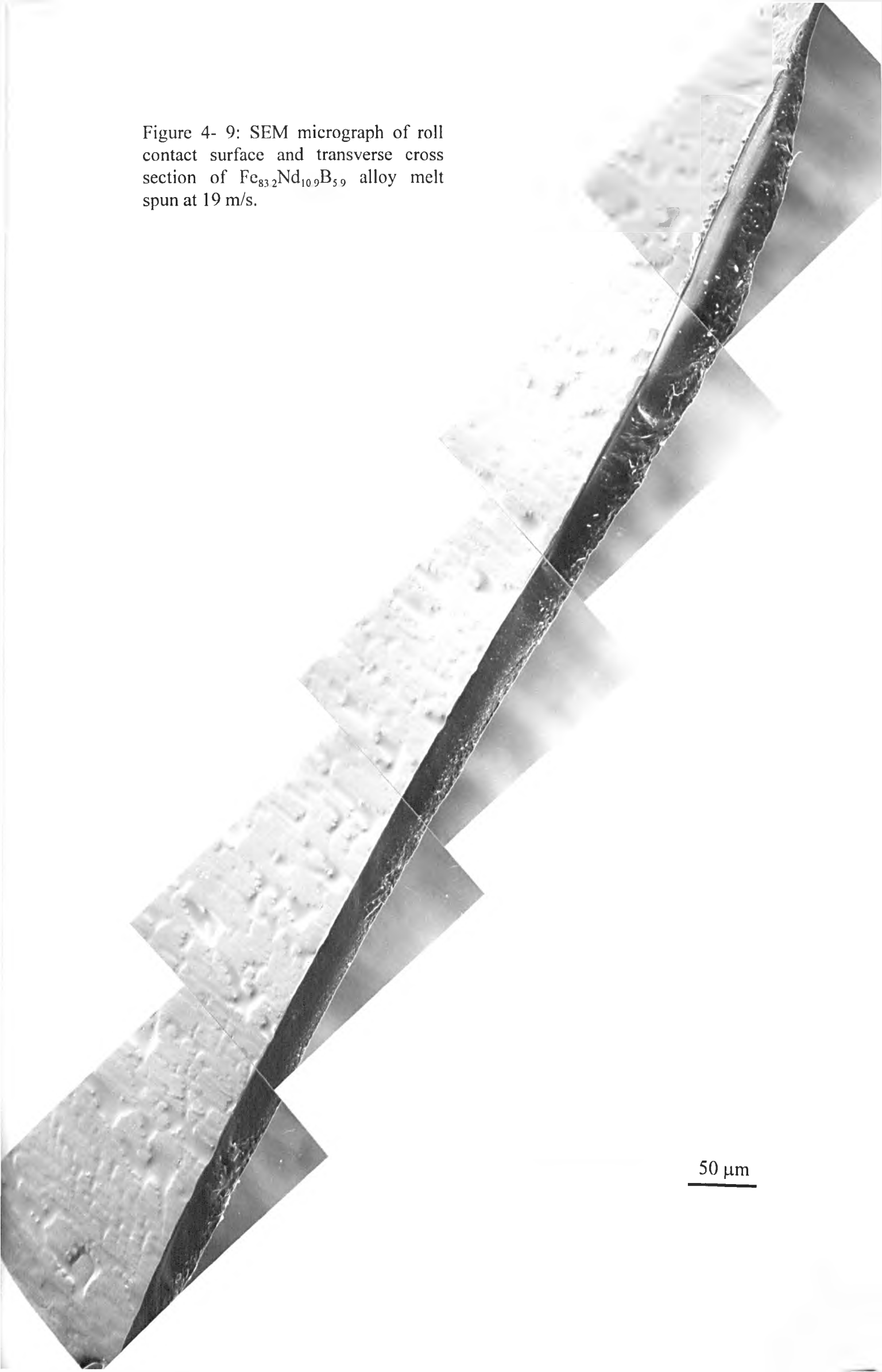

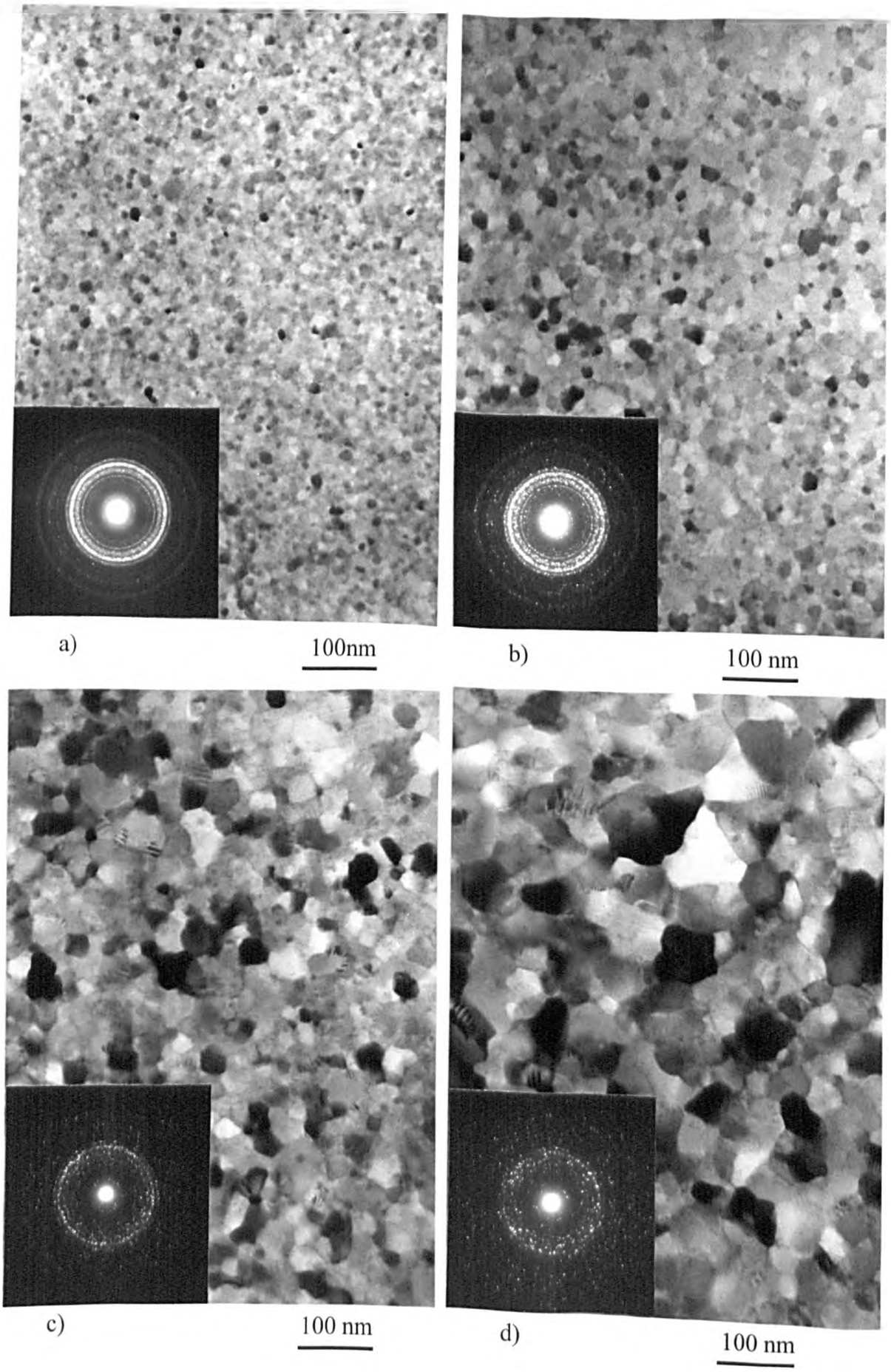

Figure 4- 10: TEM bright field images and corresponding diffraction patterns of $Fe_{79.8}Nd_{11.8}B_{5.9}Ga_{2.5}$ sample melt spun at 21.5 m/s, showing different grain sizes observed in a TEM thin foil sample.

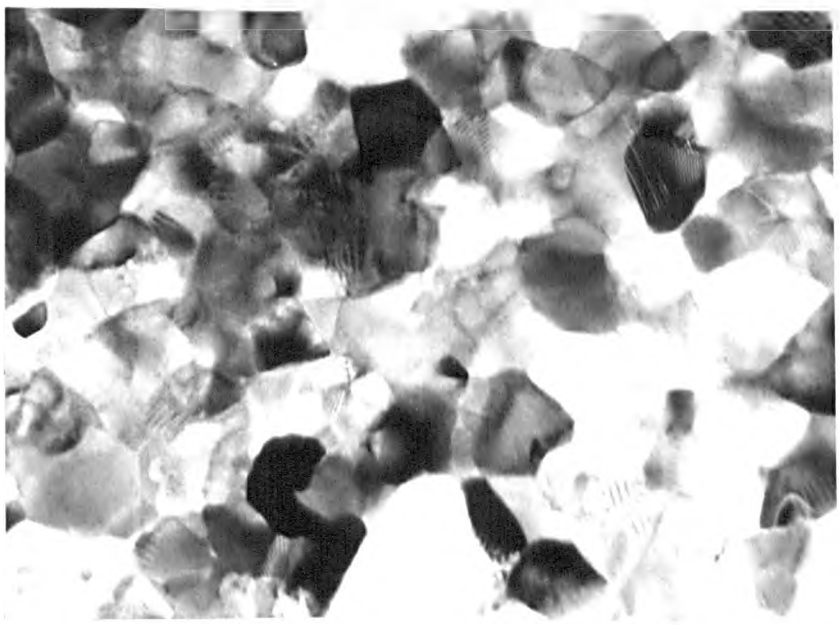

e) 100nm

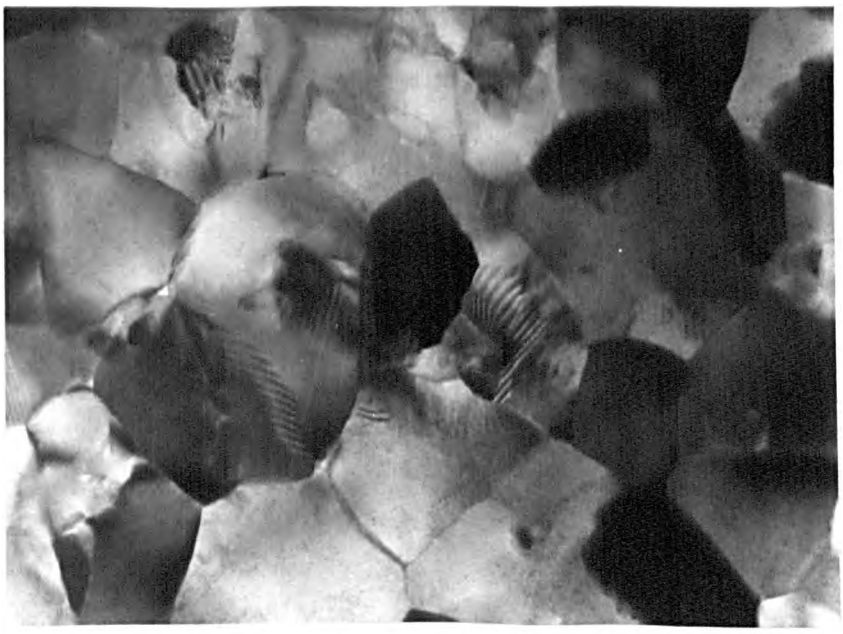

f) 100 nm

Figure 4- 10, continued.

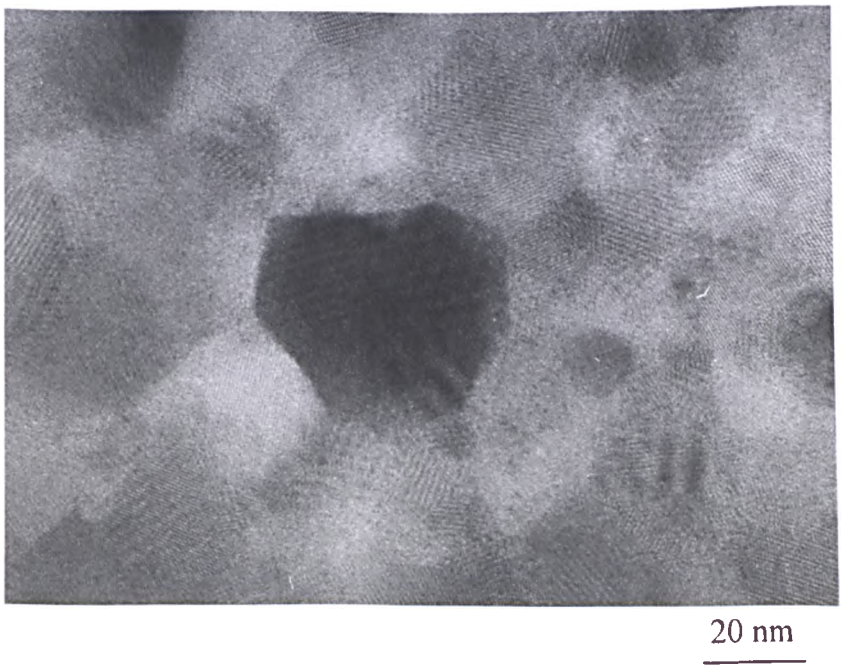

Figure 4- 11: High resolution TEM for $Fe_{82.3}Nd_{11.8}B_{5.9}$ alloy melt spun at 22 m/s.

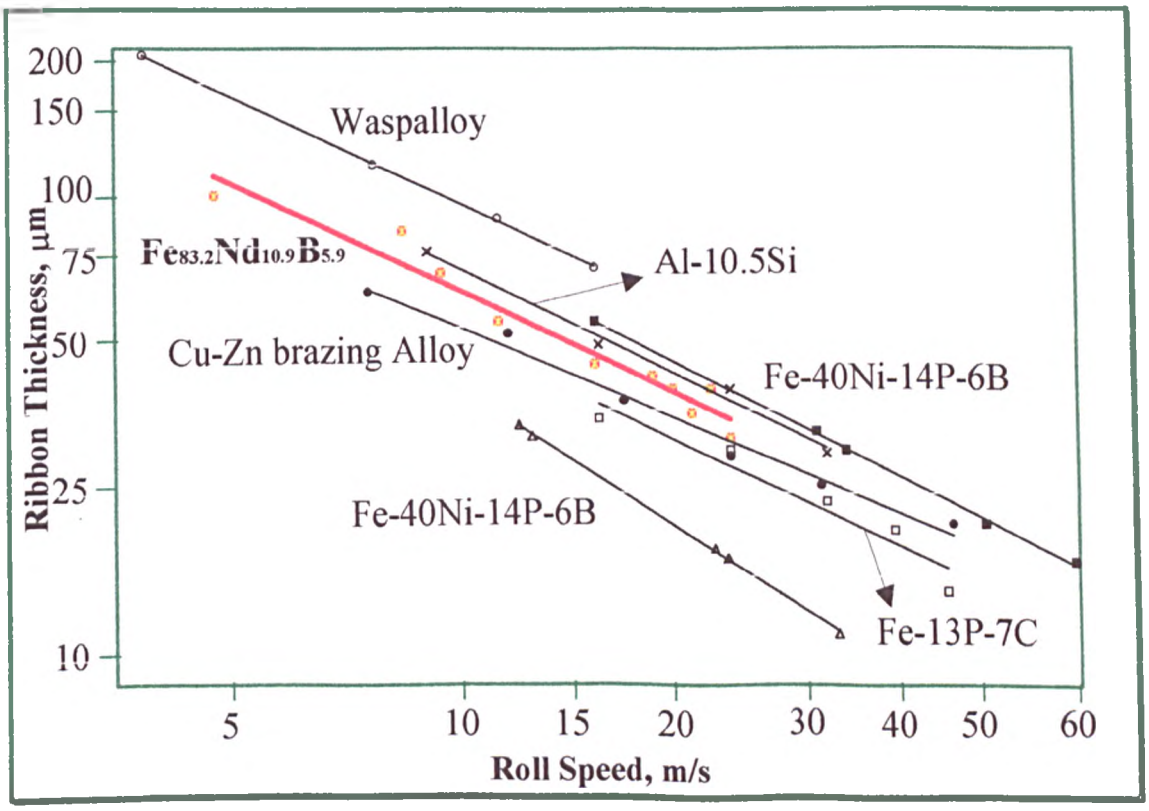

Figure 4- 12: Roll speed dependence of ribbon thickness for $Fe_{83.2}Nd_{10.9}B_{5.9}$ together with that for other alloys reported by Vincent and Davies [57].

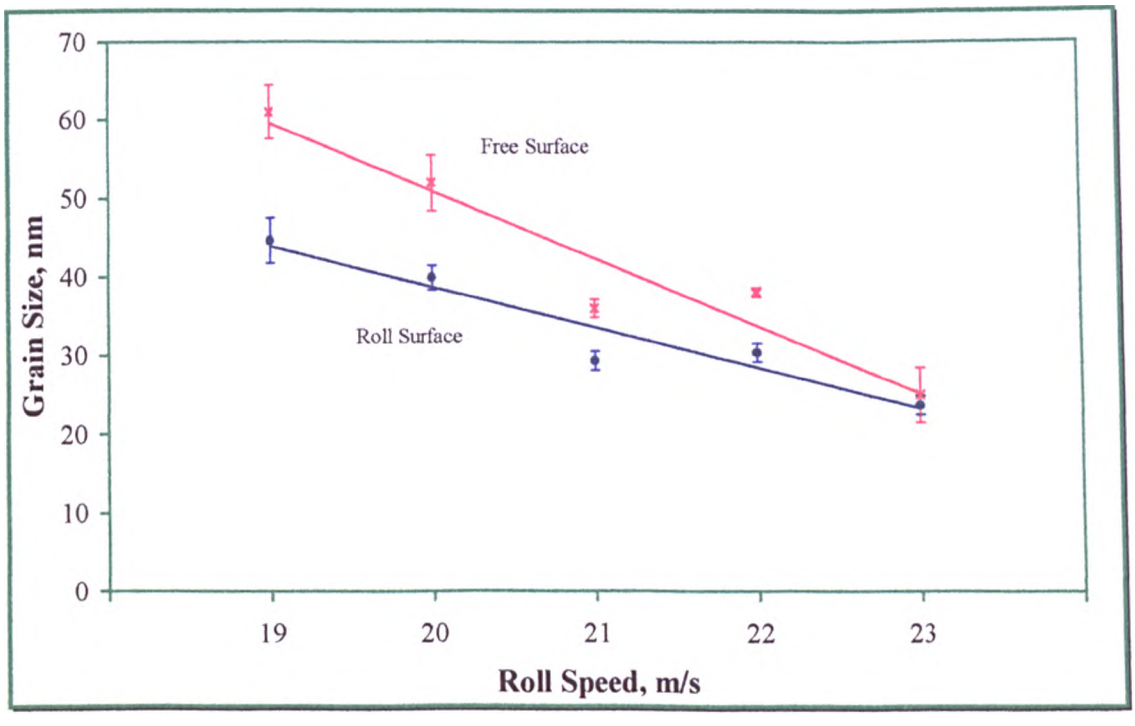

Figure 4- 13: Grain size as a function of roll speed for $Fe_{83.2}Nd_{10.9}B_{5.9}$

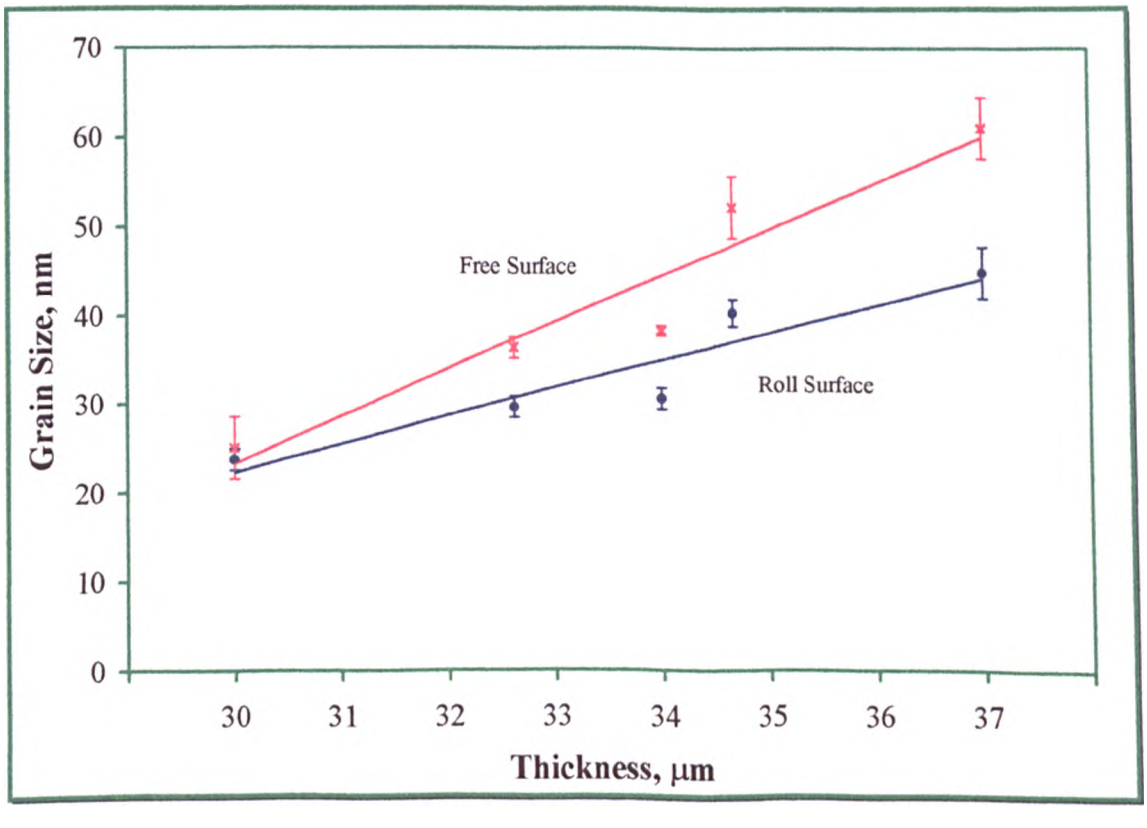

Figure 4- 14: Grain size as a function of ribbon thickness for $Fe_{83.2}Nd_{10.9}B_{5.9}$ melt spun at different roll speeds.

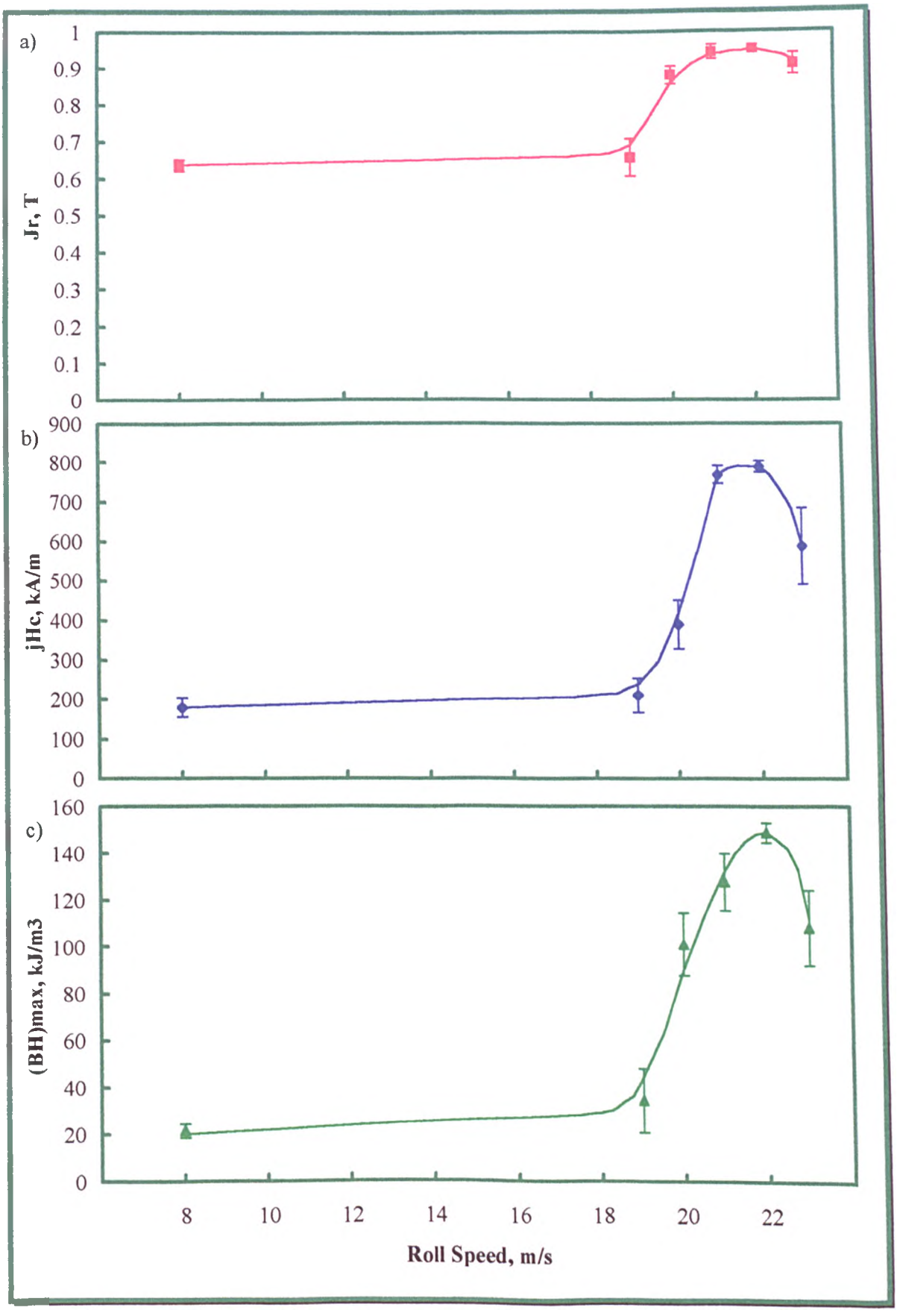

Figure 4- 15: a) J_r ■ b) $_jH_c$ ◆ and c) $(BH)_{max}$ ▲ as a function of roll speed for $Fe_{83.2}Nd_{10.9}B_{5.9}$.

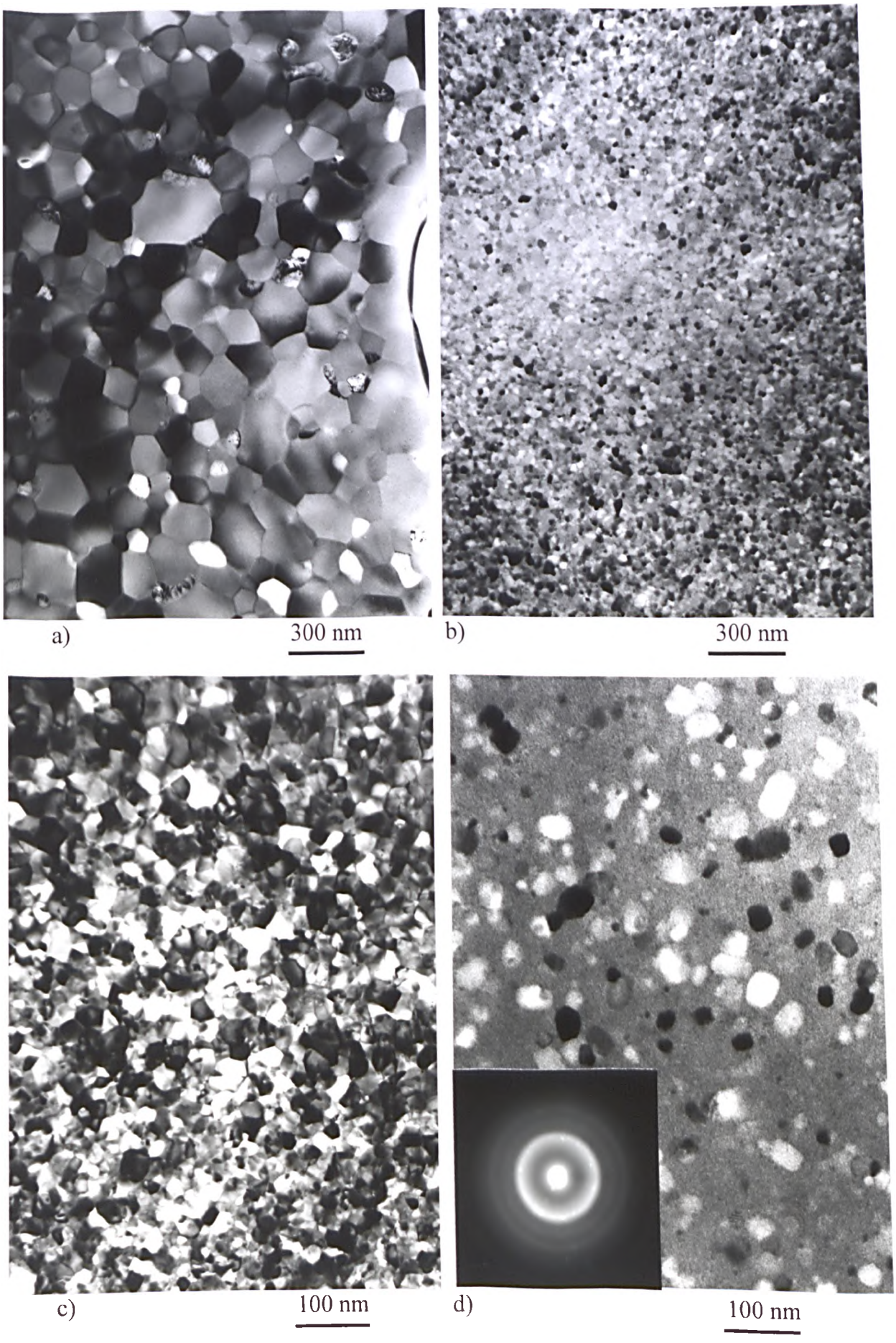

Figure 4- 16: TEM bright field images of $Fe_{83.2}Nd_{10.9}B_{5.9}$ melt spun at a) 20 m/s, b) 22 m/s and c), d) both 23 m/s.

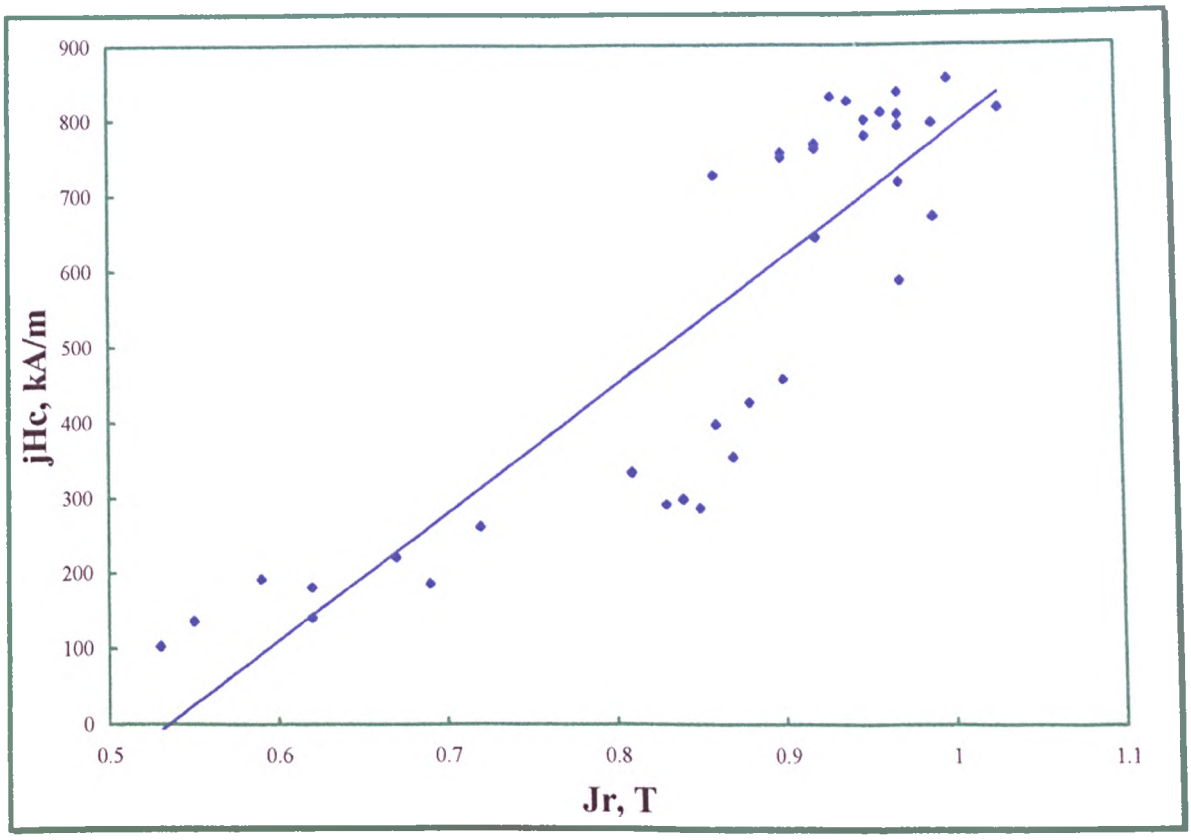

Figure 4- 17: $_{I}H_{c}$ as a function of J_{r} for $Fe_{83.2}Nd_{10.9}B_{5.9}$ melt spun at different roll speeds.

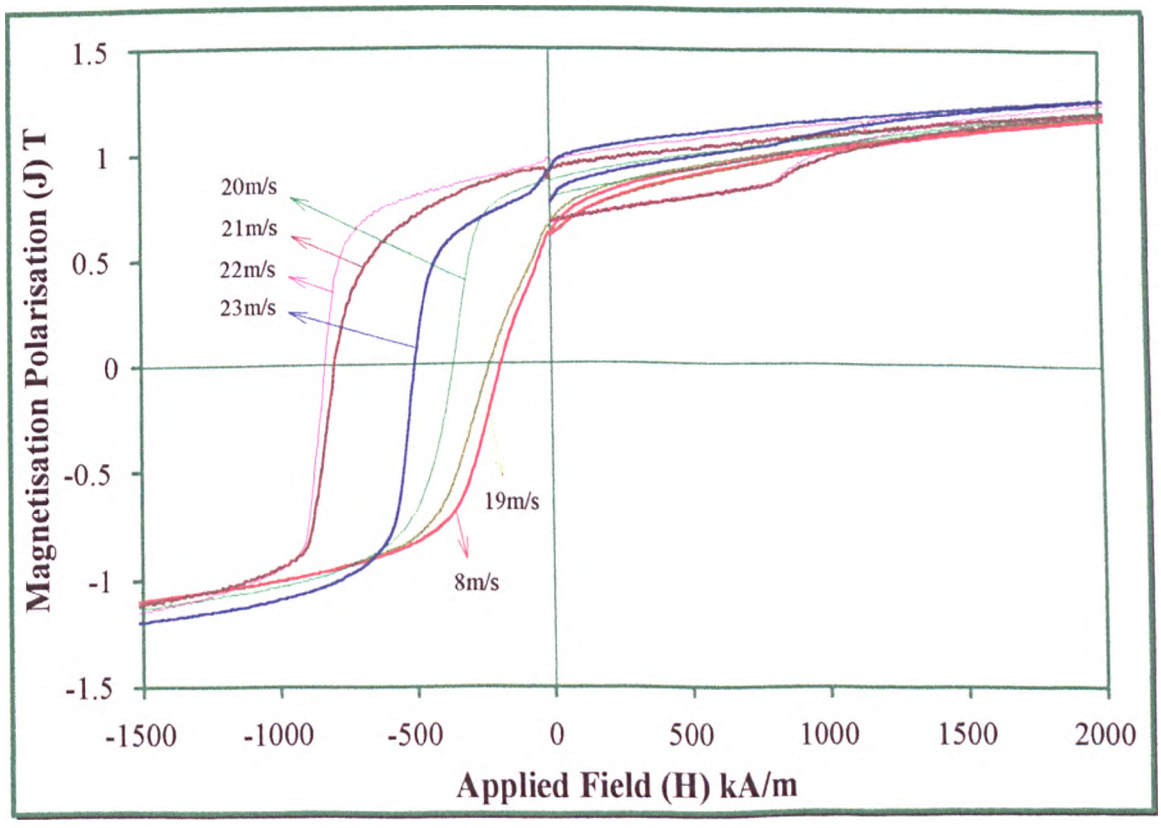

Figure 4- 18: Hysteresis loop shape as a function of roll speed for $Fe_{83.2}Nd_{10.9}B_{5.9}$.

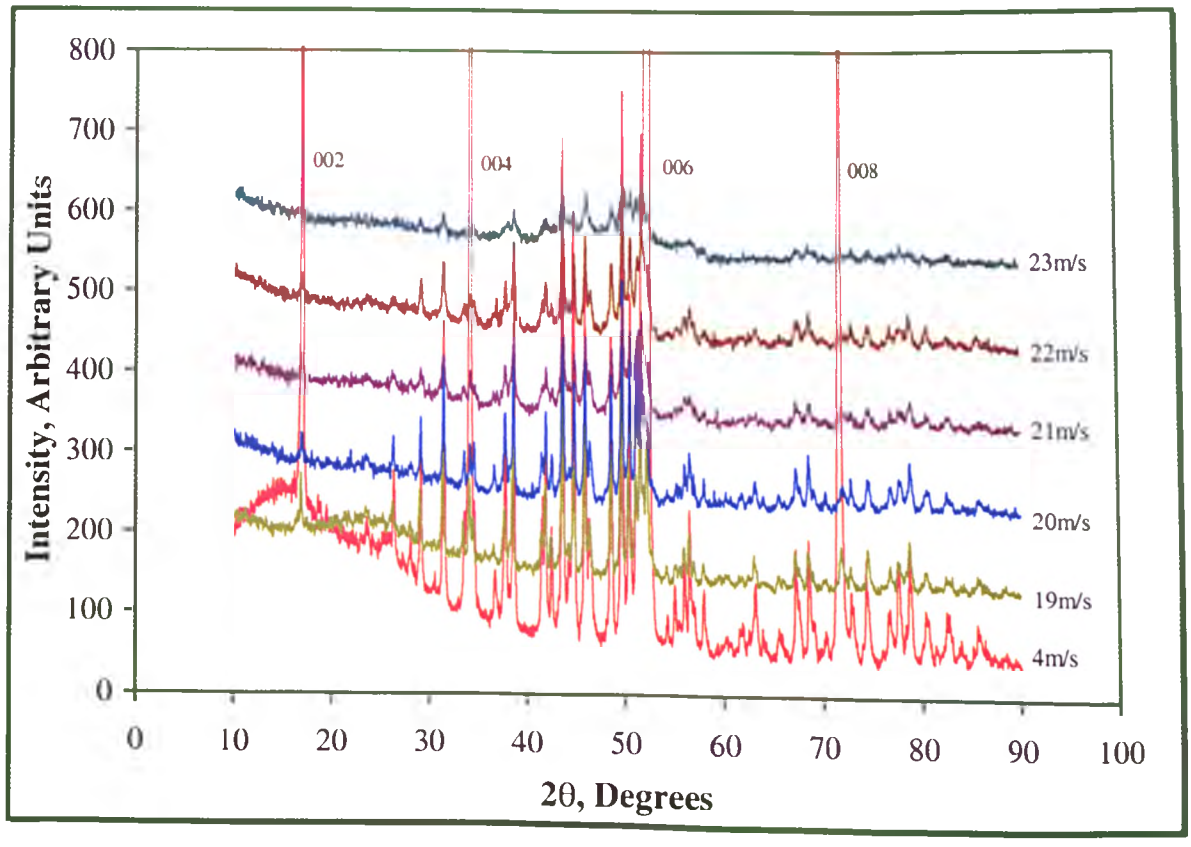

Figure 4- 19: X-ray diffraction traces of $Fe_{83.2}Nd_{10.9}B_{5.9}$ spun at different roll speeds.

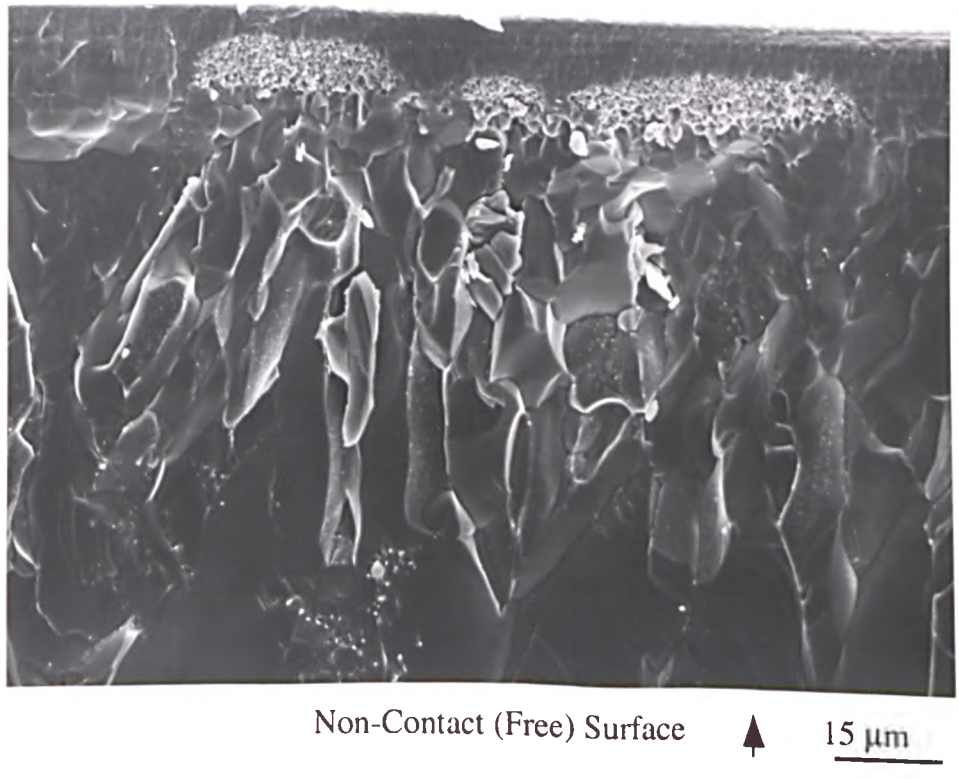

Figure 4- 20: SEM micrograph of transverse cross section of $Fe_{83.2}Nd_{10.9}B_{5.9}$ alloy, melt spun at 4 m/s.

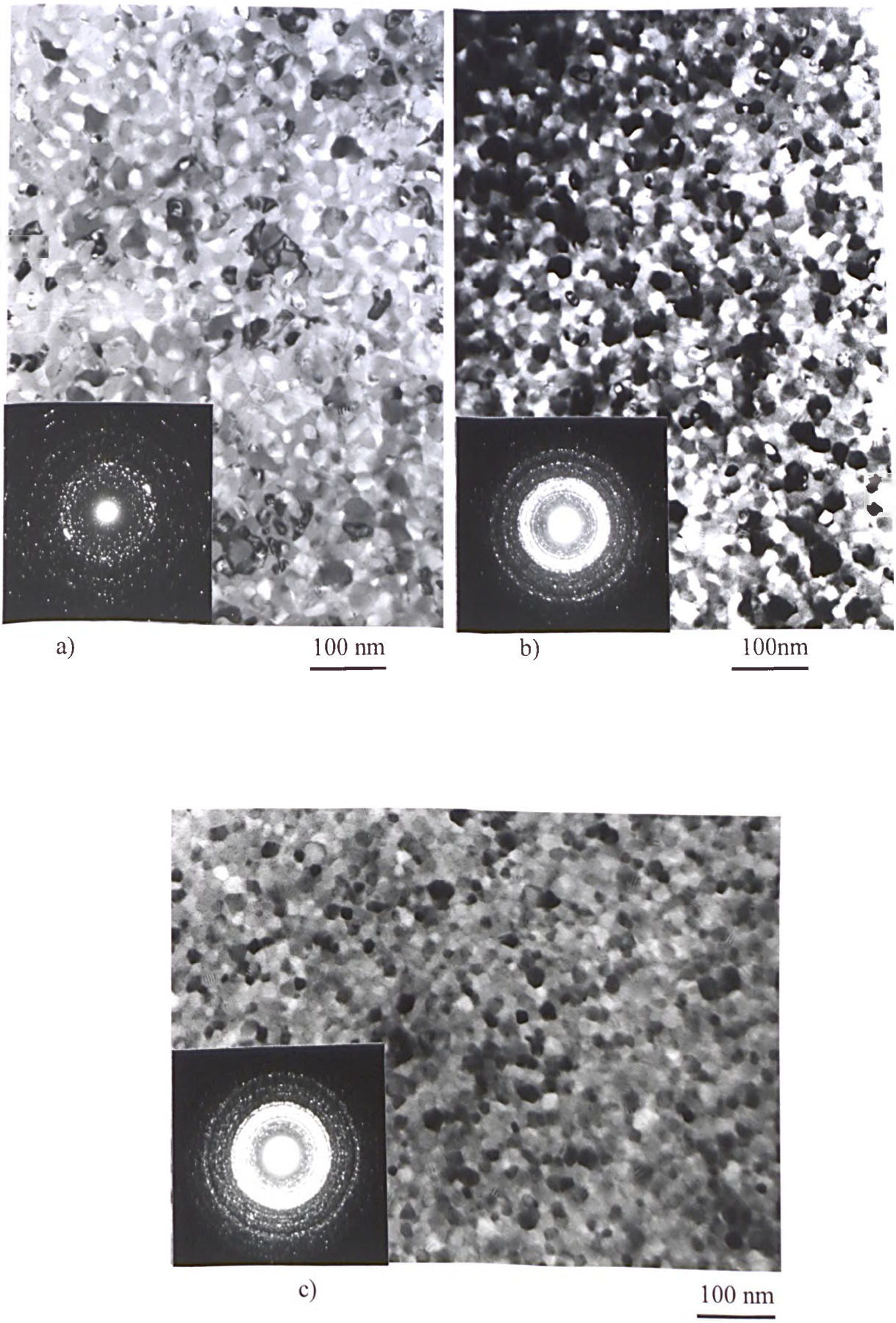

Figure 4- 21: TEM bright field images of a) $Fe_{89}Nd_7B_4$, b) $Fe_{85.1}Nd_9B_{5.9}$ and c) $Fe_{82.3}Nd_{11.8}B_{5.9}$ alloys, melt spun at a) 21 m/s, b) and c) 22 m/s.

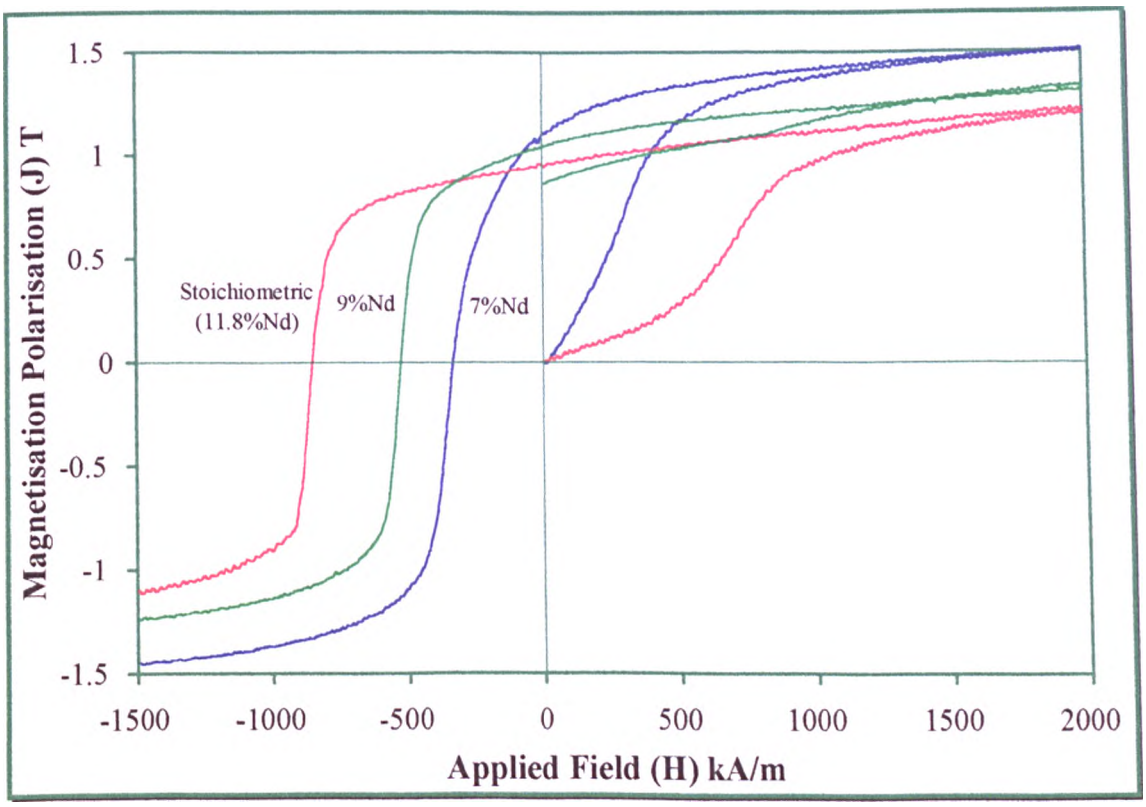

Figure 4- 22: Hysteresis loop shape as a function of Nd content for $Fe_{94\ 1-x}Nd_xB_{5\ 9}$ alloys.

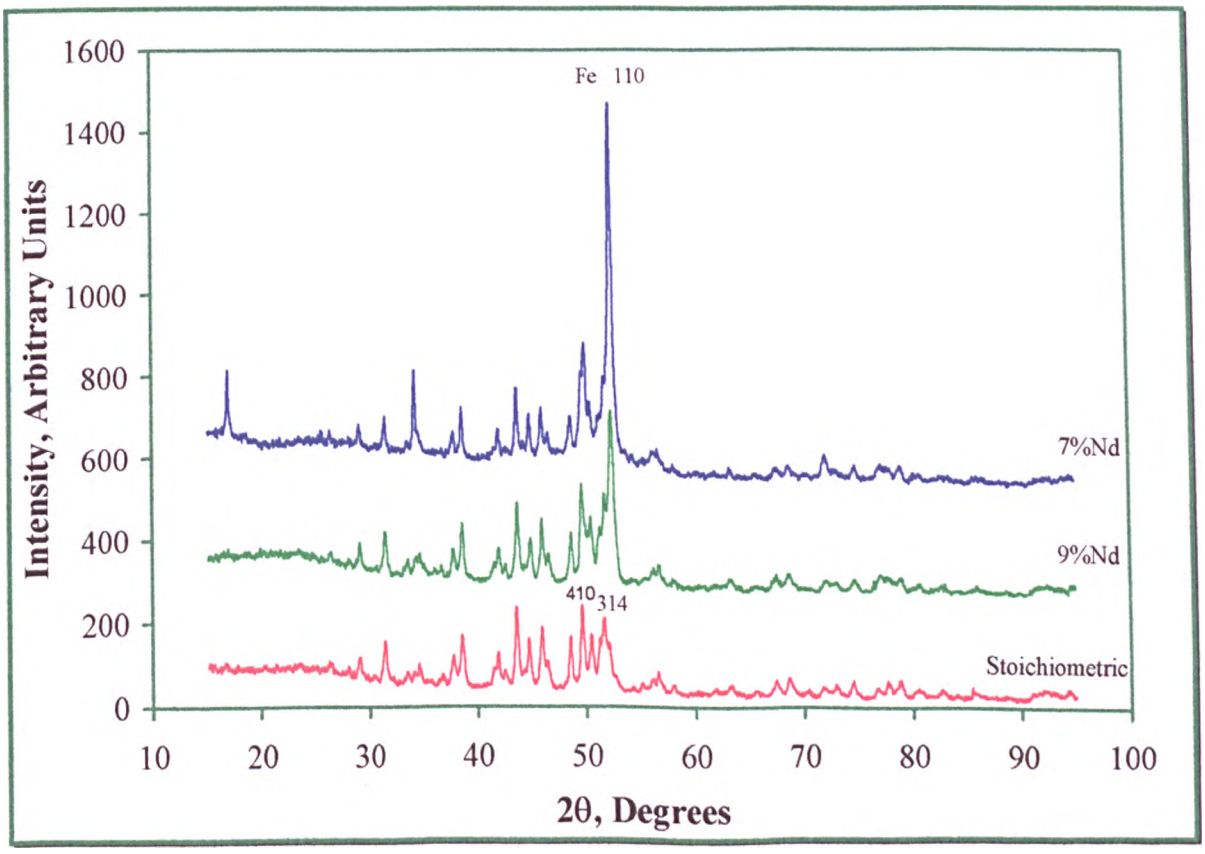

Figure 4- 23: X-ray diffraction traces of melt spun stoichiometric ($Fe_{82.3}Nd_{11.8}B_{5\ 9}$), 9%Nd and 7%Nd alloys.

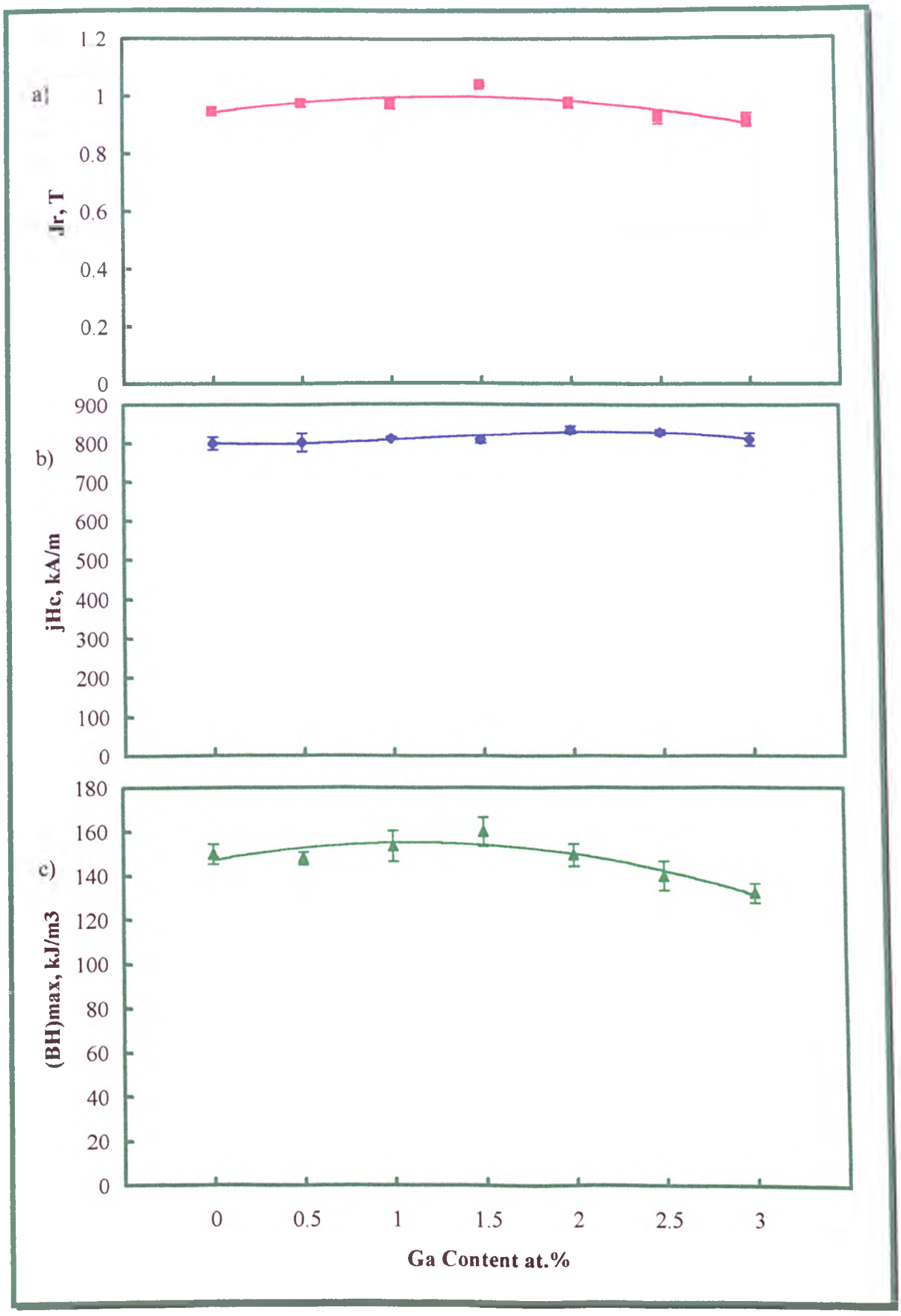

Figure 4- 24: a) J_r ■ b) $_jH_c$ ◆ and c) $(BH)_{max}$ ▲ as a function of Ga content for $Fe_{82.3-x}Nd_{11.8}B_{5.9}Ga_x$ melt spun at optimum conditions, in each case.

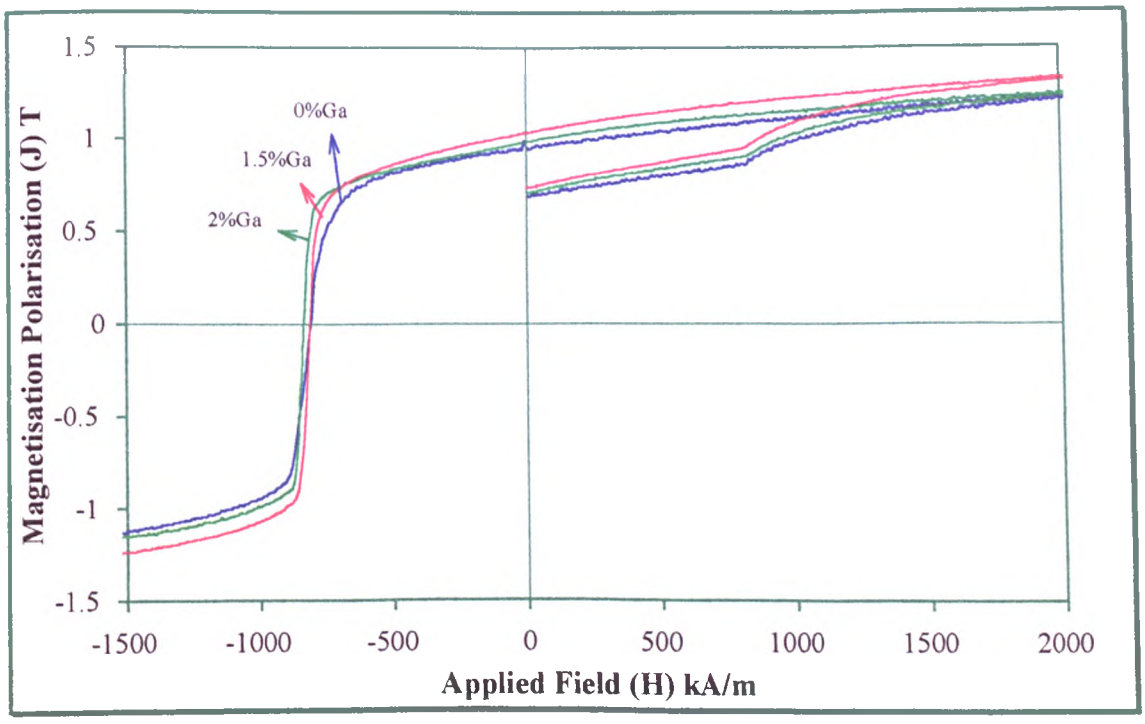

Figure 4- 25: Hysteresis loops for $Fe_{82.3}Nd_{11.8}B_{5.9}$, $Fe_{80.8}Nd_{11.8}B_{5.9}Ga_{1.5}$ and $Fe_{80.3}Nd_{11.8}B_{5.9}Ga_2$ melt spun at 22 m/s for the first two and 23 m/s for the last sample.

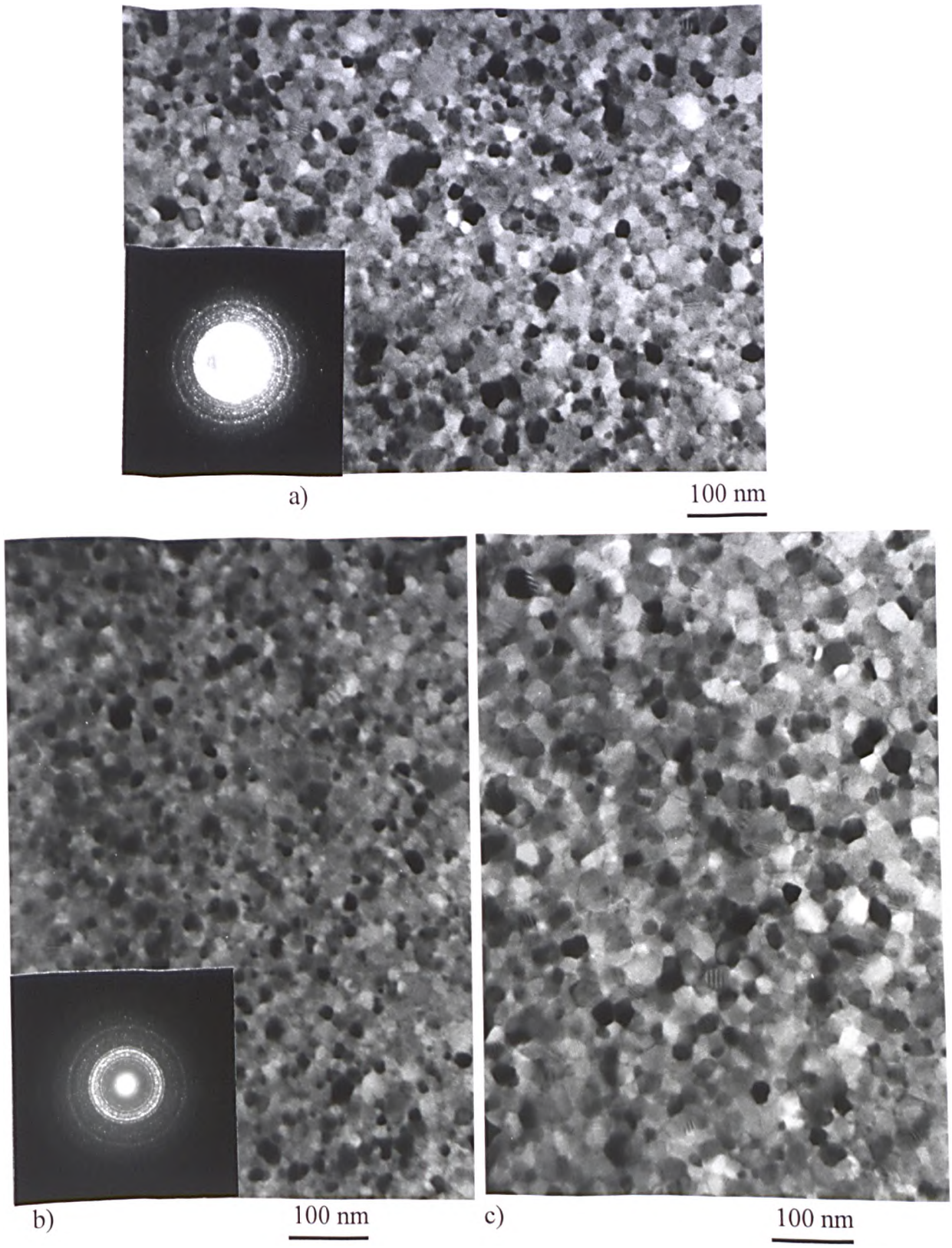

Figure 4- 26: TEM bright field images for a) $Fe_{80.8}Nd_{11.8}B_{5.9}Ga_{1.5}$ and b) $Fe_{80.3}Nd_{11.8}B_{5.9}Ga_2$ melt spun at 22 m/s and 23 m/s, c) as (b) but showing coarser grains.

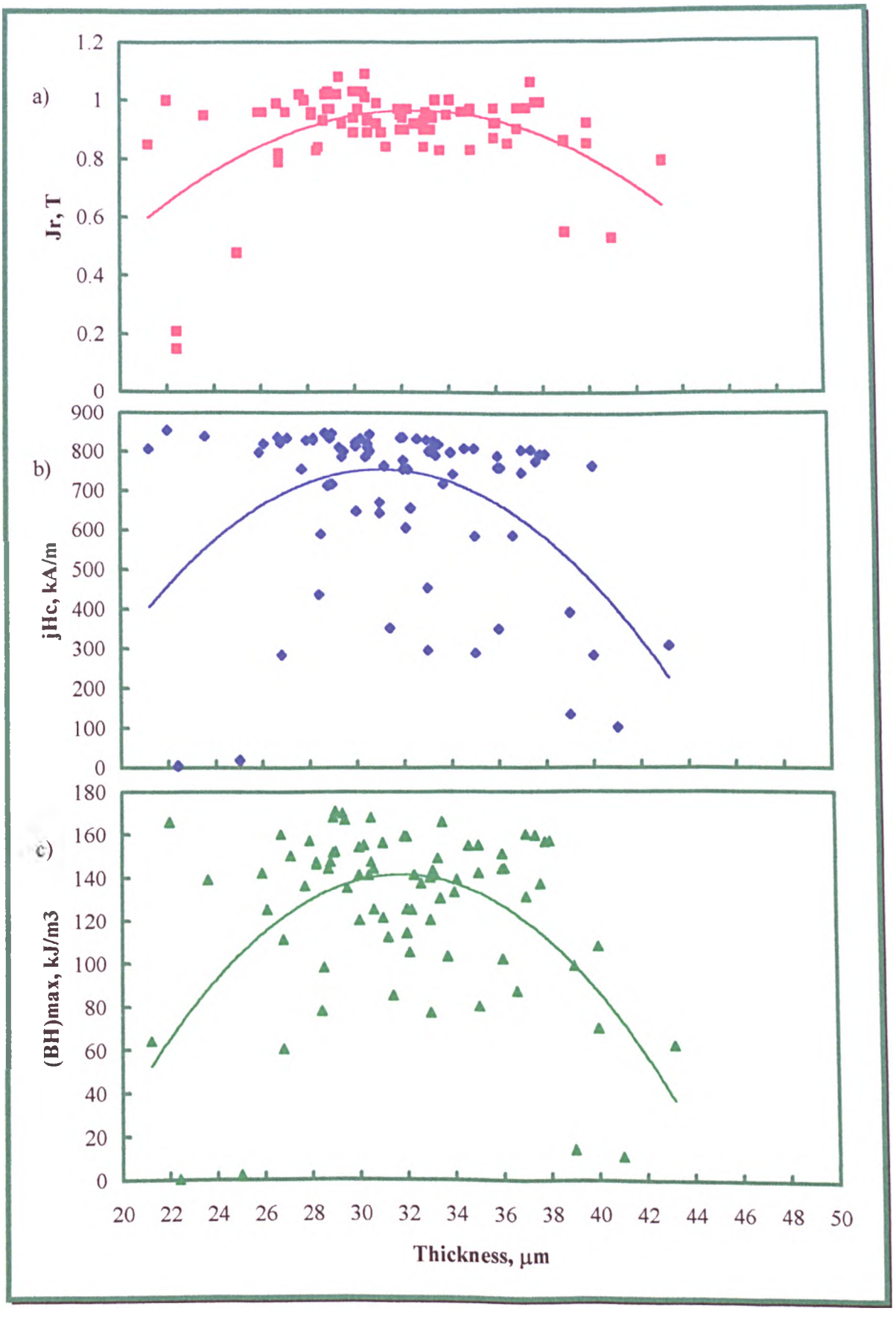

Figure 4- 27: a) J_r ■ b) $_jH_c$ ◆ and c) $(BH)_{max}$ ▲ as a function of ribbon thickness for melt spun $Fe_{82.3-x}Nd_{11.8}B_{5.9}Ga_x$.

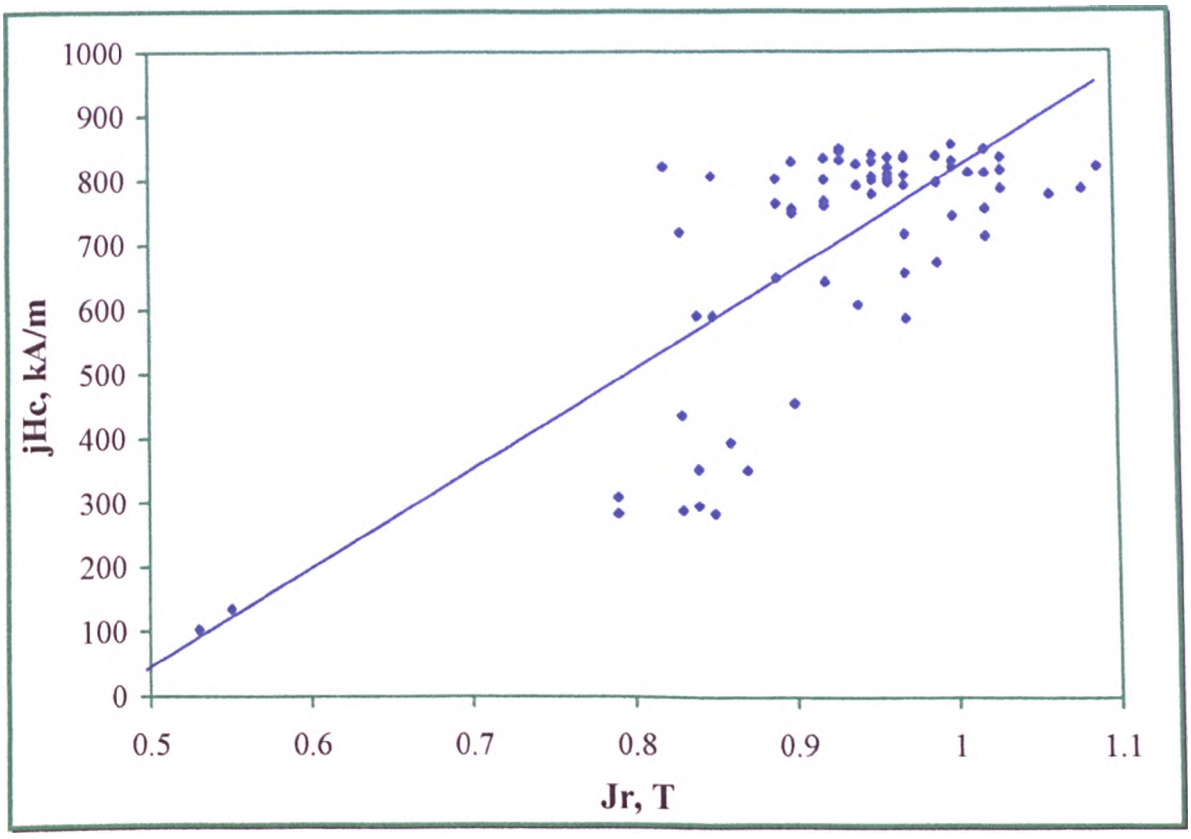

Figure 4- 28: $_{J}H_{c}$ as a function of J_{r} for directly quenched $Fe_{82.3-x}Nd_{11.8}B_{5.9}Ga_{x}$ alloy ribbons.

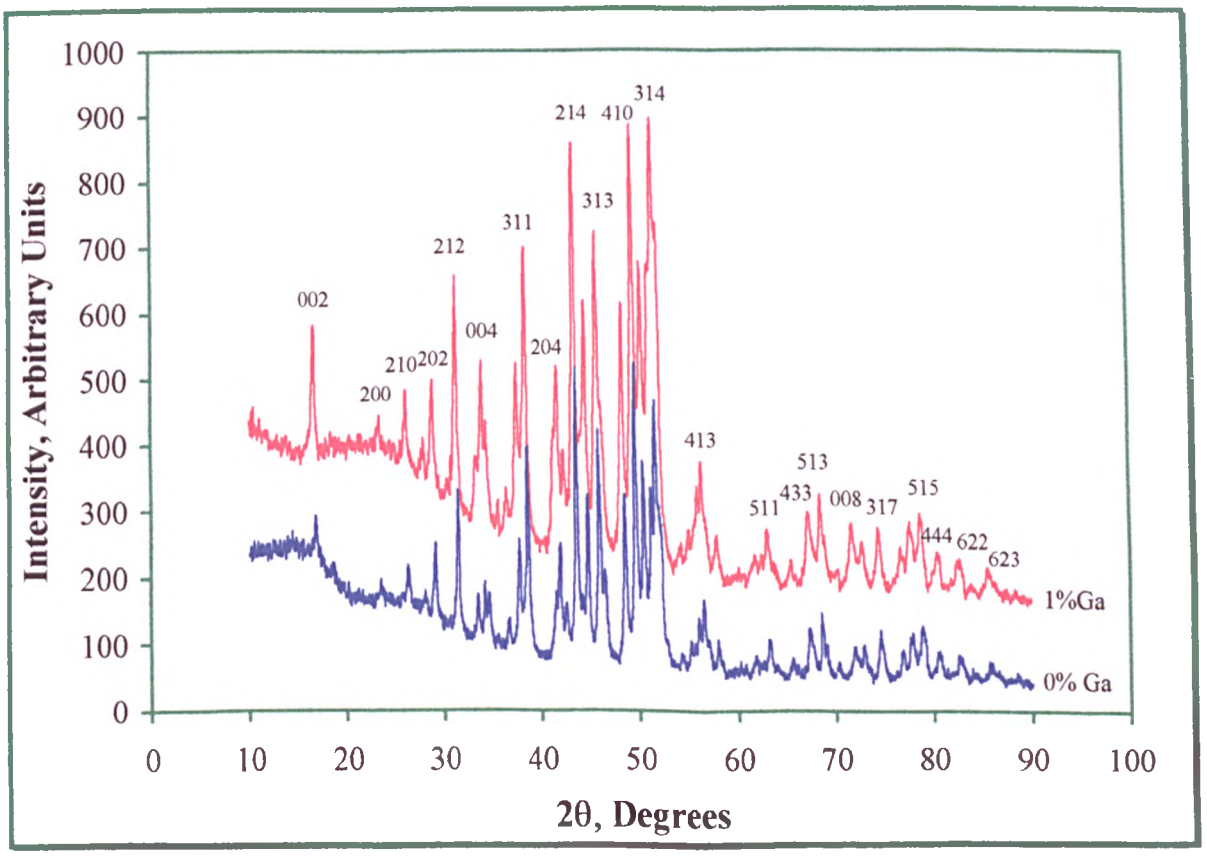

Figure 4- 29: X-ray diffraction traces of $Fe_{82.3}Nd_{11.8}B_{5.9}$ and $Fe_{81.3}Nd_{11.8}B_{5.9}Ga$, melt spun at 22 m/s and 21 m/s, respectively.

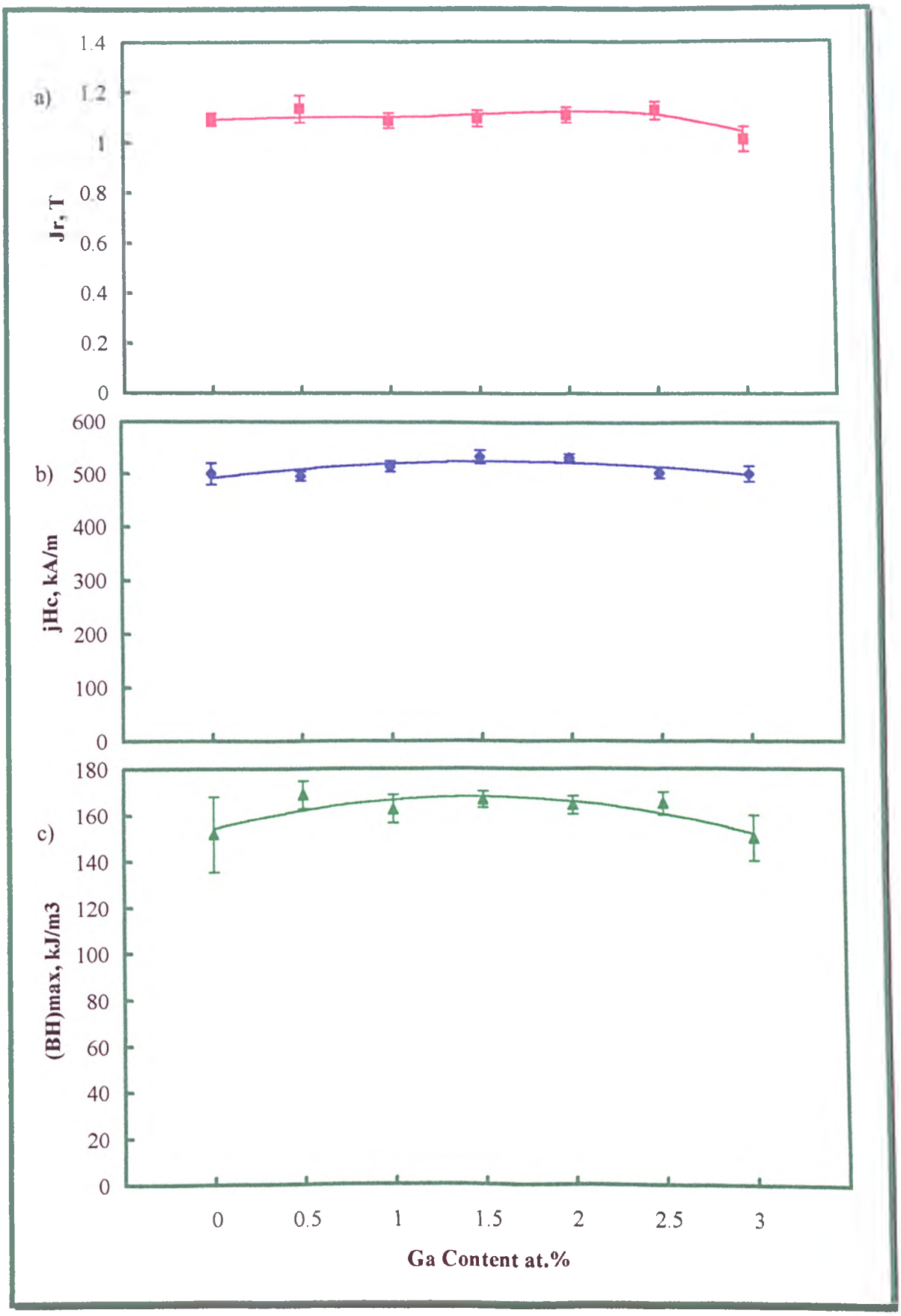

Figure 4- 30: a) J_r ■ b) $_jH_c$ ◆ and c) $(BH)_{max}$ ▲ as a function of Ga content for $Fe_{85.1-x}Nd_9B_{5.9}Ga_x$ melt spun at optimum conditions.

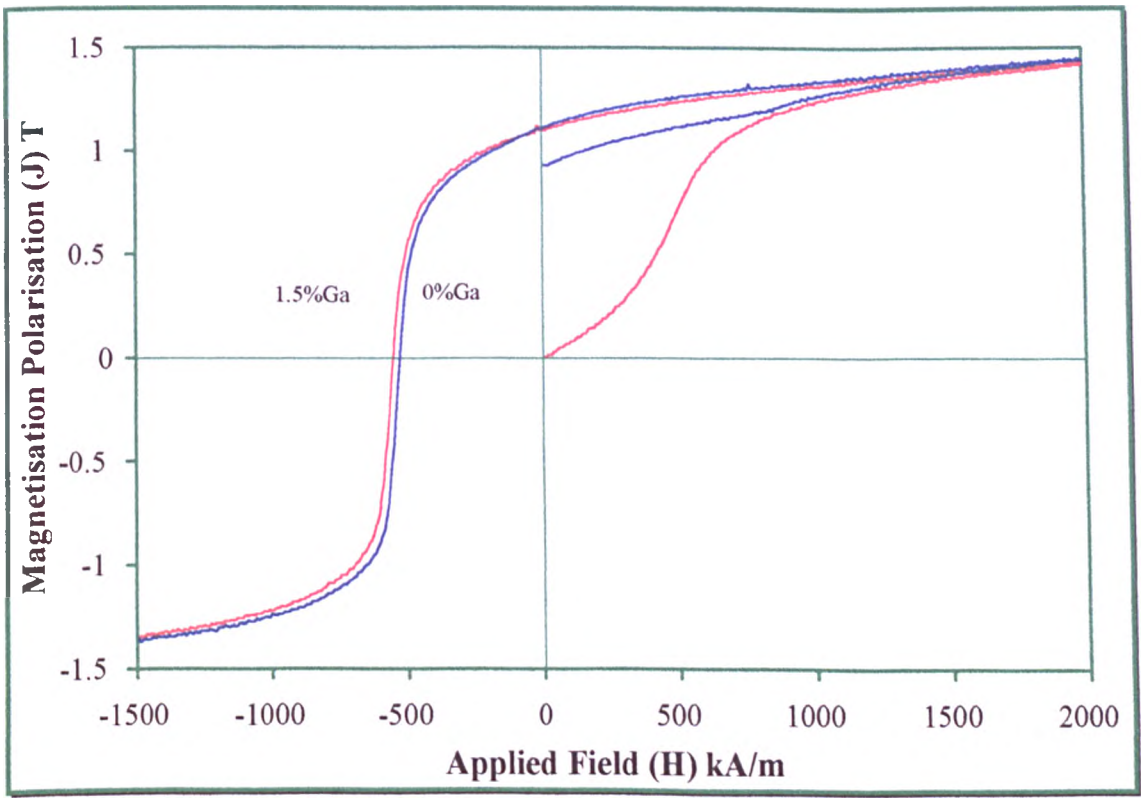

Figure 4- 31: Hysteresis loop for $Fe_{85.1}Nd_9B_{5.9}$ and $Fe_{83.6}Nd_9B_{5.9}Ga_{1.5}$ melt spun at 22 m/s and 21 m/s, respectively.

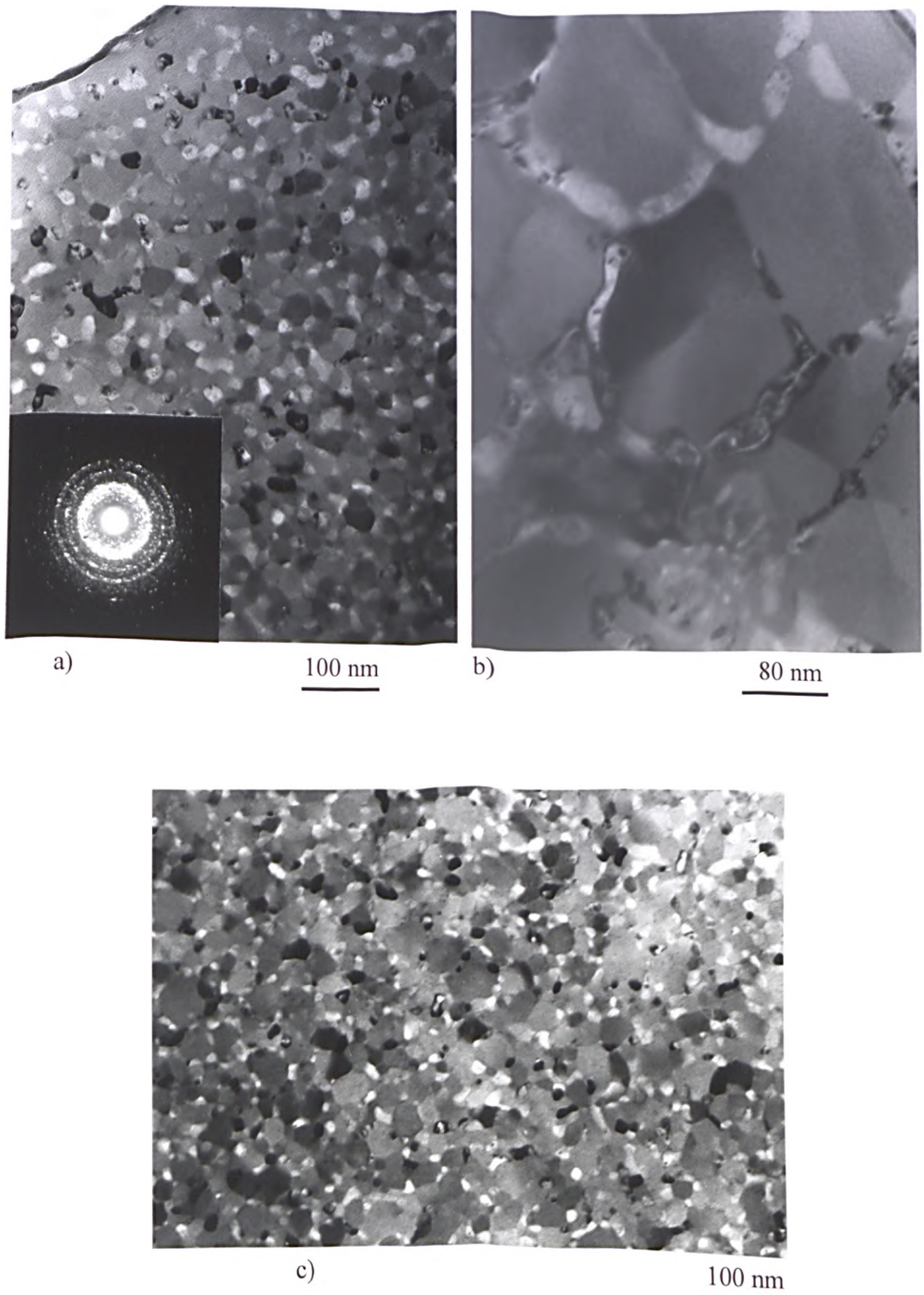

Figure 4- 32: TEM bright field images of a) $Fe_{85.1}Nd_9B_{5.9}$ melt spun at 22 m/s, b) as (a) from coarse grains and c) $Fe_{83.6}Nd_9B_{5.9}Ga_{1.5}$ alloy melt spun at 21 m/s.

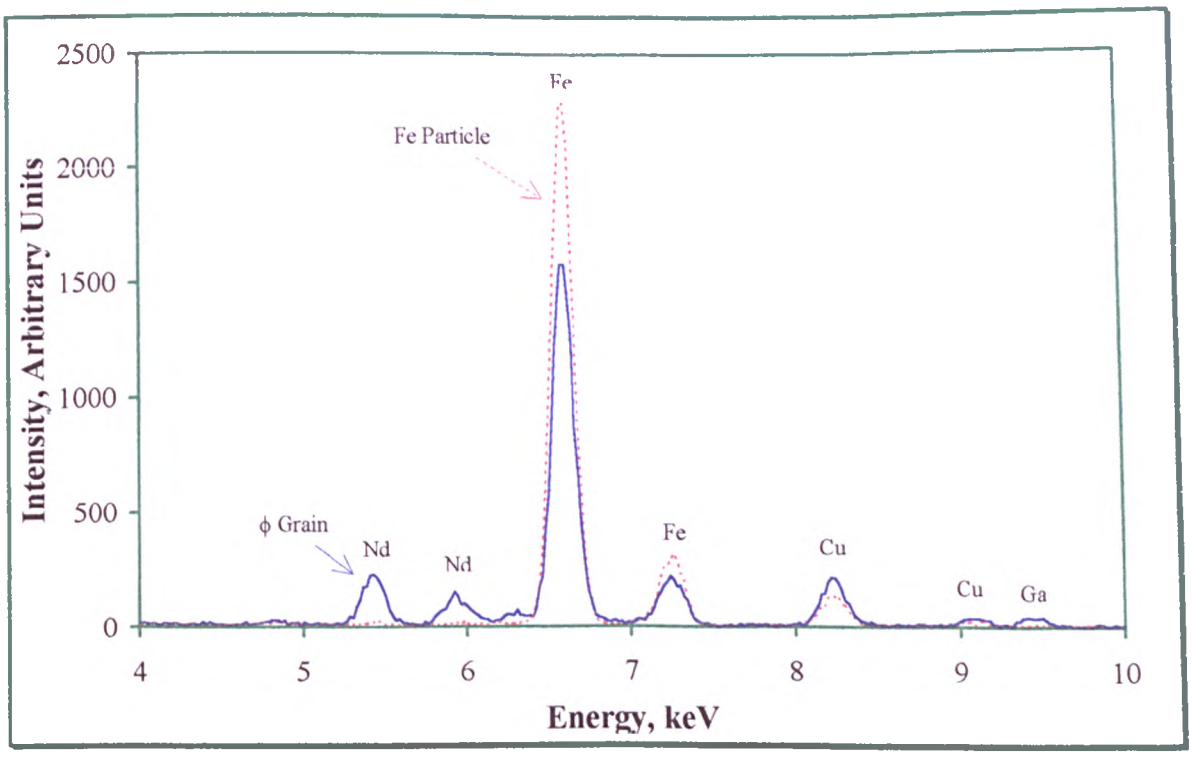

Figure 4- 33: EDS analysis of a $Nd_2Fe_{14}B$ (ϕ) grain and an α-Fe particle of $Fe_{83.6}Nd_9B_{5.9}Ga_{1.5}$ TEM sample.

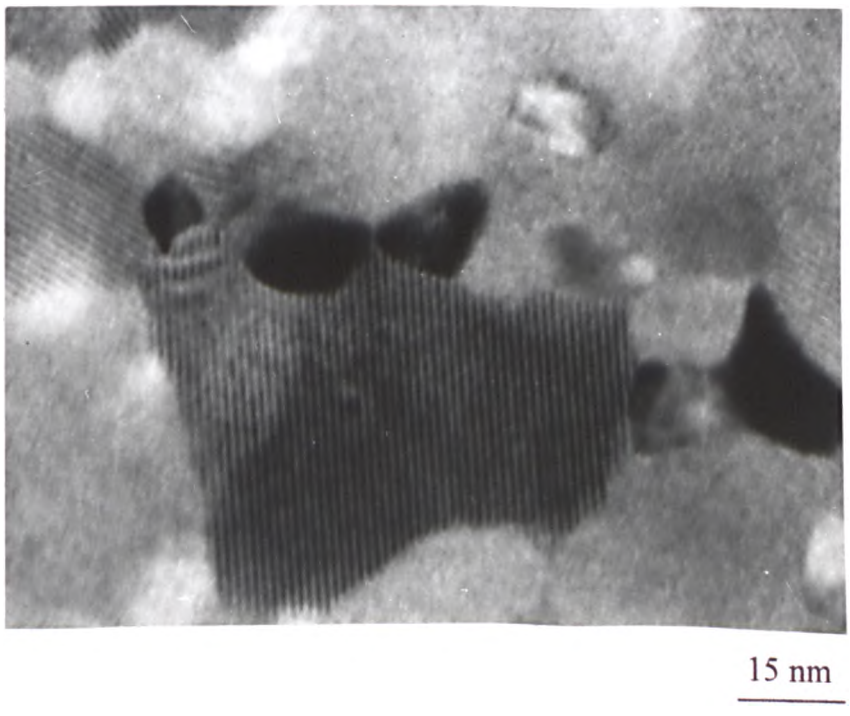

Figure 4- 34: TEM bright field image of $Fe_{83.6}Nd_9B_{5.9}Ga_{1.5}$ alloy, melt spun at 21 m/s.

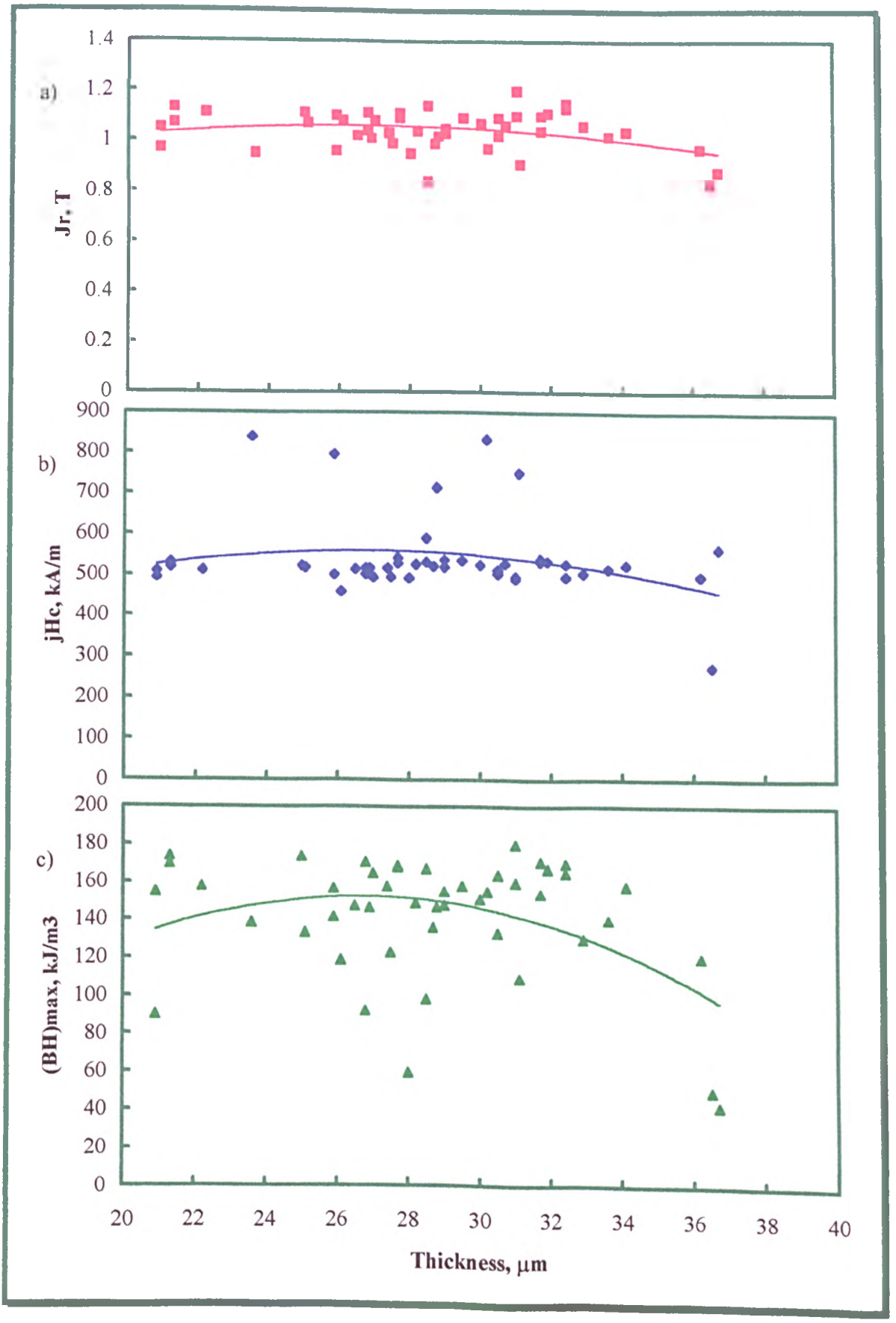

Figure 4- 35: a) J_r ■ b) $_jH_c$ ◆ and c) $(BH)_{max}$ ▲ as a function of ribbon thickness for directly quenched $Fe_{85\ 1-x}Nd_9B_{5\ 9}Ga_x$ alloys.

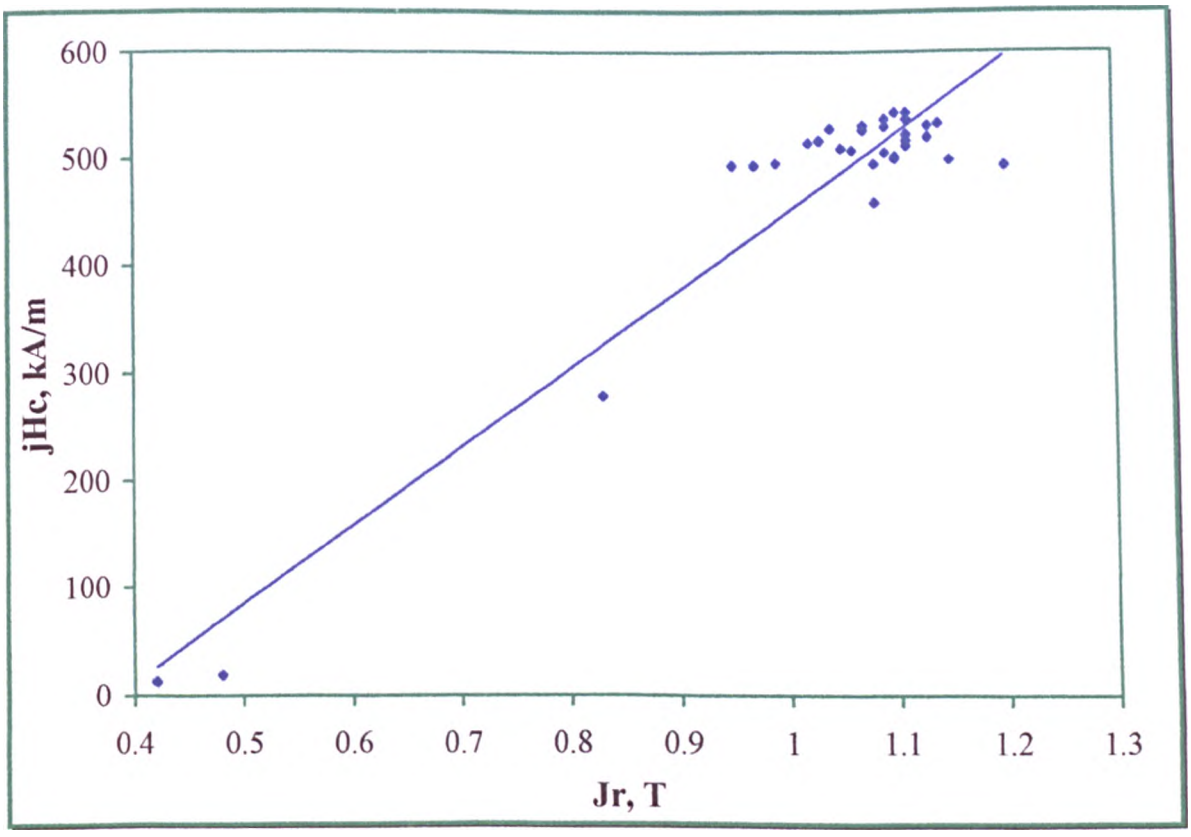

Figure 4- 36: $_jH_c$ as a function of J_r for $Fe_{85\ 1-x}Nd_9B_{5\ 9}Ga_x$ melt spun at optimum conditions.

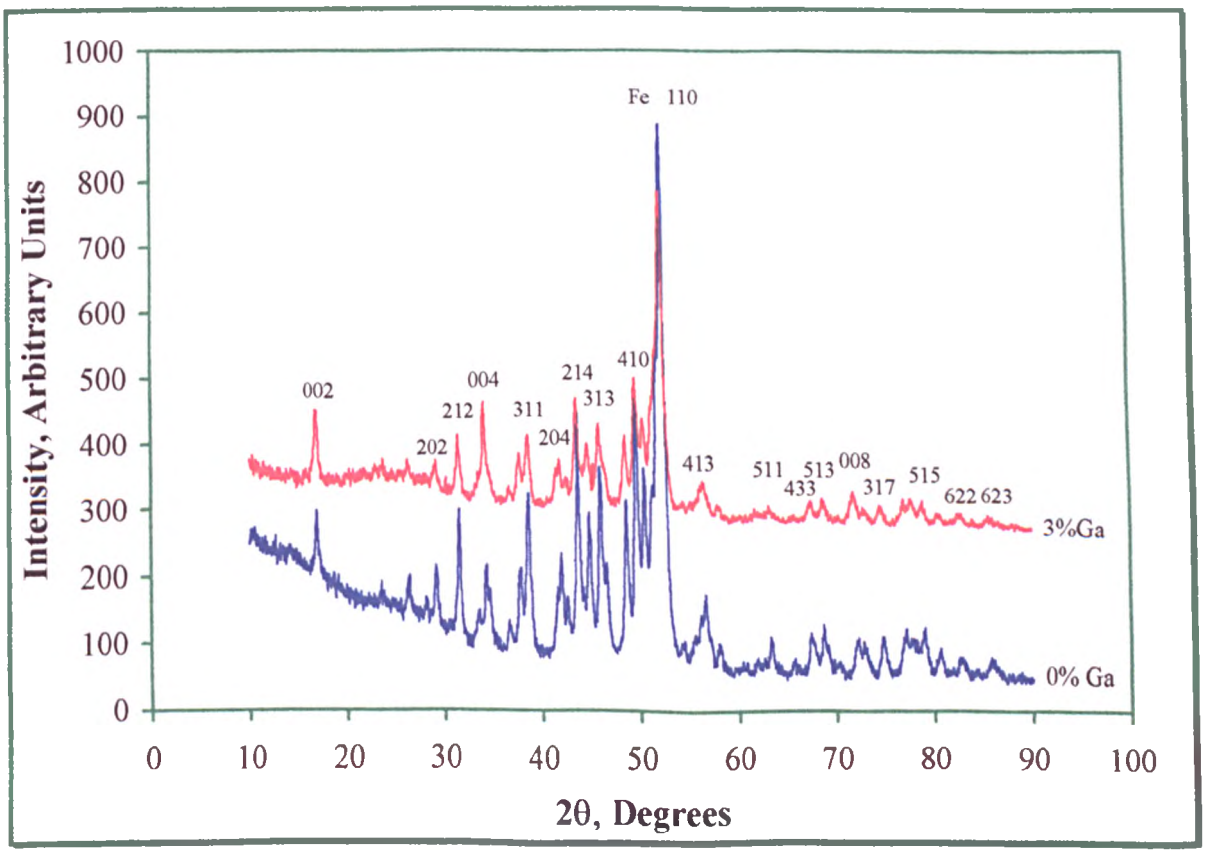

Figure 4- 37: X-ray diffraction traces of directly quenched $Fe_{85.1}Nd_9B_{5.9}$ and $Fe_{82.1}Nd_9B_{5.9}Ga_3$ alloy ribbons.

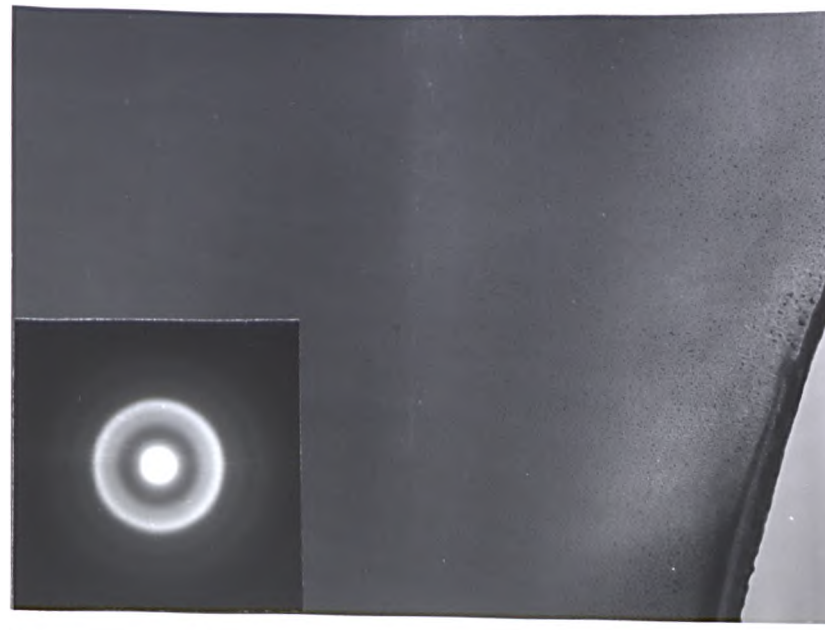

a) 200 nm

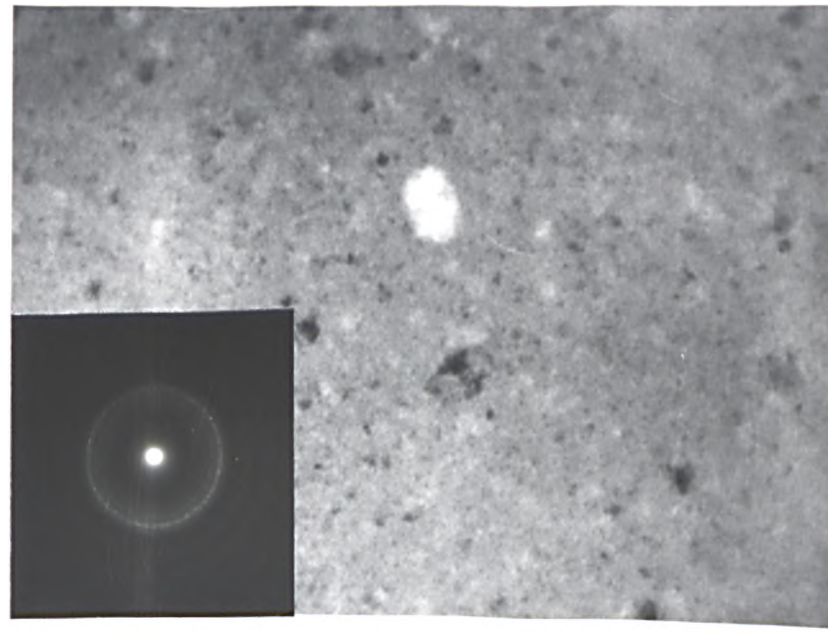

b) 100 nm

Figure 4- 38: TEM bright field images of $Fe_{82.3}Nd_{11.8}B_{5.9}$ alloy ribbons melt spun at 26 m/s.

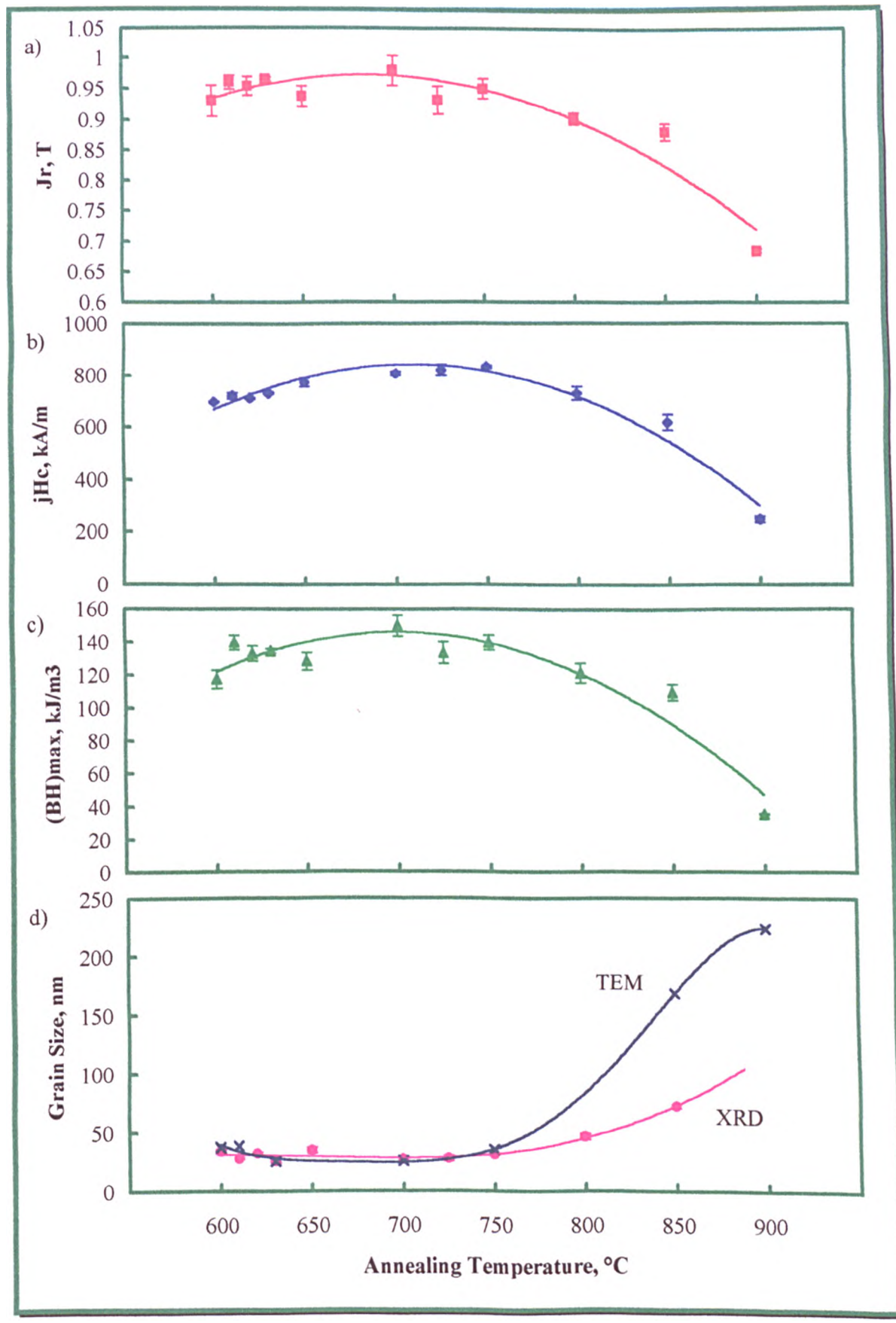

Figure 4- 39: a) J_r ■ b) $_jH_c$ ◆ c) $(BH)_{max}$ ▲ and d) grain size as a function of annealing temperature for ribbon samples of the stoichiometric $Fe_{82.3}Nd_{11.8}B_{5.9}$ alloy ribbons, over quenched at 26 m/s and annealed for 4 minutes.

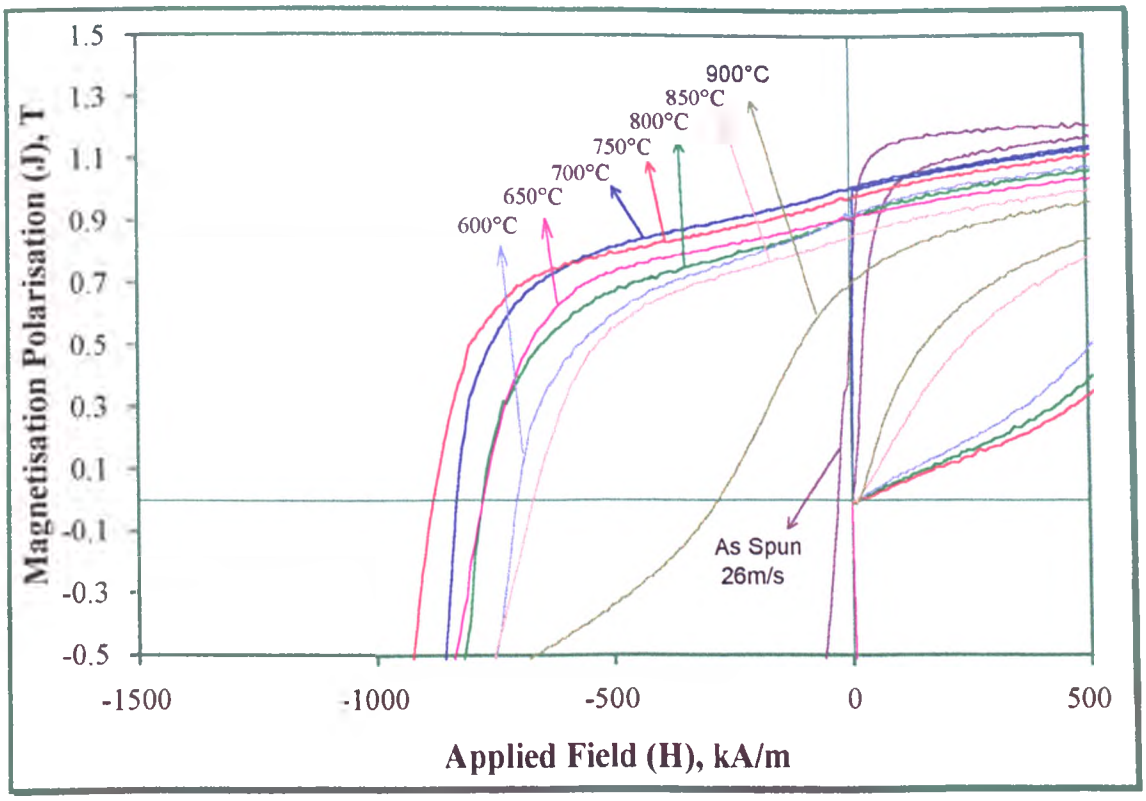

Figure 4- 40: Hysteresis loop second quadrants as a function of annealing temperature for $Fe_{82.3}Nd_{11.8}B_{5.9}$ ribbons, melt spun at 26 m/s and annealed for 4 minutes.

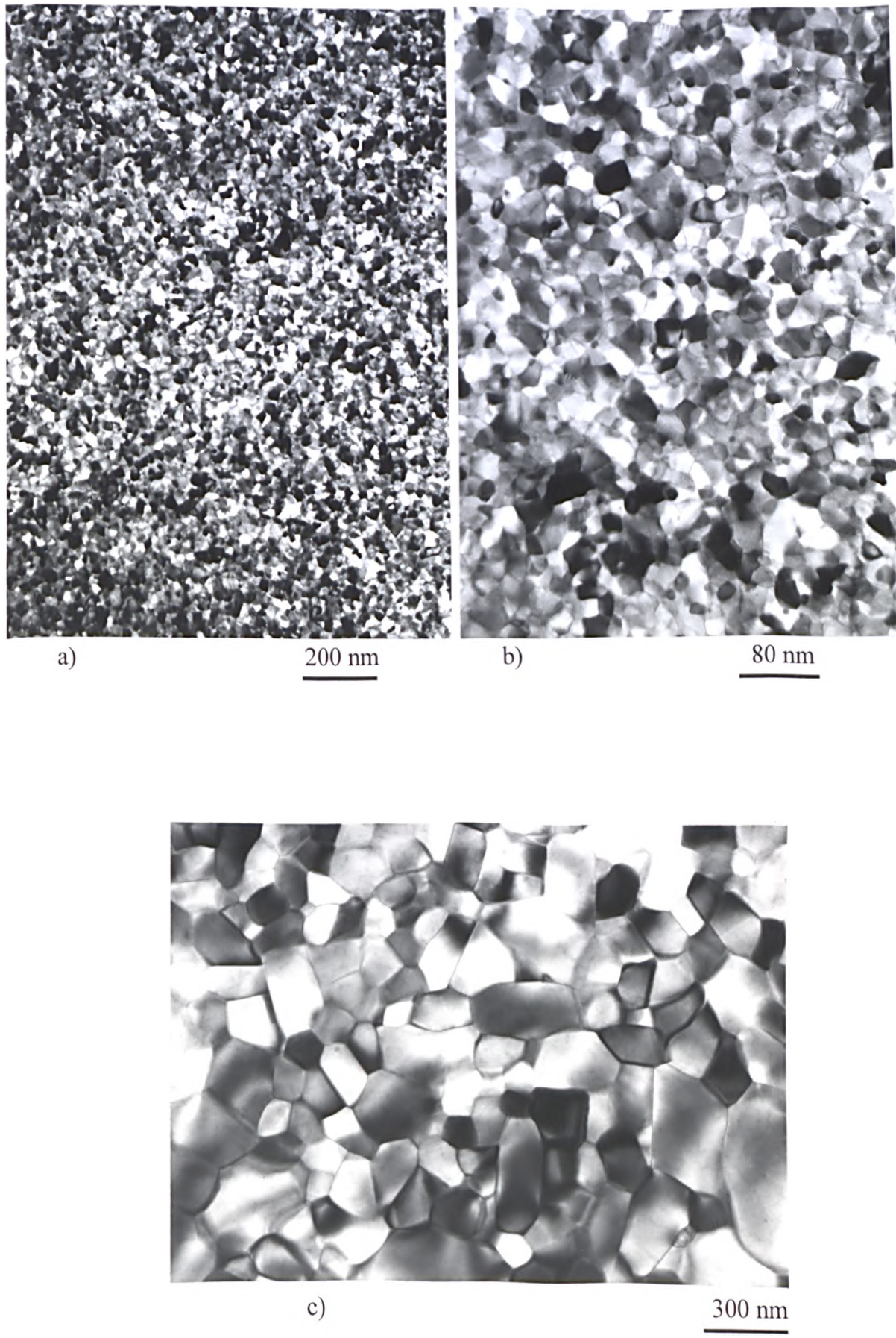

Figure 4- 41: TEM bright field images of $Fe_{82.3}Nd_{11.8}B_{5.9}$ ribbons melt spun at 26 m/s and annealed at a) 700°C, b) as (a) at higher magnification, and c) 850°C for 4 minutes.

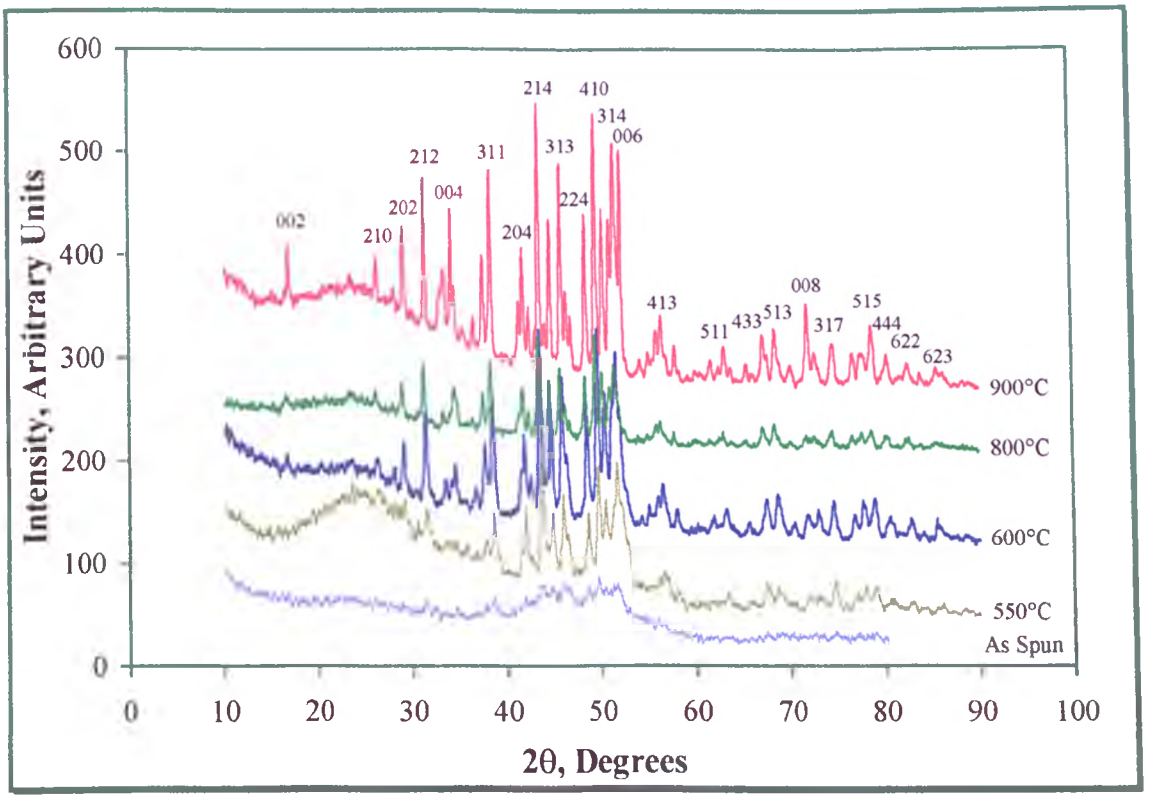

Figure 4- 42: X-ray diffraction traces of $Fe_{82.3}Nd_{11.8}B_{5.9}$ ribbons, melt spun at 26 m/s and annealed for 4 minutes at different temperatures.

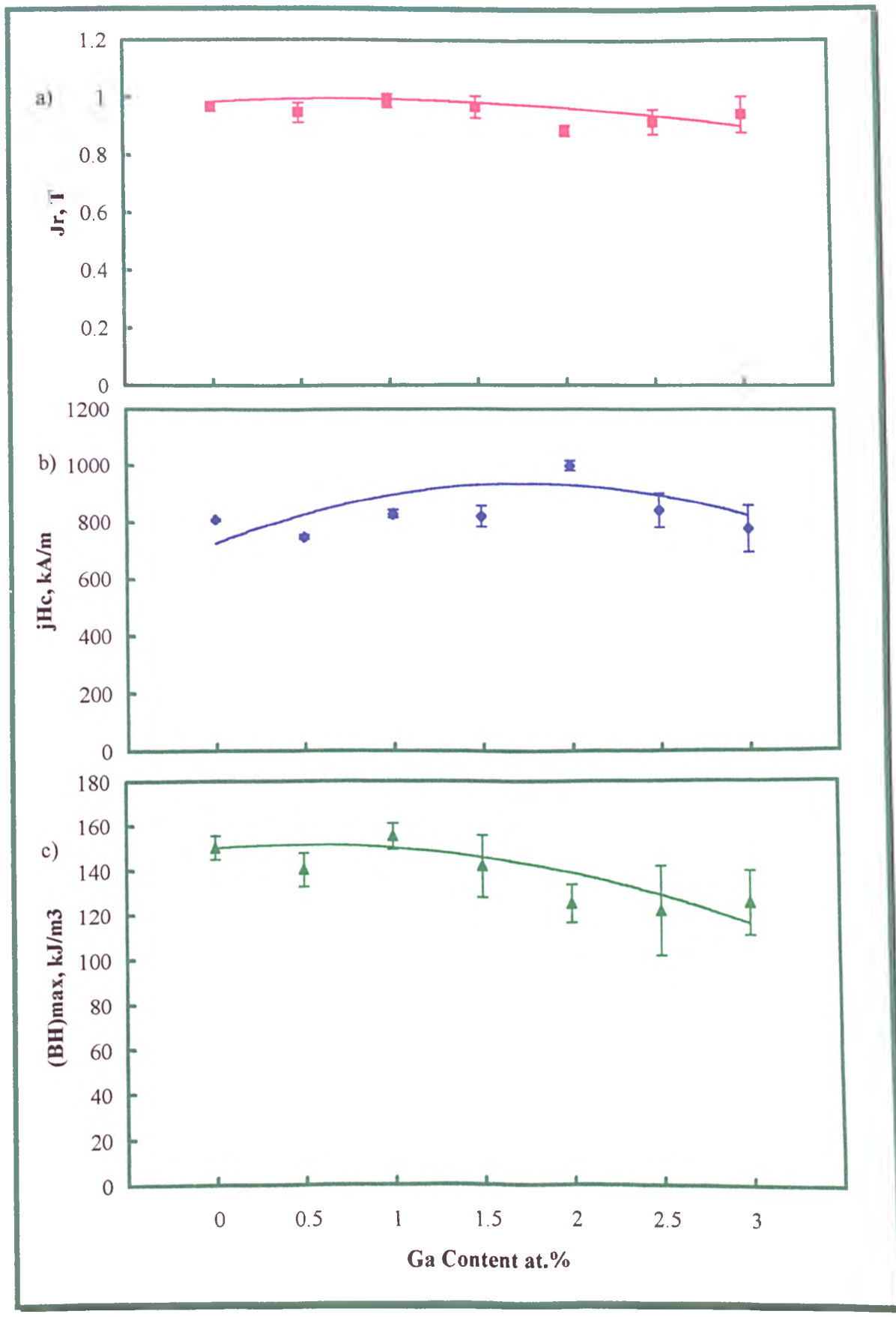

Figure 4- 43: a) J_r ■ b) $_jH_c$ ◆ and c) $(BH)_{max}$ ▲ as a function of Ga content for $Fe_{82.3-x}Nd_{11.8}B_{5.9}Ga_x$ alloy ribbons, over quenched at 26 m/s and annealed for 4 minutes at 700°C.

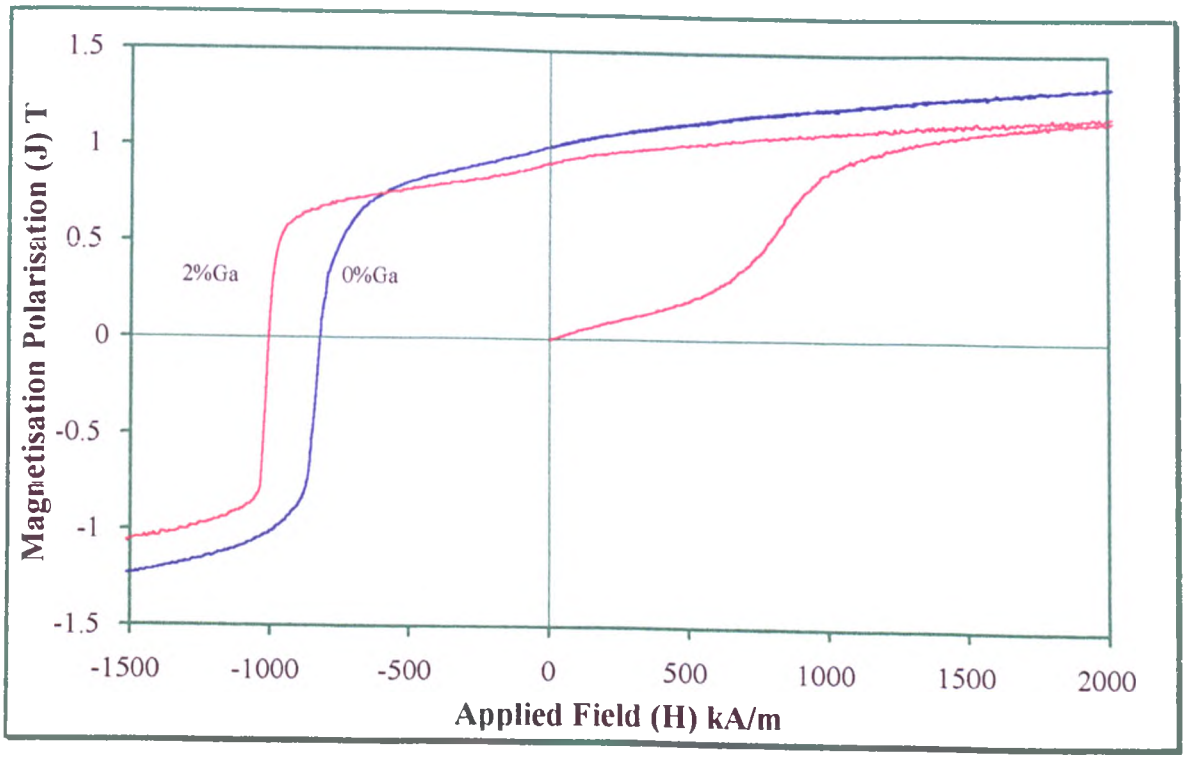

Figure 4- 44: Hysteresis loop for $Fe_{82.3}Nd_{11.8}B_{5.9}$and $Fe_{80.3}Nd_{11.8}B_{5.9}Ga_2$ alloy ribbons, melt spun at 26m/s and annealed for 4 minutes at 700°C.

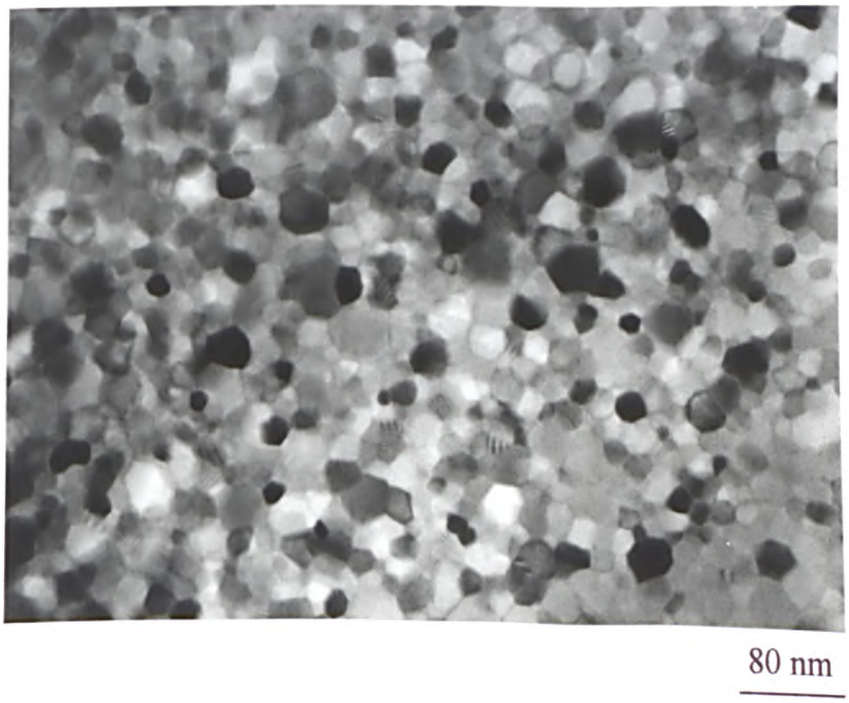

Figure 4- 45: TEM bright field image of $Fe_{80.3}Nd_{11.8}B_{5.9}Ga_2$ alloy ribbons, melt spun at 26 m/s and annealed at 700°C for 4 minutes.

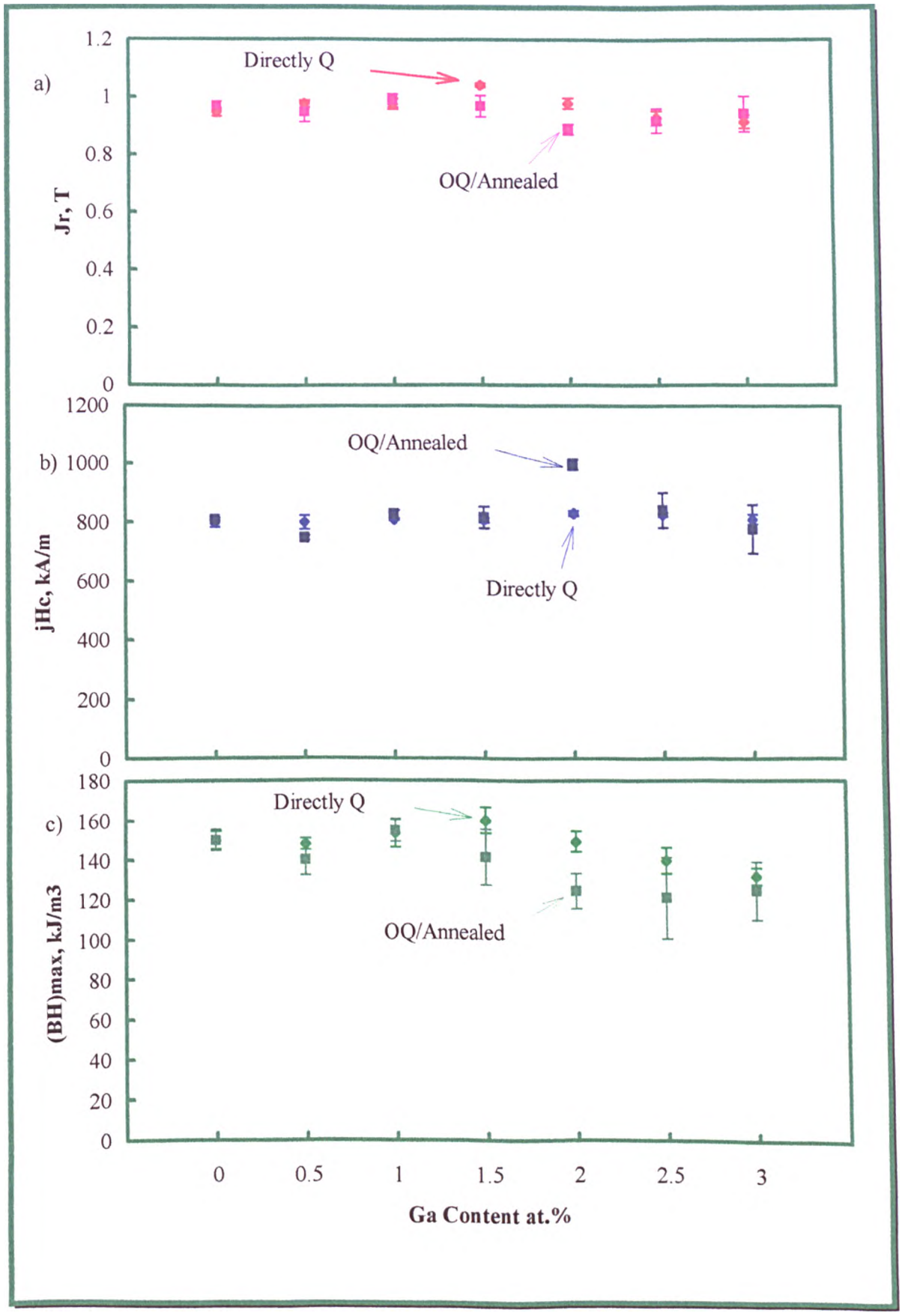

Figure 4- 46: a) J_r, b) $_jH_c$ and c) $(BH)_{max}$ as a function of Ga content for $Fe_{82.3-x}Nd_{11.8}B_{5.9}Ga_x$ ribbon samples in i) the optimum directly quenched ◆ and ii) over quenched (26 m/s) and annealed (4 min/700°C) ■ conditions.

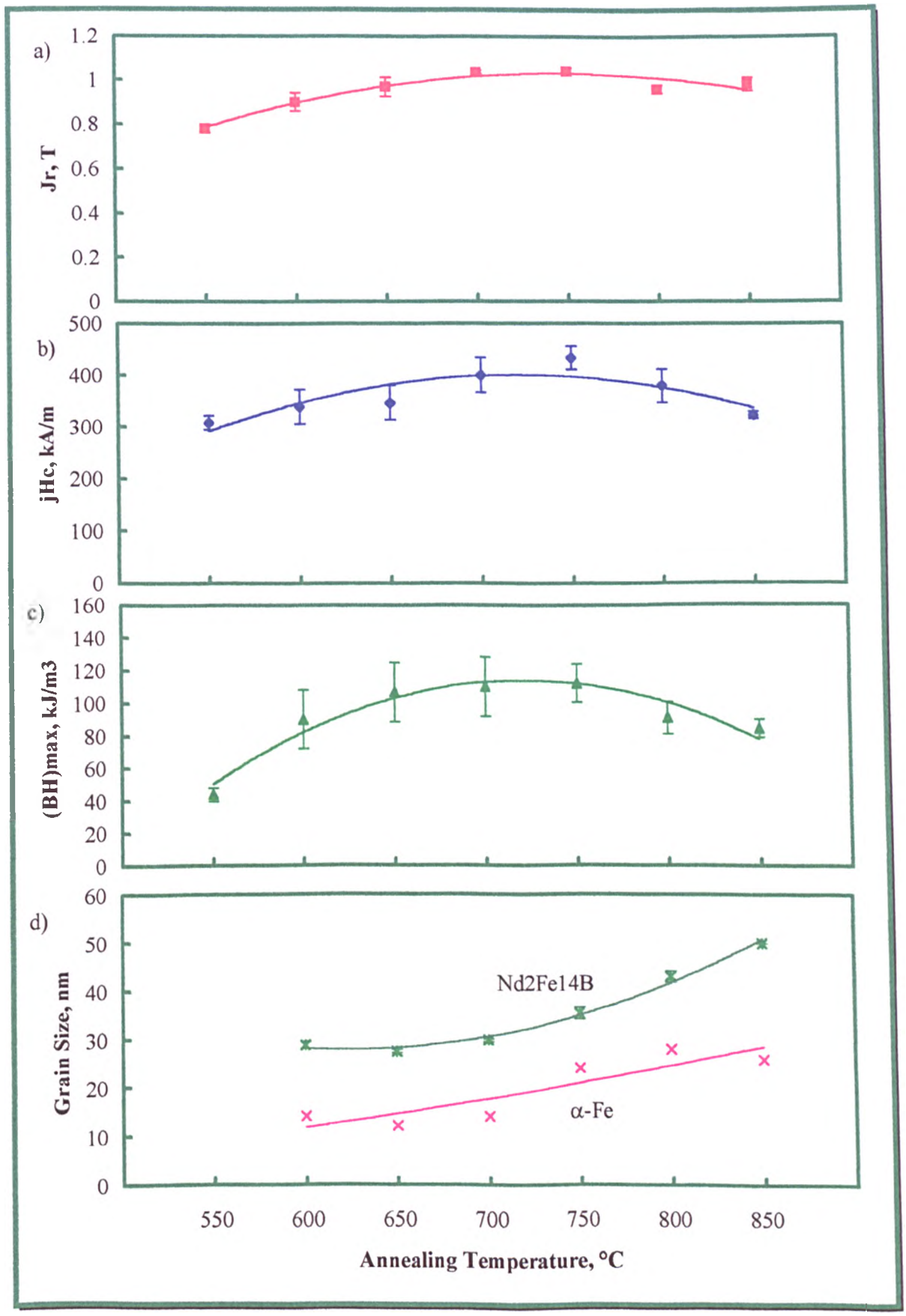

Figure 4- 47: a) J_r ■, b) $_jH_c$ ◆ and c) $(BH)_{max}$ ▲ as a function of annealing temperature for $Fe_{85.1}Nd_9B_{5.9}$ ribbon samples over quenched at 26 m/s and annealed for 4 minutes.

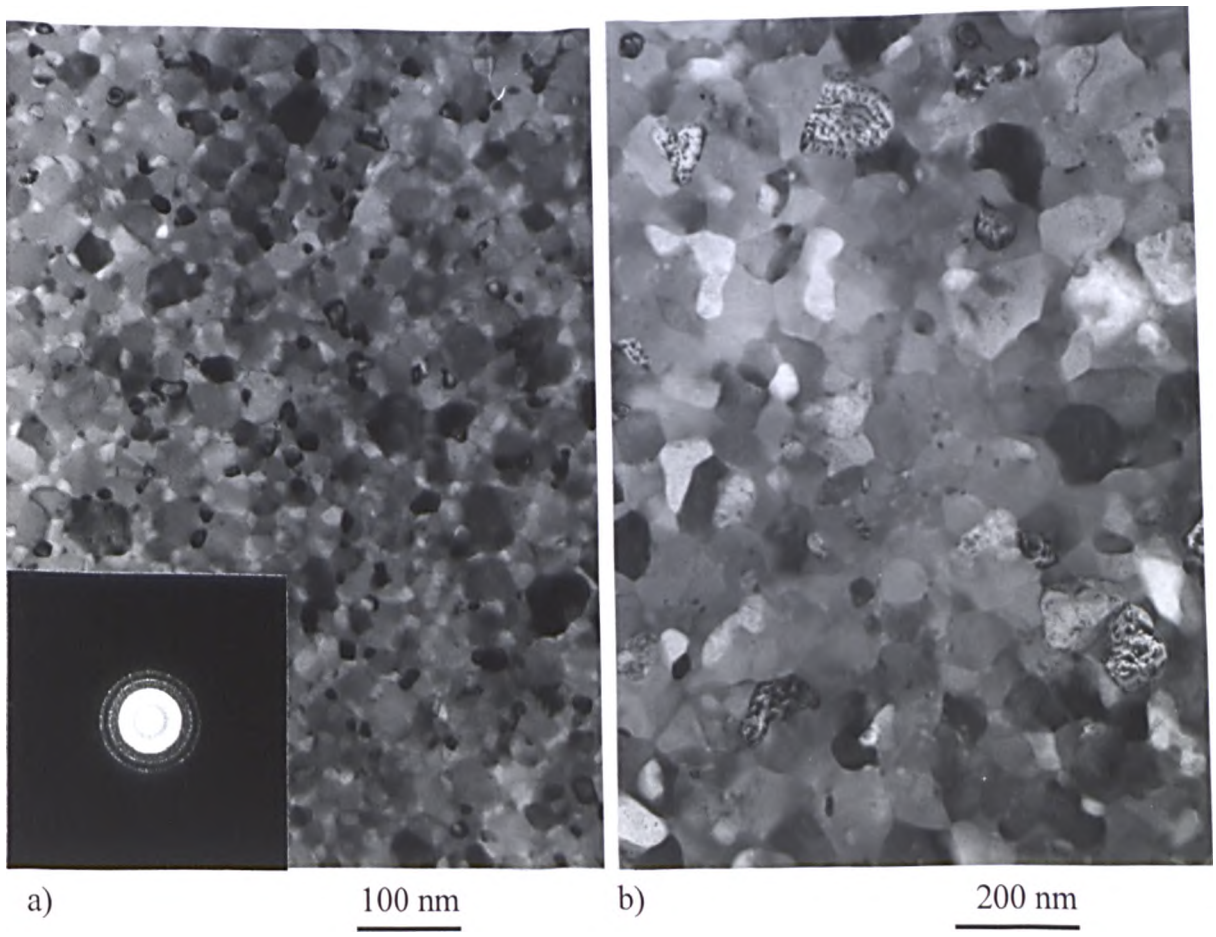

Figure 4- 48: a) TEM bright field image of a typical $Fe_{85.1}Nd_9B_{5.9}$ alloy ribbon melt spun at 26 m/s and annealed at 700°C for 4 minutes, b) as (a) from coarse grains.

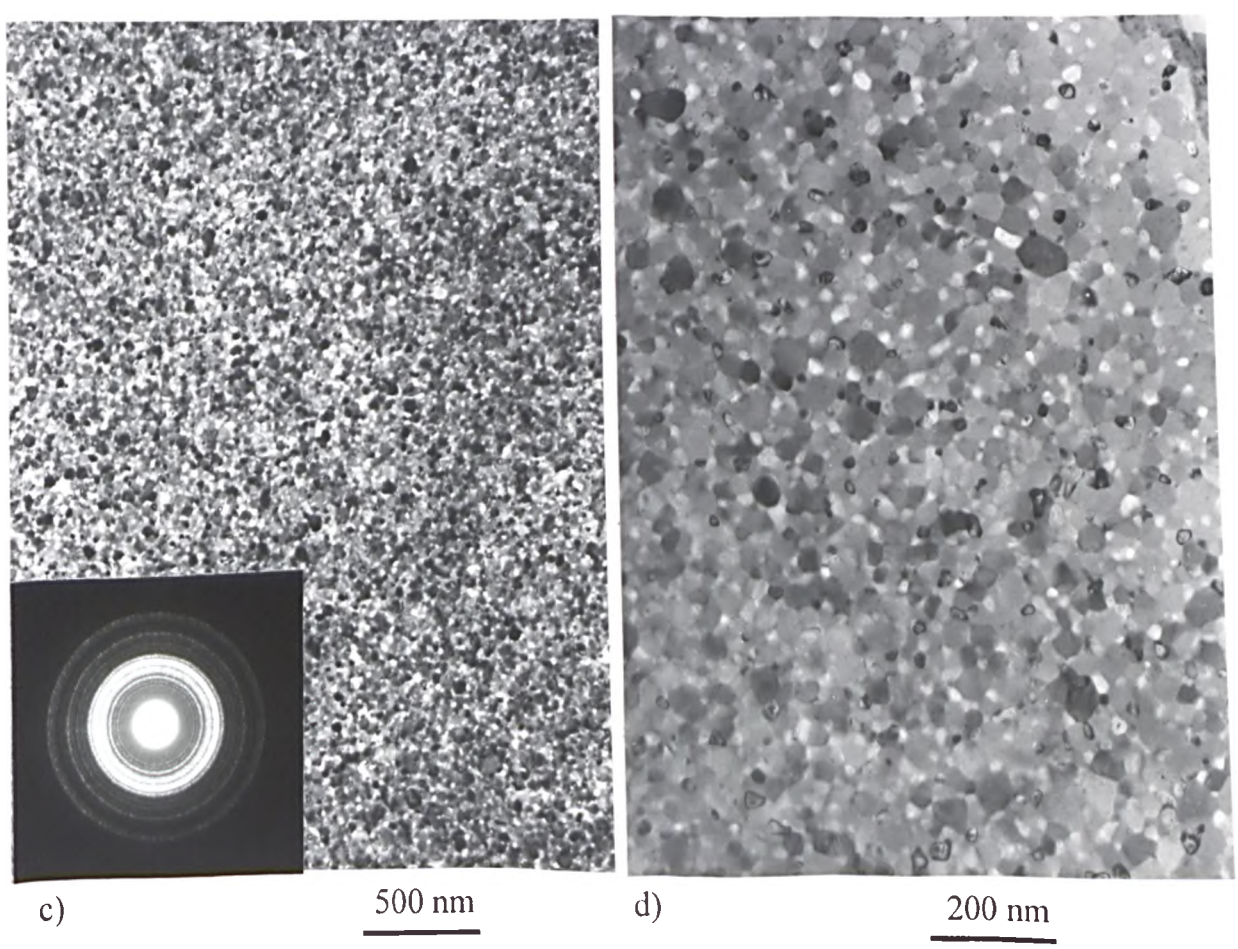

Figure 4- 49: a) Same as Figure 4- 48 but from a ribbon having magnetic properties of J_r=1.1 T, $_jH_c$=500 kAm^{-1}, $(BH)_{max}$=147 kJm^{-3}, b) as (a) at higher magnification .

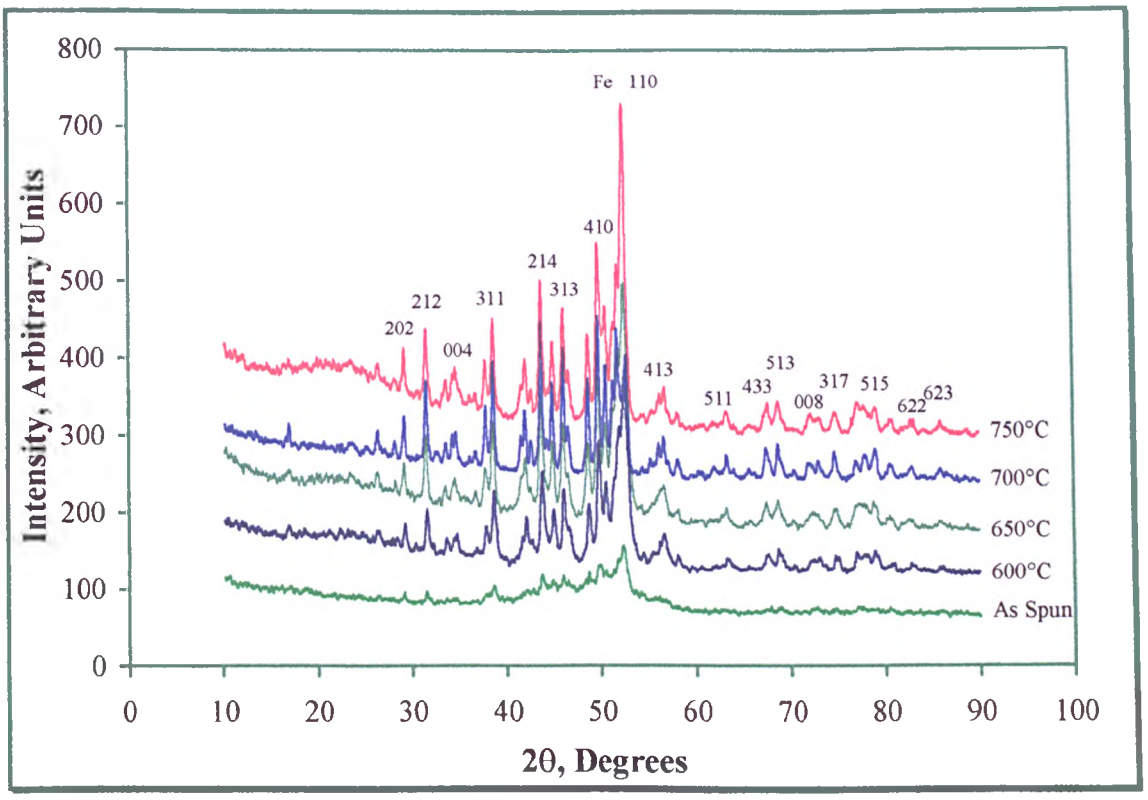

Figure 4- 50: X-ray diffraction traces of $Fe_{85.1}Nd_9B_{5.9}$ ribbon samples, melt spun at 26 m/s and annealed for 4 minutes at different temperatures.

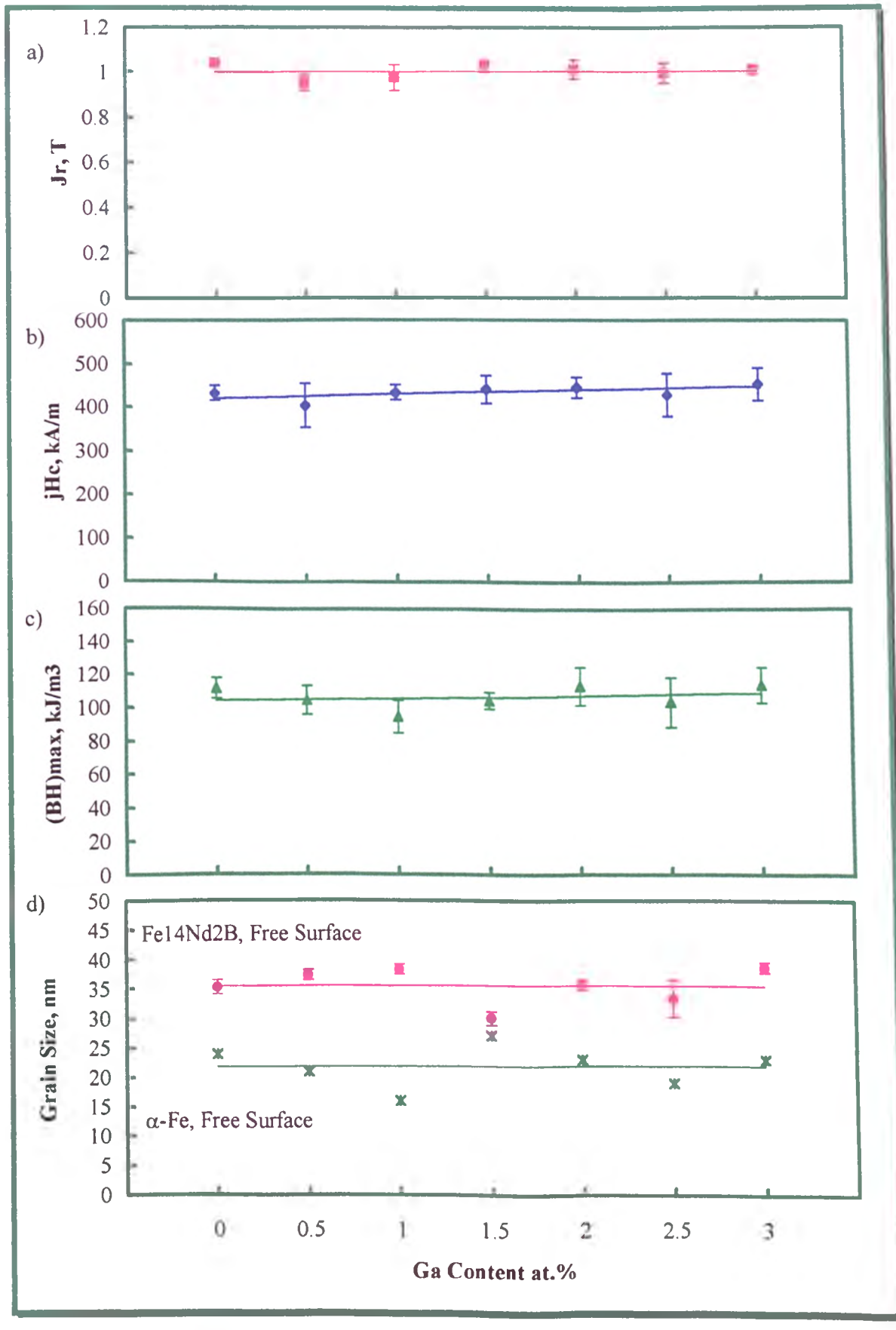

Figure 4- 51: a) J_r ■ b) $_jH_c$ ◆ and c) $(BH)_{max}$ ▲ as a function of Ga content for $Fe_{85.1-x}Nd_9B_{5.9}Ga_x$ alloy ribbons over quenched at 26 m/s and annealed for 4 minutes at 750°C.

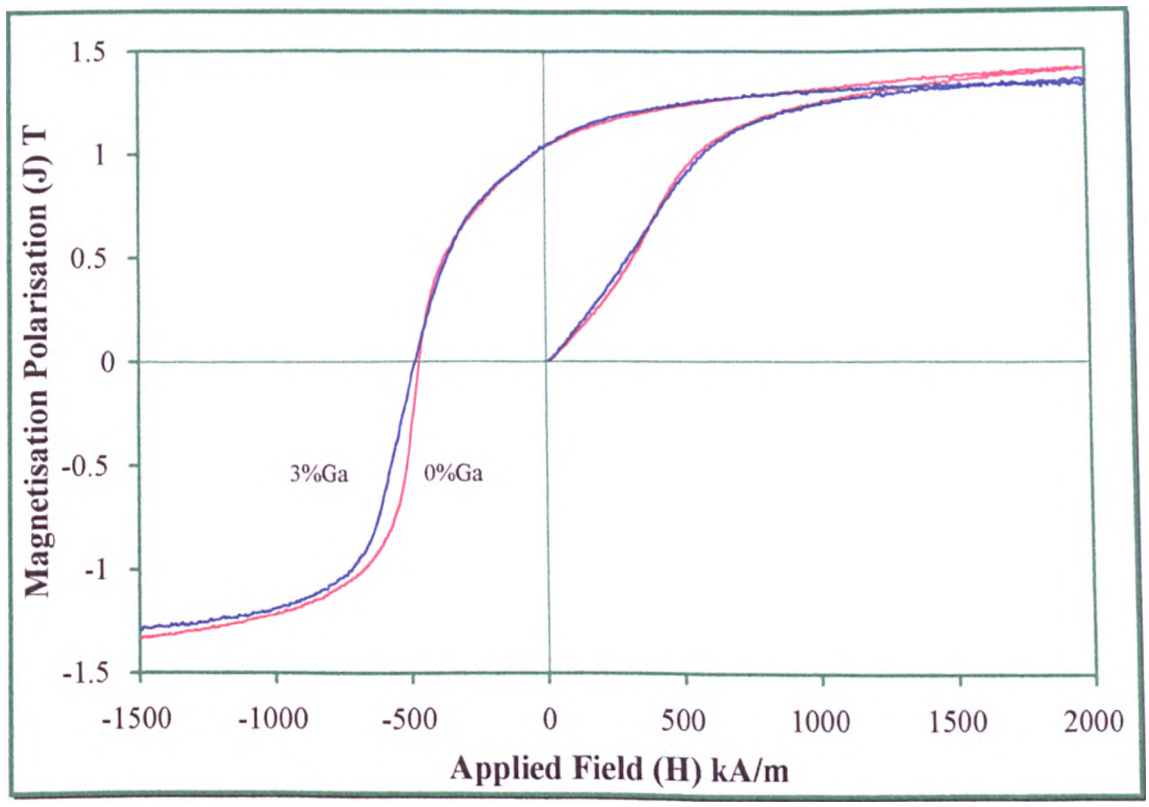

Figure 4- 52: Hysteresis loop for $Fe_{85.1}Nd_9B_{5.9}$ and $Fe_{82.1}Nd_9B_{5.9}Ga_3$ alloy ribbons melt spun at 26 m/s and annealed for 4 minutes at 750°C.

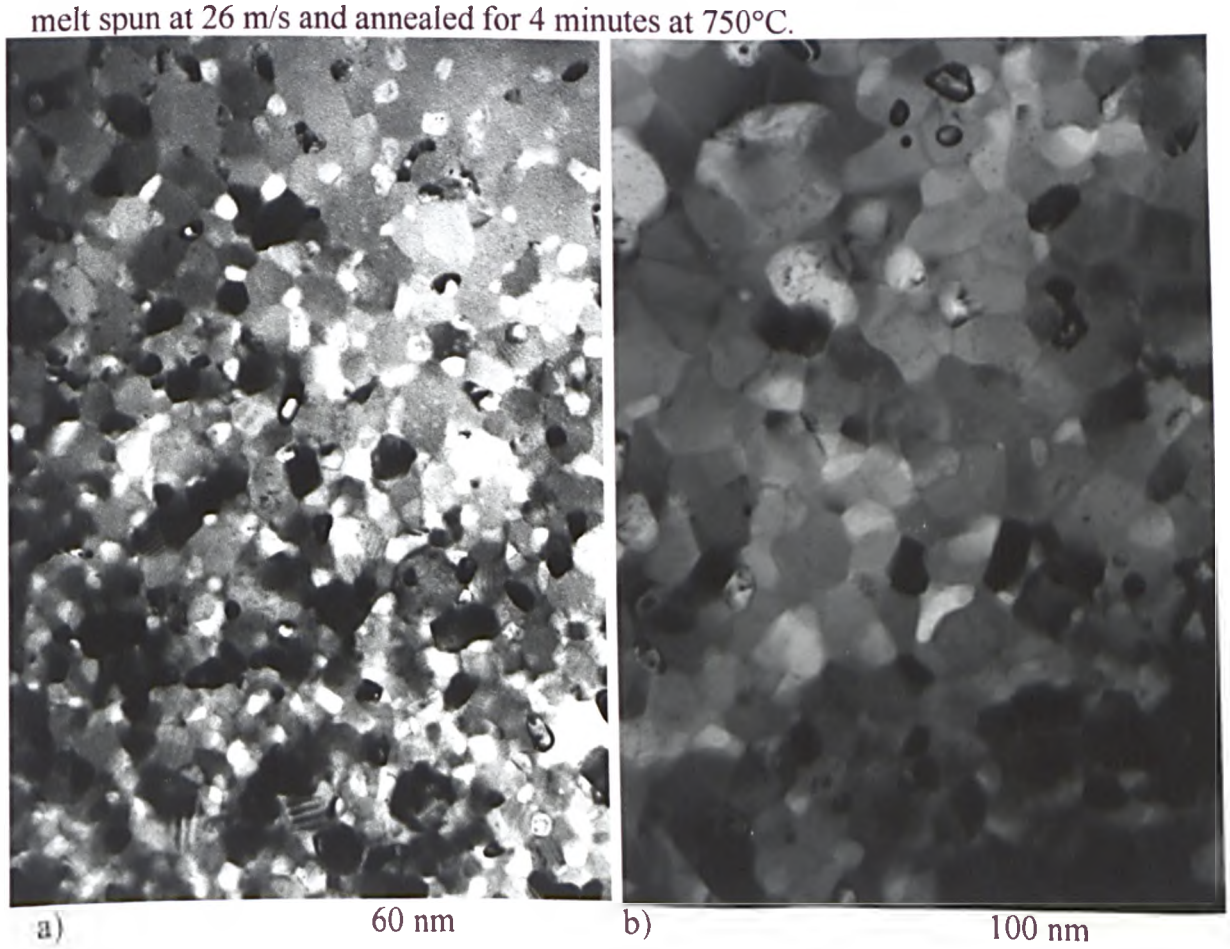

Figure 4- 53: TEM bright field image for $Fe_{82.1}Nd_9B_{5.9}Ga_3$ alloys, melt spun at 26 m/s and annealed for 4 minutes at 750°C, b) as (a) from coarse grains.

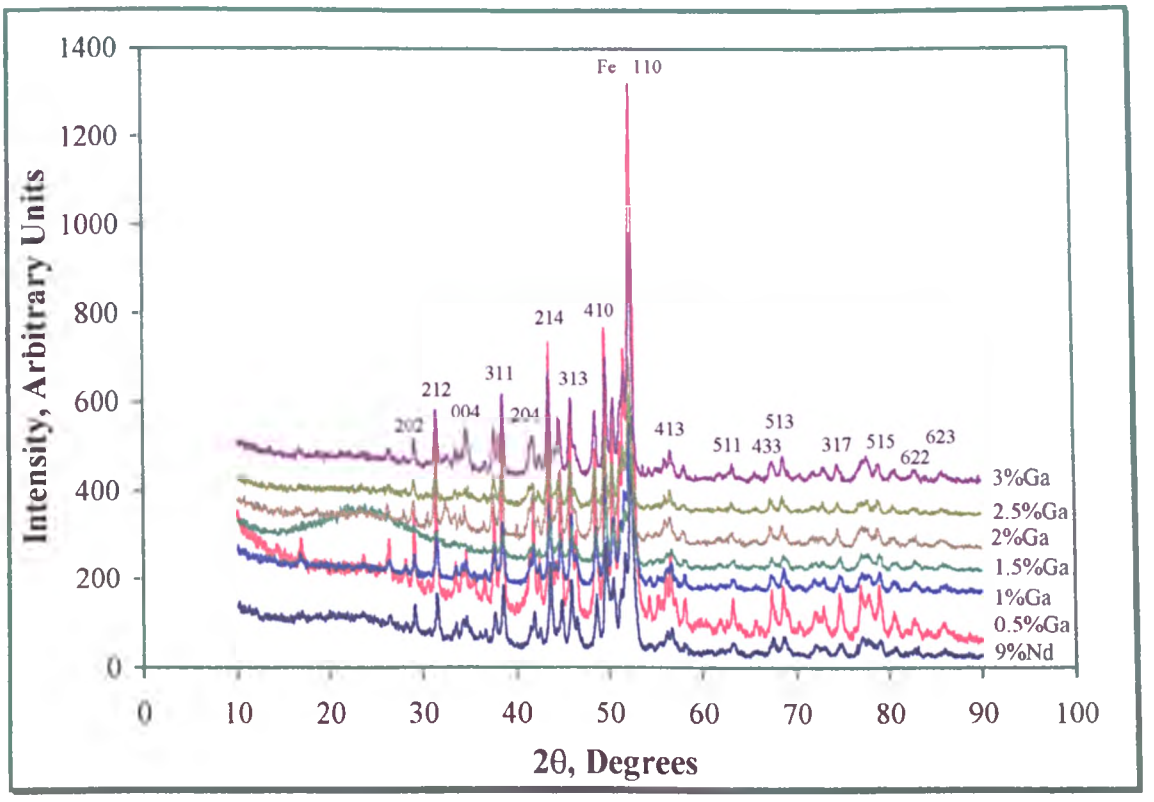

Figure 4- 54: X-ray diffraction traces of $Fe_{85\ 1-x}Nd_9B_{5\ 9}Ga_x$, melt spun at 26 m/s and annealed for 4 minutes at 700°C.

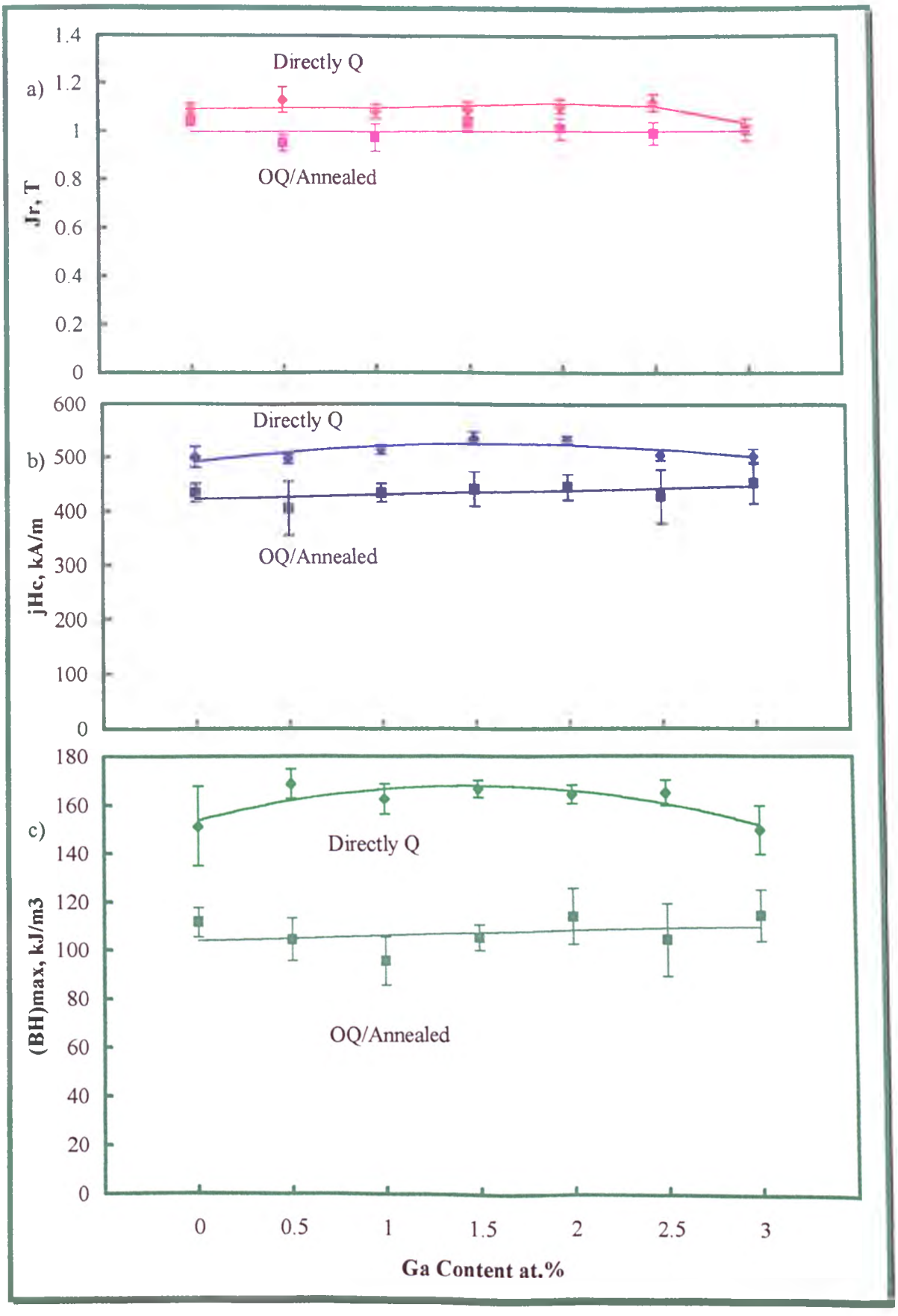

Figure 4- 55: a) J_r, b) $_jH_c$ and c) $(BH)_{max}$ as a function of Ga content for $Fe_{85\ 1-x}Nd_9B_{5\ 9}Ga_x$ samples in i) the optimum directly quenched ◆ and ii) over quenched (26 m/s) and annealed (4 min/700°C) ■ conditions.

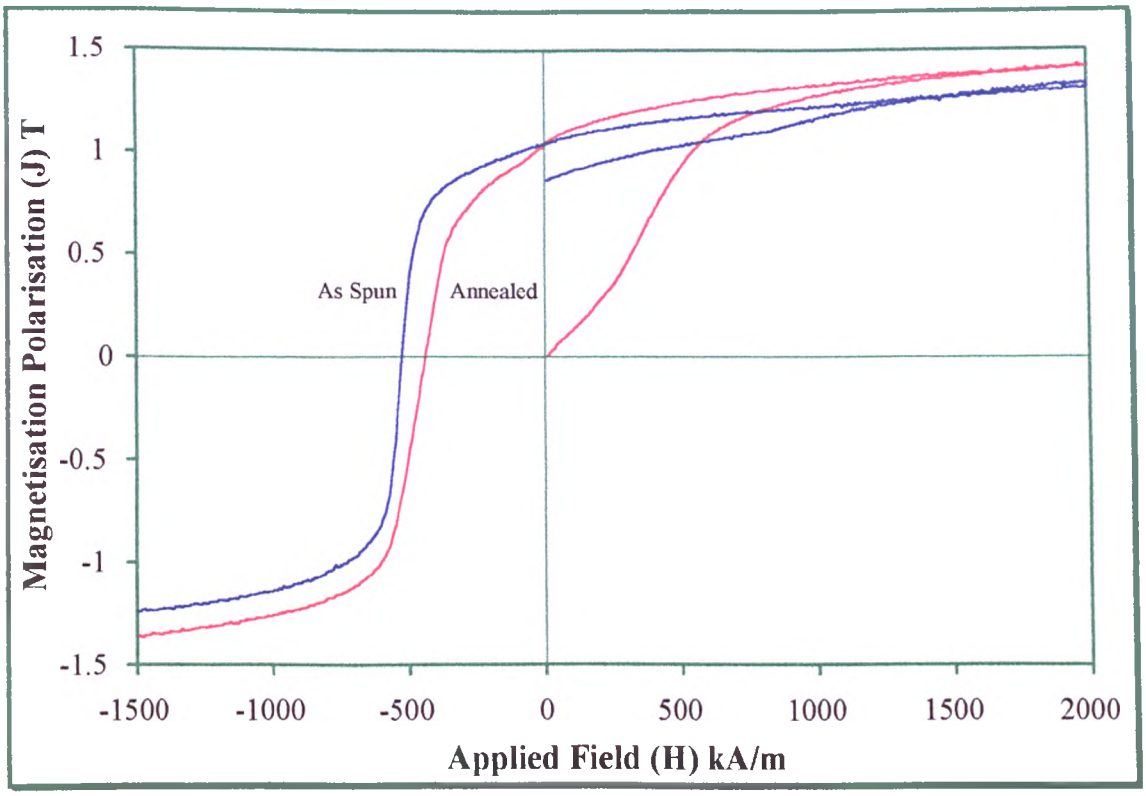

Figure 4- 56: Hysteresis loop for directly quenched and over-quenched and annealed $Fe_{85.1}Nd_9B_{5.9}$.

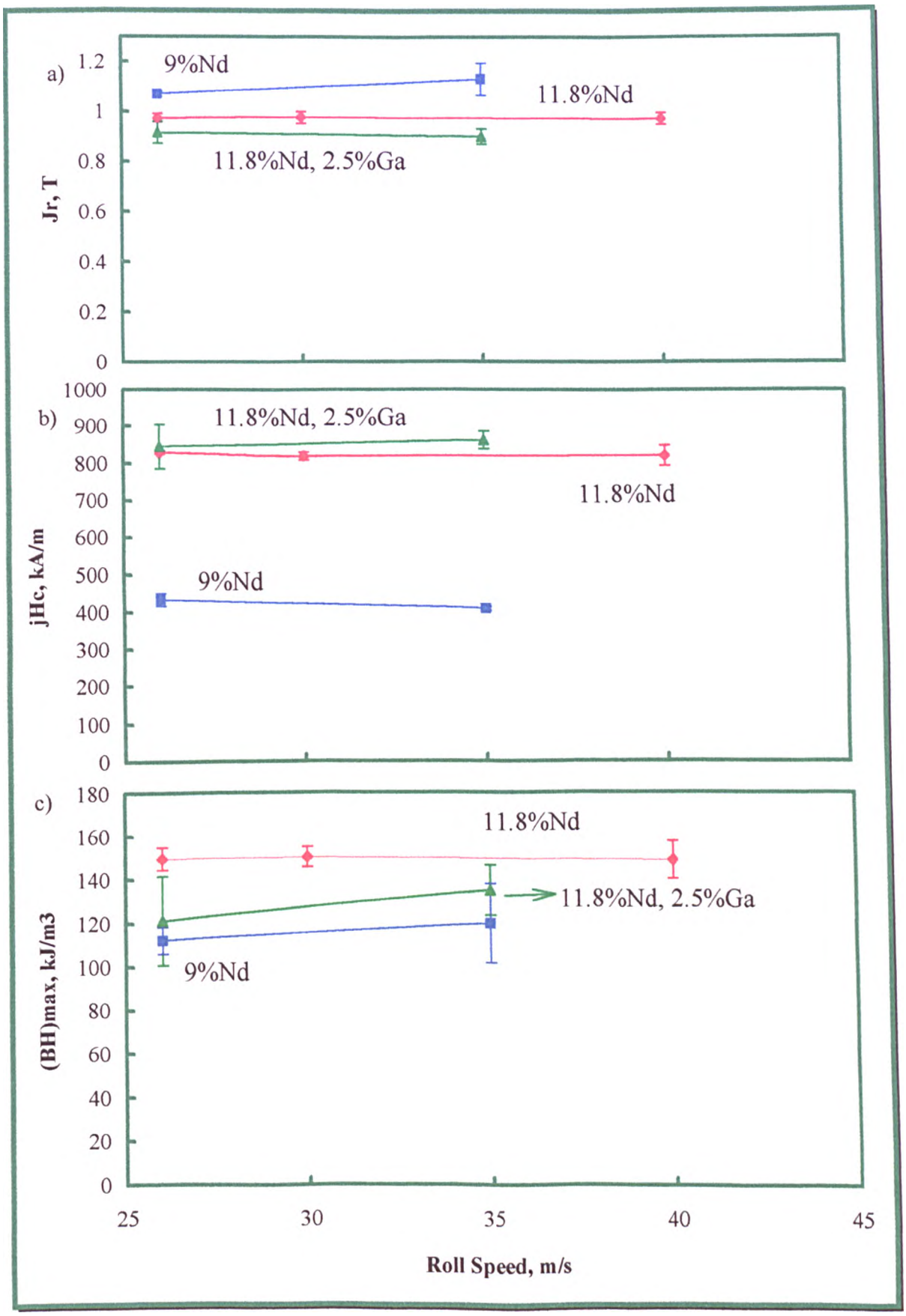

Figure 4- 57: a) J_r, b) $_jH_c$ and c) $(BH)_{max}$ as a function of roll speed during quench for $Fe_{82.3}Nd_{11.8}B_{5.9}$ ◆ , $Fe_{79.8}Nd_{11.8}B_{5.9}Ga_{2.5}$ ▲ and $Fe_{85.1}Nd_9B_{5.9}$ ■ ribbon samples, for the overquenched and optimally annealed condition.

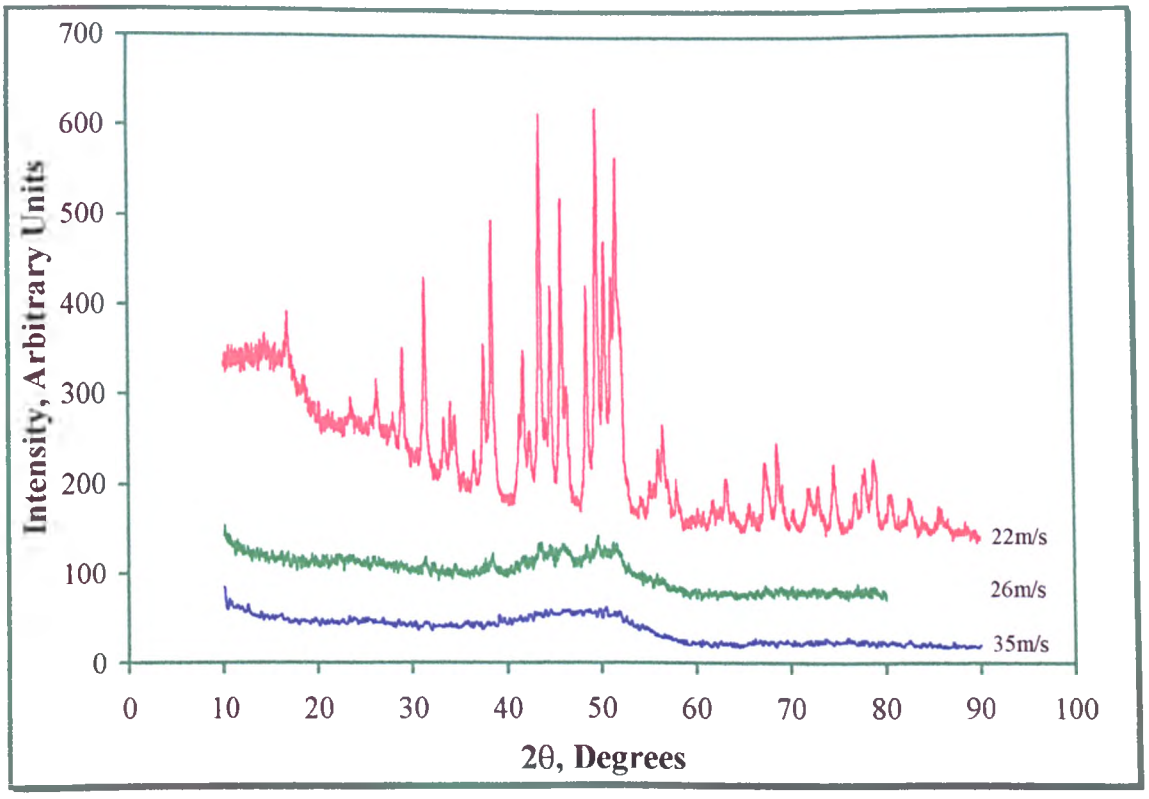

Figure 4- 58: X-ray diffraction traces of $Fe_{82.3}Nd_{11.8}B_{5.9}$, melt spun at different roll speeds.

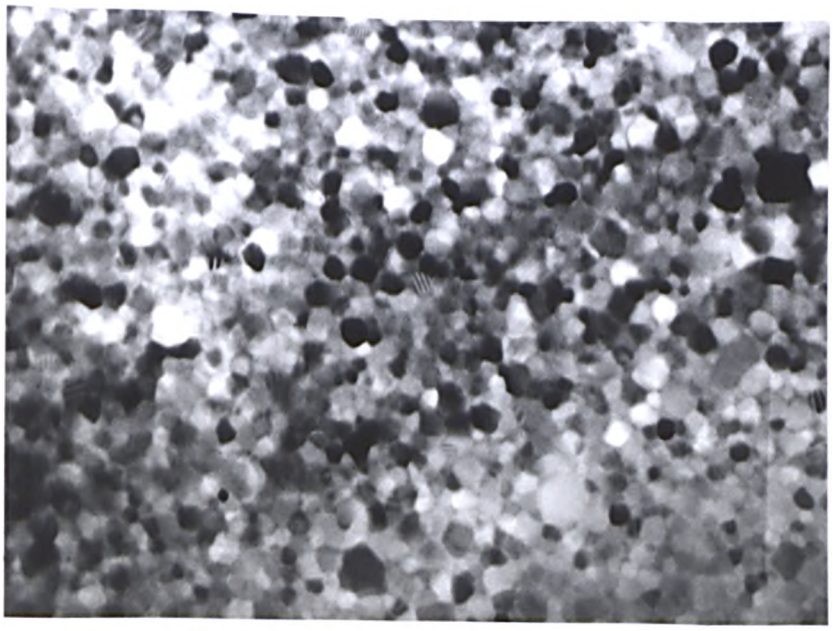

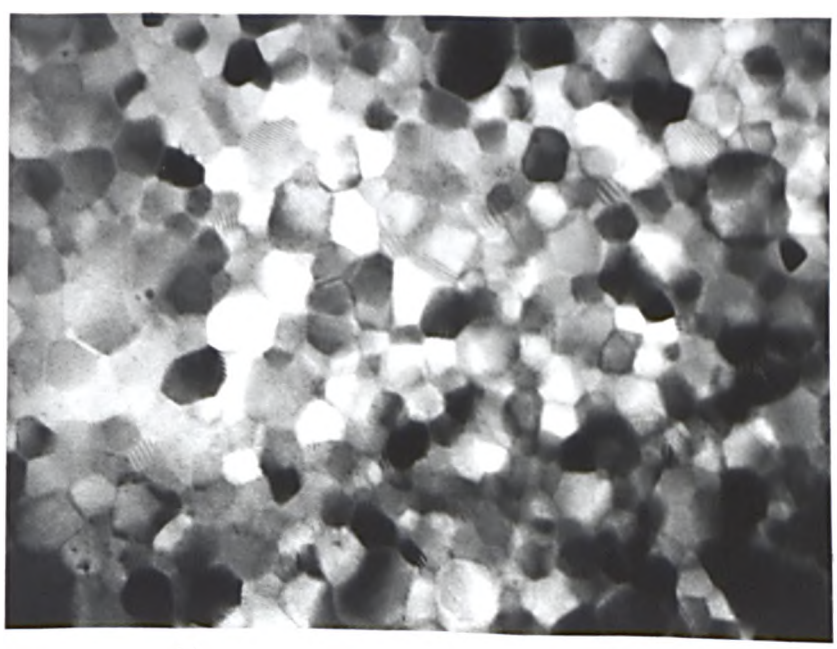

Figure 4- 59: a) TEM bright field image of $Fe_{82.3}Nd_{11.8}B_{5.9}$ melt spun at 40 m/s and annealed at 650°C for 4 minutes, b) as a) shows coarser grains.

Figure 4- 60: TEM bright field images of $Fe_{85.1}Nd_9B_{5.9}$ alloy melt spun at 26 m/s and annealed for 4 minutes at 600 °C.

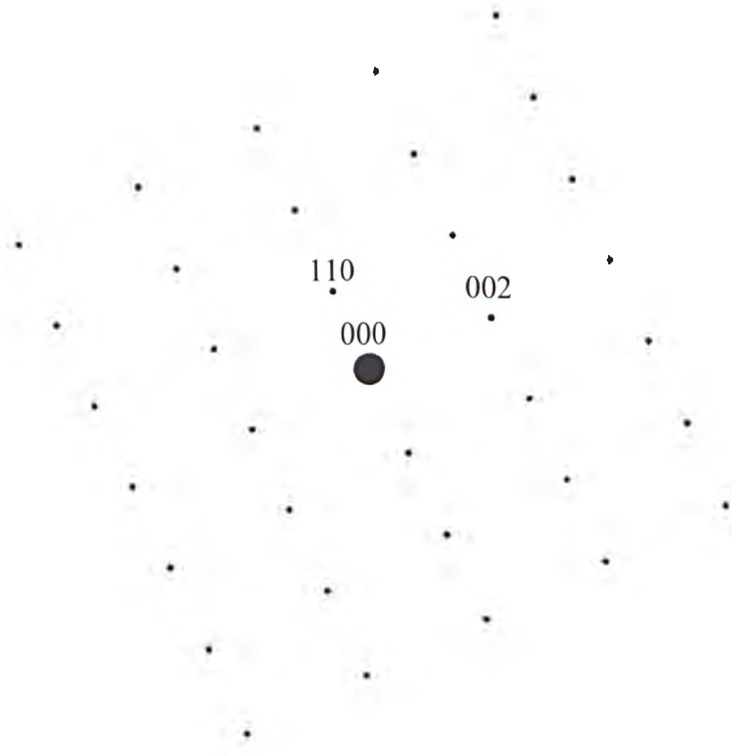

c)

Figure 4- 61: a) TEM bright field image of $Fe_{83.2}Nd_{10.9}B_{5.9}$ alloy melt spun at 20 m/s, b) nanodiffraction pattern of an α-Fe particle, taken from [$2\bar{2}0$] zone axis, c) indexed schematic of (b).

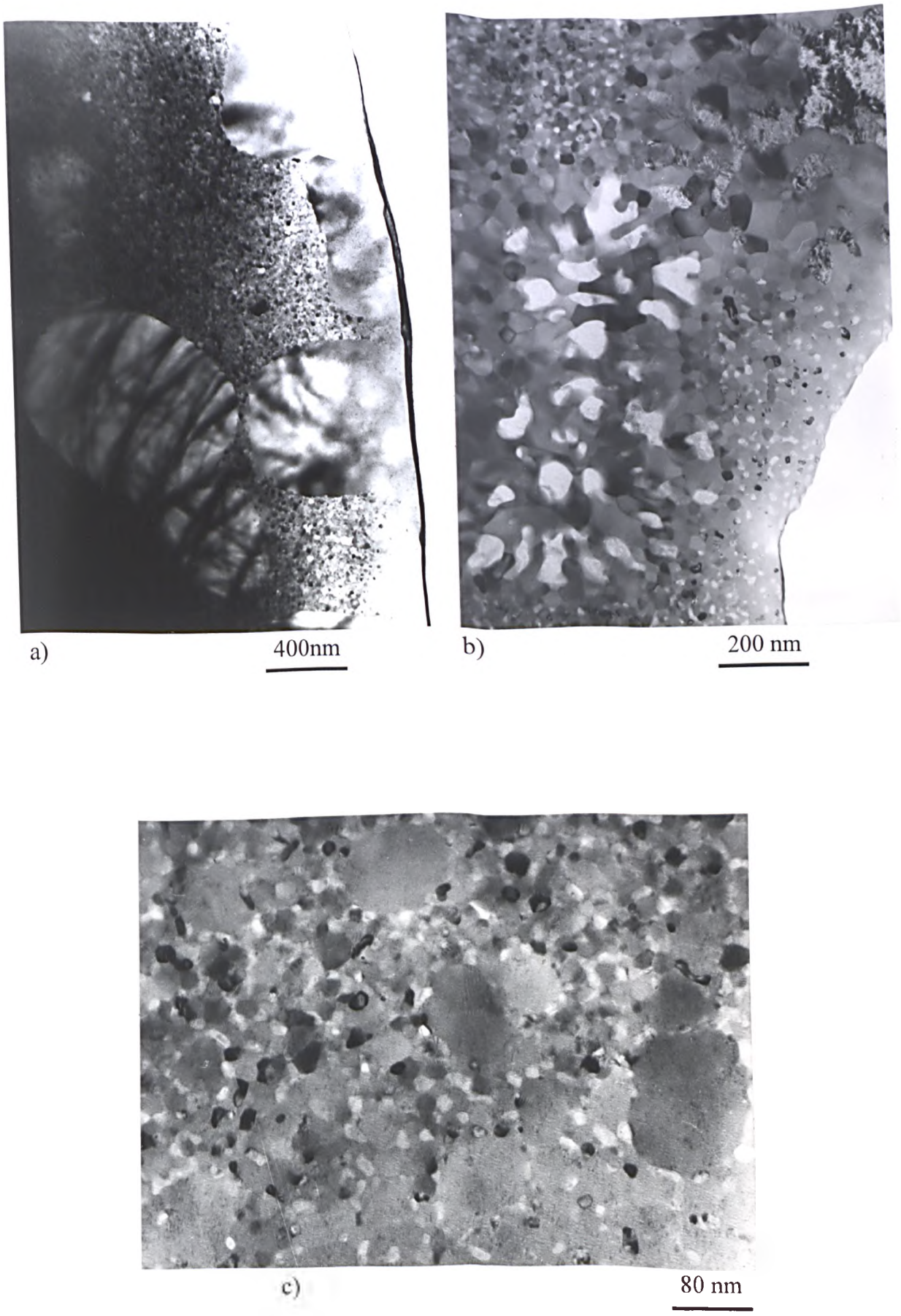

Figure 4- 62: TEM bright field images of a) $Fe_{82.3}Nd_{11.8}B_{5.9}$, b) $Fe_{85.1}Nd_9B_{5.9}$, and c) $Fe_{84.1}Nd_9B_{5.9}Ga$ alloy melt spun at a) 20, b) and c) 22 m/s.

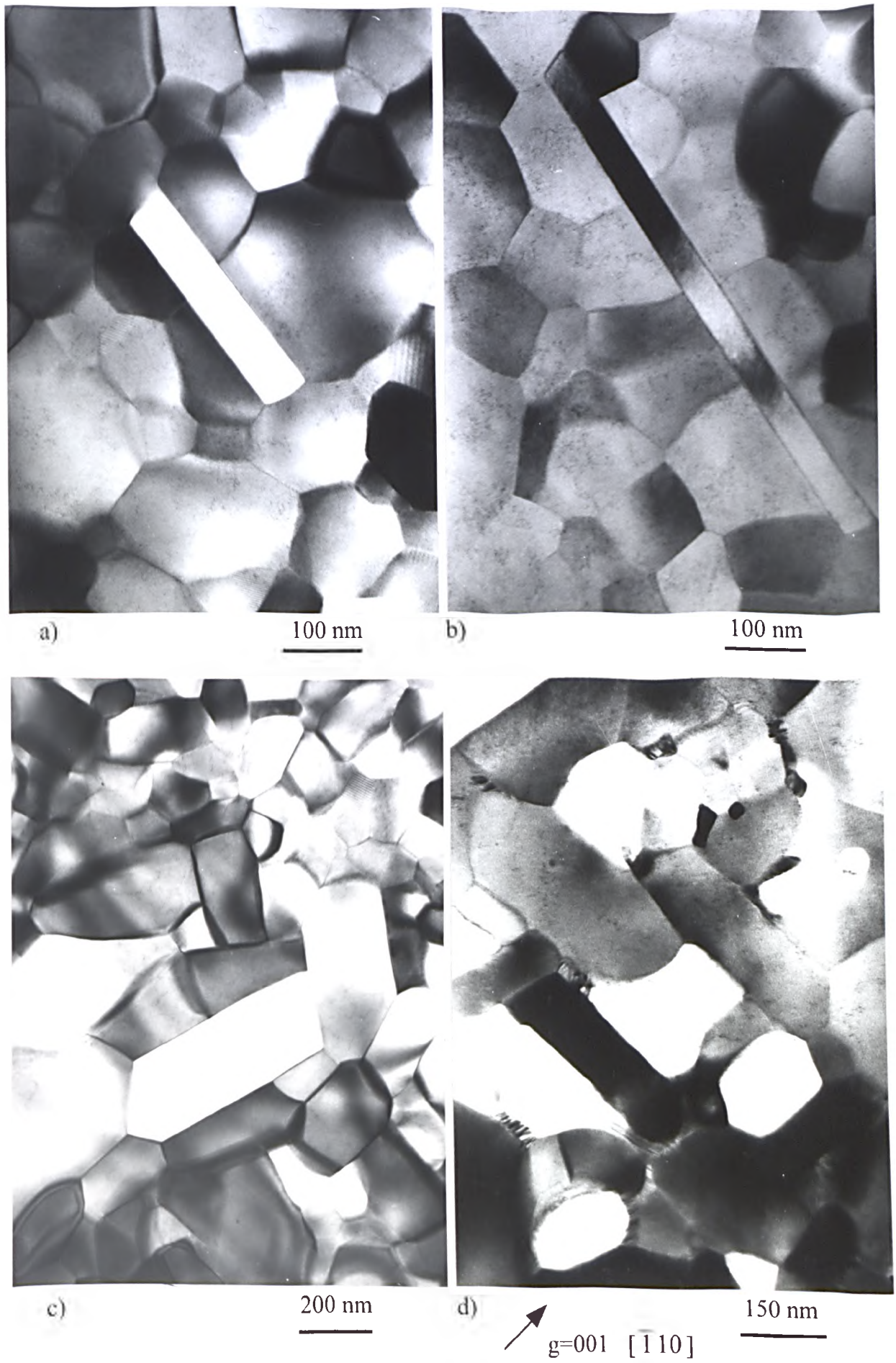

Figure 4- 63: TEM bright field images of $Fe_{82.3}Nd_{11.8}B_{5.9}$ alloy melt spun at 26 m/s and annealed for 4 minutes at 800°C for (a) and (b), and 850°C for (c). Micrograph (d) is taken from $Fe_{85.1}Nd_9B_{5.9}$ alloy melt spun at 22 m/s, the arrow shows g=001 direction for the dark grain on bottom left corner of this picture.

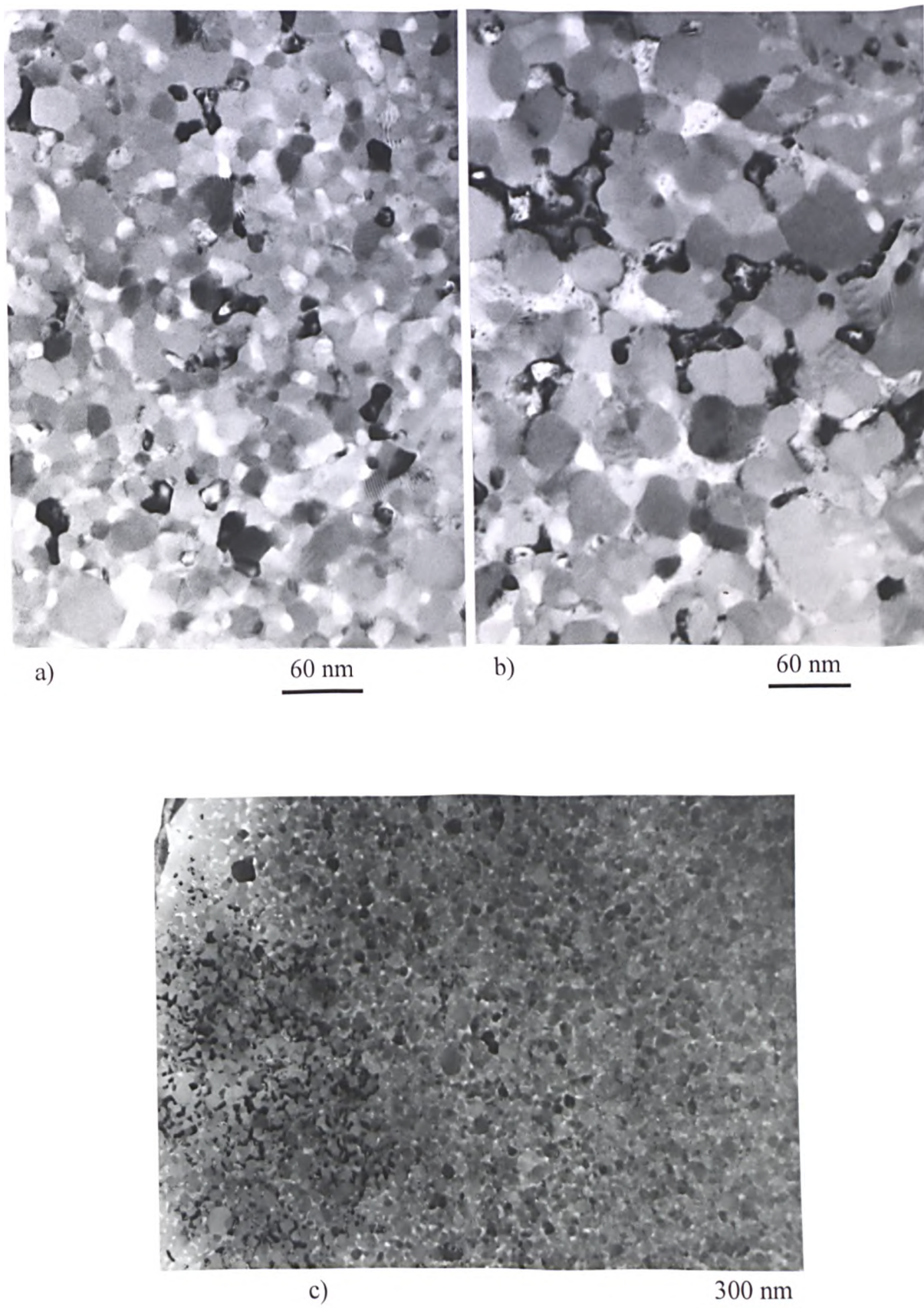

Figure 4- 64: a) and b) TEM bright field images of $Fe_{82.6}Nd_9B_{5.9}Ga_{2.5}$ alloy melt spun at 21 m/s, c) the same area as (a) and (b) at lower magnification.

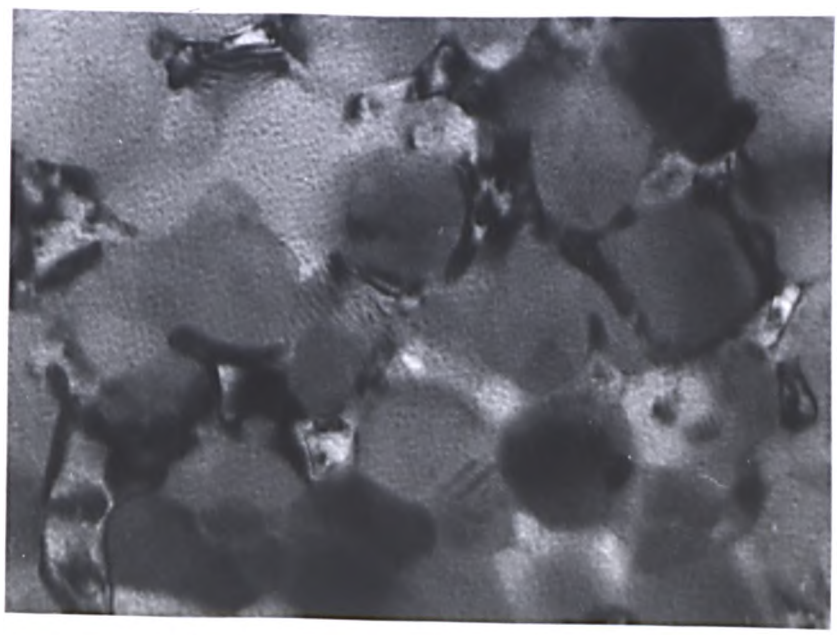

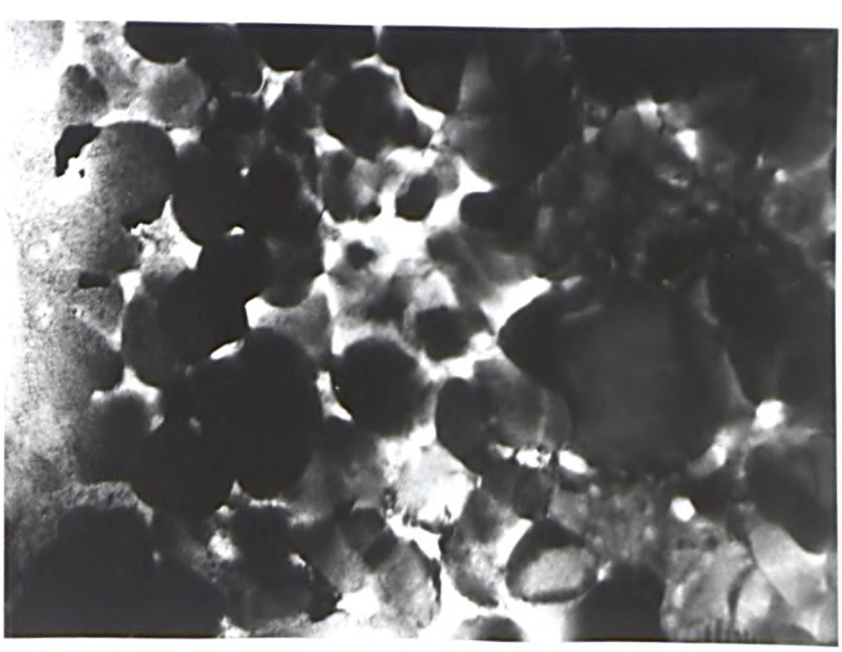

Figure 4- 65: TEM bright field images of: a) $Fe_{83.6}Nd_9B_{5.9}Ga_{1.5}$ alloy and b) $Fe_{85.1}Nd_9B_{5.9}$ alloy, both melt spun at 22 m/s.

a)

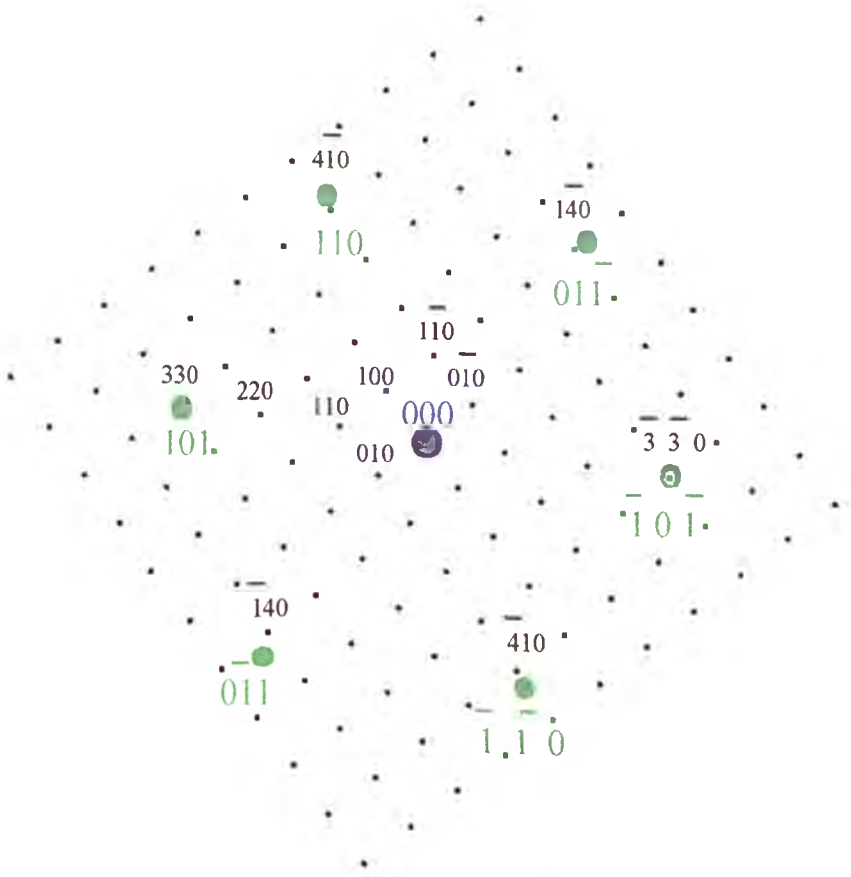

b) $Nd_2Fe_{14}B$ α-Fe

Figure 4- 66: a) selected area diffraction pattern (SAD) and b) indexed schematic of SAD of $Nd_2Fe_{14}B$ and α-Fe phase indicating $[001]_{\phi} \,||\, [1\bar{1}\bar{1}]_{\alpha\text{-Fe}}$ and $(110)_{\phi} \,||\, (101)_{\alpha\text{-Fe}}$.

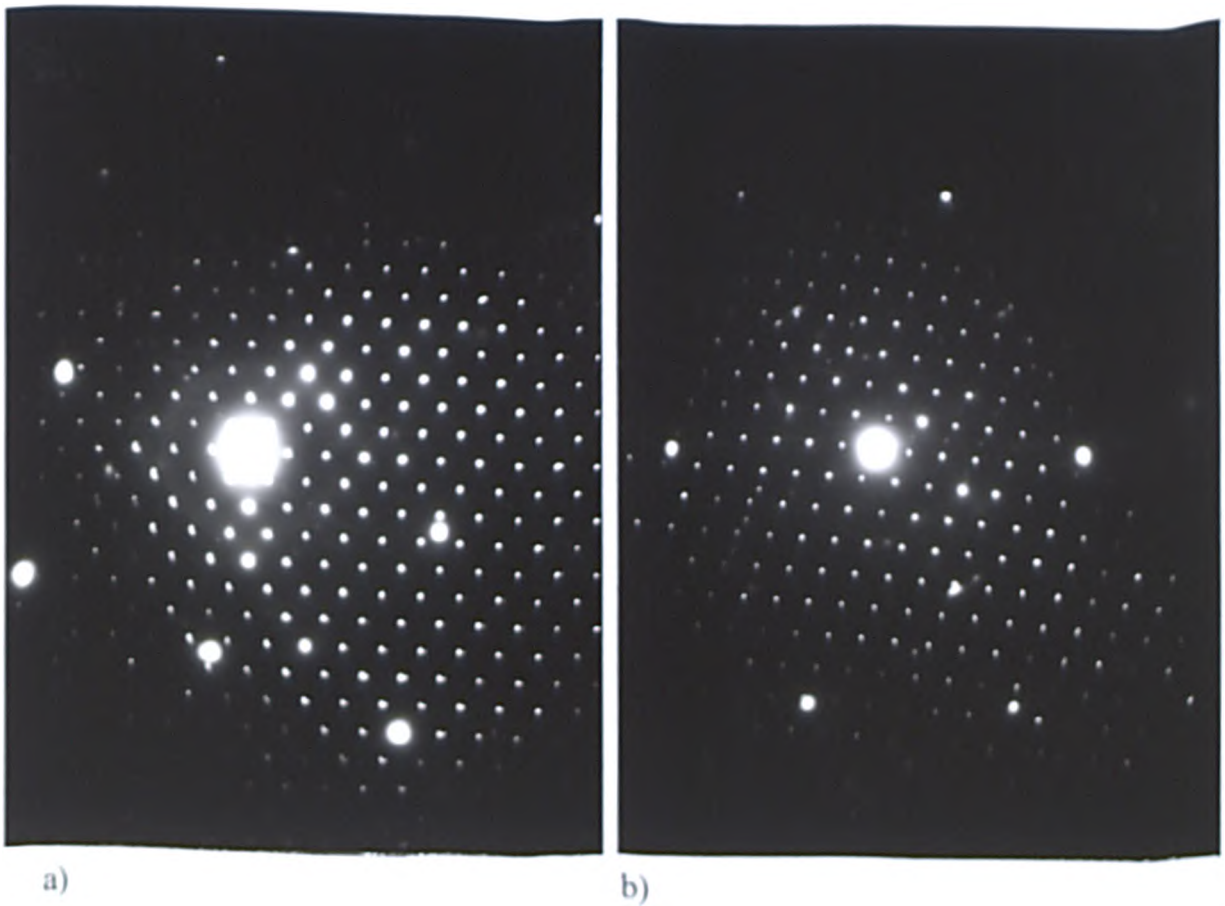

Figure 4- 67: a) Superimposed selected area diffraction patterns (SADs) from [010] zone axis for $Nd_2Fe_{14}B$ and [$\bar{1}$ 3 5] zone axis for α-Fe precipitate b) same as a from [1 1 1] and [3 2 $\bar{1}$] zone axes, respectively, and c) TEM dark field image taken from $Fe_{80.2}Nd_{10.3}B_{5.5}Ga_1$ alloy melt spun at 4 m/s using (110) reflection of α-Fe.

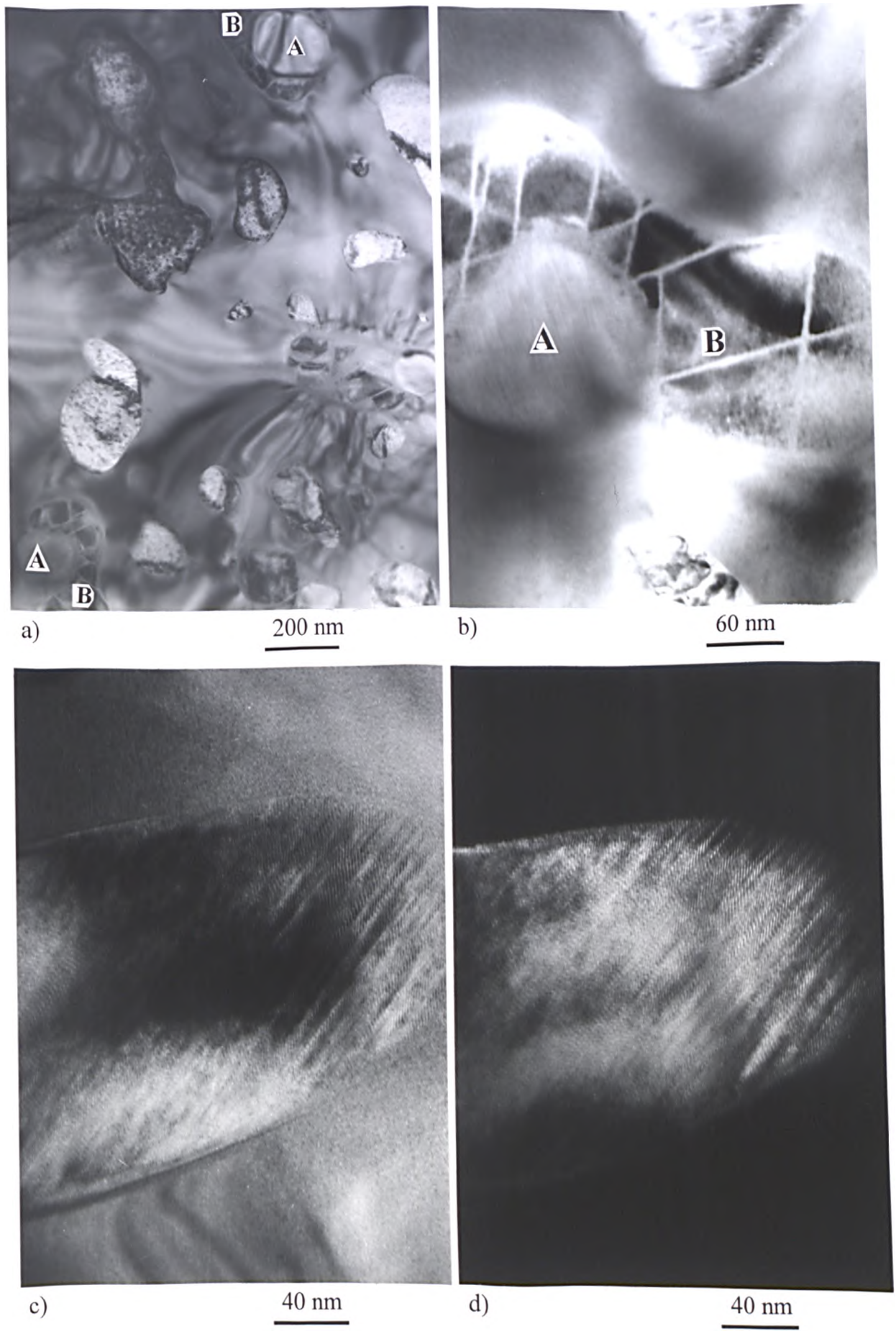

Figure 4- 68: a) TEM bright field image of $Fe_{79.3}Nd_{11.8}B_{5.9}Ga_3$ alloy melt spun at 4 m/s; b) same as (a) at higher magnification; c) and d) bright field and dark field images, respectively, of phase A in the same TEM thin foil specimen.

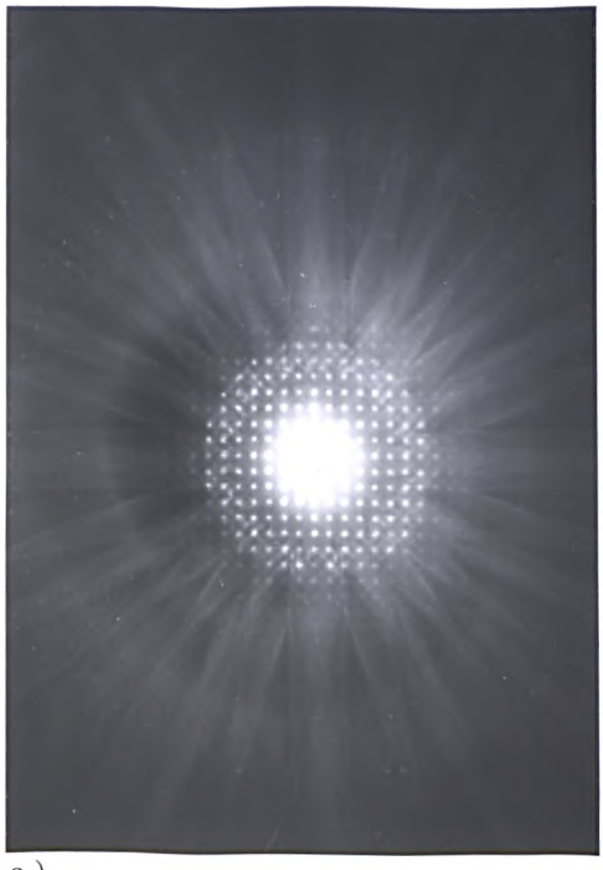

a_1)

a_2)

a_3)

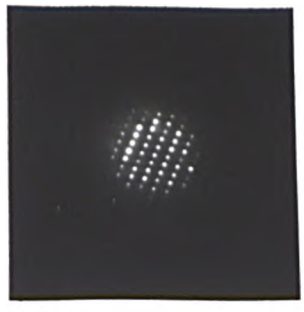

b_1)

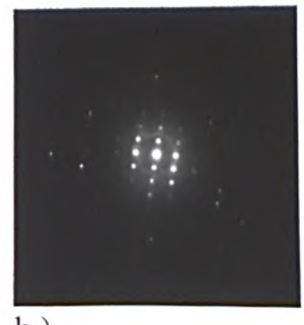

b_2)

b_3)

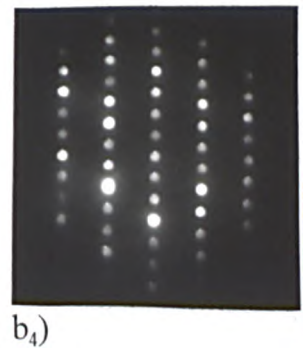

b_4)

Figure 4- 69: a_1) Convergent beam diffraction pattern and a_2) and a_3) nanodiffraction patterns from phase A and (b_1-b_4) nanodiffraction patterns from phase B taken from $Fe_{80.2}Nd_{10.9}B_{5.9}Ga_3$ alloy, melt spun at 4 m/s.

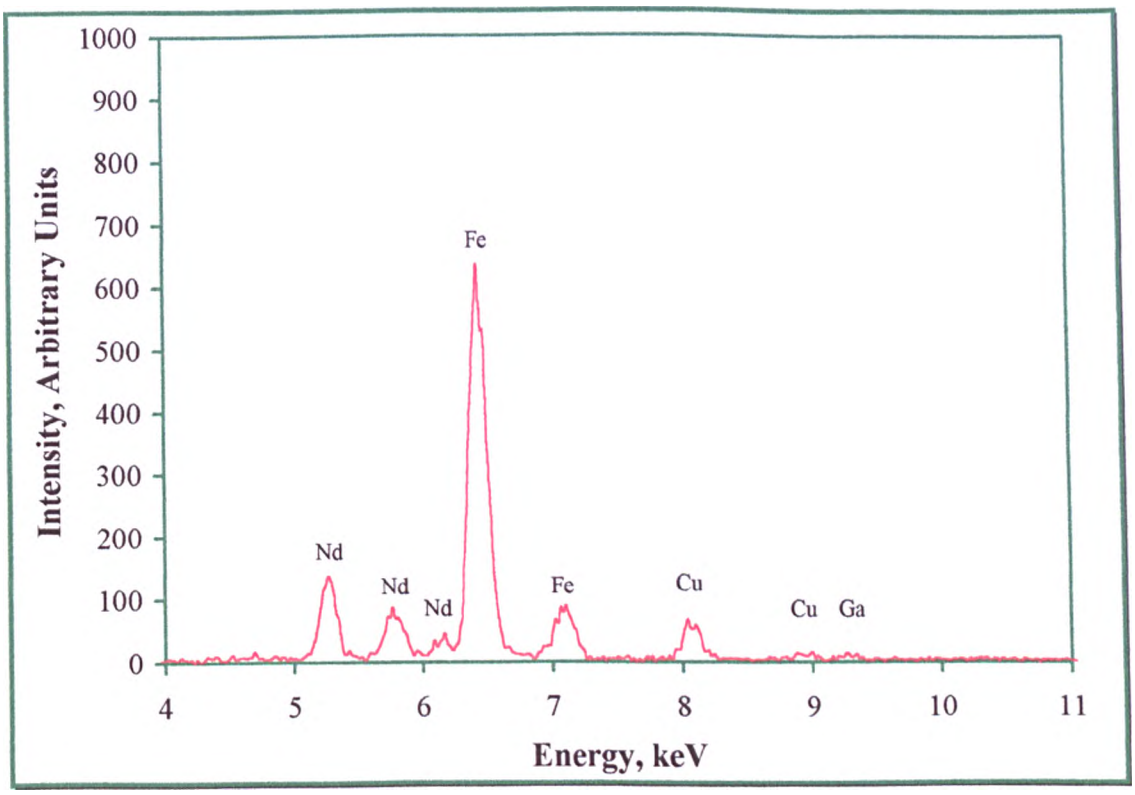

Figure 4- 70: EDS analysis of phase (A), elongated phase with zigzag pattern, showing a chemical analysis of 77 at.% Fe, 22.8 at.% Nd and 0.2 at.% Ga.

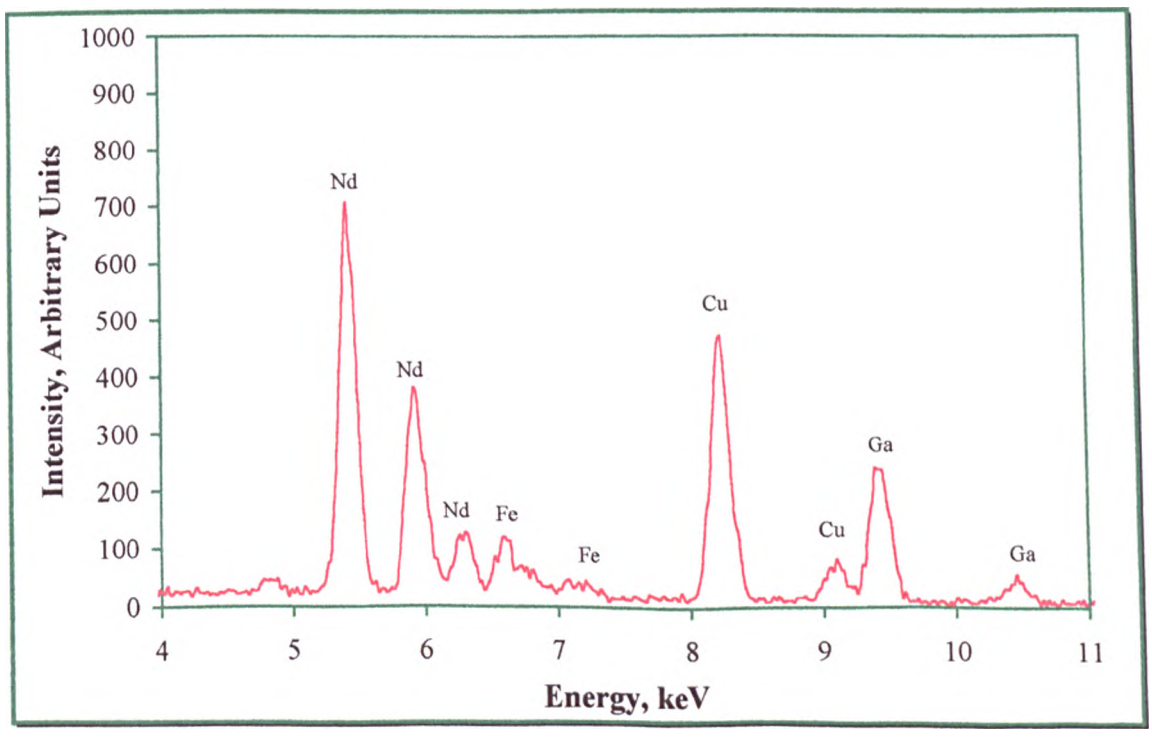

Figure 4- 71: EDS analysis of phase (B), spherical phase with bands, showing a chemical composition of 8.7 at.% Fe, 63.4 at.% Nd and 27.9 at.% Ga.

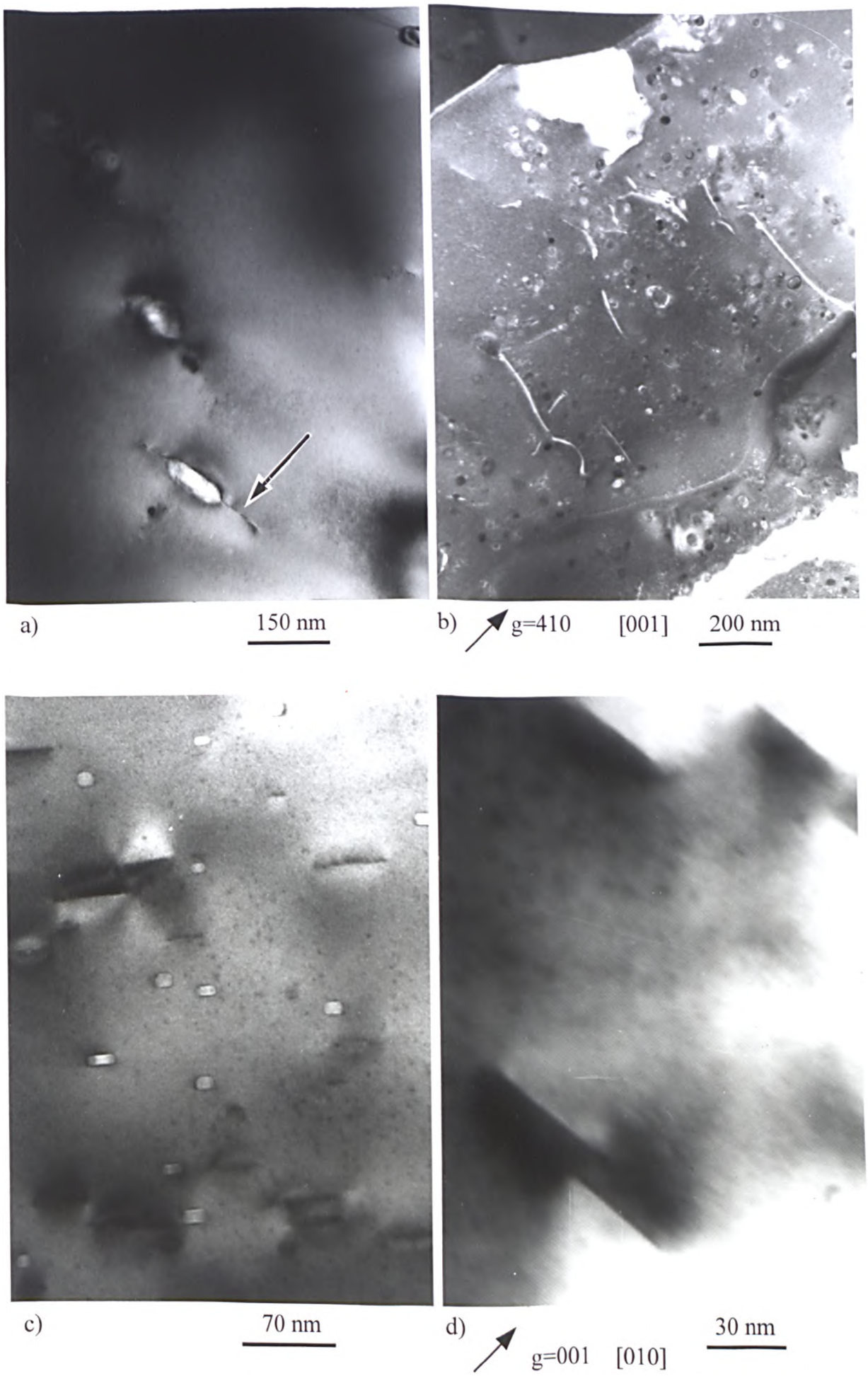

Figure 4- 72: a) TEM bright field (BF) image of $Fe_{83.2}Nd_{10.9}B_{5.9}$ melt spun at 23 m/s, b) weak beam dark field (WBDF) image of $Fe_{82.3}Nd_{11.8}B_{5.9}$ melt spun at 26 m/s and annealed for 4 minutes at 800°C, c) are TEM bright field (BF) image of $Fe_{83.2}Nd_{10.9}B_{5.9}$ melt spun at 23 m/s, d) as (c) at higher magnification.

Figure 4- 73: HREM of $Fe_{81.2}Nd_{10.9}B_{5.9}$ melt spun at 23 m/s.

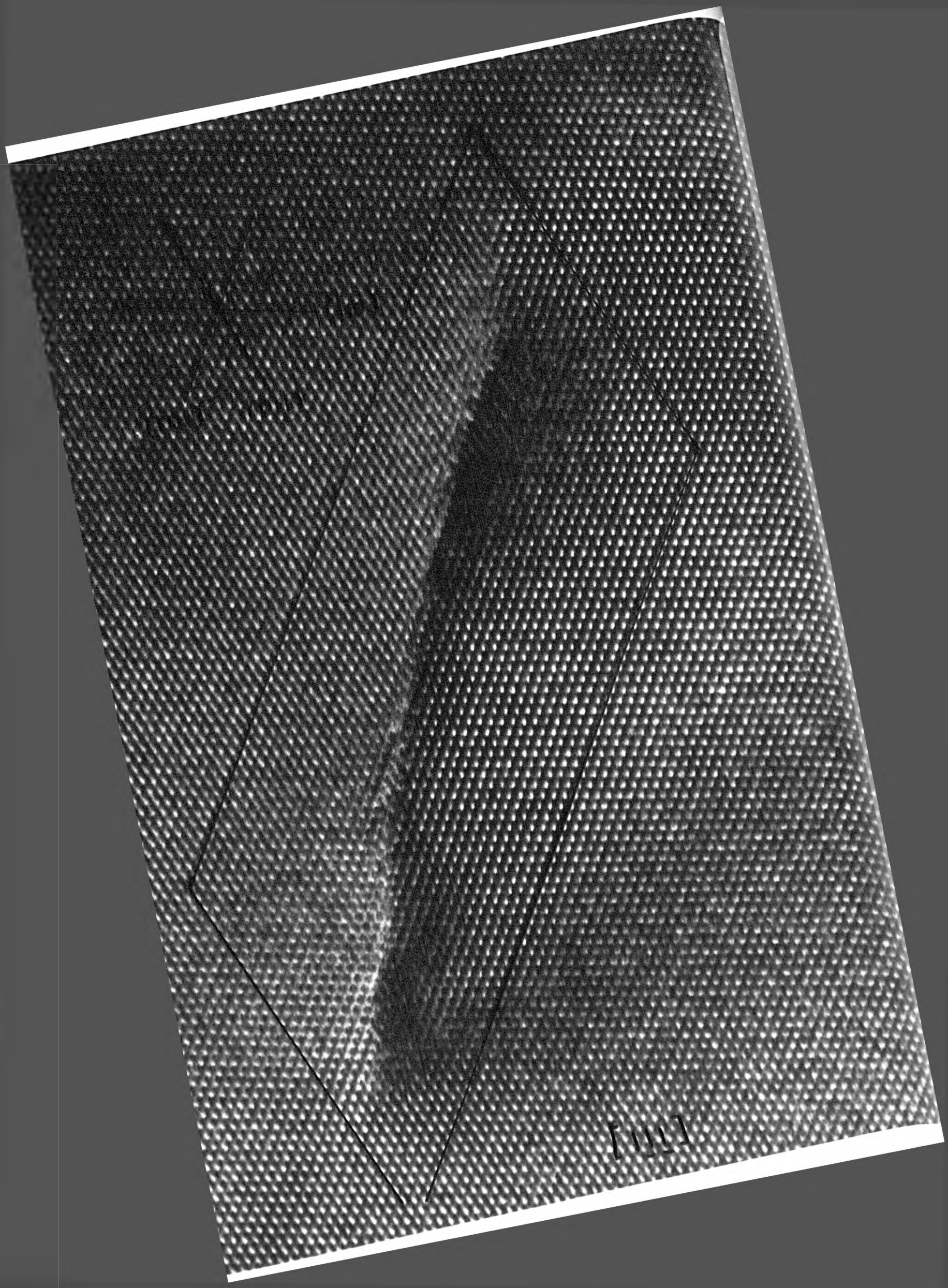
[111]

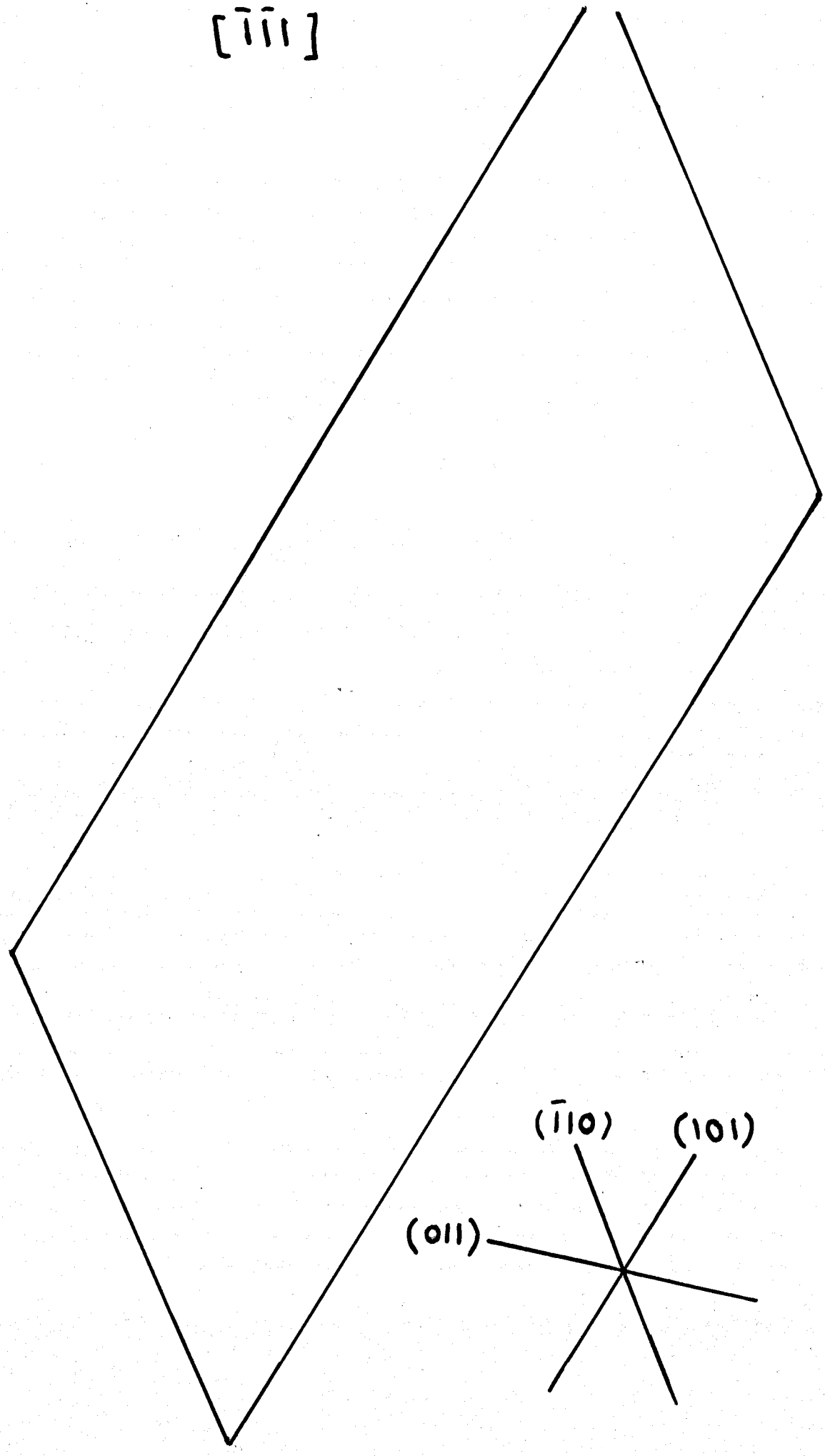
[$\bar{1}\bar{1}1$]
($\bar{1}10$)
(101)
(011)

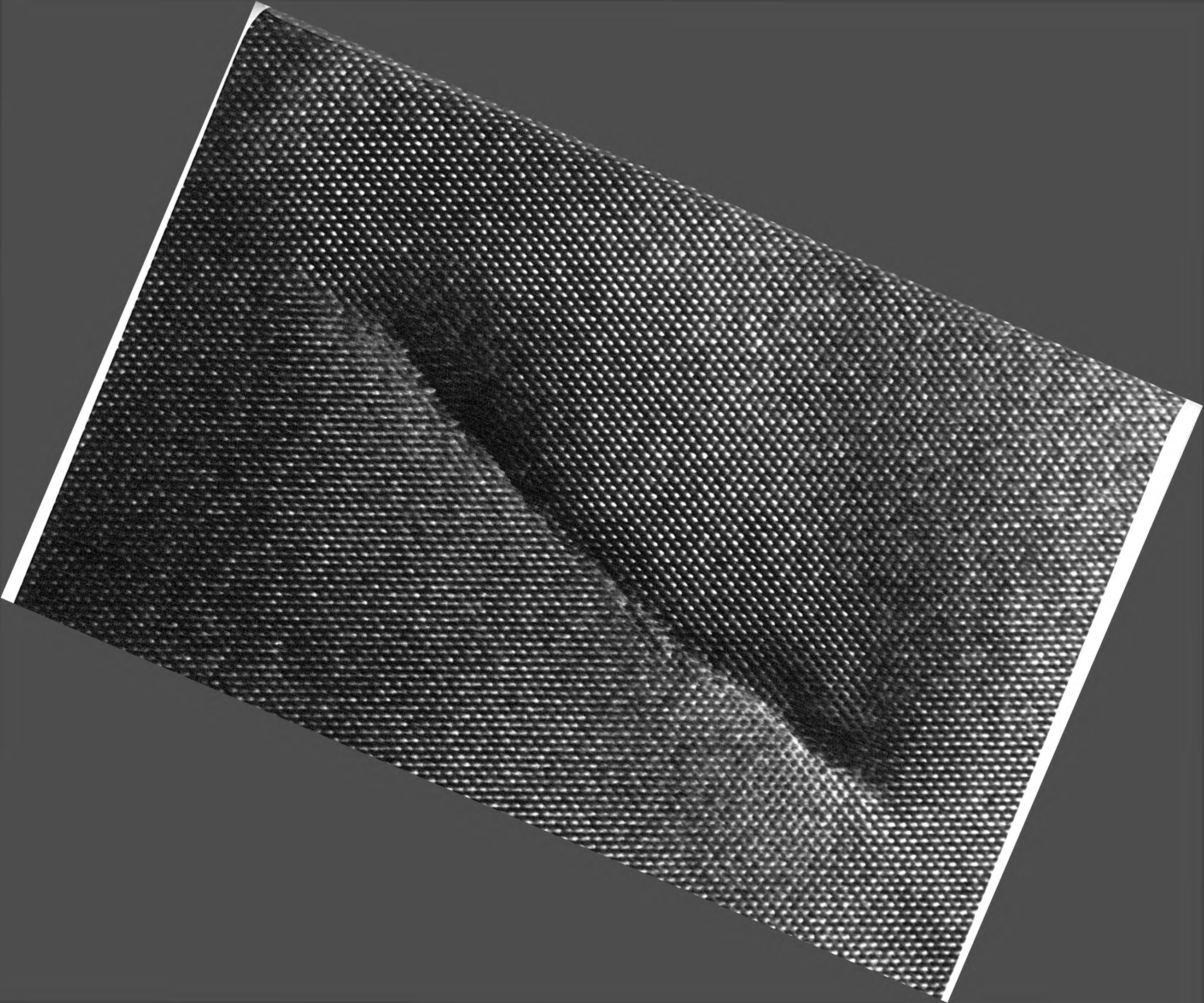

(a)

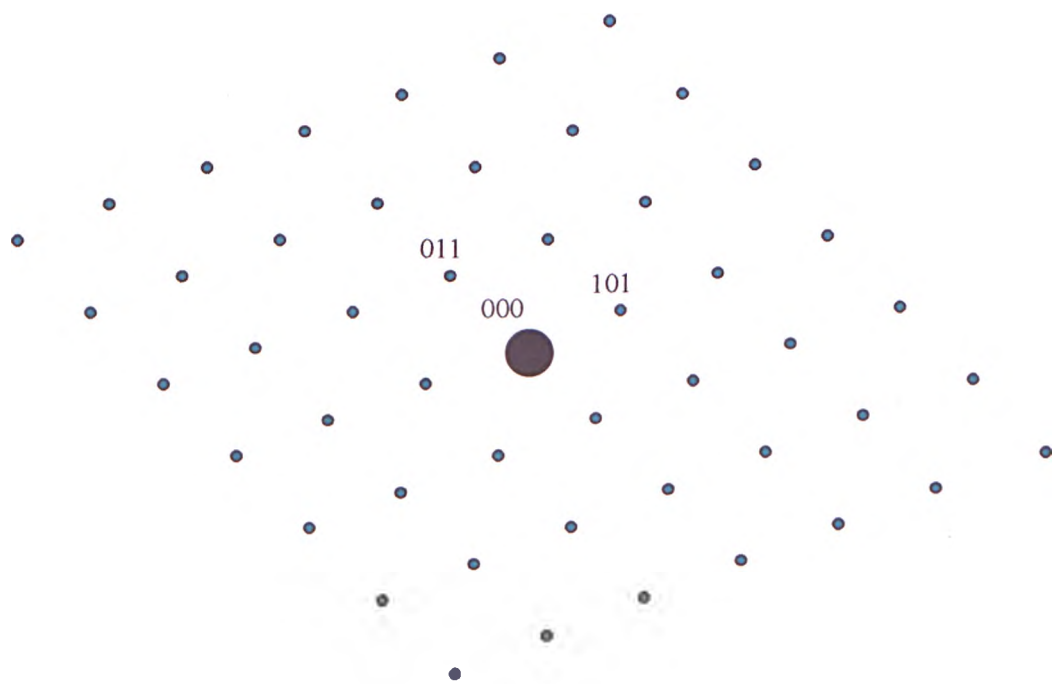

(b)

Figure 4- 74: a) Optical diffraction pattern for HREM of Figure 4- 73 from [$1\,1\,\bar{1}$] zone axis, b) indexed schematic of a.

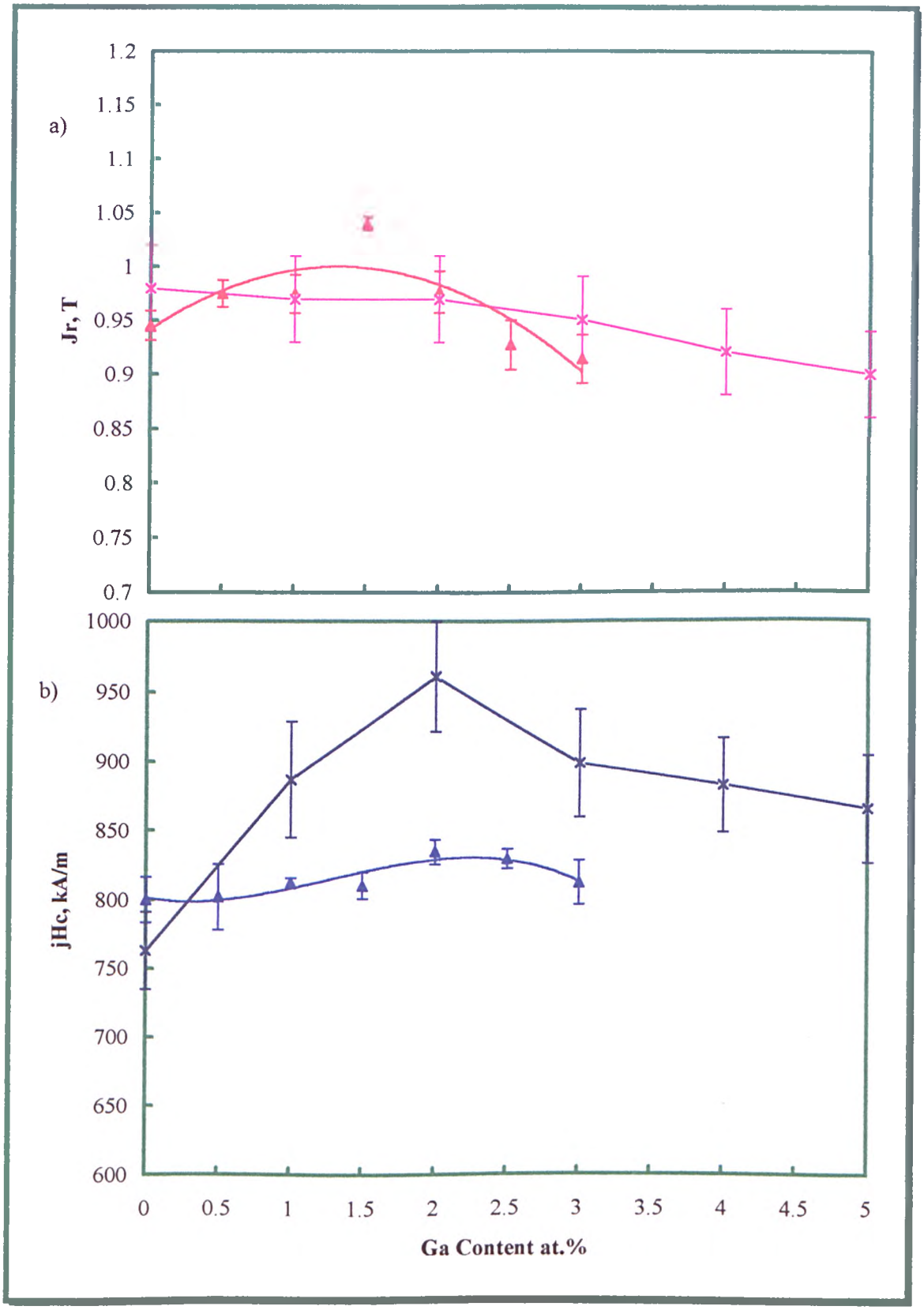

Figure 5- 1: Effect of gallium addition on the remanence and coercivity of directly quenched $Nd_{11.8}Fe_{82.36-x}B_{5.88}Ga_x$ ribbons (Δ) together with those values obtained by Liu et al. [202] for the same alloys melt spun at 20 m/s (*).

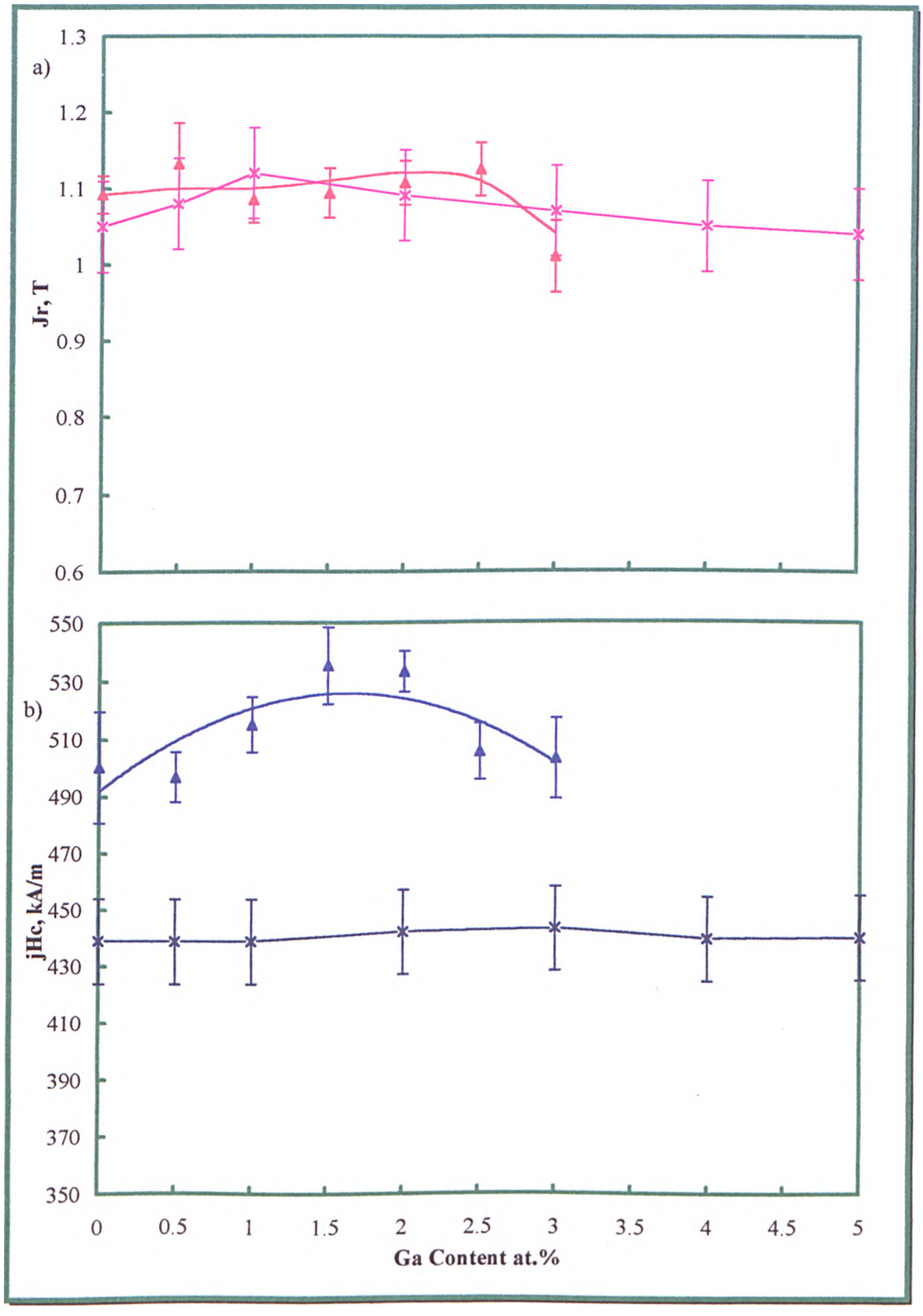

Figure 5- 2: Effect of gallium addition on the remanence and coercivity of directly quenched $Nd_9Fe_{85-x}B_6Ga_x$ ribbons (Δ) together with those values obtained by Liu et al. [202] for the same alloys melt spun at 19 m/s (*).